INFORMATION TO USERS

This manuscript has been reproduced from the microfilm master. UMI films the text directly from the original or copy submitted. Thus, some thesis and dissertation copies are in typewriter face, while others may be from any type of computer printer.

The quality of this reproduction is dependent upon the quality of the copy submitted. Broken or indistinct print, colored or poor quality illustrations and photographs, print bleedthrough, substandard margins, and improper alignment can adversely affect reproduction.

In the unlikely event that the author did not send UMI a complete manuscript and there are missing pages, these will be noted. Also, if unauthorized copyright material had to be removed, a note will indicate the deletion.

Oversize materials (e.g., maps, drawings, charts) are reproduced by sectioning the original, beginning at the upper left-hand corner and continuing from left to right in equal sections with small overlaps. Each original is also photographed in one exposure and is included in reduced form at the back of the book.

Photographs included in the original manuscript have been reproduced xerographically in this copy. Higher quality 6" x 9" black and white photographic prints are available for any photographs or illustrations appearing in this copy for an additional charge. Contact UMI directly to order.

UMI

A Bell & Howell Information Company
300 North Zeeb Road, Ann Arbor MI 48106-1346 USA
313/761-4700 800/521-0600

Heat conduction in unconventional superconductors

Benoit Lussier
Centre for the Physics of Materials
Department of Physics, McGill University
Montréal, Québec, Canada

A Thesis submitted to the
Faculty of Graduate Studies and Research
in partial fulfillment of the requirements for the degree of
Doctor of Philosophy

Je dédie cette thèse à mon épouse, à ma famille, et à ma grand-mère

CONTENTS

FIGURES AND TABLES

FIGURES

TABLES

RÉSUMÉ

La conductivité thermique est une excellente sonde des quasiparticules électroniques présentes dans les phases supraconductrices et normales des supraconducteurs. Nous avons utilisé cette technique pour l'étude de deux supraconducteurs non-conventionnels, soit le composé à fermions lourds UPt_3 et le supraconducteur à haute température critique $YBa_2Cu_3O_{7-\delta}$.

Dans le cas de UPt_3, nous démontrons pour notre cristal de haute pureté, que la conductivité thermique est complètement dominée par les électrons, fournissant ainsi une sonde directe de la symétrie du gap supraconducteur. Nous soulignons que nos mesures de l'anisotropie entre les axes b et c de ce cristal hexagonal restreignent le nombre de candidats possibles pour la symétrie du gap telle que déduite à partir d'arguments de théorie des groupes. En comparant nos résultats à des calculs récents, nous concluons qu'un gap de symétrie hybride II fournit un bon accord entre la théorie et l'expérience. Ceci favorise un paramètre d'ordre de symétrie E_{2u} dans le cas d'un couplage spin-orbite fort, ou A_{2u} pour un couplage spin-orbite faible.

Pour $YBa_2Cu_3O_{7-\delta}$, la conductivité thermique possède une contribution électronique et phononique. Nous mettons en évidence la présence d'un terme de nature électronique, même à des températures $\sim T_c/1000$. Ceci est une indication claire de la présence d'un gap supraconducteur non-conventionel dans ce composé. Par la suite, nous présentons notre étude de dopage au zinc dans $YBa_2Cu_3O_{7-\delta}$ et démontrons la présence d'un régime *universel* à T=0. L'ordre de grandeur de ce terme électronique residuel est très près de la valeur prédite par certaines théories récentes. Nos résultats confirment la validité d'une approche "diffusion résonnante par les impuretés" dans les supraconducteurs à haute température critique, et l'excellent accord avec la théorie renforce l'énoncé que la symétrie du gap dans $YBa_2Cu_3O_{7-\delta}$ est de type $d_{x^2-y^2}$.

Finalement, nous présentons des mesures de diffusion de neutrons dans UPt_3. Dans ce chapitre, nous étudions la dépendance en champ magnétique du moment antiferromagnétique dans le plan de base. Nous montrons qu'un champ magnétique de l'ordre de 3 Tesla n'a aucun effet sur l'ordre magnétique: le champ ne peut ni sélectionner un domaine magnétique, ni induire une rotation des moments. Très simples en apparence, ces résultats ont un impact important sur les théories du diagramme de phase supraconducteur de UPt_3.

ABSTRACT

Thermal conductivity is an excellent probe of quasiparticle excitations in superconductors both in the normal and superconducting state. We have applied this technique to the study of two unconventional superconductors, namely the heavy fermion superconductor UPt_3 and the high-T_c cuprate $YBa_2Cu_3O_{7-\delta}$.

In the case of UPt_3, after reviewing previous low temperature thermal conductivity measurements, we show that, for our high quality single crystals, the thermal conductivity is totally dominated by electrons and therefore provides a direct probe of the superconducting gap structure. We demonstrate that our measurements of the anisotropy of heat conduction between b-axis and c-axis in this hexagonal crystal provide strong constraints with respect to the possible gap structures inferred by group theoretical arguments. By comparing our results with recent theoretical calculations, we show that a hybrid II gap structure provides good agreement between theory and experiments favoring an order parameter of E_{2u} (strong spin-orbit coupling) or A_{2u} (weak spin-orbit coupling) symmetry.

For $YBa_2Cu_3O_{7-\delta}$, the thermal conductivity typically consists of both a phononic and an electronic contribution. After reviewing low temperature thermal conductivity measurements that address this question, we demonstrate the presence of electronic quasiparticles even at temperatures of $\sim T_c/1000$, a clear indication of an unconventional gap structure. We then proceed to discuss zinc doping studies in $YBa_2Cu_3O_{7-\delta}$ and show that we find a *universal* residual linear term at T=0 of a magnitude very close in value to that predicted by recent theories. These results validate the approach of resonant impurity scattering in the high-T_c, and our excellent agreement with theory reinforces the view that the gap structure in $YBa_2Cu_3O_{7-\delta}$ is of $d_{x^2-y^2}$ symmetry.

Finally, we present neutron scattering results in UPt_3. In this chapter, we study the magnetic field dependence of the antiferromagnetic moment lying in the basal plane. We find that magnetic fields of order 3 Tesla have no effect on the magnetic order: it can neither make the sample a magnetic monodomain in field cooling nor can it rotate the moment. The results, very simple in appearance, have profound consequences for the superconducting phase diagram of this heavy-fermion compound.

STATEMENT OF ORIGINALITY

The following thesis reports on new contributions I have made to scientific knowledge. I briefly outline those here:

- My thermal conductivity results on UPt_3 are the first instance of the successful use of heat conduction to probe the superconducting gap anisotropy in an unconventional superconductor. One similar attempt had previously been made on UPt_3 by another group but with no success. This original contribution has lead several theorists to use my data in comparing their calculations to experiments, and a comprehensive understanding of heat transport in UPt_3 is near.

- A systematic study of high-quality zinc-doped crystals of $YBa_2Cu_3O_{7-\delta}$ had never been performed at low temperature. I provide the first firm evidence for a universal transport coefficient at $T \rightarrow 0$ in any superconductor. This confirms current theories of transport in unconventional superconductors based on a d-wave gap and resonant impurity scattering. Having shown that the conventional analysis of low temperature data in $YBa_2Cu_3O_{7-\delta}$ made by most other groups is not adequate, I provide a way of accounting for my low temperature thermal conductivity results over the whole temperature range covered by the experiments.

- Finally, my neutron scattering results are also an original contribution. The behavior of the magnetic moments in UPt_3 had been taken for granted without any measurements as to the domain behavior and possible reorientation of the moments in the presence of a magnetic field. The simple result of no rotation and no domain re-population has profound implications for theories of the phase diagram in UPt_3.

I should stress that these experimental results were only possible after a large amount of time was invested in designing a reliable thermal conductivity setup and several problems (wiring, sample mounts, thermometry, electronics, ...) linked with the installation of a new dilution refrigerator were solved. This occupied a great deal of my first years at McGill. I can say that most problems were solved and that thermal conductivity results can now be routinely obtained in our lab at temperatures down to 50 mK.

My work at McGill has led to the following publications:

1. *Published work*

   - B. Lussier, B. Ellman, and L. Taillefer. Anisotropy of heat conduction in the heavy fermion superconductor UPt_3. *Phys. Rev. Lett.*, 73:3294-3297, 1994.
   - B. Lussier, B. Ellman, and L. Taillefer. Determination of the gap structure in UPt_3 by thermal conductivity. *Phys. Rev. B*, 53:5145-5148, 1996.
   - B. Lussier, L. Taillefer, W. J. L. Buyers, T. E. Mason, and T. Petersen. Influence of a magnetic field on the antiferromagnetic order in UPt_3. *Phys. Rev. B*, 54:R6873-R6876, 1996.

2. *Publications to appear*

   - M. Chiao, B. Lussier, B. Ellman, and L. Taillefer. Heat conduction in the heavy fermion superconductor UPd_2Al_3. *Physica B, Proceedings SCES96*, to be published.
   - L. Taillefer, B. Ellman, B. Lussier, and M. Poirier. On the gap structure of UPt_3: phases A and B. *Physica B, Proceedings SCES96*, to be published.

3. *Papers in preparation*

   - B. Ellman, M. Sutton, B. Lussier, R. Brüning, L. Taillefer, S. Hayden, and G. Shea-McCarthy. Search for structural modulations in UPt_3 using Laue X-ray diffraction. *preprint*, 1996.
   - B. Lussier, R. Gagnon, L. Taillefer, H. Aubin, and K. Behnia. Universal heat conduction in $YBa_2Cu_3O_{7-\delta}$. *preprint*, 1996.

ACKNOWLEDGMENTS

I did start by writing conventional acknowledgements but it turned out I had too many people to thank for so many reasons. So I decided that since I have borrowed Martin Lacasse's thesis format, I might as well steal his check-in boxes acknowledgements. But before, there are a few persons that I should thank personally.

L'approche de Louis vis-à-vis un problème est toujours calme, posée et systématique. Après avoir vaincu ma peur de toujours le déranger dans son bureau, j'ai pu m'imprégner de cette approche et je dois dire que ca m'a beaucoup rapporté. Il m'a permis de démystifier les théories en apparence si compliquées mais dont les résultats se résument souvent en une ligne. Il est inutile d'énumérer tout ce qu'il m'a appris, mais il est certain qu'il a joué un rôle majeur autant pour ma formation de scientifique que pour le support moral dans les moments difficiles. Merci Louis.

Et oui, Robert mérite son propre paragraphe de remerciements ! Premièrement pour son assistance technique, sa dextérité légendaire pour monter les cristaux microscopiques et son devouement sans borne pour contribuer à l'avancement de la science (ou plutôt de ma thèse), même lorsque cela implique de revenir au labo plusieurs soirées pendant ses vacances pour me sortir du pétrin. Je tiens aussi à le remercier pour toutes ses histoires drôles et juteuses.

Despite his unpredictable mood swings that swept the lab like a tornado, Brett was a big help especially at the beginning when I knew close to nothing with regards to low temperature physics. He taught me that, NO, dilution fridge experiments are not like helium experiments where the temperature is simply lower. He also showed me how to cope with frustrating ground loops, where to randomly add a capacitor to cut high frequency noise, namely what it ment to be a good experimentalist.

The funding organizations also deserve special thanks, without them none of the fun we have working in physics would be possible. Thanks to Conseil de recherche en sciences naturelles et génie, Fonds pour la formation de chercheurs et l'aide à la recherche, the Centre for the Physics of Materials and the Canadian Institute for Advanced Research for their generous contributions to my financial well-being.

Je tiens tout particulièrement à remercier ma famille pour son support constant tout au long de mes études, pour les petits coups de pouce occasionels et pour sa compréhension pour mes visites peu fréquentes même si j'habite à quelques minutes.

Finalement, je voudrais remercier mon épouse Julie pour son soutien, sa patience

et son intarissable support pendant les moments difficiles.

For the rest of you who also deserve special attention but are too numerous to name, thanks for (check where appropriate):

◯ your friendship;

◯ providing me with food and/or entertainment for those long nights around the fridge;

◯ saying "ATTENTION" everytime we met in the hallway;

◯ the nice and interesting discussions we had about physics;

◯ the nice and interesting discussions we had about anything else;

◯ proof-reading this thesis;

proof-reading this thesis over and over and over again;

avoir fait parti de la mafia séparatisssse de McGill. Je vous remercie pour les dîners causeries passés à discuter de l'oppression fédérale, des excellents (sic) éditoriaux de Diane Francis, de l'excellent journalisme objectif (sic encore) de CTV et de The Gazette, et j'en passe. Merci aussi aux bons joueurs fédéralistes qui ont encaissé les coups sans broncher mais qui, malheureusement, concervent quand même la foi dans un régime fédéral.

◯ being a member of the McGill staff and coping with my unreasonable demands;

◯ being a member of the McGill staff and coping with my unreasonable demands on week-ends, during your vacation or outside *normal* working hours;

◯ being patient, persistent and understanding when I kept whining about LaTeX, Unix, postscript and the rest of the computer related crap;

◯ trying to make an X-ray scattering experimentalist out of me but failing. I did really enjoy this goose chase in k-space;

◯ trying to make a neutron scattering experimentalist out of me and partly succeeding. Working in Chalk River with you guys was really a great learning experience;

providing me with stuff, specifically Robert Cochrane for the sputtered heaters, Petru Ciuranu for the use of the wire bonding machine, Sid Kreitzman for the ruthenium-oxyde thermometers, and Kamran Behnia for the non-superconducting solder, the vespel and the strain-gauge heater idea;

◯ organizing, attending or funding the CIAR summer schools;

◯ the violent hockey games we played;

◯ something I did not mention above;

◯ something I could not mention above.

Benoit Lussier

Montréal, Novembre 1996

Heat conduction in unconventional superconductors

1

INTRODUCTION

Since the late 1970's, great achievements in the field of superconductivity have reshaped the landscape of solid-state physics especially with regards to strongly correlated electron systems. It all began with the discovery of superconductivity in the heavy fermion materials, first in $CeCu_2Si_2$ by Steglich *et al.* [1]. This discovery was very surprising since these materials are close to magnetic instabilities and in some cases, superconductivity was found to coexist with magnetic order. There are, at present, six heavy fermion superconductors all with a transition temperature below 2 K. In 1986, the work of Bednorz and Müller [2] opened the ever growing field of high-T_c superconductivity. Their discovery of superconductivity in $(La,Sr)_2CuO_4$ in the 30 K range was followed by a worldwide investigation of copper-oxide systems resulting in the synthesis of new families of systems each with a higher superconducting transition temperature now reaching up to 150 K. Even though both classes of systems have superconducting transition temperatures differing by two orders of magnitude, they share common features: both are strongly correlated electron systems, both are close to magnetic instabilities and both are thought to be unconventional superconductors[1]. Other classes of unconventional superconductors have been discovered, such as the organic superconductors (for a review see [3]). In this thesis, all of our attention will be devoted to the heavy fermions, represented by UPt_3 ($T_c = 0.5$ K), and to the high-T_c cuprates, represented by $YBa_2Cu_3O_{7-\delta}$ ($T_c = 93$ K for δ=0.1).

Heavy fermions systems are inter-metallic compounds containing rare-earth or actinide ions whose *f*-shell electrons are only slightly delocalized and therefore strongly correlated. These systems display a variety of ground states such as antiferromagnetic order in U_2Zn_{17} and UCd_{11}, no order at all in $CeAl_3$ and $CeCu_6$, and superconductivity

[1] What we mean by *unconventional superconductor* will be defined in section 2.3.

in $CeCu_2Si_2$ (0.6 K), UBe_{13} (0.9 K), UPt_3 (0.5 K), URu_2Si_2 (1.2 K), UNi_2Al_3 (1 K), and UPd_2Al_3 (2 K). It should be noted that in four out of the six superconductors the superconducting order is preceeded by magnetic order with $T_N \sim 10T_c$ *i.e.* UPt_3 (T_N = 5 K), URu_2Si_2 (T_N = 17 K), UNi_2Al_3 (T_N = 5 K), and UPd_2Al_3 (T_N = 14 K). The magnetic order is found to coexist with superconductivity. The name heavy-fermion arises from the large effective masses that can be deduced from the electronic linear term γ in the specific heat. For an ordinary metal, the γ-value is of the order of 1–10 mJ/K^{2}mol. For heavy-fermion systems, it ranges from 400 to 1000 mJ/K^{2}mol or more *i.e.* a factor up to 10^2 to 10^3 times larger. In this thesis, our attention will be focussed on UPt_3 as this material is the most studied of all heavy fermion compounds because it shows the strongest evidence for unconventional superconductivity.

The high-T_c cuprates are all highly anisotropic oxides and belong to the wide class of perovskites. They are characterized by two-dimensional copper-oxygen planes from where the superconductivity is thought to arise. Some widely studied materials in this class include $La_{2-x}Sr_xCuO_4$ (T_c=38 K), $YBa_2Cu_3O_7$ (T_c=93 K), $Bi_2Ca_2Sr_2Cu_3O_{10}$ (T_c=110 K), and $Tl_2Ca_2Ba_2Cu_3O_{10}$ (T_c=125 K). We concentrate on $YBa_2Cu_3O_{7-\delta}$. Note that this compound can have its properties tuned by changing the oxygen concentration (*i.e.* δ). It is an insulating antiferromagnet for δ=1 while it becomes superconducting for $\delta \lesssim 0.6$.

The thesis is divided as follows. Chapter 2 outlines the basic properties of simple metals, conventional and unconventional superconductors, all in the context of heat transport. Chapters 3 and 4 review the basic properties of the two compounds with respect to normal and superconducting state properties. Chapter 5 summarizes the experimental aspects of our thermal conductivity setup. In chapters 6 and 7, a brief review of previous thermal conductivity measurements is given, followed by the presentation and discussion of the measurements we have performed. A detailed comparison between our experimental data and current theories of transport in unconventional superconductors is made. Before concluding the thesis, our neutron diffraction results on UPt_3 are presented, and their implications on the phase diagram will be discussed in light of recent theoretical developments.

2

THERMAL CONDUCTIVITY: A REVIEW

2.1 *Heat transport in metals*

In this section, we present an outline of transport theory for both charge and heat as applied to typical metals. We will derive the well-known equations for electrical ($\sigma = \frac{ne^2\tau}{m}$) and thermal ($\kappa_e = \frac{1}{3}c_V v_F^2 \tau$) conductivities, whose terms will be defined later. This will serve to illustrate one fundamental property of metals, namely the Wiedemann-Franz law. We will then proceed to discuss the possible scattering mechanisms that can diminish the conduction of charge and heat, whereby the infinite conductivity derived via Bloch's formalism becomes finite in the presence of lattice vibrations (which scatter electrons) and static defects. The reader is also referred to the book by Abrikosov [4] for a more detailed treatment of the Boltzmann equation, while the book by Berman [5] gives a longer discussion on the applicability of the Wiedemann-Franz law and transport by phonons. Furthermore, the paper by Klemens [6] (and references therein) discusses in detail the various scattering mechanisms. Before the derivation of transport theory, we briefly sketch the general behavior of the electrical and thermal conductivities in a typical metal, *i.e.* one for which the electronic contribution to thermal conductivity is much larger than the phonon contribution at all temperatures.

In a solid, heat is conducted by electrons, phonons, magnetic excitations, etc., namely:

$$\kappa = \kappa_e + \kappa_{ph} + ... \tag{2.1}$$

In typical metals, the heat transport is totally dominated by electrons while in dirty alloys both phonons and electrons have comparable contributions. In insulating solids, only phonons carry heat.

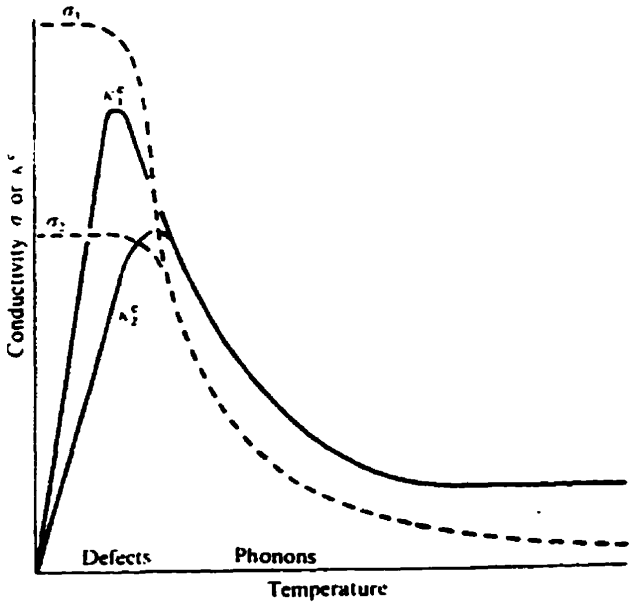

Figure 2.1: Electrical (σ) and electronic thermal (κ^e) conductivities of a metal as a function of temperature. The dominant electron scattering mechanisms are indicated along the abscissa. The upper curves in each case are for more perfect specimens than the lower curves (after [5]).

Figure 2.1 displays the electrical and thermal conductivities of a metal as a function of temperature along with the electron-scattering mechanisms responsible for the shape of the curve. At high temperatures, the effectiveness of the lattice in scattering electrons is proportional to the lattice vibrational energy, which in turn is proportional to temperature. The mean-free path ℓ is then inversely proportional to T and so is the electrical conductivity. As the temperature is decreased, phonons are less effective in limiting the mean-free path and the increase in conductivity is faster than the 1/T regime established at higher temperatures. Eventually, the electronic mean-free path reaches a constant value determined by elastic scattering, *i.e.* impurities or imperfections in the lattice and the electrical conductivity becomes constant. As for the thermal conductivity, it is a constant at high temperatures because the specific heat is linear in temperature (as long as $k_B T \ll \varepsilon_F$) while the mean-free path is again inversely proportional to temperature. As the temperature is reduced, the heat conduction changes from being a constant to varying as $1/T^2$ because the scattering time for electron-phonon processes is proportional to T^{-3}. At the lowest temperature, the mean-free path being a constant, the only temperature dependence remaining is that of the specific heat and the thermal conductivity is linear.

2.1.1 Charge transport

We start this discussion with the Boltzmann equation, which states that the driving force is equal to the dissipative effects of collisions. The central quantity is the non-equilibrium distribution function f.

$$\frac{\partial f}{\partial t} - \frac{e\vec{E}}{\hbar}\vec{\nabla}_k f + \vec{v}\cdot\vec{\nabla}_r f = \left(\frac{\partial f}{\partial t}\right)_{coll} \tag{2.2}$$

with $\vec{v}$ the velocity and $\vec{E}$ the electric field.

The collision term on the right hand side of equation 2.2 is very difficult to calculate from first principles. One often makes the relaxation-time approximation:

$$\left(\frac{\partial f}{\partial t}\right)_{coll} = -\frac{f(\vec{k}) - f_0(\vec{k})}{\tau_k} \tag{2.3}$$

where f_0 is the equilibrium distribution, namely the Fermi function $f_0 = \left(\exp\left(\frac{\epsilon-\mu}{k_B T}\right) + 1\right)^{-1}$ and τ is the relaxation time[1]. This approximation is exact for an isotropic Fermi surface, isotropic impurity scattering and for a spatially homogeneous temperature gradient [4].

We now focus on the conduction of charge in a metal. When an electric field is applied, it causes variation in the k-space distribution leading to a non-zero $\vec{\nabla}_k f$ term. In steady-state conditions and with no spatial inhomogeneties, the first and third terms on the left hand side of equation 2.2 are zero and to first order:

$$\vec{\nabla}_k f \approx \vec{\nabla}_k f_0 = \frac{\partial f_0}{\partial \epsilon_k}\vec{\nabla}_k \epsilon_k = \vec{v}_k \frac{\partial f_0}{\partial \epsilon_k} \tag{2.4}$$

Substituting in equation 2.2 and making use of the relaxation time approximation, we get:

$$f_k - f_0 = -e\vec{E}\cdot\vec{v}_k\tau_k\frac{\partial f_0}{\partial \epsilon_k} \tag{2.5}$$

The expression for the electric current is simply:

$$\vec{j}_e = 2\sum_{\substack{all\\states}}\begin{pmatrix} distribution\ function \\ displaced\ from\ equilibrium\end{pmatrix}(charge\ carried)(velocity) \tag{2.6}$$

$$= 2\int [f_k - f_0] e\vec{v}_k \frac{d^3k}{(2\pi)^3} \tag{2.7}$$

[1] The scattering rate Γ, which will be discussed later in the thesis, is simply the inverse of the scattering time *i.e.* $\Gamma = 1/\tau$.

Inserting equation 2.5 into the last expression, changing the integration over k into an integral over energy and carrying out the angular integration, we get:

$$\vec{j}_e = -\frac{1}{3}e^2 v_F^2 \tau_N \vec{E} \int_0^{+\infty} \frac{\partial f_0}{\partial \varepsilon} N(\varepsilon) d\varepsilon \tag{2.8}$$

where we have assumed an isotropic Fermi surface (*i.e.* $v_k \rightarrow v_F$) and isotropic scattering (*i.e.* $\tau_k \rightarrow \tau_N$)[1]. To first order $\frac{\partial f_0}{\partial \varepsilon}$ is a δ-function centered at the Fermi level (*i.e.* $\int \frac{\partial f_0}{\partial \varepsilon} F(\varepsilon) d\varepsilon = -F(\varepsilon_F) + ...$). The charge current then becomes:

$$\vec{j}_e \simeq \frac{1}{3}e^2 v_F^2 \tau_N N(\varepsilon_F) \vec{E} \tag{2.9}$$

up to corrections of order $(k_B T)^2 / \varepsilon_F^2$. By replacing the density of states at the Fermi level by the known result $N(\varepsilon_F) = \frac{3n}{2\varepsilon_F} = \frac{3n}{m v_F^2}$ and making use of the definition of the electrical conductivity which states that $\vec{j}_e = \sigma \vec{E}$, we get the well known result:

$$\sigma = \frac{n e^2 \tau_N}{m} \tag{2.10}$$

2.1.2 *Electronic thermal conductivity*

We now turn to the heat conduction by electrons in a metal. We again apply the Boltzmann equation 2.2 to heat transport. In this case, the presence of a temperature gradient causes the spatial gradient term $\vec{\nabla}_r f$ to be non-zero. In steady-state conditions and with no electromagnetic forces, the first two terms on the left hand side of equation 2.2 are zero. Using the relaxation-time approximation, we then get:

$$f_k - f_0 = -\tau_k \vec{v} \cdot \vec{\nabla}_r f_k \tag{2.11}$$

To first order, we can replace $\vec{\nabla}_r f$ by $\vec{\nabla}_r f_0$. Then making use of the fact that f_0 is the Fermi function, we get:

$$\vec{v} \cdot \vec{\nabla}_r f_0 = \vec{v}_k \cdot \vec{\nabla} T \frac{\partial f_0}{\partial T} = -\frac{\varepsilon_k}{T} \frac{\partial f_0}{\partial \varepsilon_k} \vec{v}_k \cdot \vec{\nabla} T \tag{2.12}$$

[1] The *s*-wave scattering approximation will always be used even when we discuss resonant impurity scattering. The implications of this is that the scattering rate does not depend on the initial direction of the electron but depends only on energy. When discussing superconductors, special attention has to be given in order to avoid confusion between *s*-wave scattering, *s*-wave potential and *s*-wave gap.

Equation 2.11 then reduces to:

$$f_k - f_0 = -\varepsilon_k \tau_k \vec{v}_k \cdot \frac{\vec{\nabla} T}{T} \frac{\partial f_0}{\partial \varepsilon_k} \tag{2.13}$$

The heat current due to an electron with wavevector k is given by the product of the thermal energy of that mode and the velocity of propagation times the distribution function, namely:

$$\vec{j}_q = 2 \sum_{\substack{all \\ states}} \begin{pmatrix} distribution\ function \\ displaced\ from\ equilibrium \end{pmatrix} (energy\ carried)\,(velocity) \tag{2.14}$$

$$= 2 \sum_k [f_k - f_0] \varepsilon_k \vec{v}_k \tag{2.15}$$

$$= -\frac{2}{T} \sum_k \mu_i^2 \varepsilon_k^2 \frac{\partial f_0}{\partial \varepsilon_k} v_k^2 \tau_k \vec{\nabla} T \tag{2.16}$$

where μ_i is the direction cosine *i.e.* $\cos\theta$ where θ is the angle with respect to the temperature gradient axis. Again, we assume an isotropic Fermi surface and isotropic scattering. Substituting and changing the summation over momentum into an integration over energy:

$$\vec{j}_q = -\left\{ v_F^2 \tau_N \frac{2}{T} \int_0^{+\infty} \varepsilon^2 \frac{\partial f_0}{\partial \varepsilon} N(\varepsilon) d\varepsilon \int \cos^2\theta \frac{d\Omega}{4\pi} \right\} \vec{\nabla} T \tag{2.17}$$

Carrying out the angular integration, and using the definition of thermal conductivity $\vec{j}_q = -\kappa_e \vec{\nabla} T$, we get:

$$\kappa_e = \frac{1}{3} c_V v_F^2 \tau_N \tag{2.18}$$

where we have made use of the fact that:

$$c_V = \frac{d}{dT} \int \varepsilon N(\varepsilon) f_0(\varepsilon) d\varepsilon = -\frac{1}{T} \int \varepsilon^2 N(\varepsilon) \frac{\partial f_0}{\partial \varepsilon} d\varepsilon \tag{2.19}$$

2.1.3 The Wiedemann-Franz law

Integrating equation 2.19 and writing it in terms of the density of states at the Fermi level, we get:

$$c_V \approx \frac{\pi^2}{9} N(\varepsilon_F) k_B^2 T \tag{2.20}$$

up to corrections of order $k_B T / \varepsilon_F$. Inserting this expression into that for the thermal conductivity and assuming the same scattering time for both thermal and electrical

relaxation processes, we get:

$$\frac{\kappa_e}{\sigma T} = \frac{\pi^2 k_B^2}{3e^2} \tag{2.21}$$

Equation 2.21 is called the Wiedemann-Franz (WF) law while the ratio $\frac{\kappa_e}{\sigma T}$ is the Lorenz number. The constant $\frac{\pi^2 k_B^2}{3e^2} = L_0 = 2.44 \times 10^{-8}$ WΩK^{-2} is the Sommerfeld value.

We now discuss the validity of the Wiedemann-Franz law. Since the electronic charge is fixed, the only way collisions can degrade an electric current is by changing the momentum of the electrons. In analogy with the electrical conductivity, for thermal conductivity, the "charge" carried by the electron is simply the energy of that electron. Therefore, in the case of elastic collisions, the energy will be conserved and both the thermal and electric currents will be degraded in the same way hence the Wiedemann-Franz law holds. However, in the case of inelastic collisions, the thermal current has a degradation mechanism with no analog in electrical current (*i.e.* charge is conserved but not the kinetic energy) and the Wiedemann-Franz law is expected to fail.

At low temperatures, the main scattering mechanism for electrons comes from impurities. This being an elastic process, the WF law holds and the thermal conductivity is simply $\frac{\kappa}{T} = \frac{L_0}{\rho_0}$ with ρ_0 the residual electrical resistivity. The law will also hold if scattering by phonons involves large changes in momentum as is the case for Umklapp processes. Such processes occur at high temperature, namely for $T > \theta_D$. As discussed at the beginning of section 2.1, in this temperature range, κ_e is constant while $\sigma \propto 1/T$ and the WF law is obeyed. Therefore, as the temperature is reduced, the WF law breaks down when the dominant phonons have such small wavevectors that they cannot bring about, in one collision, the large wavevector changes needed to produce electrical resistance, but can yet bring about the small wavevector changes effective in causing thermal resistance (by inelastic scattering). Finally, in the presence of electron-electron interactions (an inelastic process) one finds again $\frac{\kappa_e}{\sigma T} < L_0$. This effect is small in simple metals such as nickel [7] (since the electron-electron interaction is small), but is much larger in heavy-fermion compounds like UPt_3 (see section 6.2).

2.1.4 Scattering mechanisms

We now turn to the various scattering mechanisms which can impede the flow of heat, thereby causing thermal resistivity. The discussion will cover phonons and electrons separately. In UPt_3 (see section 6.3), we will show that the electrons are the dominant carriers of heat over the whole temperature range. This is not the case for $YBa_2Cu_3O_{7-\delta}$ and inclusion of phonons and their various scattering mechanisms is necessary.

Table 2.1: Frequency variation of the scattering rate and low-temperature dependence of the thermal conductivity for phonon heat carriers in the presence of various scattering mechanisms (after [6]).

Phonons

Scattering mechanism	$\Gamma(\omega)$	$\kappa_{ph}(T)$
Boundaries	ω^0	T^3
Mosaic + stacking faults	ω^2	T^1
Phonon-electron	ω^1	T^2
Dislocations (strain field)	ω^1	T^2
Dislocations (core)	ω^3	T^0
Point defects	ω^4	T^{-1}
Umklapp processes	-	$T^3 e^{\theta/\alpha T}$
Tunneling states	-	T^2

Table 2.1 compiled by Klemens [6] summarizes the various scattering mechanisms affecting phonons heat carriers, their frequency variation and the temperature dependence of the thermal conductivity (κ_{ph}) when the process dominates. For each item in the table, we give a short definition (see [5, 6, 8] and references therein):

1. *Boundaries.* The external boundaries of a crystal or the grain boundaries in a polycrystalline solid can limit the heat conduction. Such boundaries give rise to a scattering rate independent of frequency and the heat conduction is then proportional to the phonon specific heat, which at low temperature goes as $\sim T^3$. In this case and for a sample with rough surfaces (diffuse scattering), the phonon mean-free path is simply the smallest dimension of the crystal for

single-crystals or the average size of the grains composing a polycrystal.

2. *Mosaic and stacking faults.* Sheet-like faults and crystal mosaic causes phonon scattering due to the small difference in orientation of the domains. The scattering rate is proportional to ω^2 and the thermal resistivity to T^{-1}. Stacking faults also behave in a way similar to mosaic and have the same frequency dependence of the scattering rate.

3. *Phonon-electron.* When the phonon conduction is limited by conduction electrons, the scattering rate is proportional to ω^1 and the thermal resistivity is proportional to T^{-2}.

4. *Dislocations.* The main features of the scattering by static dislocations can be deduced by considering separately the effects of the core and of the surrounding strain field. The core of a dislocation consists of a narrow region along its axis, within which there is a drastically altered structure which can be represented by a change in density. As for the strain field from a dislocation, it can be understood with the following analogy borrowed from optics: owing to the anharmonicity in real crystals, the strain alters the phonon velocity and this corresponds to a change in refractive index so that the wave deviates upon passing through the strained material. The core (strain field) leads to a ω^3 (ω^1) dependence in the scattering rate resulting in a T^0 (T^2) dependence of the thermal conductivity.

5. *Point defects.* A defect which extends over a volume with linear dimensions much smaller than the phonon wavelength can be considered a point defect. An atom on the wrong lattice site substituting for the correct atom[1], a vacancy at a lattice site, an interstitial atom, or a combination of these are all candidates for a point defect. The scattering is then caused by the difference in mass and the

[1] We illustrate this in the case of UPt_3 for two cases: substitutional impurity and disorder. In the first case an impurity atom can substitute for one of the atoms of the compound, for example a Pd atom is found on a Pt site. The second case refers to disorder within the compound: a U atom is located on a Pt site or vice-versa.

difference in bonding between the atoms. Point defects have a ω^4 dependence on the scattering rate leading to a thermal conductivity varying as T^{-1}.

6. *Umklapp processes.* Umklapp processes are elastic and involve three phonons. The process obeys the conservation of energy, and the conservation of momentum involves a reciprocal lattice vector $\vec{g}$: $\vec{k}_1 + \vec{k}_2 = \vec{k}_3 + \vec{g}$. Such processes can be shown to be dominant at high temperatures in insulating crystals with their thermal conductivity varying as $T^3 e^{\theta/\alpha T}$. Due to the exponential behavior, this scattering mechanism will be neglected at low temperatures.

7. *Tunneling states.* The tunneling states model was developed by Phillips [9] and by Anderson *et al.* [10] to explain the non-Debye behavior of glassy materials at low temperatures. These materials showed an unexpectedly large specific heat with an unusual T^2 variation in the thermal conductivity. The model is based on the idea that in a disordered solid, certain atoms or groups of atoms can occupy two different configurational sites represented by a double-well potential. Because of the amorphous state, one expects a broad distribution of potential barriers, and consequently a wide range of tunneling-state relaxation times. In these conditions, it is possible to show that the thermal conductivity will have a quadratic temperature dependence.

Once again, by using the Boltzmann equation formalism in the relaxation-time approach, the thermal conductivity for phonon heat carriers can be derived (see for example [5]):

$$\kappa_{ph} = \frac{k_B}{2\pi^2 v_{ph}} \left(\frac{k_B}{\hbar}\right)^3 T^3 \int_0^{\theta/T} \tau(x) \frac{x^4 e^x}{(e^x - 1)^2} dx \qquad (2.22)$$

with θ the Debye temperature, v_{ph} an average phonon velocity and $x = \hbar\omega/k_B T$. The scattering time $\tau(x)$ is simply the inverse of the sum of the various scattering rates (*i.e.* Matthiesen's rule $\tau^{-1} = \sum_i \tau_i^{-1}$) listed in table 2.1 relevant to the crystal under investigation. When the phonon velocities are known, the average phonon velocity v_{ph} is given by $v_l(2s^2 + 1)/(2s^3 + 1)$ (see [5]) where s is the ratio of longitudinal to transverse phonon velocity, v_l/v_t. In general, integrals of the form (2.22) have to be

evaluated numerically with:

$$\tau(x) = A\left(1 + \delta x T + \beta x^2 T^2 + \varepsilon x^3 T^3 + \alpha x^4 T^4 + \ldots\right)^{-1} \tag{2.23}$$

The term δ includes the effects of the strain field of dislocations (δ_{dis}) and electron-phonon coupling (δ_{e-ph}). The β term is for sheet-like faults, ε for the core of dislocations and α for point defects. Finally, the constant A is for boundary scattering and is proportional to the phonon mean-free path. More specifically, it is equal to the sample thickness in the case of diffuse scattering off the crystal boundaries. Specular reflections can lead to a phonon mean-free path larger than the thickness. Note that for the remainder of the thesis, we make a particular choice of units for the scattering time τ: the numerical constant $\frac{k_B}{2\pi^2 v_{ph}}\left(\frac{k_B}{\hbar}\right)^3$ in equation 2.22 will be included in the A term of equation 2.23. The units for A will then be mW s/K^{4}cm, δ will be expressed in $s^{-1}K^{-1}$ while β will be in $s^{-1}K^{-2}$.

Table 2.2: Temperature variation of the electrical resistivity and the thermal conductivity for electronic heat carriers in the presence of various scattering mechanisms (after [5]).

Electrons

Scattering mechanism	$\rho(T)$	κ_e(T)
Impurities or defects	T^0	T^1
Phonon-electron *	T^5	T^{-2}
Electron-electron	T^2	T^{-1}
Kondo effect	-ln T	–

*This is in the limit where $T \ll \theta_D$ only.

We now turn to a discussion of some of the processes that can cause resistance to the electronic flow of heat (or charge). The conclusions are summarized in table 2.2.

1. *Impurities or defects.* In this case all the electrons involved in conduction have a small wavelength and there is little change in their energy with temperature. The impurity scattering cross-section is then effectively independent of the electron wavevector, hence the electrical resistance is then independent of temperature (and leads to the residual resistivity at low temperature), while

the electronic thermal conductivity is proportional to temperature (due to the linear specific heat).

2. *Electron-phonon.* For $T > \theta_D$, the number of phonons in a mode is proportional to temperature and therefore, the electrical resistivity limited by electron-phonon scattering will also be linear in temperature. For temperatures well below the Debye temperature θ_D, the change in electron energy, after an interaction with a phonon, will be small but since the phonon wavector q_D can be comparable to k_F, the change in the electron wavector can be large. One can show (see [11]) that the relaxation rate for such a process is proportional to T^3. and that the thermal resistivity is proportional to T^2 while the electrical resistivity is proportional to T^5.

3. *Electron-electron.* In simple metals, electron-electron scattering processes can be shown to dominate only in exceptionally perfect metallic specimens (see [7]). It gives rise to a T^2 scattering cross-section, a thermal resistivity proportional to T and an electrical resistivity proportional to T^2. In heavy fermion compounds, the electron-electron cross-section is enhanced by the large effective masses and does become very significant.

4. *Kondo effect.* Small concentrations of magnetic ions in a non-magnetic metal can have important consequences. In the vicinity of the magnetic impurity, the conduction electron gas becomes polarized. This results in an antiferromagnetic exchange interaction which produces a virtual bound state between the magnetic moments and the conduction electrons. This is the well-known single-ion Kondo interaction. The trademark of this is a resistivity minimum and a logarithmic increase of resistivity with decreasing temperature below the minimum. For example, the minimum occurs around 30 K for 0.1–0.2% of Fe in Cu [12]. This mechanism is thought to play a fundamental role in the origin of the large effective masses in heavy fermion compounds which are viewed as lattices of Kondo impurities.

In UPt_3 at low temperature, where electronic carriers dominate, a direct application of Matthiesen's rule in the presence of impurities and electron-electron inter-

actions leads to an electrical resistivity of the form $\rho = \rho_0 + AT^2$ and a thermal conductivity $\frac{\kappa}{T} = (a + bT^2)^{-1}$ which is precisely what is observed below 1 K.

2.2 Conventional superconductors

The theory of Bardeen, Cooper and Schrieffer (BCS) [13] is a complex many-body theory that can account for many of the unusual properties of superconductors. In this section, only the main ingredients of BCS theory will be outlined. This will then be followed by the Boltzmann equation treatment of thermal conductivity in conventional superconductors. A more complete review of BCS theory can be found in the books by Tinkham [14] and de Gennes [15]. As for the thermal conductivity, we refer the reader to the original paper by Bardeen, Rickayzen and Tewordt (BRT) [16].

2.2.1 Pairing mechanism and the energy gap

The phenomenon of superconductivity was discovered by Heike Kamerlingh Onnes in 1911, when he found that below a critical temperature labelled T_c, the resistivity of mercury abruptly dropped to zero. Numerous metals were then investigated leading to the discovery of the highest transition temperature in the elemental metals: $T_c = 9.2$ K in niobium. In 1933, Meissner and Ochsenfeld noticed that the magnetic flux was expelled from the interior of a sample when cooled below the superconducting transition. Various authors put forward different phenomenological models to account for the stunning properties of superconductors: the London model for the Meissner effect, the two fluid model for the temperature dependence of certain properties, the Pippard model to explain the non-local electrodynamics of superconductors and the Ginzburg-Landau (GL) theory, a general phenomenological theory of phase transitions[1]. Theoretical developments culminated with the microscopic theory of superconducticity by Bardeen, Cooper and Schrieffer (BCS) [13] which we now proceed to outline.

The BCS theory is based on the fact that in the presence of an attractive potential between electrons, an instability in the electron gas develops leading to the formation

[1] A detailed discussion of GL theory is delayed until section 3.2.2, where both conventional and unconventional superconductors will be treated within this formalism.

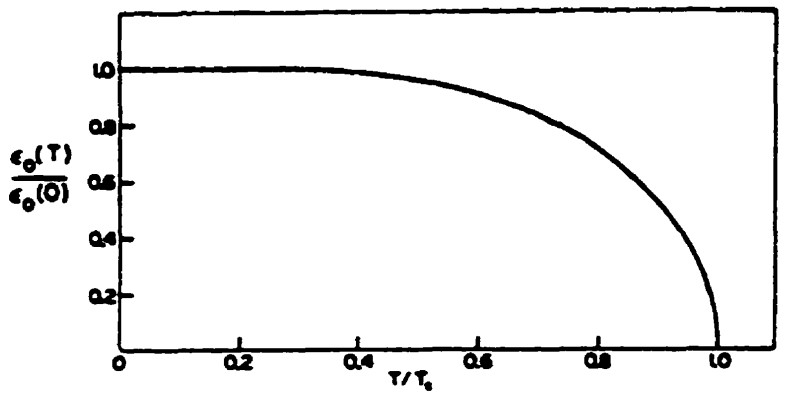

Figure 2.2: Temperature dependence for the isotropic BCS gap in the weak-coupling limit (after [3]). In their notation, ε_0 is the gap parameter.

of bound electron pairs, the so-called Cooper pairs. The electrons in a pair have the same momentum but in opposite directions. The pairing leads to the formation of a many-body coherent superposition of identical pair states that can be described by a macroscopic wave function Ψ_{BCS}:

$$\Psi_{BCS} = \prod_{\vec{k}} \left(u_{\vec{k}} + v_{\vec{k}} a^{\dagger}_{\vec{k}\uparrow} a^{\dagger}_{-\vec{k}\downarrow} \right) |vac\rangle \tag{2.24}$$

where $\left|v_{\vec{k}}\right|^2$ is the probability of a pair state $\vec{k}$ being occupied, $\left|u_{\vec{k}}\right|^2$ is the probability of a pair state $\vec{k}$ being unoccupied and the $a^{\dagger}$'s are standard creation operators from second quantization.

In conventional superconductors, the attractive pairing interaction is mediated by the lattice and can be accounted for schematically in the following way: a first electron passes through point $\vec{r}$ at time t and polarizes the medium by attracting the neighbouring positive ions. While the electron moves off very fast *i.e.* at the Fermi velocity, the disturbance in the lattice relaxes slowly with a characteristic frequency of the order of the Debye frequency. At a later time t', a second electron passes at a point $\vec{r}\,'$ nearby and is attracted by the still partially polarized lattice. Due to the retardation, the interacting electrons are spatially separated thereby reducing the repulsive Coulomb interaction. This distance between the two electrons in a Cooper pair is called the coherence length ξ. For example, $\xi = 16000$ Å in pure aluminum and $\xi = 380$ Å in niobium.

The next step in understanding superconductors has to do with the presence of an

energy gap Δ of order $k_B T_c$ in the quasi-particle excitation spectrum of the system. A solution of the BCS Hamiltonian using equation 2.24 as a variational wavefunction is obtained by making a series of substitutions (see for example [14]): $u_k = \sin\theta_k$, $v_k = \cos\theta_k$ and defining $\Delta_k = -\frac{1}{2}\sum_l V_{kl}\sin 2\theta_l$. Using these, Bardeen *et al.* [13] arrived at a self-consistent gap equation directly relating the k-dependence of the superconducting gap Δ_k to the symmetry of the pairing potential V_{kl}:

$$\Delta_k = -\frac{1}{2}\sum_l \frac{\Delta_l}{(\Delta_l^2 + \varepsilon_l^2)^{1/2}} V_{kl} \tag{2.25}$$

where ε_k is the electron energy measured with respect to the Fermi energy. In their derivation, the potential is taken to be isotropic (*i.e.* *s*-wave symmetry) and non-zero only in a thin shell of thickness $\sim \omega_D$ about the Fermi surface. This leads to a gap with no k-dependence. As we shall see later, symmetries other than *s*-wave are possible for the pairing potential which would lead to an anisotropic gap.

In solving the gap equation (eq. 2.25), the BCS model being a mean field theory, one finds that close to T_c, the gap order parameter behaves as $\frac{\Delta(T)}{\Delta(0)} \propto (T_c - T)^{\frac{1}{2}}$, with $\Delta(0) = 1.76 k_B T_c$ being the conventional BCS value, chosen to be isotropic and finite over the whole Fermi surface. Since numerical solution of equation 2.25 is necessary when calculating physical properties that depend on the gap, an analytic approximation is often made to simplify calculations:

$$\Delta(T) = \Delta(0)\tanh\left[\pi\frac{k_B T_c}{\Delta(0)}\left(\frac{2}{3h}\frac{\Delta C}{C}\frac{T_c - T}{T}\right)^{1/2}\right] \tag{2.26}$$

where $\Delta C/C$ is the specific heat jump at T_c and h is the mean square value of the gap relative to the maximum value (defined in equation 2.65). For an isotropic BCS gap, $\Delta C/C = 1.43$ and $h = 1$. The temperature dependence of the superconducting gap, as derived by BCS, is displayed in figure 2.2. From this figure, one can notice that the gap becomes essentially constant (*i.e.* $\Delta(T) \approx \Delta(0)$) below $T/T_c \approx 0.4$.

An important quantity that needs to be introduced when discussing excited states and transport properties in the superconducting state is the quasiparticle energy E_k:

$$E_k = \sqrt{\varepsilon_k^2 + |\Delta_k|^2} \tag{2.27}$$

where ϵ_k is the single quasiparticle energy measured from the Fermi level and Δ_k is the energy gap. It turns out that the elementary excitations, called quasiparticles, out

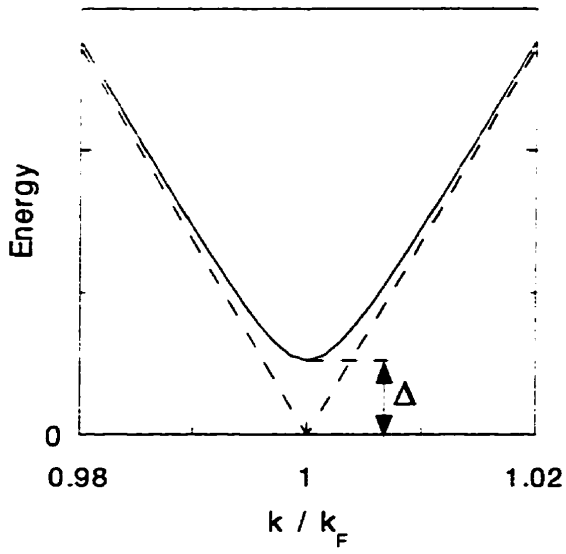

Figure 2.3: Superconducting quasiparticle energy spectrum (solid line) as a function of its wavevector. The energy spectrum in the metallic state, given by $|\varepsilon_k|$, is represented by the dashed line. Notice that both quantities differ only in a narrow region around k_F where E_k has a minimum in energy equal to the superconducting gap.

of the BCS ground state behave like fermions with energy E_k. The gap then plays the role of a minimum excitation energy, as displayed in figure 2.3. This quantity will be used extensively in the next section when we discuss thermal conductivity in superconductors. Such an excitation gap can either be accessed via thermal properties such as specific heat or heat transport, electromagnetic absorption or tunneling experiments. For thermal properties, the gap leads to an exponentially activated behavior at low temperatures. As an example, figure 2.4 displays the specific heat in aluminum.

We conclude this section by deriving the superconducting density of states $N_s(E)$. In going through T_c, the number of quantized states is preserved and therefore $N_s(E)dE = N(\varepsilon)d\varepsilon \approx N(0)d\varepsilon$. We find:

$$N_s(E) \approx N(0)\frac{d\varepsilon}{dE} = \begin{cases} \frac{N(0)E}{(E^2-\Delta^2)^{1/2}}, & E > \Delta \\ 0, & E < \Delta \end{cases} \tag{2.28}$$

This quantity is plotted in figure 2.5. We immediately notice that (i) there are no states below Δ, (ii) there is a significant increase in the density of states just above $E{=}\Delta$ and (iii) a superconductor behaves like a normal metal for $E \gtrsim 3\Delta$. The absence of states below Δ leads to an absorption edge as seen in microwave and far infrared

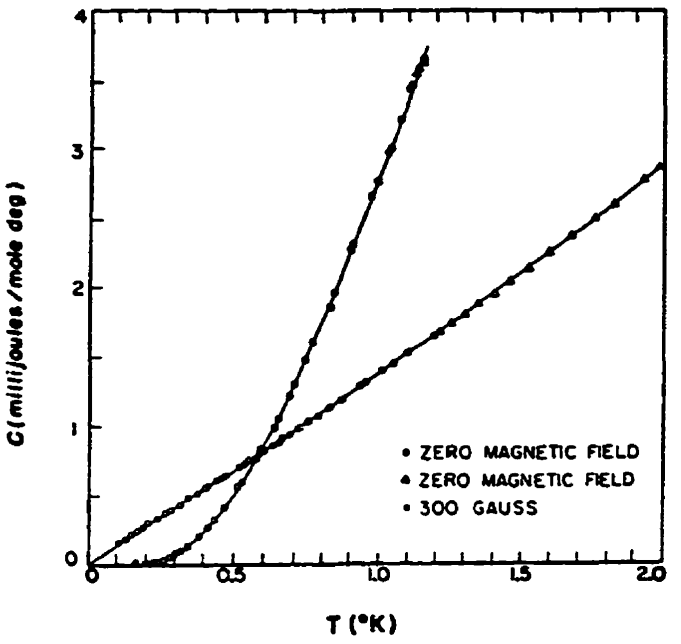

Figure 2.4: Specific heat for aluminum as a function of temperature in both the normal and superconducting state (after [17]). Notice the exponential behavior at low temperature in the superconducting state.

experiments (see for example [18]). For energies $\hbar\omega < 2\Delta$, the superconductor is totally reflecting while for $\hbar\omega > 2\Delta$ absorption by the material under investigation can be measured.

In summary, we have explained that superconductivity arises from a pairing between electrons and that there exists a gap between the ground state and the first excited state which gives rise to exponentially activated behavior in many physical properties.

2.2.2 *Thermal conductivity in conventional superconductors*

Let us now mention two properties of the condensate that derive from BCS theory: (i) Cooper pairs carry no entropy – only thermally excited quasiparticles can carry thermal currents – and (ii) Cooper pairs are not effective in scattering phonons or electrons. Item (i) implies that at low temperatures, due to a finite gap, the number of excited quasiparticles will have an exponentially activated behavior and therefore κ_{es} will fall off exponentially. Item (ii) implies that since the paired electrons can no longer scatter phonons, the phononic mean-free path will increase as the tempe-

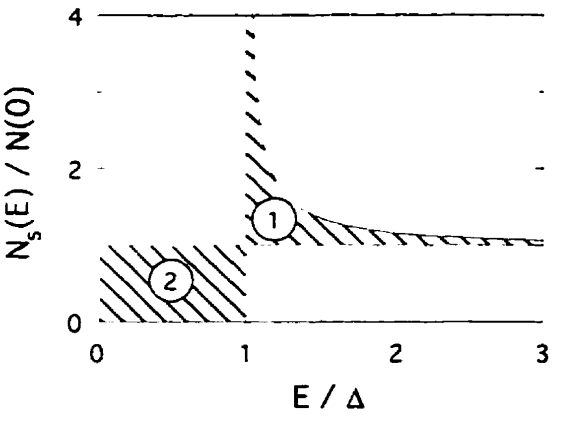

Figure 2.5: Superconducting density of states for a BCS superconductor as a function of the quasiparticle energy. The loss in density of states for $E/\Delta < 1$ (area 2) is exactly compensated by the increase just above $E/\Delta = 1$ (area 1).

rature is lowered until it is limited by defects or the size of the sample much as in an insulator. This means that in the superconducting state, the phonon contribution to thermal conductivity can become comparable to or even dominant over the electronic contribution. These general conclusions will become useful when looking at experimental data.

In this section, we present a brief sketch of transport theory in conventional superconductors treating only the simplest case of impurity scattering as first derived by Bardeen, Rickayzen and Tewordt (BRT) [16].

We start with equation 2.16 in which we replace the free-electron energy by the quasiparticle energy E_k defined in the previous section:

$$\vec{j}_q = -\frac{2}{T}\sum_k \mu_i^2 E_k^2 \frac{\partial f_0}{\partial E_k} v_k^2 \tau_k \vec{\nabla} T \tag{2.29}$$

The problem is then to calculate the relaxation time τ_k and the group velocity v_k of the quasiparticles in the superconducting state.

The group velocity is given by:

$$v_k = \frac{1}{\hbar}\nabla_k E_k \tag{2.30}$$

$$= \frac{1}{E_k}\left(|\epsilon_k|\frac{1}{\hbar}\nabla_k \epsilon_k + |\Delta_k|\frac{1}{\hbar}\nabla_k \Delta_k\right) \tag{2.31}$$

The last term on the right can be shown to be small, and thus will be neglected.

Hence:

$$v_k = \left|\frac{\varepsilon_k}{E_k}\right| v_F = \frac{N(0)}{N_s(E)} v_F \tag{2.32}$$

with N(0) the density of states at the Fermi level in the normal state and $N_s(E)$ the quasiparticle density of states. Note that in the limit of low energies, $\lim_{\varepsilon_k \to 0} v_k = 0$, *i.e.* quasiparticles at k_F have zero group velocity. We will come back to the implications of this when we discuss the results for the scattering time.

Then, Bardeen *et al.* proceeded to compute the scattering time in the superconducting state τ_s. They start with Fermi's Golden rule which we write schematically:

$$\begin{pmatrix} probability \\ of\ an\ event \end{pmatrix} = \frac{2\pi}{\hbar} \begin{pmatrix} matrix\ element \\ of\ potential \end{pmatrix} \begin{pmatrix} probability\ of \\ initial\ state\ occupied \end{pmatrix} \times \begin{pmatrix} probabilitiy\ of \\ final\ state\ unoccupied \end{pmatrix} \begin{pmatrix} conservation \\ of\ energy \end{pmatrix} \tag{2.33}$$

We sum all scattering processes which lead to transition into states with wave vector $\vec{k}$ minus those out of $\vec{k}$. We get for the collision integral:

$$\left(\frac{\partial f}{\partial t}\right)_{coll} = \frac{2\pi}{\hbar} \sum_{k'} |\langle k' | V | k \rangle|^2 \left[f_{k'}(1 - f_k) - f_k(1 - f_{k'})\right] \delta(E_k - E_{k'}) \tag{2.34}$$

By taking into account all possible elastic scattering mechanisms, Bardeen *et al.* showed that:

$$|\langle k' | V | k \rangle|^2 = |V(k' - k)|^2 \frac{1}{2} \left(1 + \frac{\varepsilon_k \varepsilon_{k'} - \Delta_k \Delta_{k'}}{E_k E_{k'}}\right) \tag{2.35}$$

where the factor multiplying $|V(k' - k)|^2$ is called the coherence factor. It will play a major role when we come to discussing transport properties in unconventional superconductors (see section 2.3.2). The physical origin of these coherence factors has to do with the BCS wavefunction which is a coherent superposition of identical pair-states. This means that when an electron is scattered, one cannot make a single-particle approximation, as in the normal state, because the occupancy of the final state will depend on all other pair-states through the coefficients u_k and v_k introduced in equation 2.24. See the book by Schrieffer [19] for a thorough discussion of these coherence factors and their physical meaning.

In going back to our discussion, Bardeen *et al.* assume that the departure from equilibrium is given by:

$$f_k = f_k^0 - k_z C(E) \frac{\partial f_k^0}{\partial E} \tag{2.36}$$

where f_k^0 is the Fermi function, z is the direction of the disturbance and $C(E)$ an arbitrary function of energy.

Replacing equation 2.35 in equation 2.34 and converting the sum over k' into an integral over energy:

$$\left(\frac{\partial f}{\partial t}\right)_{coll} = \frac{2\pi}{\hbar}\int N(\varepsilon)d\varepsilon \int \frac{d\Omega}{4\pi}|V(k'-k)|^2 \frac{1}{2}\left(1+\frac{\varepsilon'\varepsilon-\Delta_k\Delta_{k'}}{EE'}\right) \times \left[k_z C(E)\frac{\partial f_k^0}{\partial E} - k'_z C(E')\frac{\partial f_k^0}{\partial E'}\right]\delta(E-E') \tag{2.37}$$

Assuming an isotropic gap ($\Delta_k\Delta_{k'} \rightarrow \Delta^2$) and integrating over energy:

$$\left(\frac{\partial f}{\partial t}\right)_{coll} = \frac{N(0)}{2\hbar}k_F C(E)\frac{\partial f_k^0}{\partial E}\left|\frac{\varepsilon}{E}\right|\int d\Omega\,|V(k'-k)|^2\left(\frac{k_z-k'_z}{k_F}\right) \tag{2.38}$$

We now apply the relaxation time approximation in the normal state ($E \rightarrow \varepsilon$), assuming isotropic scattering *i.e.* $\tau_k \rightarrow \tau_N$ and using equation 2.36, we find the scattering rate:

$$\frac{1}{\tau_N} = \frac{N(0)}{2\hbar}\int d\Omega\,|V(k'-k)|^2\left(\frac{k_z-k'_z}{k_F}\right) \tag{2.39}$$

Returning to the superconducting state, we find that using the relaxation time approximation[1] and replacing the normal state scattering rate in equation 2.38,

$$\tau_s = \left|\frac{E}{\varepsilon}\right|\tau_N = \frac{N_s(E)}{N(0)}\tau_N \tag{2.40}$$

We see that at low energies, the scattering time diverges: $\lim_{\varepsilon_k \rightarrow 0}\tau_k \rightarrow +\infty$ but, combining this last expression with the group velocity (equation 2.32), we see that this divergence is cancelled by the energy dependence of the group velocity yielding a constant mean-free path: $\ell_s = \ell_N$.

By going back to equation 2.29 and changing the sum into an integral, and inserting the expression for the scattering time (equation 2.40) and the group velocity (equation 2.32), we get:

$$\kappa_{es} = \frac{2}{T}v_F^2\tau_N N(0)\int_{\Delta(T)}^{+\infty} dE\; E^2\left(-\frac{\partial f}{\partial E}\right)\int \frac{d\Omega}{4\pi}\cos^2\theta \tag{2.41}$$

[1] In this case also, we assume *s*-wave scattering, namely: $\tau_k \rightarrow \tau_s$.

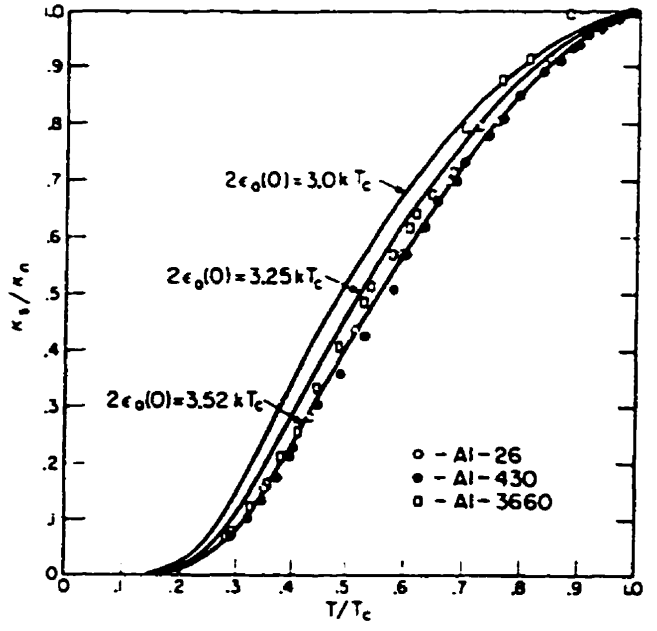

Figure 2.6: Ratio of superconducting to normal state thermal conductivity for aluminum as a function of T/T_c for samples of various purities indicated by the residual resistivity ratio $\rho(273K)/\rho(1.2K)$ of 26, 430 and 3660 (after [20]). The solid lines represent the BRT calculation [16] in the presence of impurity scattering for three values of the gap parameter, namely $2\Delta(0) = 3.00$, 3.25 and 3.52 k_BT_c.

By letting $\Delta \rightarrow 0$, we obtain the expression for the normal state thermal conductivity κ_N (equation 2.18). Dividing κ_{es} by κ_N, we finally get:

$$\boxed{\frac{\kappa_{es}(T)}{\kappa_N} = \int_{\Delta(T)}^{+\infty} dE\ E^2 \frac{\partial f}{\partial E} \Big/ \int_0^{+\infty} d\varepsilon\ \varepsilon^2 \frac{\partial f}{\partial \varepsilon}} \tag{2.42}$$

For T$\ll T_c$ this expression reduces to [16]:

$$\frac{\kappa_{es}}{\kappa_N} \propto \left(\frac{\Delta}{k_BT}\right)^2 e^{-\Delta/k_BT} \tag{2.43}$$

A comparison of the theory with experimental data on aluminum is provided in figure 2.6. BRT theory with the BCS value for the gap provides an excellent agreement with the experimental data for the three samples of varying impurity concentration.

In the case of niobium (T_c =9.1 K), the critical temperature is 8 times higher than in aluminum. According to BRT, this implies a negligible electronic contribution for T <2 K[1]. In this case the phonon contribution, which has increased due to the

[1] κ_{es}/κ_N has dropped to 4% at T/T_c=0.25.

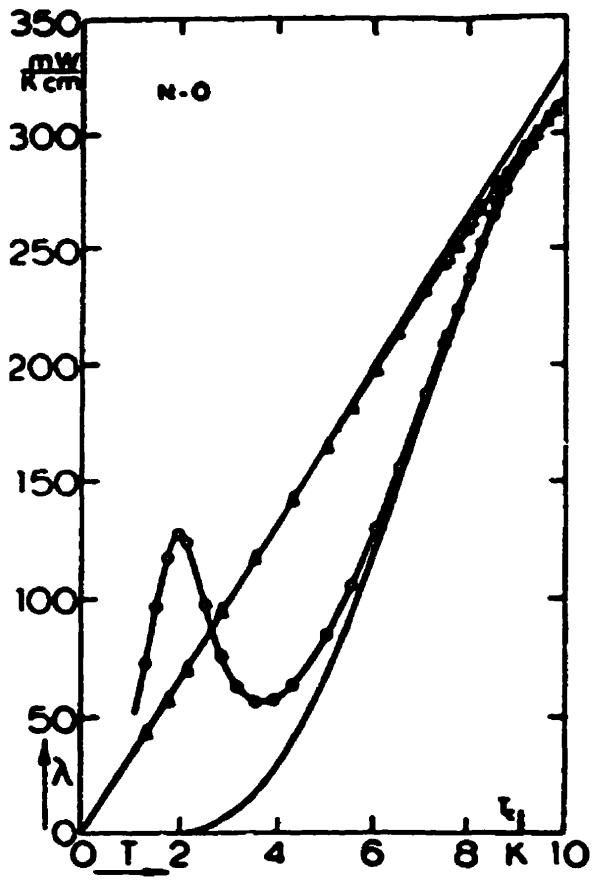

Figure 2.7: Thermal conductivity of niobium in the normal (triangles) and superconducting (circles) state. The solid lines through the points are guides to the eye while the lowest curve is the expected result from BRT theory (after [21]). Notice the strong deviation from BRT theory at low temperatures arising from the phonon contribution.

disappearance of electron scattering, becomes large and even dominates at low temperatures. This is what was observed by Kes *et al.* [21] whose findings are displayed in figure 2.7. The low temperature peak arises from the competition between the increasing phonon mean-free path (until limited by the sample boundaries) and the decrease in the number of phonons.

In the preceeding discussion, it was assumed that the thermal conductivity was mostly electronic in the normal state and that the electron mean-free path was limited by impurities. Other cases may become relevant later on in the thesis and will be discussed here.

We discuss the case when phonon conduction is not negligible in the normal state. As seen above, in going through T_c, the decrease in the number of unpaired electrons

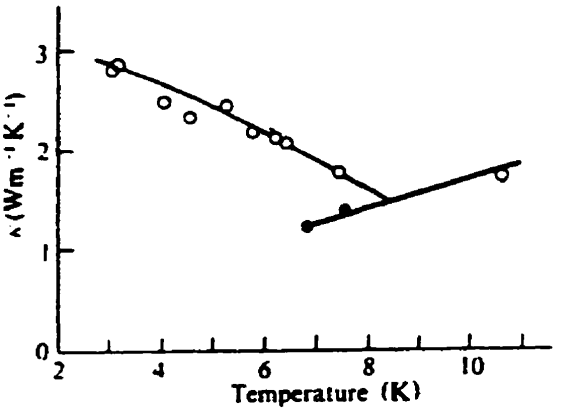

Figure 2.8: The thermal conductivity of lead-30% bismuth as a function of temperature in both the normal (solid circles) and superconducting state (open circles) (after [22]). The normal state conductivity is obtained by applying a magnetic field larger than the critical field.

reduces the amount of electron-phonon scattering. This leads to an increase of the phonon conductivity which usually for pure metals is small compared with the fall in the electronic contribution. However, in disordered alloys, where the phonon conductivity provides a significant fraction of the total normal state conductivity, this rise in phonon conductivity can lead to a thermal conductivity which is higher in the superconducting state than in the normal state. This is shown for an alloy of lead-bismuth in of figure 2.8.

2.2.3 Thermal conductivity as a probe of anisotropic conventional superconductors

In this section, we illustrate how thermal conductivity can be used to probe an anisotropic superconducting gap. The reader is referred to the study on zinc and cadmium [23] and on gallium [24] by N. V. Zavaritskii in the late 50's and early 60's. Only the latter will be discussed in this section. We provide a rather lengthy discussion of Zavaritskii's results as a way of illustrating what we have discussed until now with regards to thermal conductivity in normal metals and conventional superconductors. A detailed discussion is also justified in light of our results on UPt_3: anisotropy of the thermal conductivity and thermal conductivity ratios will be briefly discussed here in the simpler case of BCS superconductors. The experienced reader

can skip this section (and refer back if necessary) while people unfamiliar with this field should benefit from this discussion.

Measurement of the electronic thermal conductivity in the superconducting state (κ_{es}) and along various crystallographic directions can reveal anisotropy of both the absolute value of κ_{es} and also in its temperature dependence. The former can be related to the anisotropy of the normal state, which simply reflects anisotropy in the Fermi velocities, while the latter can be related to the superconducting gap.

In light of the fact that the electronic thermal conductivity is greatly reduced upon entering the superconducting state, the phonon heat conductivity can start to play an increasingly important role as the temperature is lowered. Therefore, Zavaritskii [24] chose to make use of superconductors with a minimum ratio of T_c/θ_D such as cadmium[1] (T_c = 0.56 K, θ_D = 209 K), zinc (T_c = 0.88 K, θ_D = 327 K), aluminum (T_c = 1.14 K, θ_D = 428 K), gallium (T_c = 1.09 K, θ_D = 320 K) or rhenium (T_c = 1.4 K, θ_D = 430 K), in order to have the largest possible ratio of $\kappa_{es}/\kappa_{phonon}$. We illustrate his findings for one anisotropic superconductor: gallium.

This metal crystalizes in an orthorhombic lattice with a = 4.526 Å, b = 4.520 Å and c = 7.660 Å. The single crystals were grown from starting material of different impurity concentrations ranging in concentration from 0.1% down to 0.001%. The samples from the highest purity batch are denoted by the letter P while the lower purity samples are denoted by the letter D (see figure 2.9).

As a first result, Zavaritskii [24] showed that in the normal state in the temperature range from 2.0 to 4.2 K, the thermal conductivity obeyed the following equation:

$$\frac{T}{\kappa_N} = \frac{1}{\kappa_0} + \alpha T^3 \tag{2.44}$$

where $\kappa_0 = L_0/\rho_0$ represents the scattering of the electron heat carriers by defects and L_0 is the Sommerfeld value and ρ_0 is the residual resistivity. The second term represents the scattering of electrons by thermal vibrations. The author showed that in the range from 2 K down to T_c = 1.08 K, the scattering of electrons by phonons is negligible in comparison with their scattering with defects; for example, for sample 3PI oriented along the c-axis (largest electron-phonon coupling), one can compute $\frac{1/\kappa_0^{(c)}}{\alpha^{(c)}T_c^3} \approx 0.8\%$ and similarly for the a and b directions.

[1] All values for T_c and θ_D were taken from tables compiled by Kittel (1986) [25].

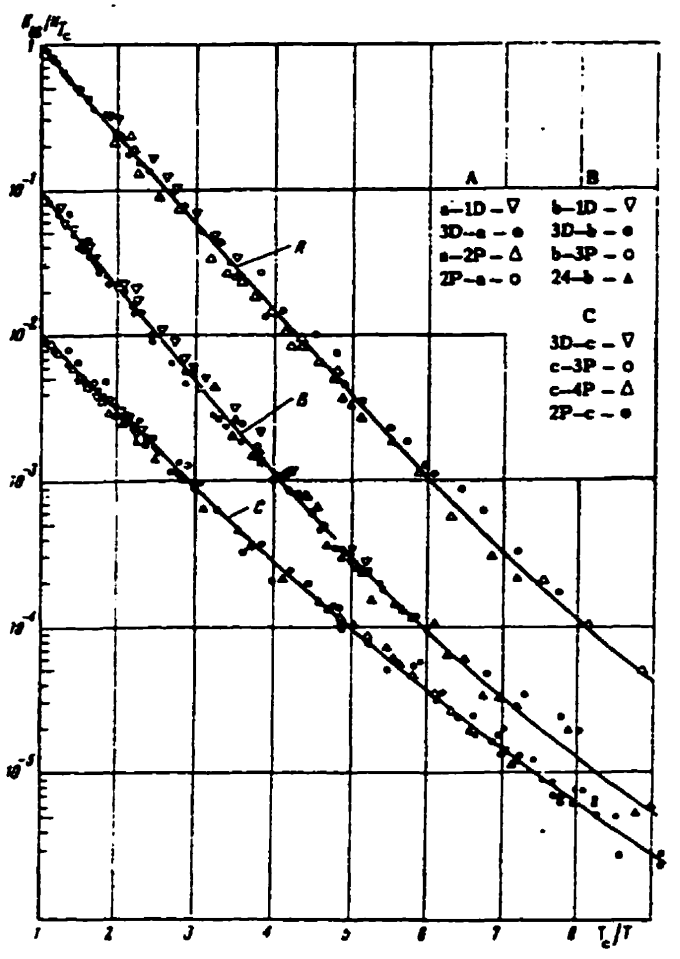

Figure 2.9: Temperature variation of the electronic thermal conductivity of gallium (normalised at T_c) in the superconducting state in the principal crystallographic directions. The solid lines are guides to the eye and the curves for the b and c axis have been shifted for clarity (after [24]).

In the superconducting state, the author proceeded to estimate the phonon thermal conductivity. By using $\kappa_{ph} = \frac{1}{3} C_{ph} v_{ph} l_{ph}$ and substituting the known Debye temperature in the expression for the phonon specific heat C_{ph}, the mean-phonon velocity v_{ph} known for gallium, and using the phonon mean-free path l_{ph} to be the diameter of the sample, the author was able to compute the phonon conductivity. For his lower purity samples, this contribution is shown to be dominant at temperatures lower than 0.2–0.3 K while for the purest samples, where the normal state thermal conductivity exceeds by a factor 10 that of the impure samples, the phonon contribution can be neglected over the whole temperature range. Explicitely, for the b-axis samples of the series 3D and 2P, at 0.3 K, the ratio $\frac{\kappa_{ph}}{\kappa_{meas}}$ exceeds 45% in the lowest purity samples

(3D) while it is around 0.1% in the purest samples (2P). For the high purity samples, the phonon heat conduction estimated for boundary scattering does not exceed 2% even at the lowest temperatures reached by the experimentalist. Furthermore, one has to note that the phonon contribution of 45% to the total thermal conductivity is certainly an overestimate: for instance, again for boundary scattering, the ratio $\frac{\tau_{ph}}{\tau_{meas}}$ amounts to 120% at 0.15 K showing that electrons must still be playing a role in diffusing the phonons at these temperatures even for the impure samples. Moreover, the exponential activation in the number of quasiparticles displayed by BCS superconductors will certainly cause the phonon conduction to drop rapidly as the temperature is increased, making it negligible for temperatures above 0.4 K.

Figure 2.9 shows the electronic thermal conductivity normalized at T_c as a function of T_c/T for all samples[1]. From this figure, it is clear that the dependence of the thermal conductivity with T_c/T follows a universal law for samples grown in one direction. Neither the purity (varied by a factor of 100 which affects the electronic mean free path) nor the method of preparation (multiple recrystallization) nor the sample's dimensions influence this dependence. Furthermore, Zavaritskii [24] not only showed that the absolute value of thermal conductivity differed for different crystalline directions but also that the temperature dependence in the superconducting state was different. The author noticed that from T_c down to $\sim 0.25T_c$ there was a linear relationship between $\log(\kappa_{es}(T)/\kappa(T_c))$ and T_c/T. Assuming that only excitations travelling in the direction of the temperature gradient contribute to the thermal conductivity and that in this temperature range $\kappa_{es} \propto e^{-\Delta T}$, he was able to extract the gap parameter for all three directions: 1.49 K (a-axis), 1.57 K (b-axis) and 1.26 K (c-axis). The author claims that the deviation from linear behavior at lower temperature results from the temperature dependence of the factor multiplying the exponent. Furthermore, he claims that the deviation is close to what is predicted theoretically. Even though, the author seems to be unaware of the BRT paper [16] published earlier that year, an exact determination of the gap parameter would require a full calculation assuming an ellipsoid of revolution for the gap parameter.

[1] Zavaritskii [24] included the data for the impure samples for the temperatures where he estimated the phonon contribution to heat conduction to be smaller than ~20%.

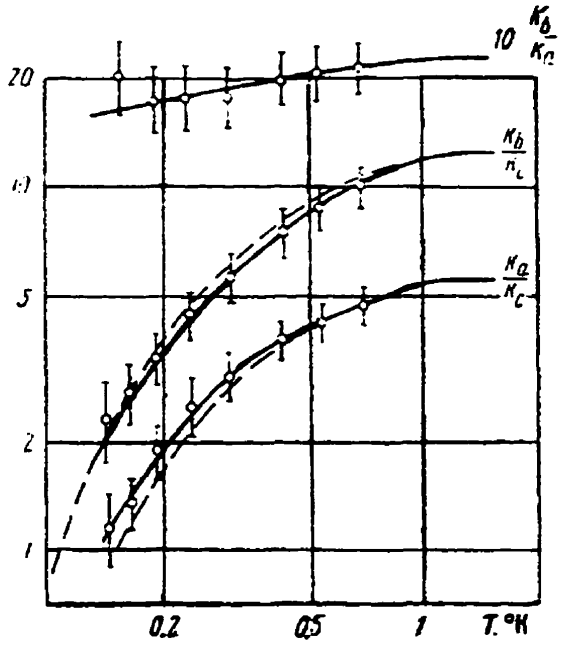

Figure 2.10: Temperature dependence of the relative anisotropy of the electronic thermal conductivity of gallium. The curves shown are $10\kappa_b/\kappa_a$ (upper curve), κ_b/κ_c (middle curve) and κ_a/κ_c (lower curve). The solid lines are guide to the eye while the dashed line corresponds to exp(-0.29/T) (after [24])

Nevertheless, this measurement shows different temperature dependence in different crystallographic directions and that can only be ascribed to an anisotropic gap.

By plotting the ratio of thermal conductivities for different directions, the temperature dependence of the prefactor in front of $e^{-\Delta T}$ might cancel. The remaining curve would then simply be proportional to $e^{(\Delta_1-\Delta_2)T}$. Figure 2.10 shows the relative anisotropy ratios of thermal conductivity. Notice that the ratio κ_b/κ_c (middle curve) and κ_a/κ_c (lower curve) both go to zero due to a smaller gap in the c-direction. This is reflected by the dashed line which represents an exponential $e^{-0.29/T}$. In the case of the ratio κ_b/κ_a, it extrapolates to a finite value reflecting the fact that both gaps are identical (within experimental error [24]). The finite ratio is simply the normal state anisotropy. Thermal conductivity ratios will be exploited in section 6.3 in comparing the results for UPt_3 with various theories for the gap structure of this compound.

The measurements of Zavaritskii, in the case of anisotropic conventional superconductors, show the power of thermal conductivity as a directional probe for gap anisotropy when the heat conduction is dominated by electrons.

2.3 Unconventional superconductors

We start this section by emphasizing the difference between the BCS model and the generalized BCS theory.

The BCS model rests on four basic assumptions: (i) an electron-phonon mechanism is responsible for the formation of Cooper pairs, (ii) an s-wave potential is assumed *i.e.* there is no angular dependence to the pairing interaction, (iii) the gap in the excitation spectrum is isotropic and (iv) the weak-coupling limit is assumed. As discussed earlier, the BCS model can be extended to encompass anisotropic superconductors such as zinc and gallium. Furthermore, generalization to strong coupling superconductors can be made to account for the properties of lead and mercury. The BCS model can be relaxed further so as to account for non-phononic pairing mechanisms such as spin-fluctuations as in ^{3}He[1]. The case of ^{3}He is also relevant for assumptions (ii) and (iii) because in this case, the pairing potential is p-wave and the gap has nodes. We will therefore speak of BCS theory as long as there is a pairing of fermions mediated by some attractive interaction. Keeping all the generalizations in mind, in the strictest sense, an unconventional superconductor is a superconductor in which the superconductivity is *not* due to a pairing of electrons. However, the term "unconventional superconductor" is now employed more loosely to also encompass those superconductors that can be described by BCS theory (*i.e.* pairing of electrons) but in which the pairing potential is non-s-wave and the superconductivity is non-phonon mediated. Thus there can be additional broken symmetries[2] such as point group and or time reversal symmetry. This typically yields a superconducting gap with nodes, but it can also lead to a possible magnetic moment associated with the Cooper pairs or to multiple superconducting phases. In this sense, ^{3}He is a truly unconventional superfluid: the pairing is not via phonons, the symmetry is p-wave and there is more than one superfluid phase. In studying unconventional superconductors, one is interested in the fundamental question: "Can pairing be purely electronic?" This is unconventional superconductivity and it typically implies a gap with nodes and non-s-wave symmetries. For the remainder of the thesis, we use the term "un-

[1] Liquid ^{3}He also causes us to generalize the pairing, not only for electrons, but also to encompass fermions such as ^{3}He atoms.

[2] A conventional superconductor only breaks gauge symmetry.

conventional superconductor" to represent superconductors that can be described by BCS theory but for which the electron (or fermion) pairing potential, and hence the gap, is non-*s*-wave.

We will now proceed in the same way as with conventional superconductors and discuss the pairing mechanism and the energy gap followed by a discussion of thermal conductivity in unconventional superconductors.

2.3.1 *Pairing mechanism and the energy gap*

This section is devoted to pointing out some of the evidence indicative of unconventional superconductivity in UPt_3 and $YBa_2Cu_3O_{7-\delta}$. Experimental properties displaying unconventional behavior in these compounds will be reviewed in more detail in chapters 3 and 4. Our intent is only to convince the reader, by some simple arguments, that these two compounds are unconventional. But first, in analogy with the lattice polarization mechanism for conventional pairing, we discuss the spin fluctuation mechanism believed to be responsible for the unconventional superfluidity in ^{3}He. A similar mechanism, in which the ^{3}He atoms are replaced by the conduction electrons, is one of the postulated mechanisms for superconductivity in UPt_3 and $YBa_2Cu_3O_{7-\delta}$.

Consider the spin polarization mechanism described by Leggett [26]: a ^{3}He atom at point $\vec{r}$ and time t will produce a molecular field which in turn produces a spin polarization of the neighboring liquid. This polarization persists for a fair time before dying out. If now at time t' a second ^{3}He atom comes by at point $\vec{r}\,'$, it will either be attracted or repelled (depending on its spin) by the liquid polarization. The attraction arises from the Pauli exclusion principle and the dipole-dipole interaction between the ^{3}He atom and the polarized medium. In this way, a spin-dependent effective interaction is generated between two ^{3}He atoms. In the case of the lattice polarization mechanism, the lattice is essentially an independent system and its motion is almost unaffected by the pairing occuring in the electron gas. For the spin polarization mechanism in ^{3}He, the medium which is polarized is *identical* to the atoms undergoing the indirect attraction. Therefore, if as a result of the attraction, the behavior of the atoms is changed (*i.e.* when they form Cooper pairs), the response of the polarizable medium is automatically affected. The pairing mechanism produces an attraction

between parallel spin particles and a repulsion between antiparallel spin ones. Thus, it intrinsically favors spin triplet pairing and tends to suppress singlet pairing.

1. *Evidence of unconventional superconductivity in UPt_3*

In heavy fermions, the Fermi and the Debye temperatures are of the same order of magnitude *i.e.* the Fermi velocity is approximatly $v_F \approx 5000$ m/s, while the sound velocity is around $c_s \approx 3000$ m/s. An electron-phonon type interaction is therefore unlikely responsible for the superconductivity in the sense that the electrons move so slowly that the lattice follows the electrons adiabatically. Therefore, in order for a second electron to profit from the polarized lattice, it would need to be very close to the first one making the Coulomb repulsion so large as to prevent any pairing. The observation that the ratio of the normal and superconducting specific heats $(C_s - C_n)/C_n$ is close to unity suggested that the heavy quasiparticles were participating in the superconducting state. These observations led several theorists to postulate that in order to avoid the large overlap of the wave functions of the paired particles, the system would choose an anisotropic channel, like a p-wave spin triplet or a d-wave spin singlet or triplet state, as is done in superfluid ^{3}He (p-wave spin triplet pairing). Following these conclusions, alternative mechanisms mediated by antiferromagnetic spin fluctuations have been proposed for UPt_3 (see for example [27, 28, 29] and references therein). Furthermore, several properties of the superconducting state do not display exponentially activated behavior, the trademark of a s-wave gap. As will be discussed in section 2.3.2, nodes in the gap result in power law dependence, as a function of temperature, of thermodynamic and transport properties. Finally, the observation of multiple superconducting phases in UPt_3 has provided the strongest case for unconventional superconductivity in this system. The superconducting state properties, with respect to multiple superconducting phases and power law dependences, will be reviewed in chapter 3.

2. *Evidence of unconventional superconductivity in $YBa_2Cu_3O_{7-\delta}$*

Following the book by Burns [30], we proceed to list some of the unusual features of the cuprates, as they stood in late 1990.

There are many reasons why phonon-mediated superconductivity in the high-T_c's

is unlikely. First, the T_c values are too high with $T_c \sim \theta_D$. Thus, extremely strong-coupled BCS theory would be needed, but such large electron-phonon coupling would likely cause a structural phase transition. Secondly, early specific heat measurements gave a residual linear term which was interpreted as residual normal fluid[1] indicating an unconventional gap or no gap at all. Furthermore, there are many suggestions that the cuprates could well be non-Fermi liquids and many exotic models for the superconductivity were put forward. These models will not be reviewed here.

On the other hand, several experiments indicated that electrons were paired. This would seem to favor a BCS theory with a pairing mechanism other than phonon mediated and possibly with a superconducting gap symmetry other than s-wave. Due to its proximity to an antiferromagnetic ordered phase, spin fluctuations are thought to play a role in the pairing. Furthermore, several experiments indicate power law behavior, suggesting that the superconducting gap has nodes. At the moment, the leading scenario for the gap parameter is that it has the $d_{x^2-y^2}$ symmetry. Since most papers discussing heat conduction in $YBa_2Cu_3O_{7-\delta}$ adopt this point of view, it is the example that we choose for the discussion in the remainder of the thesis. We caution the reader that just because this viewpoint appears to be the most popular does not necessarily make it the correct one even though several experiments confirm the features of this gap symmetry.

3. *Generalization of the BCS model to unconventional superconductivity*

For this brief description, we follow the reasoning of Mineev [32]. The paper of Sigrist and Ueda '33' also provides a good (and lengthy) discussion of what we are about to describe.

As we have seen above, the superconducting ground state is composed of electronic pairs that can be represented by a two-electron wavefunction $\Delta_{\alpha\beta}(\hat{k})$, a gap function, where we have explicitly introduced the spin indices α and β, and where $\hat{k}$ is a unit vector in the direction of the momentum of one of the electrons in the pair. Since we are dealing with fermions, the function $\Delta_{\alpha\beta}(\hat{k})$ should be antisymmetric with respect

[1] We will review some experiments that see a residual linear term in the specific heat in chapter 4.

Table 2.3: D_{6h} basis functions for UPt_3 for strong spin-orbit coupling and $\hat{d} \parallel \hat{z}$ (after [31]).

Even parity

Γ	ψ, $\vec{\psi}$	node topology	name
A_{1g}	1	none	s-wave
A_{2g}	$Im(k_x - ik_y)^6$	lines at $k_z = 0$ and $k_y = 0$ and 8 "special" lines *	-
B_{1g}	$k_z Im(k_x - ik_y)^3$	lines at $k_z = 0$ and $k_y = 0$ and 4 "special" lines	-
B_{2g}	$k_z Re(k_x - ik_y)^3$	lines at $k_z = 0$ and $k_x = 0$ and 4 "special" lines	-
E_{1g}	$k_z \begin{pmatrix} k_x \\ k_y \end{pmatrix}$	line at $k_z = 0$ and points at $k_x = k_y = 0$	hybrid I
E_{2g}	$\begin{pmatrix} k_x^2 - k_y^2 \\ 2k_x k_y \end{pmatrix}$	points at $k_x = k_y = 0$	axial II

Odd parity

A_{1u}	$\hat{z}k_z$	line at $k_z = 0$	polar
A_{2u}	$\hat{z}k_z Im(k_x + ik_y)^6$	same as A_{2g} + line at $k_z = 0$	-
B_{1u}	$\hat{z} Im(k_x + ik_y)^3$	line at $k_y = 0$ and 4 "special" lines	-
B_{2u}	$\hat{z} Re(k_x + ik_y)^3$	line at $k_x = 0$ and 4 "special" lines	-
E_{1u}	$\hat{z} \begin{pmatrix} k_x \\ k_y \end{pmatrix}$	points at $k_x = k_y = 0$	axial I
E_{2u}	$\hat{z}k_z \begin{pmatrix} k_x^2 - k_y^2 \\ 2k_x k_y \end{pmatrix}$	line at $k_z = 0$ and points at $k_x = k_y = 0$	hybrid II

*For the A_{2g}, the 8 "special" lines occur when $\sin\phi = \pm\sqrt{\frac{3}{8}}$ and $\sin\phi = \pm\sqrt{\frac{1}{8}}$. Four other gap structures have "special" lines with either $\sin\phi = \pm\frac{\sqrt{3}}{2}$ or $\cos\phi = \pm\frac{\sqrt{3}}{2}$. This type of node will not be considered for the remainder of the thesis.

to the permutation of two particles:

$$\Delta_{\alpha\beta}(\hat{k}) = -\Delta_{\beta\alpha}(-\hat{k}) \tag{2.45}$$

Furthermore, in the presence of an inversion center (as in UPt_3 and $YBa_2Cu_3O_{7-\delta}$), this function also has a definite parity, namely:

$$\hat{P}\Delta_{\alpha\beta}(\hat{k}) = \Delta_{\alpha\beta}(-\hat{k}) = \pm\Delta_{\alpha\beta}(\hat{k}) \tag{2.46}$$

where $\hat{P}$ is the parity operator. We therefore find $\Delta_{\alpha\beta}(\hat{k}) = -\Delta_{\beta\alpha}(\hat{k})$ for P = +1 and $\Delta_{\alpha\beta}(\hat{k}) = \Delta_{\beta\alpha}(\hat{k})$ for P = -1. The general shape of $\Delta_{\alpha\beta}(\hat{k})$ can therefore be expressed explicitly, using Pauli matrices, into an even or an odd function:

$$\Delta_{\alpha\beta}(\hat{k}) = f(\hat{k})i\sigma_y \tag{2.47}$$

with $f(-\hat{k}) = f(\hat{k})$ (even parity) and,

$$\Delta_{\alpha\beta}(\hat{k}) = \left(\vec{d}(\hat{k}) \cdot \vec{\sigma}\right) i\sigma_y \tag{2.48}$$

where $\vec{d}(-\hat{k}) = -\vec{d}(\hat{k})$ (odd parity). The functions $f(\hat{k})$ and $\vec{d}(\hat{k})$ are eigenfunctions of the spin operator $\vec{S}$ of the Cooper pair. The function $f(\hat{k})$ represents the amplitude of the spin zero antisymmetric pairing state $|\uparrow\downarrow\rangle - |\downarrow\uparrow\rangle$. The components $(-d_x + id_y)$, d_z, $(d_x + id_y)$ are the amplitudes of spin up $|\uparrow\uparrow\rangle$, symmetric spin zero $|\uparrow\downarrow\rangle + |\downarrow\uparrow\rangle$, and spin down $|\downarrow\downarrow\rangle$ pairing states, respectively.

As is the case for the motion of a particle in a central potential where the different values of angular momentum L determine the values of the energy, the order parameter can be decomposed in a linear combination of spherical harmonics $Y_L^m(\hat{k})$. So, L determines the type of pairing (s, p, d, f, ...) such that $T_c = T_c(\mathrm{L})$. Explicitly:

$$f^L(\hat{k}) = \sum_{m=-L}^{L} \eta_m Y_L^m(\hat{k}) \tag{2.49}$$

$$\vec{d}^{\,L}(\hat{k}) = \sum_{m=-L}^{L} \vec{\eta}_m Y_L^m(\hat{k}) \tag{2.50}$$

where L=0, 2, 4, ...in equation 2.49 and L=1, 3, 5, ...in 2.50.

When crystal anisotropy is present, the spherical harmonics have to be replaced by the basis functions of the different irreducible representations Γ of the point group of the crystal symmetry. Equations 2.49 and 2.50 now look like:

$$f^\Gamma(\hat{k}) = \sum_{i=1}^{d} \eta_i \psi_i^{\Gamma_g}(\hat{k}) \tag{2.51}$$

$$\vec{d}^{\,\Gamma}(\hat{k}) = \sum_{i=1}^{d} \vec{\eta}_i \psi_i^{\Gamma_u}(\hat{k}) \tag{2.52}$$

where the subscript g and u refer to even and odd basis functions respectively. One then invokes group theoretical arguments to decompose the point group symmetry into its irreducible representations. This procedure has been carried out by numerous authors [34, 33] in the case of strong spin-orbit coupling and by Ozaki *et al.* [35] for weak spin-orbit coupling. Table 2.3 summarizes the D_{6h} basis functions, relevant for UPt_3, for strong spin-orbit coupling (with the special choice $\hat{d} \parallel \hat{z}$ in the case of odd

parity wavefunction) as compiled by Sauls [31] for uniaxial symmetry only. A similar table can be generated for the point group symmetry of $YBa_2Cu_3O_{7-\delta}$.

A schematic k-space representation of some of the gaps listed in table 2.3 is shown in figure 2.11. We emphasize that these gaps are drawn *not* for a crystal with hexagonal symmetry but for uniaxial symmetry only. From this figure, we see that the conventional s-wave gap is finite everywhere, while the polar gap has a line of zeros in the basal plane and the axial[1] gap vanishes along points at the poles. The hybrid gap is simply a combination of a polar and axial gap with both a line of zeros in the basal plane and points along the c-axis. The tropical gap, not mentioned in this table, has two line nodes at the "tropics". This case will become relevant when we discuss the ellipsoidal harmonics decomposition of Norman and Hirschfeld [36] in chapter 6. The line nodes of this gap are not imposed by symmetry considerations but arise from an accidental cancellation. Furthermore, we stress that in figure 2.11 the plotted quantity is $|\Delta|$ so that any ϕ dependence is not obvious from such drawings. We emphasize that in thermal conductivity measurements, one probes the magnitude of the gap. The phase cannot be directly measured but enters in a subtle way through the coherence factors.

2.3.2 *Thermal conductivity and unconventional superconductors*

In this section we discuss the electronic thermal conductivity in both the heavy-fermions and the high-T_c. The main emphasis will be put on resonant impurity scattering of electrons as a means of qualitatively understanding the magnitude and the temperature dependence of the thermal conductivity at low temperature. Due to their relative simplicity and to the direct parallel that can be drawn with the previous sections, we only discuss the early models which use the Boltzmann equation approach. This will enable us to draw some general conclusions and to better grasp the physics underlying such calculations. Since these models were first developed in the context of heavy fermions, the discussion will be more detailed for these systems while only the main results will be given for the cuprates. We will also point out the limitations of such calculations which will pave the way for the more recent theoretical

[1] We use the term axial to refer to gaps with nodes at the poles with a *linear* k-dependence near the node *i.e.* axial I.

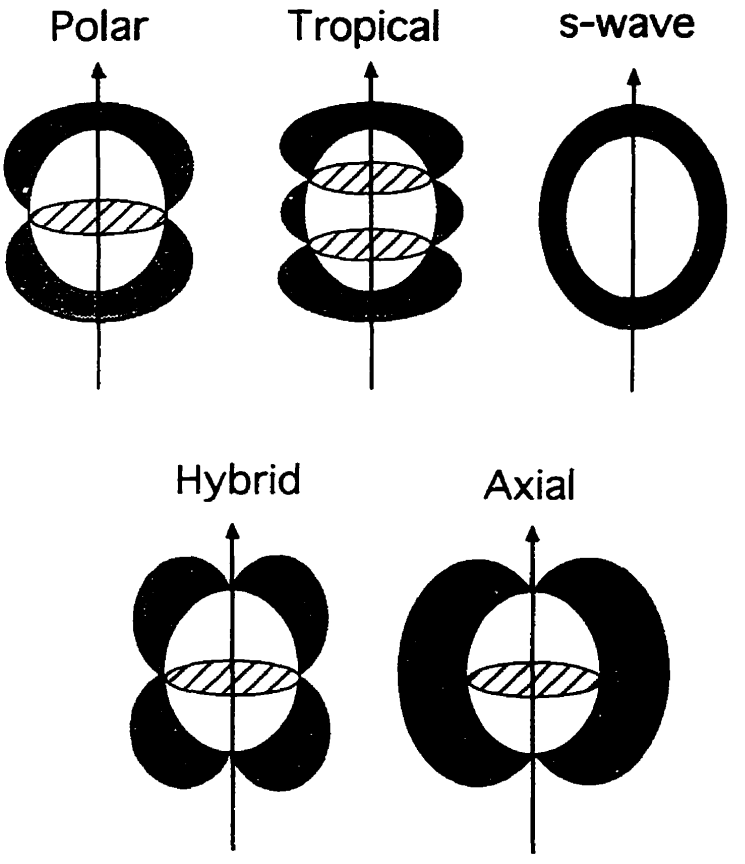

Figure 2.11: Schematic k-space representation for 5 possible gap structures in UPt_3.

results presented along with our experimental data in chapters 6 and 7.

1. *Heavy fermions and resonant impurity scattering*

In the superconducting state of conventional superconductors, the electronic thermal conductivity falls off exponentially with decreasing temperature as $T \rightarrow 0$. So does the specific heat and the ultrasound attenuation. Early measurements on polycrystalline UPt_3 showed $\kappa(T)$ to vary roughly as T^2 between 35 and 100 mK [37]. These results combined with the anisotropy of transverse sound seen by Shivaram *et al.* [38] established UPt_3 as a strong candidate for an unconventional superconductor. At the same time, theorists were examining gap structures similar to the polar p-wave state of ^{3}He. Calculations of the quasiparticle mean free path by Coffey *et al.* [39] and by Pethick and Pines [40] showed that the mean free path diverges at low tem-

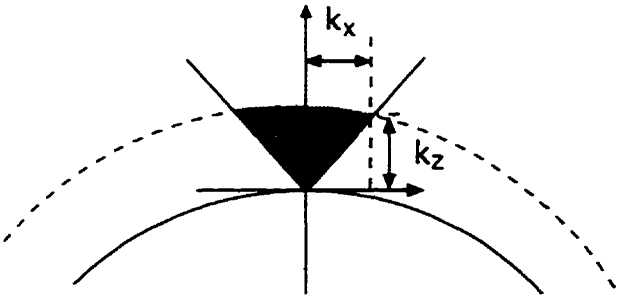

Figure 2.12: Schematic representation of the k-space volume of quasiparticles participating in transport near a node at the pole.

perature for the axial and polar p-wave states if the scattering is treated in the Born approximation. The latter authors showed that the ultrasonic attenuation in the superconducting state is of the same order as in the normal state and, that the thermal conductivity over temperature would tend to a large finite value as $T \rightarrow 0$, contrary to what was observed experimentally. We proceed to illustrate this. Recall that the scattering time in the superconducting state is given by $\tau_k = \frac{N_s(E)}{N(0)}\tau_N$ (equation 2.40) for a singlet state. For a triplet superconducting state, such as the axial and polar gaps considered by Pethick and Pines [40] and Coffey *et al.* [39], these authors show that in the Born approximation:

$$\tau_k = \frac{N(0)}{N_s(E)}\tau_N \tag{2.53}$$

The difference with respect to the s-wave result (equation 2.40) comes from the coherence factors. For example, consider an axial state with $\Delta = \Delta_0 \sin\theta = \Delta_0 \frac{k_x}{k_F}$. The number of states with energy lower or equal to E, n(E) is given by:

$$n(E) = \frac{V}{4\pi^3} \times (volume\ in\ k-space) = \frac{V}{4\pi^3}\left(\frac{1}{3}\pi k_x^2 k_z\right) \tag{2.54}$$

and is represented by the dashed region in figure 2.12.

The density of states is by definition:

$$N_s(E) = \frac{\partial n(E)}{\partial E} = \frac{V}{12\pi^2}\left(k_x^2\frac{\partial k_z}{\partial E} + 2k_x k_z \frac{\partial k_x}{\partial E}\right) \tag{2.55}$$

Using simple geometric arguments, we can show that $\frac{\partial k_x}{\partial E} = \frac{k_F}{\Delta_0}$ and that $\frac{\partial k_z}{\partial E} = \frac{m}{\hbar^2 k_F}$. Combining these, we get that the superconducting density of states for a linear point

node is proportional to E^2:

$$N_s(E) = \left(\frac{V k_F m}{4\pi^2\hbar^2}\right)\frac{E^2}{\Delta_0^2} \tag{2.56}$$

Similarly, it is possible to show that $N_s(E) \propto E$ for a line node (as with the polar gap, $\Delta \propto \cos\theta$) and that $N_s(E) \propto E$ for a quadratic point node (as with the hybrid II gap, $\Delta \propto \sin^2\theta\cos\theta$ near $\theta = 0$). As first pointed out by Coffey *et al.* [39], this leads to a mean-free path that diverges as $1/\varepsilon^2$ and $1/\varepsilon$ in the axial and polar cases respectively. Using equation 2.29 and in the case of the axial gap, we can show that in the case of a heat current along the node direction (*i.e.* for $\hat{k} \parallel \hat{c}$, $v_k \approx v_F$):

$$\frac{\kappa_{es}(T)}{T} \sim \frac{1}{T^2}\sum_k \left(-\frac{\partial f}{\partial E_k}\right) E_k^2 v_k^2 \tau_k \tag{2.57}$$

$$\sim \frac{1}{T^2}\sum_k \left(-\frac{\partial f}{\partial E_k}\right) E_k^2 v_F^2 \frac{N(0)}{E_k^2}\tau_N \tag{2.58}$$

$$\sim \frac{\kappa_N(T_c)}{T_c} \tag{2.59}$$

where we have used the fact that near a node $v_k \to v_F$ because $E = \varepsilon$. Furthermore, the density of states derived above enters in many physical properties such as the specific heat. It is possible to show (see for example [41]) that a linear point node results in a T^3 specific heat at low temperature, while a line and a quadratic point both result in a T^2 power law.

Table 2.4: Summary of scattering time and group velocity for the BRT theory and the axial state treated in the Born and resonant impurity scattering (RIS) approximations.

	BRT	axial (Born)	axial (RIS)
τ_s^{-1}	$\tau_N^{-1}\frac{N(0)}{N_s(E)}$	$\tau_N^{-1}\frac{N_s(E)}{N(0)}$	$\tau_N^{-1}\frac{1}{\lvert g(E)\rvert^2}\frac{N(0)}{N_s(E)}$
v_k $(\hat{k} \parallel \hat{z})$	$\frac{N(0)}{N_s(E)}v_F$	v_F	v_F

We find it convenient to pause here and summarize the results for the scattering rate and the group velocity for the BRT theory and for the Born approximation result

for the axial state. Table 2.4 includes these results along with what we are going to find when we discuss the resonant impurity scattering approach to calculate thermal conductivity. Note that in going from BRT to the axial state in the Born approximation, the density of states are reversed and this leads to a divergent scattering time for the axial state. As we saw, a consequence of this is a large finite linear term in the thermal conductivity. The function $g(E)$, introduced below, will solve this problem and enable a qualitative comparison of theoretical calculations with experimental data.

Pethick and Pines [40] showed that if, instead of using the Born approximation, one assumes that multiple interactions of a quasiparticle with an impurity are important, which corresponds to the phase shift in the normal state being close to $\pi/2$, the qualitative temperature dependence of the transport coefficients in the superconducting phase is in better agreement with experiment. The physical motivation for the large phase shifts arises from the fact that in the heavy fermion materials, the *f*-electron atoms, such as U and Ce, are thought to be responsible for the heavy-electron behavior. When non-magnetic impurities are introduced into a heavy-electron material, it is possible for an impurity to replace an *f*-electron atom. The impurity then corresponds to the absence of a magnetic site, and might therefore be expected to give rise to a phase shift close to $\pi/2$. In the case where the impurity replaces one of the other atoms, the phase shift is likely to be small.

Various authors [42, 43, 44] then proceeded to calculate specific heat and transport properties using a self-consistent T-matrix approach in the case of resonant impurity scattering for both an axial and a polar gap. Comparison with experiments by these authors seemed to favor the polar gap, even though a perfect agreement could not be obtained. Because of their Boltzmann equation approach, similar to that described in sections 2.1.2 and 2.2.2, we choose to illustrate the later findings of Arfi and Pethick [45]. These authors calculated the thermal conductivity in anisotropic superconductors in the limit where the scattering of quasiparticles by non-magnetic impurities is the dominant process. The calculations where performed in the Born approximation where $\delta_N \ll \pi/2$ and in the resonant impurity scattering limit where $\delta_N = \pi/2$. Their approach was not self-consistent in the sense that they did not consider the effect of

the impurities on the gap parameter, but they argue that such effects would only be present at the lowest temperatures, *i.e.* that their approach is valid for $k_B T \gtrsim \hbar\Gamma_0$ which in good crystals means $T/T_c \gtrsim 0.1$. It is instructive to discuss their results as they contain many ingredients of the more recent theories discussed in chapter 6.

As with our description of the BRT theory, we start with equation 2.16 in which we replace the free-electron energy by the quasiparticle energy E_k[1]:

$$\vec{j}_q = \frac{1}{T}\sum_{k\sigma} \mu_i^2 E_k^2 \frac{\partial f_0}{\partial E_k} v_k^2 \tau_k \vec{\nabla} T \tag{2.60}$$

The problem is again to calculate the relaxation time τ_k and the group velocity v_k of the quasiparticles in the case of resonant impurity scattering and for gaps with nodes.

In a similar approach as in BRT theory, Arfi and Pethick [45] computed the quasiparticle relaxation time in the case of interest starting from Fermi's golden rule. They arrive at the result (valid in the unitary limit only):

$$\frac{1}{\tau_k} = \frac{1}{\tau_N} \frac{1}{|g(E_k)|^2} \frac{N_s(E_k)}{N(0)} \tag{2.61}$$

where the function $g(E_k)$ is defined by:

$$g(E) = \int \frac{d\Omega}{4\pi} \frac{E}{\left(E^2 - |\Delta_k|^2\right)^{1/2}} \tag{2.62}$$

The function $g(E)$ has a real contribution proportional to the density of states, and an imaginary part which corresponds to a dispersive correction to the quasiparticle self-energy [45]. The imaginary part vanishes if the magnitude of the energy is above the maximum value of the energy gap as a function of angle on the Fermi surface, but is non-zero below. As a consequence, this function is important only in unconventional superconductors (with anisotropic gaps), since in isotropic ones there are no excitations with energies less than the maximum energy gap[2]. The function $g(E)$ was computed for the axial, polar and hybrid I[3] gaps by Arfi and Pethick [45] and we show their results in figure 2.13 for the scattering time as a function of energy for both small phase shifts ($\delta \ll \pi/2$) and for resonant impurity scattering ($\delta = \pi/2$).

[1] The factor 2 difference arises from the sum over spin indices σ explicitly put in by Arfi and Pethick.

[2] Note that in putting $g(E) = 1$ we do not recover the BRT result (equation 2.40) because the coherence factors are different for a triplet state (axial and polar gap) than that of a singlet state (BCS gap).

[3] In their paper, the hybrid I gap is called the *d*-wave gap.

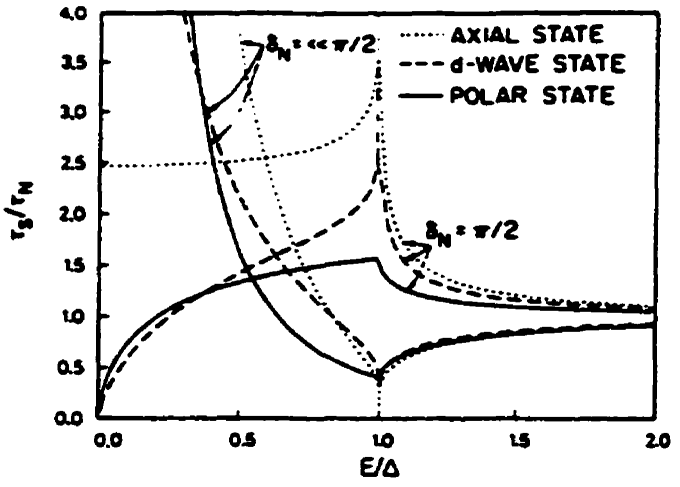

Figure 2.13: Quasiparticle relaxation times in the axial, polar and hybrid I or d-wave states as a function of energy for the cases of small phase shifts ($\delta \ll \pi/2$) and for resonant impurity scattering ($\delta = \pi/2$) (after [45]).

Replacing equation 2.61 for the scattering time and equation 2.32 for the group velocity (identical to the BRT case for gaps with nodes) into equation 2.60 and as usual, changing the sum into an integral, Arfi and Pethick found:

$$\kappa_{ii} = 4N(0)\frac{v_F^2}{T}\int_0^{+\infty} dE\ E^2\left(-\frac{\partial f_0}{\partial E}\right)\tau_s(E)\int_{|\Delta_k|^2<E^2}\frac{d\Omega}{4\pi}\mu_i^2\frac{\left(E^2-|\Delta_k|^2\right)^{1/2}}{E} \tag{2.63}$$

By letting $\Delta \to 0$, the integral can be evaluated to yield the normal state thermal conductivity. Normalized by the normal state, equation 2.63 becomes:

$$\frac{\kappa_{ii}}{\kappa_N(T_c)} = \frac{T}{T_c}\frac{18}{\pi^2}\int_0^{+\infty} dE\ \frac{E^2}{T^2}\left(-\frac{\partial f_0}{\partial E}\right)\frac{\tau_s(E)}{\tau_N}\int_{|\Delta_k|^2<E^2}\frac{d\Omega}{4\pi}\mu_i^2\frac{\left(E^2-|\Delta_k|^2\right)^{1/2}}{E} \tag{2.64}$$

Arfi and Pethick computed this integral for the three gaps discussed above for a heat current in the basal plane (in their notation XX) and along the c-axis (ZZ). They assumed a BCS temperature dependence for the superconducting gap as approximated by equation 2.26. They chose a $\Delta C/C = 0.86$ from Sulpice *et al.*'s data [37] and the parameter h, being the mean square value of the gap relative to its maximum value was computed according to:

$$h = \frac{\int \frac{d\Omega}{4\pi}|\Delta_p|^2}{\Delta^2} \tag{2.65}$$

The results of Arfi and Pethick are presented in figure 2.14 for the axial, polar and hybrid I gaps. Notice that in the Born approximation, κ_{zz}/T in the axial case and

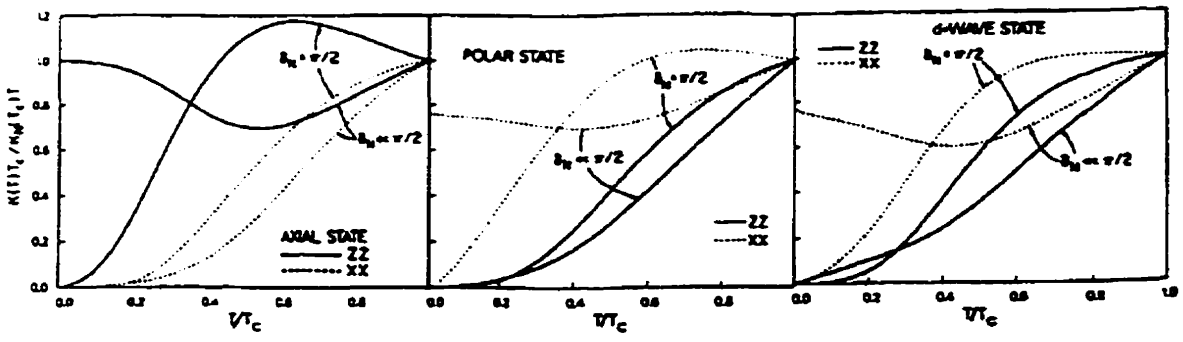

Figure 2.14: Normalized thermal conductivity over temperature along (ZZ) and perpendicular (XX) to the c-axis for $\delta_N \ll \pi/2$ and $\delta_N = \pi/2$ for the axial (left panel), polar (middle panel) and hybrid I or d-wave state (right panel), after [45].

κ_{zz}/T for both the polar and hybrid I gaps, all tend to values 0.8–1.0 of the value at T_c as was qualitatively argued above. Comparison with Arfi and Pethick's results will be provided in chapter 6 when discussing our thermal conductivity results on UPt_3.

Before concluding this section, we go back to discuss the function $g(E)$ and its physical implication on the thermal conductivity. In normal metals or in the BRT case, the thermal conductivity is simply a peak average (because of the directional cosine μ_i) in the direction of the propagation of heat. Therefore, if we imagine a pathological case of an anisotropic s-wave gap with nodes along the c-axis treated in the Born approximation, *i.e.* $g(E) = 1$, then the thermal conductivity at low temperature would be dominated by the narrow region near the node in the direction of propagation yielding a power law dependence, and would be exponentially activated for a direction perpendicular to the nodes. A consequence of the numerous collisions of the carriers undergoing resonant impurity scattering, the function $g(E)$ samples all of the Fermi surface. This can lead to non-negligible contributions from parts of the Fermi surface *not* in the vicinity of the nodes. The papers by Barash and Svidzinsky [46] and Arfi and Pethick [45] provide a good discussion of the function $g(E)$ with respect to its real and imaginary parts and its effect on the thermal conductivity.

Finally, Arfi *et al.* [47], in a following paper, also calculated the viscosity which is proportional to the ultrasonic attenuation. By comparing their calculations with experimental results on UPt_3, they are able to deduce a normal state scattering rate of 3×10^{10} s^{-1}. This estimate will be compared with estimates from resistivity and dHvA in chapter 3. Its importance will become clear when we discuss the recent self-

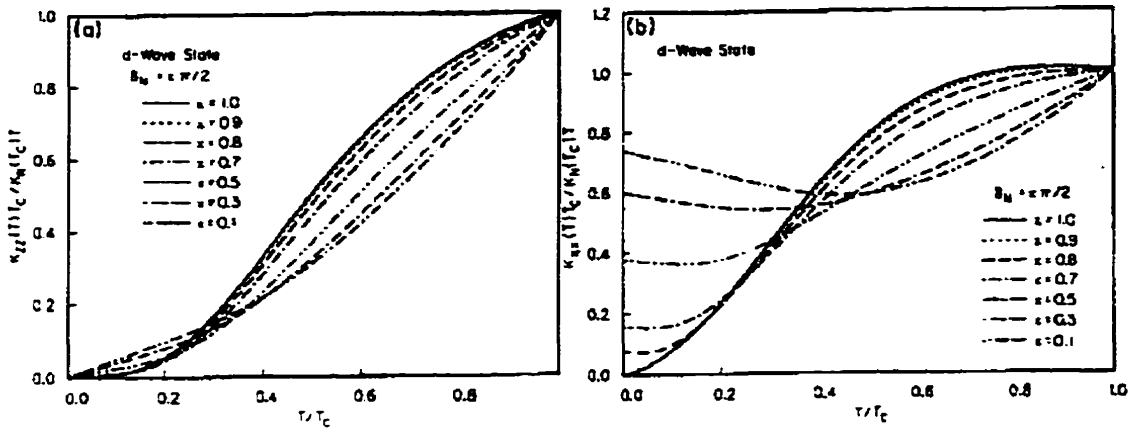

Figure 2.15. Normalized thermal conductivity over temperature as a function of reduced temperature for $\delta_N = x\pi/2$ where x=0.1, 0.3, 0.5, 0.7, 0.8, 0.9 and 1.0 for the c-axis (ZZ) and basal plane (XX) thermal conductivity for the hybrid I gap (after Arfi *et al.* 1989).

consistent theory of thermal conductivity and compare those with our experimental results on UPt_3.

2. *Resonant impurity scattering and the influence of an arbitrary phase shift*

In a subsequent paper, Arfi *et al.* [47] investigated the effect of an arbitrary phase shift in the normal state. This approach is justified since when an impurity replaces a Kondo lattice atom it results in a large phase shift, as discussed above, while the replacement of any other atom would not. Since the impurities are expected to be distributed at random, an intermediate overall phase shift would be expected. We will come back to such an hypothesis in chapter 6.

The reasoning of Arfi *et al.* [47] is again based on a Boltzmann equation formalism. In the case of arbitrary phase shifts, the calculations are somewhat more involved and only the results will be given here. Figure 2.15 summarizes their results for both heat current directions for a *d*-wave gap (or hybrid I) structure previously discussed.

They find that for all superconducting states, and for all phase shifts, the thermal conductivity shows a strong anisotropy. This is a consequence of the enhanced conductivity when the heat flow is along the direction of nodes (axial state), or in the plane of nodes (polar and hybrid I) compared with a direction orthogonal to the nodes. Another common feature is that the results for a phase shift $\delta_N = 0.9\pi/2$ or

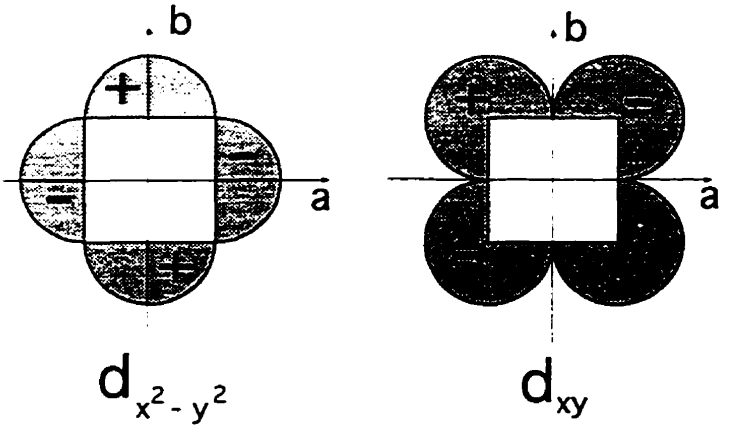

Figure 2.16: Schematic representation of the two gap structures investigated by Arfi [48]. The Fermi surface is taken to be square (*i.e.* tetragonal symmetry) and the gap is represented by the shaded area. The + or - signs refer to the phase of the gap.

greater are almost indistinguishable from those obtained in the unitary limit, except at low temperatures. At the lowest temperatures, the authors note that the thermal conductivity increases as the phase shift decreases. The dependence is reversed in the intermediate temperature range.

We would like to emphasize that the study of the anisotropy of the thermal conductivity seems to be well suited for distinguishing different gaps (see figure 2.14).

3. *Resonant impurity scattering applied to the high-T_c superconductors*

Arfi *et al.*'s formalism discussed above in the case of the three dimensional heavy-fermions was also applied to high-temperature superconductors by Arfi [48]. A key feature of these materials, as will be discussed in chapter 4, is the important role of the copper-oxygen planes. These planes give rise to a quasi-two dimensional character. The author calculated the thermal conductivity using the formalism developed by Arfi *et al.* [45] using Boltzmann's equation for *s*-wave scattering by nonmagnetic impurities at a very dilute concentration for a two-dimensional square lattice. As before, two cases were studied: the Born approximation and the unitary limit. Furthermore, two superconducting order parameters were considered, namely those with $d_{x^2-y^2}$ and d_{xy} symmetries (see figure 2.16). These two gaps differ only in the position of the nodes on the Fermi surface. The calculated thermal conductivity, in the approximation

of a circular Fermi surface, is found to be equal for both gap symmetries which is a consequence of the fourfold symmetry of the square lattice. As for heavy fermions, Arfi found a large intercept for κ/T of the order of $0.8\kappa(T_c)/T_c$ in the Born approximation, but found a power law dependence at low temperature for resonant impurity scattering (see figure 2.17):

$$\frac{\kappa/T}{\kappa_N/T} = \frac{4}{5}\left(\frac{T}{\Delta(T)}\right)^2 \tag{2.66}$$

Assuming[1] $\Delta(0) = 2.14 k_B T_c$ and taking $\frac{\kappa_N}{T} = \frac{L_0}{\rho_0}$=24.4 mW/K^{2}cm (see section 7.1) we get that at low temperature, the electronic thermal conductivity should follow $\kappa/T = 4.87 \times 10^{-4} T^2$ mW/K^{2}cm. We will see that at 100 mK, our measured thermal conductivity over temperature is $\sim$ 0.5 mW/K^{2}cm, 6 orders of magnitude larger than Arfi's estimate. Furthermore, the theory does not yield a residual linear electronic term as observed in $YBa_2Cu_3O_{7-\delta}$ (see chapter 7). On the other hand, it provides a qualitative understanding of heat conduction by electrons in the cuprates ruling out the Born approximation and generalizing the conclusions of resonant impurity calculations to the high-T_c cuprates. Some of the problems of Arfi's formalism at low temperature may well be corrected by including self-consistency (essentially at low temperature) and inelastic scattering of quasiparticles (essentially at high temperature). The models of Graf *et al.* [49] and Hirschfeld and Putikka [50] include these and a direct comparison of their findings with our experimental results will be provided in chapter 7.

4. *Summary*

To conclude this chapter, we would like to emphasize that the results of Arfi *et al.* [45, 47, 48] lack several of the ingredients used in current theories of thermal conductivity in the heavy-fermions and the cuprates. For example, they lack the self-consistency that enable direct comparison with experimental results at the lowest temperatures. This might not be a problem in UPt_3 but is certainly so in $YBa_2Cu_3O_{7-\delta}$. They also neglect anisotropy of the Fermi surface and inelastic scattering which are known to be important near T_c in the case of UPt_3. Nevertheless, their theory provides strong qualitative results, namely that the Born approximation cannot account for

[1] This value is the weak-coupling *d*-wave gap ratio (see for example [49]).

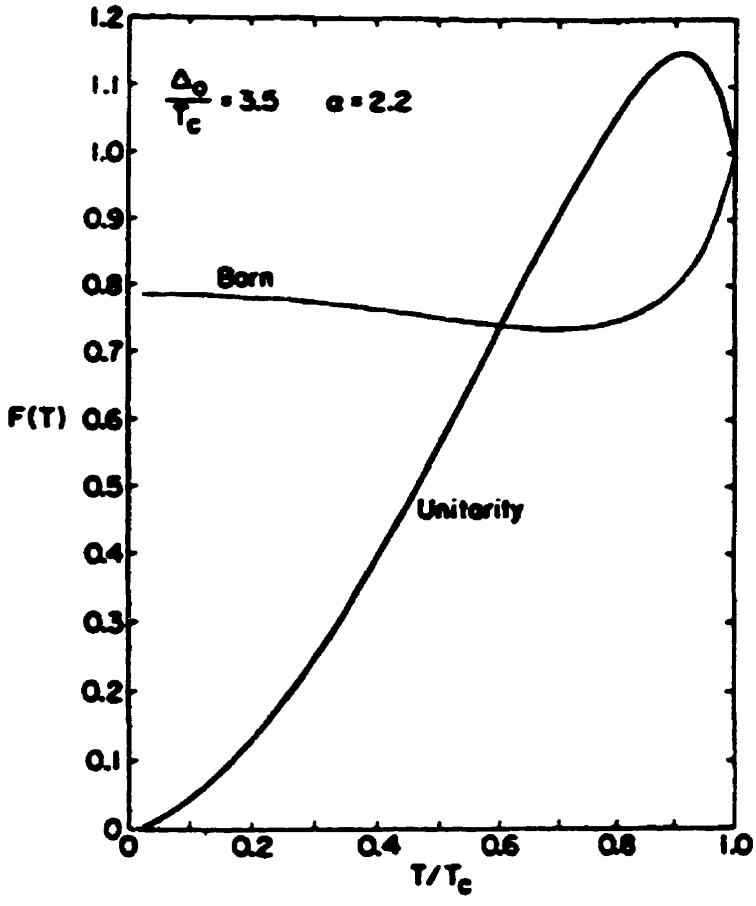

Figure 2.17: Normalized κ/T (F(T)=$\kappa T_c/\kappa_N(T_c)T$) as a function of reduced temperature in the unitary limit and Born approximation case for a $d_{x^2-y^2}$ gap structure (after [48]).

the observed behavior of the thermal conductivity below T_c. Furthermore, in the case of UPt_3, their thermal conductivity curves display anisotropy in the superconducting state that could be detected by measuring thermal conductivity on *one* single crystal along both the basal plane and the c-axis direction. We will come back to all of these points when we discuss the more complete theories of Fledderjohann and Hirschfeld [51], Norman and Hirschfeld [36], Graf *et al.*[52, 49] and Hirschfeld and Putikka [50].

3

THE HEAVY FERMION COMPOUND UPt_3

In this chapter, the normal and superconducting state properties of UPt_3 will be reviewed. The reader is also referred to the papers by de Visser [53, 54] and Rauchschwalbe [55] for early normal state and magnetic properties while Grewe and Steglich [56] review both early normal and superconducting properties. More recent reviews, mostly concerning the superconducting state can be found in the paper of Taillefer [57], Löhneysen [58] and Heffner and Norman [59].

3.1 Normal state properties

In this section, we review some of the normal state properties of UPt_3. Our attention will be focussed mainly on low temperature properties of quantities that will be useful later on in the thesis. The normal state properties represent a vast subject (especially with respect to the origin of the large effective masses) which we will not discuss. We simply mention that the Kondo effect and spin fluctuations are the leading mechanisms thought to be responsible for the unusual normal state properties and possibly also for the superconducting pairing.

3.1.1 Crystal structure

UPt_3 crystallizes in the $MgCd_3$-type structure, a closed-packed hexagonal structure with 2 formula per unit cell. The compound belongs to the space group $P6_3/mmc$ and the lattice parameters are given by : a = b = 5.764 Å and c = 4.899 Å. The crystal structure is shown in figure 3.1 along with the magnetic moments (to be discussed in section 3.1.3). One should note that when discussing transport properties such as resistivity or thermal conductivity, the b-axis is chosen *perpendicular* to the a-axis and therefore corresponds to the b*-axis.

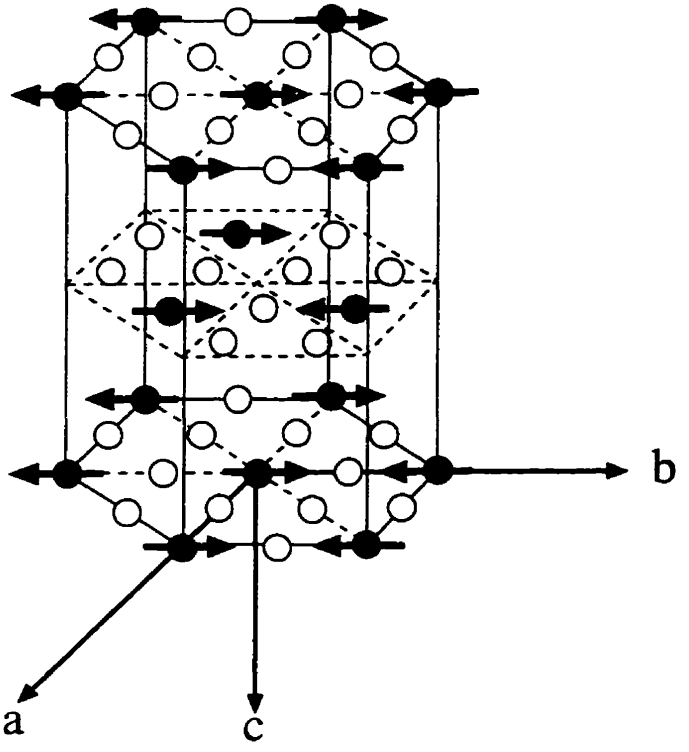

Figure 3.1: Crystal structure of UPt_3. The solid circles represent the position of the uranium atoms while the open circles are for the platinum. The arrows indicate the direction of the magnetic moment (for one possible domain) detected by neutron diffraction (to be discussed in section 3.1.3). Note that when discussing transport properties, the b-axis is chosen perpendicular to the a-axis and corresponds to the b*-axis.

Recent transmission electron microscope results (TEM) found an incommensurate structural modulation of the hexagonal structure [60, 61]. In these papers, satellites were shown to exist around the structural Bragg peaks. These correspond to real-space modulations with domain size of $\sim$ 5000 Å or more. Such modulations have not been observed in careful X-ray studies [62] nor in neutron diffraction experiments and might therefore correspond to an artifact inherent to the surface preparation necessary for TEM measurements. The presence of such modulations could have repercussions on the superconducting phase diagram to be discussed later in this chapter but will be ignored in light of the absence of conclusive evidence.

3.1.2 Thermal, transport and elastic properties

We now proceed to briefly discuss the specific heat, the charge transport, the elastic properties and the Fermi surface topology. Discussion of previous thermal conductivity results is left for chapter 6.

1. *Specific heat*

For temperatures below 20 K, the normal-state specific heat of UPt_3 obeys the relationship:

$$c = \gamma T + \beta_{ph} T^3 + \ldots \tag{3.1}$$

The first term of equation 3.1 represents the electronic specific heat, the $\beta_{ph}T^3$ is the phonon specific heat while other terms are attributed to spin fluctuations [54]. Contributions to specific heat arising from long-range magnetic order, crystal-field effects, magnetic impurities and band-structure effects can all be shown to be absent by studying the specific heat in magnetic fields [54]. A fit to equation 3.1 gives γ=422 mJ/K^{2}mol U and β_{ph}=0.85 mJ/K^{4}mol U (other terms are not discussed). The γT term, about 10^2 to 10^3 times larger than in simple metals, can be related to the effective mass through $m^* = 3\hbar^2\gamma / k_B^2 k_F V_M$. Assuming a Fermi wave-vector of $k_F = (3\pi^2 Z/\Omega)^{1/2}$=1.06 Å^{-1} where Z is the number of heavy electrons per unit cell of volume (Ω), using the measured molar volume $V_M = 42.43 \times 10^{-6}$ m^3/mol and making use of the fitted value for γ, an average effective mass of $m^* = 180 m_e$ (m_e is the free electron mass) can be deduced [54]. These results will be compared with the direct mass measurements by the de Haas-van Alphen effect.

2. *Sound velocities*

Crystals with hexagonal symmetry require five independent elastic constants to specify the relationships between stresses and strains. They may be listed as c_{11}, c_{12}, c_{13}, c_{33}, and c_{44}. These quantities can be determined by sending ultrasonic waves through properly oriented crystals and measuring the sound velocities which depend on the elastic constants and the density. The results obtained by de Visser *et al.* are summarized in table 3.1 [54]. These constants are weakly temperature dependent and they typically increase by ~2% in going from room temperature down to 4 K.

Table 3.1: Sound velocities and elastic constants of UPt_3 at room temperature. The c_{ij} values are based on a density $\rho = 1.940 \times 10^4$ kg/m^3. $\vec{k}$ is the direction of propagation and $\vec{\epsilon}$ is the polarization. $c_{12} = 1.421$ Mbar comes from a combination of c_{11} and c_{66} while c_{13} is calculated from four velocities (see [54] and references therein). v_8 served as a cross check. The b′ direction is oriented at 45° between the b and c-axis but in a plane perpendicular to the a-axis.

Mode type	$\vec{k}$	$\vec{\epsilon}$	velocity (m/s)	elastic constant (Mbar)
longitudinal	c	c	$v_1 = 3860$	$c_{33} = \rho v_1^2 = 2.891$
shear	c	ab	$v_2 = 1385$	$c_{44} = \rho v_2^2 = 0.372$
longitudinal	b	b	$v_3 = 3993$	$c_{11} = \rho v_3^2 = 3.093$
shear	b	a	$v_4 = 2076$	$c_{66} = \frac{1}{2}(c_{11} - c_{12}) = \rho v_4^2 = 0.836$
shear	b	c	$v_5 = 1388$	$c_{44} = \rho v_5^2 = 0.374$
quasi longitudinal	b′	b′	$v_6 = 3754$	$c_{13} = 1.732$
quasi shear	b′	c′	$v_7 = 1827$	$c_{13} = 1.695$
shear	b′	a	$v_8 = 1753$	$\frac{1}{4}c_{11} - \frac{1}{4}c_{12} + \frac{1}{2}c_{44} = \rho v_8^2$

By using the procedure outlined by Alers [63] for integrating the sound velocities over all crystallographic directions in hexagonal crystals, it is possible to calculate the Debye temperature. Numerical integration yields a value of 217 K which agrees perfectly with the estimate from specific heat. This number along with the sound velocities will prove useful when estimating the maximum phonon contribution in the superconducting state in UPt_3 (see section 6.3.1).

3. *Resistivity and magnetoresistance*

As seen in figure 3.2, the resistivity is strongly anisotropic between the basal plane and c-axis, while no anisotropy, within experimental uncertainty, is detected within the basal plane. The value of the resistivity at room temperature is 230 (130) $\mu\Omega$cm for the b (c)-axis and will be used to determine the geometric factor of our samples. Unlike most heavy-fermions, UPt_3 does not have a minimum in resistivity characteristic of the Kondo-effect.

Below 2 K, the resistivity (ρ) can be described very well by $\rho = \rho_0 + AT^2$ as expected from Fermi liquid theory with ρ_0 being the residual resistivity depending on sample quality and A represents the inelastic electron-electron term. It amounts to

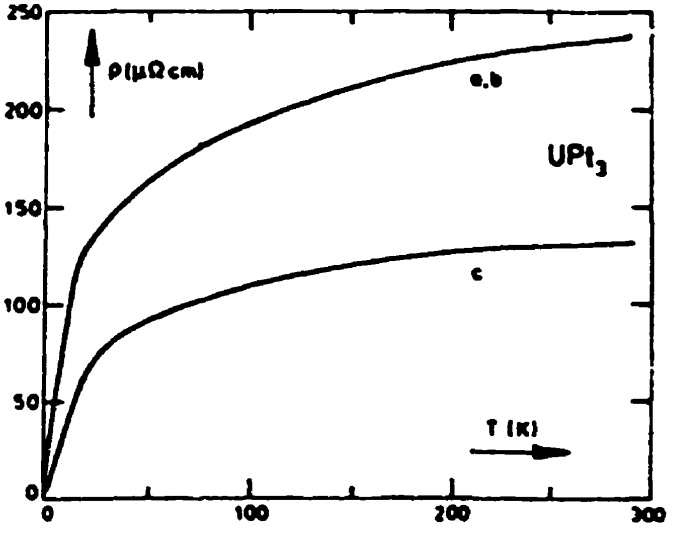

Figure 3.2: Electrical resistivity (ρ) versus temperature for unannealed single crystals of UPt_3 for current directions as indicated (after [54]).

A = 1.6 (0.58) $\mu\Omega$cmK^{-2} for b (c)-axis, namely four orders of magnitude larger than in simple metals [54]. De Visser *et al.* obtained typical values of ρ_0 of 6.2 (1.7) $\mu\Omega$cm resulting in residual resistance ratios (RRR=R(300K)/R(0K)) of 37 (76) for b (c)-axis. Crystal purity has tremendously improved since then, and RRR's of the order of 600 are not uncommon for bulk single crystals. Another way to gauge crystal quality is to look at the ratio of the inelastic term over elastic contribution in the resistivity: A/ρ_0. For de Visser's crystals, we get: 0.26 (0.34) K^{-2}. In the best crystals, this ratio is around 3 K^{-2}. Note that the uncertainty in his geometric factor is around 10%. Since we use de Visser's resistivity values to determine the geometric factor of our UPt_3 samples, the same uncertainty applies to our measured resistivities and thermal conductivities.

If we refer back to section 2.1.1, we can relate the electrical resistivity to a scattering rate Γ_0: $\rho_0 = \frac{m^*\Gamma_0}{ne^2}$ with n = $k_F^3/3\pi^2$. Taking k_F=1.06 Å^{-1} and $m^* = 180m_e$, we get $\Gamma_0 = 1.1 \times 10^{11}$ s^{-1} for de Visser's c-axis crystal. In good crystals, this residual resistivity is now down to approximately 0.2 $\mu\Omega$cm which amounts to a scattering rate of $\Gamma_0 = 1.4 \times 10^{10}$ s^{-1}. Recall that the estimate of Arfi *et al.* [47] is comparable to that of good crystals, *i.e.* 3×10^{10} s^{-1}. These are simple-minded estimates which assume a spherical Fermi surface. The de Haas-van Alphen effect provides a much more reliable and direct estimate of the scattering rate. We discuss such an esti-

mate below. The quantity Γ_0 enters as an important material parameter in theories that discuss the superconducting properties of UPt_3. We will come back to this in chapter 6.

Magnetoresistance was first measured at low temperatures by Sulpice *et al.* [37] on a good quality polycrystal. The magnetoresistance is large and positive and the authors find that:

$$\rho(H,T) = \rho_0 + AT^2 + aH \tag{3.2}$$

for temperatures lower than 1 K and fields smaller than 0.6 T. More recent results on single crystals by Taillefer (unpublished) give an anisotropic field dependence of a = 6.8×10^{-2} $\mu\Omega$cm/T for $\vec{J} \parallel \hat{c}$ and $\vec{H} \perp \hat{c}$ and is negligible for $\vec{H} \parallel \hat{c}$. These numbers obtained on crystals similar in quality to our own will be used to correct the normal state thermal conductivity.

4. *Fermi surface*

The Fermi surface of UPt_3 was mapped out by Taillefer *et al.* [64, 65] by means of angle-resolved measurements of the de Haas-van Alphen effect. The results are summarized in table 3.2 and in figure 3.3. The authors were able to resolve a total of 10 branches all for fields in the basal plane. No dHvA oscillations were observed in the vicinity of the hexagonal c-axis. By comparing their findings with Fermi surface calculations (see [65, 66] and references therein), a good agreement is found between the calculated and experimental Fermi surface topology. On the other hand, the measured and calculated cyclotron masses are far apart: the ratio of measured to band-calculated masses is in the range 10–25. This discrepancy or mass enhancement is due to the strong electron-electron interactions not included in the band structure calculations. As an example, the largest surface $\Gamma 3$, which accounts for most of the density of states has a Fermi velocity of v_F = 5500 m/s and a mean-free path of ℓ_0 = 2200 Å. The corresponding scattering rate for the electrons on this sheet is $v_F/\ell_0 = 2.5 \times 10^{10}$ s^{-1} about twice as large as what we inferred using a simple-minded estimate based on the resistivity on good crystals of comparable high quality. Note that Γ_{dHvA} is likely to be somewhat higher than $\Gamma_{transport}$ simply because dHvA is more sensitive to low angle scattering than transport. A good value for $\Gamma_{transport}$ is

Table 3.2: Experimental values of Taillefer *et al.* [64, 65] for the average wavevector (k_0) and the effective mass (in units of m_e) for various Fermi surface sheets as measured by the dHvA effect. Refer to figure 3.3 for the sheets' notation.

Sheet	k_0 (Å^{-1})	mass (m_e)	ℓ_0 (Å)
Γ1 (e)	0.12	25	1000
AL5 (h)	0.14	-	≳1000
L4 (e)	0.16	40	≳1000
K3′ (e)	0.21	50	≳1000
Γ2 (e)	0.25	60	1500
Γ3 (e)	0.43	90	2200
L4 (h)	-	-	-

1-1.5×10^{10} s^{-1} for ρ_0=0.2 $\mu\Omega$cm for crystals $\vec{J} \parallel \hat{c}$. This scattering rate corresponds to $0.15 k_B T_c$.

3.1.3 Magnetic properties

Magnetism often plays an important role in unconventional superconductors. As we will see in chapter 4, the high-T_c compounds are close to an antiferromagnetic instability as a function of oxygen doping. As to the organic superconductors, one can induce spin-waves as a function of hydrostatic pressure and magnetic field. The heavy fermions are unique in the sense that *both* the magnetic and the superconducting order are found to coexist. As discussed in chapter 2, this has led many theorists to postulate that the superconducting pairing came about through spin fluctuations.

1. *Antiferromagnetic correlations*

The fluctuation spectrum in UPt_3 was first investigated by Aeppli *et al.* [67] using inelastic neutron scattering. At a gross level, a local magnetic moment of $\sim 1\ \mu_B$ fluctuates at a typical energy of the order of 10 meV. On a finer scale, moments on neighbouring sites tend to be correlated in direction. Weak ferromagnetic alignment within the basal plane with antiferromagnetic alignment in neighbouring planes tends to appear at a fluctuation energy of the order of 5 meV. The characteristic wavevector

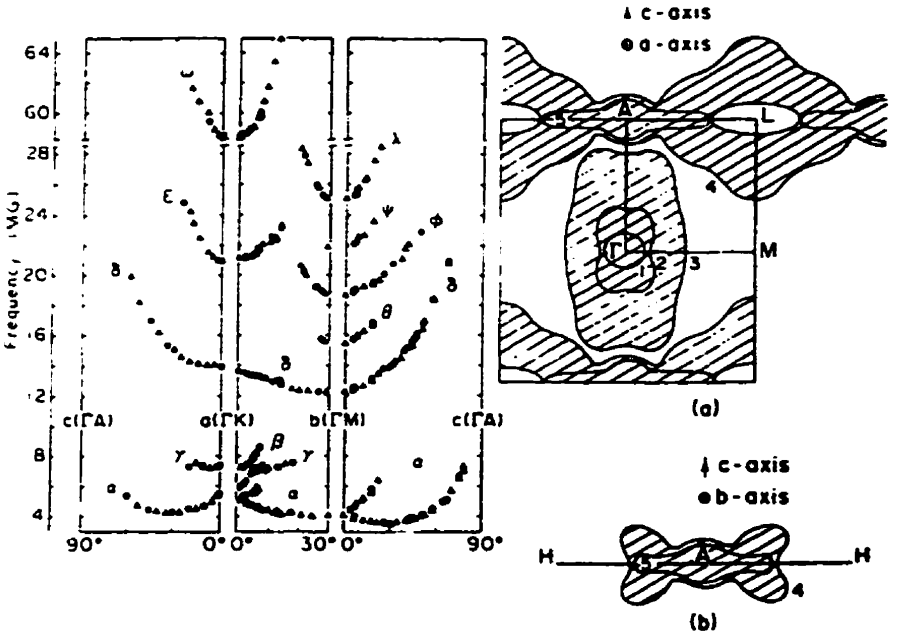

Figure 3.3: Left panel: angular variation of the fundamental dHvA frequencies with orientation of the magnetic field in the planes a-b, a-c and b-c (after Taillefer *et al.* [64, 65]). Right panel: Section of the Fermi surface as derived from conventional band-structure calculations (after [66]).

for this AFM coupling is $\vec{Q} = (0,0,1)$. At even lower energies, of the order of 0.3 meV, there is another antiferromagnetic correlation with wavevector $\vec{Q} = (\pm\frac{1}{2},0,1)$. The effective moments associated with this fluctuation is of the order of $0.1\mu_B$. Part of these low-energy fluctuating moments eventually become statically ordered at 5 K and give way to an antiferromagnetic order. The unusual properties of this ordered phase is the subject of the next paragraph.

2. *Antiferromagnetic ordering*

Aeppli *et al.* [68] were the first to establish UPt_3 as an ordered antiferromagnet. They find a doubled unit cell in the basal plane and an ordered moment of $(0.02 \pm 0.01)\mu_B$ parallel to the doubling direction (see figure 3.1). The magnetic Bragg intensity I_B proportional to the square of the magnetization is found to rise linearly with decreasing temperature below $T_N = 5\ K$. Thus, the mean-field expression $M \propto (T_N - T)^{1/2}$ adequately describes the temperature dependence of the magnetic order parameter over a much wider range in T/T_N than is ordinarily the case [68]. As we shall see in section 3.2.3, the authors showed that this linear increase in the intensity

stops when the superconducting state sets in. Finally, the measured Bragg peaks are not resolution limited indicating that the magnetic order is not of infinite range. A correlation length of ~200 Å is obtained [69].

3.2 Superconducting properties

In this section, we review the superconducting properties of UPt_3. We first proceed to discuss the multiple superconducting phases followed by some low temperature properties of the superconducting state. The interplay of magnetism and superconductivity followed by a discussion of some theoretical models for the superconducting phase diagram will conclude this section.

3.2.1 Multiple superconducting phases

The most compelling evidence for unconventional superconductivity came from the discovery of a split superconducting transition in the specific heat measurements of Fisher *et al.* [70], a feature also observed in the unconventional superfluid ^{3}He. In the case of UPt_3, only in the highest quality crystals could the splitting be resolved; the double specific heat jump is replaced by a broad transition in lower quality crystals. At present, no single discontinuity of a sharpness comparable to that associated with each double transition (equal to 15 mK) has been observed. Double transitions have now been measured in specific heat by numerous groups and are believed to be an intrinsic property of UPt_3. Furthermore, such anomalies have also been seen in sound velocity, thermal expansion and other types of measurements. The high quality single crystal measured in this thesis displays the double transition. Discussion of this is delayed to chapter 6 when we talk about sample characteristics; the reader is referred to figure 6.4.

Adenwalla and co-workers mapped out sound velocity anomalies associated with the superconducting transition in the temperature and magnetic field plane [71]. They find qualitatively the same result for a field in the basal plane and along the c-axis. Their results for a magnetic field perpendicular to the hexagonal axis are displayed in figure 3.4. The two transitions, well separated in zero field, eventually merge at $T^* = 0.39$ K and $H^* = 0.40$ T at a tetracritical point. A third line is also observed and

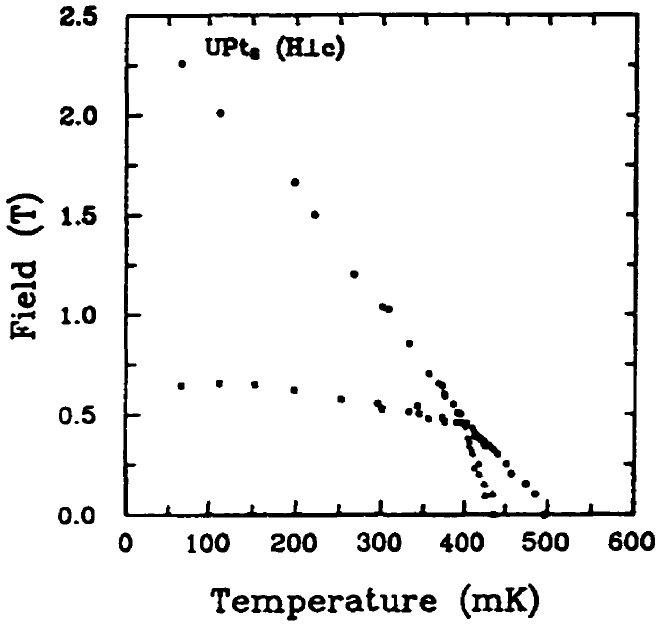

Figure 3.4: H-T phase diagram of UPt_3 for a field in the hexagonal basal plane (after [71]).

is nearly horizontal in the H-T plane. The upper critical field $H_{c2}(0)$ then displays a kink at (T^*, H^*). The phase diagram is therefore divided in three superconducting phases labeled A (high temperature, low field), B (low temperature, low field) and C (low temperature, high field). Furthermore, this phase diagram was shown to be isotropic in the basal plane [72].

From early on, it was known that uniaxial stress and hydrostatic pressure, of moderate strengths, had a profound effect on the superconducting transition (see Greiter [73] and Taillefer [72]). The phase diagram in the pressure-temperature plane was first mapped out by Trappmann *et al.* [74] and their results are displayed on the bottom panel of figure 3.6. The double superconducting transition is found to *merge*, not cross, at a critical pressure of $p^* = 3.7$ kbar and $T^* = 419$ mK. Such a tricritical point is forbidden by thermodynamic analysis (see [75]) and an additional line, close to vertical, was believed to exist from p^* down to lower pressures. A similar phase diagram was obtained later on by the specific heat measurements of Jin *et al.* [76] under uniaxial stress applied parallel to the c-axis. A complete temperature-field-stress phase diagram was recently proposed by Boukhny *et al.* [77] on the basis of their sound velocity measurements. Their measurements confirm the merging of the

double transition in the stress-temperature plane and furthermore, the authors claim, by fitting the surfaces of the field-temperature phase diagrams obtained at constant stress, an additional line in the stress-temperature plane can be inferred.

A thorough understanding of the various phase transitions under field and pressure has been one of the major pursuits in the field for the past seven years. We therefore skip directly to theoretical models for the multiple superconducting phases in UPt_3. We will come back later to the physical properties of the superconducting state.

3.2.2 *Theoretical models for the multiple superconducting phases*

Two basic models have been proposed to explain the multiple superconducting phases in UPt_3: (i) theories based on nearly degenerate order parameters belonging to *two* different irreducible representations or (ii) theories based on different order parameters belonging to a *single* two-dimensional representation. In the second model, the degeneracy of the order parameter for the different possible states within the 2D representation is lifted as a result of a coupling to a weak symmetry breaking field (such as the antiferromagnetic order in the basal plane) giving rise to two superconducting phases with very close transition temperatures. Of the four 2D representations listed in table 2.3, the E_{1g} and E_{2u} have received the most attention because the gap structure of the proposed state at low temperature (phase B) is compatible with various physical properties (see section 3.2.4) unlike the E_{2g} and E_{1u}. We start this section by discussing models with an accidental degeneracy. We then show, using Ginzburg-Landau theory how a symmetry-breaking field (SBF) could produce a split transition in zero field if the order parameter is two-dimensional (either E_{1g}, E_{2g}, E_{1u} or E_{2u}). We will then review several models which rely on a SBF.

1. *Models with accidental degeneracy*

As observed in ^{3}He for the B to A phase transition, Chen and Garg [78] have postulated that the phase diagram of UPt_3 is based on two primary order parameters belonging to different irreducible representations that are accidentally degenerate. Their goal was to search for two representations that can yield a crossing of the $H_{c2}(0)$ lines for all field directions. They chose to study a case where both order

parameter ψ_a and ψ_b have the same parity[1]. In this case, one of them must belong to an A representation (A_1 or A_2) while the other to a B representation (B_1 or B_2). Table 2.3 listed the node topology of these representations in the case $\hat{d} \parallel \hat{c}$. Chen and Garg do not assume any direction for the $\hat{d}$ vector and therefore obtain different positions for the nodes. Because of the presence of zeros in the gap implied by early transport measurements displaying power law behavior, the A_{1g} and A_{1u}[2] representations were not studied. This left the A_{2u} (axial) and the A_{2g} (2 lines and point nodes in the basal plane). The authors justify their approach by noting that the results of Hayden *et al.* [79], which seem to disfavor accidental degeneracy, pose severe thermodynamic problems: the Néel line $T_N(p)$ ends in midplane (see figure 3.6) which is impermissible, as is the junction in the T-p phase diagram of three second-order lines with non-zero specific heat jumps. Boukhny *et al.*[77], using ultrasound velocity measurements, claim to see an extra line in the T-p plane not observed in the specific heat measurements of Trappmann *et al.*[74] which would solve the thermodynamic imbroglio with respect to the stability of the tetracritical point in the T-p plane of the phase diagram. As we shall see in section 6.3, the high temperature, low field phase A cannot have an axial gap ruling out the A_{2u} representation at least for this particular choice of $\hat{d}$ vector. This leaves only the A_{2g} representation for phase A and the B_{1g} or B_{2g} representations for the low temperature low field phase, phase B. Both B-representations have a line node in the basal plane and therefore are consistent with early transport measurements. Since there is no symmetry breaking term in the GL expansion, the free energy is invariant under all rotations about the c-axis. Theories which rely on a SBF will not be invariant under rotation and therefore rotation of the moments within the plane will have to be invoked to explain the isotropy of the phase diagram. The AB theory of Chen and Garg can explain all global features of the phase diagram in going from the slope of $H_{c2}(0)$ to the specific heat jumps at the two transition temperatures and is believed by the authors to provide a strong candidate for explaining the phase diagram. On the other hand, the accidental degeneracy of

[1] It is also possible that ψ_a and ψ_b have different parity, in which case they can have any rotational symmetry. These authors do not study this possibility.

[2] When $\hat{d}$ is arbitrary, the basis function for this representation is a combination of $\hat{x}k_x + \hat{y}k_y$ and $\hat{z}k_z$ [33] and therefore has no nodes.

two transitions unrelated by symmetry, with $\Delta T_c/T_c \sim 10\%$, seems implausible to other authors [31] given the sensitivity of T_c to the strength of the pairing interaction and the disappearance of the magnetic moment at a similar pressure as the splitting in the superconducting transition would have to be regarded as coincidental.

2. *The Ginzburg-Landau approach to a split superconducting transition* [1]

The Ginzburg-Landau (GL) phenomenological theory is well known in the field of phase transitions. The central quantity is a pseudowavefunction $\psi(\vec{r})$, a complex order parameter. As was shown by Gor'kov, the GL theory is a special case of the BCS microscopic theory. The function $\psi(\vec{r})$ can be shown to be proportional to the gap parameter $\Delta(\vec{r})$ both being in general complex quantities. We now proceed to illustrate a special case of GL theory, where we neglect spatial variation in $\psi(\vec{r})$ and where there is no magnetic field. This special case is often labelled Landau theory. This short presentation will be followed by a sketch of GL theory in which a vector order parameter couples to some symmetry breaking field. The features deduced from this discussion will act as a starting point in describing models that rely on a SBF to explain the phase diagram.

We start with the free energy f_s in the superconducting state:

$$f_s = f_n + \alpha |\psi|^2 + \frac{\beta}{2} |\psi|^4 \tag{3.3}$$

where f_n is the free energy in the normal state and $\beta > 0$. We look for a minimum in the free energy:

$$\frac{\partial(\Delta f)}{\partial |\psi|} = \frac{\partial(f_s - f_n)}{\partial |\psi|} = \left(2\alpha + 2\beta |\psi|^2\right) |\psi| = 0 \tag{3.4}$$

For $\alpha > 0$, the minimum occurs for $|\psi| = 0$ which corresponds to the normal state. When $\alpha < 0$, the minimum occurs for $|\psi| = \left(-\frac{\alpha}{\beta}\right)^{1/2}$. Therefore, we can expand α close to T_c: $\alpha = \alpha_0(T - T_c)$ with $\alpha_0 > 0$. By adding gradient terms, one can also

[1] For the remainder of this chapter, the superconducting transition temperatures will be labelled T_{c+} and T_{c-} for the upper and lower transition respectively. We choose this notation for consistency reason (*i.e.* T_{c-} will be the temperature where α_- changes sign, see below) with theoretical papers in order to avoid confusion. In subsequent chapters, we will revert to the previous notation of above with T_{c_-} and T_{c_-} for the upper and lower transition temperatures.

deduce, among other quantities, the critical field, the jump in the specific heat, the coherence length and the London penetration depth.

In the case of a vector order parameter belonging to the 2D representations (*i.e.* E_{1g}, E_{2g}, E_{1u} and E_{2u}) listed in table 2.3, the free energy can be written as:

$$\Delta f = \alpha(T)\left|\vec{\psi}\right|^2 + \beta_1\left|\vec{\psi}\cdot\vec{\psi}^*\right| + \beta_2\left|\vec{\psi}\cdot\vec{\psi}\right| \tag{3.5}$$

with $\alpha(T) = \alpha_0(T - T_{c0})$. At T_{c0}, α changes sign and a minimum in the free energy can be found (provided $\beta_2 > 0$) which means that we enter the superconducting state. Four different types of order parameters can be found to minimize the free energy: two one-component ones *i.e.* the (1,0) and (0,1) types, and two two-components ones *i.e.* the real (1,1) type and the complex (1,i) type. By back substituting all four solution types in equation 3.5, we can obtain the free energy minimum for each. From this, we find that the states (1,0), (0,1) and (1,1) are degenerate with the free energy in the ordered state given by: $\Delta f_{\text{deg}} = -\frac{\alpha^2}{4(\beta_1+\beta_2)}$. The (1,i) is stabilized with a different free energy given by: $\Delta f_{(1,i)} = -\frac{\alpha^2}{4\beta_1}$. The condition $\left|\vec{\psi}\right|^2 > 0$ and $\Delta f < 0$ gives the stability of the phases as a function of temperature and also as a function of the ratio β_1/β_2.

A symmetry breaking field will couple differently to each component of the order parameter. For example, we take[1]:

$$(\Delta f)_{SBF} = \varepsilon\left|\psi_x\right|^2 - \varepsilon\left|\psi_y\right|^2 \tag{3.6}$$

with $\varepsilon > 0$. By posing $\left|\vec{\psi}\right| = (\psi_x, \psi_y) = \left(|\psi_x|, |\psi_y|\, e^{i\phi}\right)$ and including the SBF term, we can then rewrite equation 3.5:

$$\begin{aligned}\Delta f' &= \Delta f + \Delta f_{SBF} \\ &= \alpha\left|\psi_x\right|^2 + \alpha\left|\psi_y\right|^2 + (\beta_1+\beta_2)\left(\left|\psi_x\right|^4 + \left|\psi_y\right|^4\right) \\ &\quad +2(\beta_1 + \beta_2\cos 2\phi)\left|\psi_x\right|^2\left|\psi_y\right|^2 + \varepsilon\left|\psi_x\right|^2 - \varepsilon\left|\psi_y\right|^2\end{aligned} \tag{3.7}$$

By making use of the following definitions:

$$(\alpha + \varepsilon) = \alpha_0\left(T - T_{c0} + \frac{\varepsilon}{\alpha_0}\right) = \alpha_0(T - T_{c-}) \equiv \alpha_- \tag{3.8}$$

[1] Machida and Ozaki [80] use a group theoretical argument to study the subgroup of the magnetic order to justify such a coupling term.

$$(\alpha - \varepsilon) = \alpha_0 \left(T - T_{c0} - \frac{\varepsilon}{\alpha_0} \right) = \alpha_0 \left(T - T_{c+} \right) \equiv \alpha_+ \tag{3.9}$$

where T_{c0} is the superconducting temperature in the absence of a SBF, we can rewrite the free energy:

$$\begin{aligned} \Delta f' = {} & \alpha_- |\psi_x|^2 + \alpha_+ |\psi_y|^2 \\ & + (\beta_1 + \beta_2) \left(|\psi_x|^4 + |\psi_y|^4 \right) + 2(\beta_1 + \beta_2 \cos 2\phi) |\psi_x|^2 |\psi_y|^2 \end{aligned} \tag{3.10}$$

Again, there will be four cases. The minimum in free energy for each case is summarized in equations 3.11–3.14:

$$\Delta f'_{(0,1)} = -\frac{\alpha_+^2}{2(\beta_1 + \beta_2)} \tag{3.11}$$

$$\Delta f'_{(1,0)} = -\frac{\alpha_-^2}{2(\beta_1 + \beta_2)} \tag{3.12}$$

$$\Delta f'_{(1,1)} = -\frac{\alpha^2}{4(\beta_1 + \beta_2)} \tag{3.13}$$

$$\Delta f'_{(1,i)} = -\frac{\alpha^2}{4\beta_1} \tag{3.14}$$

where the prime refers to the free energy in the presence of a SBF. The highest superconducting transition being T_{c+}, a superconducting transition to the state (0,1) will occur at this temperature. At T_{c-}, α_- changes sign and a new minimum can be attained for a finite value of $|\psi_x|$ below this temperature. But the free energy $\Delta f'_{(0,1)}$ is always smaller than $\Delta f'_{(1,0)}$ such that the state (1,0) will never be stabilized. We rewrite equation 3.10:

$$\Delta f' = \alpha_+ |\psi_y|^2 + \left[\alpha_- + 2 (\beta_1 + \beta_2 \cos 2\phi) |\psi_y|^2 \right] |\psi_x|^2 + O\left(|\psi_x|^4 \right) \tag{3.15}$$

The second transition will occur when the coefficient of $|\psi_x|^2$ changes sign. If we back substitute the value of $|\psi_y|$ obtained by minimizing the free energy 3.10 for the (0,1) state into the coefficient of $|\psi_x|^2$ of equation 3.15, the value for the second superconducting transition, labelled T_{c*}, can be obtained. The (1,1) phase is found to be unstable and therefore the second transition is from the state (0,1) into state (1,i) with critical temperature given by:

$$T_{c*} = T_{c0} - \frac{\beta_1}{\beta_2} \left(\frac{\varepsilon}{\alpha_0} \right) \tag{3.16}$$

This approach clearly demonstrates the possibility of a split superconducting transition in zero field when a symmetry breaking field is coupled to a vectorial order parameter. Up to now, this approach is general to any of the 2D representations. Differences will arise when the gradient terms and the effect of a magnetic field are added to this formalism in order to explain the H-T phase diagram. It is beyond the scope of this thesis to go into details and to outline this treatment. Instead, we will overview the different approaches for calculating the phase diagram for the case of UPt_3, the problems associated with each method and their relevance to thermal conductivity calculations. Before going into the models, let us point out a difficulty that was noted early on.

Within the coupling scenarios, the kink in the $H_{c2}(0)$ curve is basically the result of a sudden reorientation of the vector order parameter $\vec{\psi}$ in the basal plane [81, 80, 82]. Both the moment $\vec{M}_s$ and the field $\vec{H}$ will couple to $\vec{\psi}$, each trying to align it in the minimum energy direction. Without loss of generality, let us consider the case of $\vec{M}_s \perp \vec{H}$ with both couplings to $\vec{\psi}$ favoring *parallel* alignment. At low fields, the coupling to the magnetic order dominates and $\vec{M}_s$ determines the orientation of $\vec{\psi}$. Then, when the field is increased to the point where its coupling dominates, a reorientation of $\vec{\psi}$ occurs, causing a kink in $H_{c2}(T)$. Of course if the field direction is instead made parallel to $\vec{M}_s$, no kink is predicted, since there is no competition between the two couplings. As a result, within a single antiferromagnetic domain, the upper critical field in the basal plaine of UPt_3 is predicted to show a sharp kink only for one direction of the field (say $\hat{H} \parallel \hat{a}$), and no kink for the $\hat{a}^*$ direction 90° away. As mentioned above, a kink is observed for any high-symmetry direction (0°, 90°, and 120° relative to $\hat{a}$) [72]. The phase diagram for a field along the hexagonal c-axis is also expected to not display a kink as again there is no competion. Within the models of accidental degeneracy, this explanation comes naturally. However, theorists working on models with a symmetry breaking field will have to find a way to solve this problem.

Machida and Ozaki [80] summarized the conditions for a split transition to occur: there must exist (i) degenerate states in the ground state which would come from either the spatial part of a vector order parameter of the wavefunction in the case of

strong spin-orbit coupling or from the spin part of a one dimensional spatial wavefunction in the case of weak spin-orbit, and (ii) external or internal perturbations which are strong enough to lower the symmetry, but weak enough so that they don't completely wipe out the lower transition. We now briefly outline the two types of scenarios based on either weak or strong spin-orbit coupling.

3. *Models that rely on a SBF*

To circumvent the difficulties associated with a qualitatively isotropic phase diagram in the basal plane and along the c-axis, Machida and Ozaki [83] consider an odd parity one dimensional pairing state in the weak spin-orbit case. This assumption rests on the argument of Miyake [84] which states that the effective spin-orbit coupling for the Cooper pair may be weak, although individual quasi-particles near the Fermi level are subject to strong spin-orbit coupling. Machida and Ozaki consider the case where the spin-space degeneracy is lifted via a symmetry breaking field associated with the antiferromagnetic moment in the basal plane. Furthermore, Machida and Ozaki point that the absence of change in the Knight shift below T_{c+} observed by both NMR [85] and μSr [86] indicate that the parity of the pairing function is odd. Machida and Ozaki [83] are able to obtain topologically identical phase diagrams for both $\vec{H} \parallel \hat{y}$ (*i.e.* $\vec{H} \perp \vec{M}$) and $\vec{H} \parallel \hat{z}$. To explain the isotropic phase diagram in the basal plane, they require that the moment rotates so as to keep $\vec{M} \perp \vec{H}$. Furthermore, the A_{2u} basis function chosen seems to have the right nodal symmetry (a hybrid II gap structure) as inferred by various experiments. Machida *et al.* [87] have extended their treatment to calculate the specific heat. They claim that the large linear term can be reconciled naturally within their 1D formalism.

Sauls [31, 88, 89] and Park and Joynt [90, 91] recently completed detailed calculations of the phase diagram of UPt_3 within a two-dimensional scenario with symmetry breaking field. It is beyond the scope of this thesis to rederive their results and we simply outline them here.

Sauls uses a odd-parity spin-triplet order parameter with $\hat{d} \parallel \hat{c}$ belonging to the E_{2u} class with the magnetic moment in the basal plane playing the role of the SBF. We summarize some of his conclusions:

- A double transition occurs in zero field and the splitting of the transition temperature is $\Delta T_c \propto M^2$ with M the magnitude of the magnetic moment. Furthermore, the correlation between magnetism and superconductivity can be accounted within this model.

- Within this scenario, it is possible to explain the anisotropy in the upper critical field over the full temperature range.

- The upper critical field exhibits a tetracritical point for $\vec{H} \perp \hat{c}$ and $\vec{H} \parallel \hat{c}$. The kink H_{c2} is isotropic in the basal plane provided $\vec{M}$ rotates so as to maintain $\vec{M} \perp \vec{H}$.

As to Park and Joynt [90, 91], they arrive at similar conclusions but by using an even parity spin-singlet order parameter belonging to the E_{1g} representation. They find that a true tetracritical point occurs only for a field in the basal plane and that the model predicts a near coincidence of the inner and outer transition lines when the field is along the c-axis. They are also able to explain the anisotropy of the upper critical field curve, a feature previously believed to be evidence for a spin-triplet state. Furthermore, these authors are able to explain the features of the phase diagram under pressure and field, a problem not yet studied with the E_{2u} model.

Our thermal conductivity measurements will be sensitive, at low temperature, to the node topology. We therefore emphasize the difference in nodal structure for the three scenarios listed above. The E_{2u} and A_{2u} both have a hybrid II structure, namely quadratic point nodes along the c-axis and a line in the basal plane while the E_{1g} gap has also a line in the basal plane but a linear node along the poles. We will come back in more details to calculations of thermal conductivity within these scenarios and compare them to our results in chapter 6. Up to now, no experimental probe has been able to distinguish between a hybrid I or II gap structure.

3.2.3 Interplay of magnetism and superconductivity

The first evidence of interplay between the magnetic order and the superconductivity came from the early neutron diffraction results of Aeppli *et al.* [68, 92]. In a first

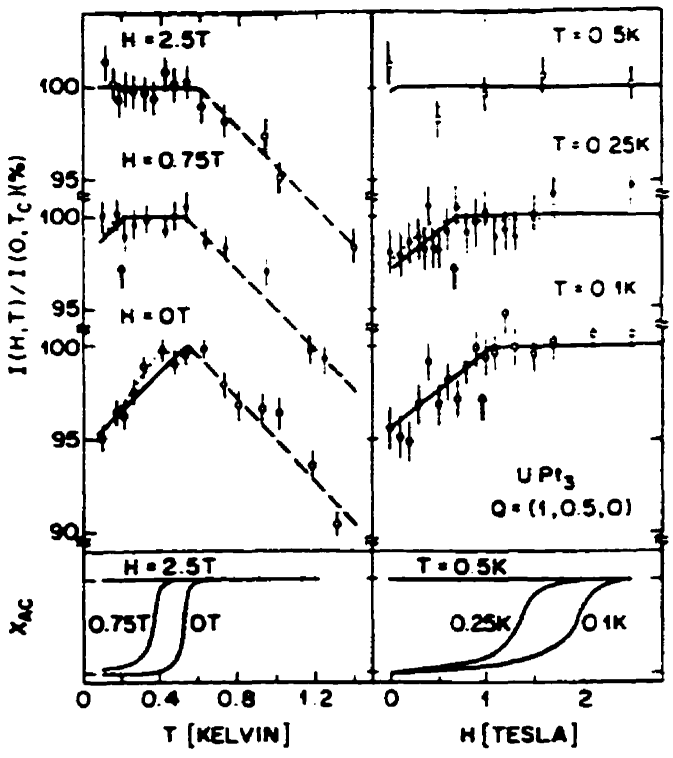

Figure 3.5: Normalized temperature-dependent (left) and field-dependent (right) $(1, \frac{1}{2}, 0)$ magnetic Bragg intensities (upper frames) and ac susceptibilities (lower frames) (after [92]).

paper, the authors showed that the magnetic Bragg[1] intensity in zero magnetic field at $Q = (\frac{1}{2}, 1, 1)$ rose linearly for $T_c < T < T_N$ and saturated below T_c. We now refer to the left hand-side of figure 3.5 where the magnetic Bragg intensity is plotted as a function of temperature for various fields directed perpendicular to the basal plane. The most important result is that at the lowest fields, the $(1, \frac{1}{2}, 0)$ peak is actually reduced by ~5% while for larger fields, the Bragg intensity is independent of temperature and field for $T < T_c$. From these results, the authors conclude that the antiferromagnetism and the superconductivity coexist and *interact* at the microscopic level.

Later on, the neutron results under hydrostatic pressure of Hayden *et al.* [79] combined with the specific heat of Trappmann *et al.* [74] clearly demonstrated the direct coupling between magnetism and superconductivity. Hayden *et al.* [79] used elastic

[1]The wave-vectors are expressed in reciprocal lattice units where $a^* = b^* = 4\pi/a\sqrt{3} = 1.261$ Å^{-1} and $c^* = 2\pi/c = 1.285$ Å^{-1}.

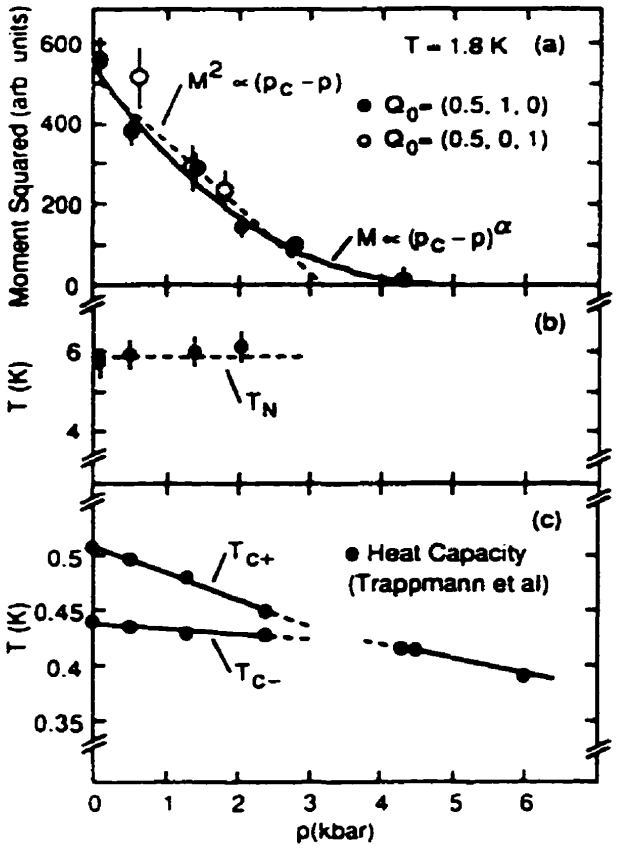

Figure 3.6: (a) Variation of the integrated intensity of the magnetic peaks $(\frac{1}{2}, 1, 0)$ (closed circles) and $(\frac{1}{2}, 0, 1)$ (open circles) with hydrostatic pressure. This is a measure of M^2. The solid line is a fit of $M \propto (p_c - p)^\alpha$ and the dashed line $M^2 \propto (p_c - p)$. (b) Variation of the Néel temperature as a function of pressure. (c) Low temperature specific heat anomalies in UPt_3 as measured by Trappmann *et al.* [74]. This figure is taken from the paper by Hayden *et al.* [79].

neutron diffraction to study the effect of hydrostatic pressure on the small ordered antiferromagnetic moment in UPt_3. They found that pressure suppresses and eventually destroys the magnetic order. A comparison of their results along with those of Trappmann *et al.* [74] is displayed in figure 3.6. Hayden *et al.* conclude that the splitting of the superconducting transition is well correlated with the magnitude of the ordered moment. The critical pressure at which the ordered moment is destroyed, $p_c = 5.4 \pm 2.9$ kbar, is found indistinguishable from that at which the two anomalies in the heat capacity cease to be resolvable. They therefore conclude that the antiferromagnetic order appears to be responsible for the double superconducting transition in UPt_3.

By combining the use of neutron scattering and magnetic X-ray scattering, Isaacs

et al. [93] repeated the experiment of Aeppli *et al.* [68, 92] and were able to draw additional conclusions. From their data, they conclude that the decrease in the intensity ($\propto M^2$) upon entering the superconducting state is not due to a rotation of the moments but is consistent with a uniform reduction of the squared staggered magnetization thus confirming the coupling between the superconductivity and the magnetism.

All these results have various implications on the phase diagram of UPt_3. Furthermore, our neutron results, presented in chapter 8, will add to the unusual properties of the magnetic moments.

3.2.4 *Physical properties of the superconducting state*

In this section, we are concerned with the superconducting properties of UPt_3. Only few experimental results will be discussed focussing mainly on results that probe the gap anisotropy. More thorough reviews can be found in the papers by Grewe and Steglich [56], by Taillefer [57], by Löhneysen [58] and by Heffner and Norman [59]. The thermal conductivity results prior to our own will be reviewed in chapter 6.

1. *Power law dependence in the superconducting state*

The specific heat has been measured by numerous groups (see the review by Brison *et al.* [94] and by Grewe and Steglich [56]) and we outline only the gross features. The specific heat over temperature is linear (not exponential as for BCS superconductors) in the range $0.2T_c$ up to close to T_c. From this dependence, one can infer a linear term ranging from 0 to 60% of the normal state value at T_c. This residual term has been attributed to residual normal fluid at T = 0 but the strong sample dependence would rather seem to favor an explanation relating this term to an extrinsic property of UPt_3. Below $0.2T_c$, deviations from linearity start to appear, and a huge upturn in c/T is observed (see for example [94]). In some samples, at the lowest temperature reached, the value of c/T is up to three times the value at T_c. This upturn has been investigated in samples of different quality and does not seem to be linked to the superconductivity as there are reports indicating it is still present in the normal state [95, 96].

Power law behavior has also been seen in NMR measurements [85, 97]. These

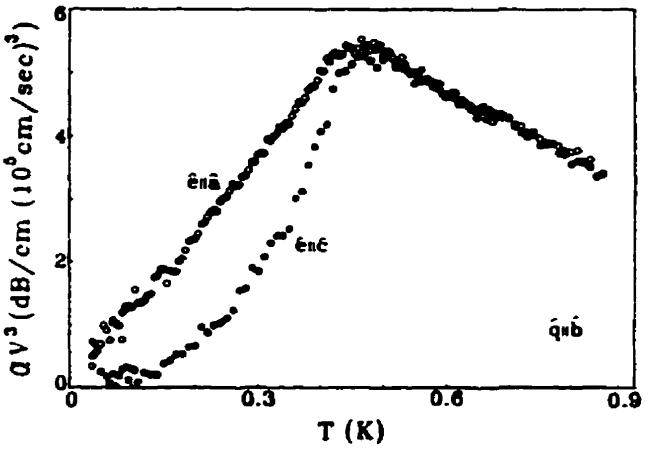

Figure 3.7: αv^3 (proportional to viscosity) versus temperature for transverse sound propagation in the basal plane ($\hat{q} \parallel \hat{b}$) with polarization $\hat{e} \parallel \hat{a}$ (open circles) and $\hat{e} \parallel \hat{c}$ (closed circles) (after [38]).

authors find a T^3 power law which points to a line node in the basal plane. Other power laws have been seen in ultrasound attenuation measurements and we proceed below to discussing one experiment by Shivaram *et al.* [38].

2. *Evidence of gap anisotropy in UPt_3*

The anisotropy in the transverse ultrasound attenuation measurements of Shivaram *et al.* [38] provided the first evidence of gap anisotropy, beyond that of the normal state. Their results, displayed in figure 3.7, showed an increasing attenuation as $T^{1.1}$ for a transverse sound polarization perpendicular to the c-axis, while sound polarized along c had a $T^{2.1}$ temperature dependence. These provided evidence for a line of zeros in the hexagonal basal plane.

The London penetration depth of Broholm *et al.* [98] was the first measurement pointing to a hybrid type of gap structure. Although their interpretation was questioned by Luke *et al.* [99], we proceed to describe their findings. At T = 0, Broholm *et al.* find slight anisotropy in the values of the penetration depths parallel and perpendicular to the c-axis, namely: $\lambda_{\parallel}$=7070±30 Å and $\lambda_{\perp}$=7820±30 Å. A different temperature dependence, *i.e.* $\lambda_{\perp}^{-2}$ decreases proportionally with temperature while λ^{-2} decreases with a higher power. Modeling of their data enables these authors to conclude to a weak-coupling superconductor, with $\Delta(0) = 940 \pm 15$ mK, with a line of nodes in the basal plane and point nodes along the c-axis.

Point-contact spectroscopy measurements by Goll *et al.* [100] and De Wilde *et al.* [101] provide a more firm basis for a hybrid type gap structure. The difference in the two measurements resides in the fact that Goll *et al.* probed the anisotropy while De Wilde *et al.* measured contacts only for currents along the c-axis. In summary, Goll and coworkers find (i) a gap-related spectra for a current flow parallel to the c-axis and only weak features (if any at all) for currents in the basal plane, and (ii) that the gap features are only observed in the low-temperature, low-field superconducting phase. This would hint at a different order parameter between the A and B phase. The authors therefore conclude that the gap must vanish on a line in the basal plane. In their measurements, De Wilde *et al.* claim that they can qualitatively model their spectra with a gap vanishing along the c-axis. Their fits would seem to indicate a hybrid II gap structure either from a E_{2u} gap as used in the theory of Sauls [31] or a A_{2u} as postulated by Machida and Ozaki [83]. More detailed calculations, including Fermi surface anisotropy, are needed to arrive at a firm conclusion.

4

THE HIGH-T_c CUPRATE $YBa_2Cu_3O_{7-\delta}$

In this chapter, the normal and superconducting state properties of $YBa_2Cu_3O_{7-\delta}$ are reviewed. To our knowledge, since the field of high-T_c evolves so fast, there is no comprehensive review of the properties of this class of superconductors. For more information, the reader is therefore referred to the original papers that discuss the properties that we quote. The books by Burns [30] and Cyrot and Pavuna [102] also provide an introduction to the properties of high-T_c up to 1991.

4.1 Normal state properties

In this section, we review some of the normal state properties of $YBa_2Cu_3O_{7-\delta}$. As was the case with UPt_3, we focus on quantities that will be useful later on in the thesis. The number of papers on high-T_c being astronomical, this review is by no means complete.

4.1.1 Crystal structure

1. *General crystallographic considerations*

As was realized early in the history of the cuprates, the existence and stacking of copper-oxygen planes is critical, since it is believed that it is those planes that are responsible for the superconductivity in these systems. In looking at all of the families of high-T_c superconductors, one can notice some general trends: (i) many compounds have more than one immediately adjacent Cu-O planes, each plane separated by a sparsely populated plane of Y or Ca atoms, and (ii) groups of immediately adjacent planes are separated from the next group by metal-oxygen isolation planes (also called charge reservoirs), where the metal atoms usually are La, Ba, Tl or Bi. This gives

this class of materials a strong quasi-two-dimensional character as evidenced by many strongly anisotropic properties.

Consider the structure of $YBa_2Cu_3O_7$ shown in figure 4.1. This compound has two adjacent (3.2 Å) Cu-O planes separated by a plane of Y atoms. This pair of Cu-O planes is ~8.2 Å from the neighboring set of planes. The presence of the chains, running along the b-axis, was at first believed to be responsible for the high critical temperature but later on, compounds with no chains were discovered that had a higher T_c. As we shall discuss in the next paragraph, when reducing the oxygen content, it is the oxygen in the chains that is removed (atom labeled O_c(b) in figure 4.1) leaving "sticks" of O-Cu-O parallel to the c-axis. The complete deoxygenation results in a tetragonal structure for the compound $YBa_2Cu_3O_6$ with similar unit cell dimensions as $YBa_2Cu_3O_7$. For $\delta \approx 0.1$[1], the lattice parameters are a = 3.84 Å, b = 3.88 Å and c = 11.63 Å for a unit cell volume of ~173 Å^3.

In this thesis, we will be only concerned with measurements along the a-axis of $YBa_2Cu_3O_{7-\delta}$ *i.e.* perpendicular to the chains and therefore they will not contribute to the thermal conductivity.

2. *Twinning*

In air and above ~800°C YBCO is tetragonal. Upon cooling, oxygen enters in the chains and makes the crystal orthorhombic creating an asymmetry between the a and b-axis. The sample becomes twinned with small domains with the b-axis along some axis $\hat{x}$ while other domains grow with the a-axis also along $\hat{x}$.

Flux grown crystals can be mechanically detwinned by applying a uniaxial stress and heating the sample at 500°C. This will favor the shorter a-axis domains to be parallel to the applied stress and therefore one obtains a *true* single crystal. The typical width of a twin domain is 1 μm which can be revealed by chemical etching, polarized optical microscopy or by scanning electron microscopy.

3. *Oxygen doping*

The physical properties of $YBa_2Cu_3O_{7-\delta}$ are strongly dependent on the oxygen content of the sample. For example, $YBa_2Cu_3O_6$ is an insulating antiferromagnet.

[1]This is the approximate oxygen content in the crystal to be discussed in this thesis.

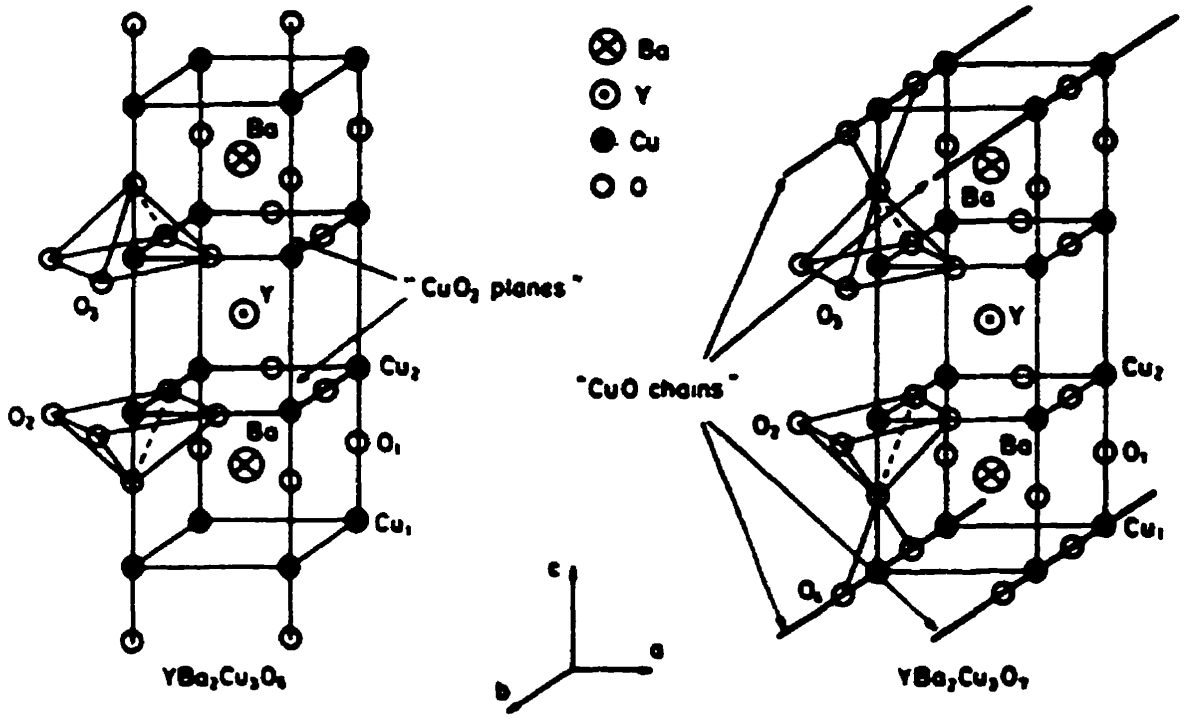

Figure 4.1: Representation of the crystal structure of $YBa_2Cu_3O_{7-\delta}$. (a) emphasizes the labeling of the atom positions and (b) shows the copper coordination polyhedra. Notice the two adjacent copper-oxygen planes separated by a Y atom and the chains running along the b-axis below (above) the lowest (highest) Ba atom (after [30]).

The ordering is with antiparallel spins in the planar Cu atoms. Increasing the oxygen content in the chains rapidly suppresses the Néel transition until it vanishes around δ=0.64[1]. Increasing the oxygen content further from δ=0.64 down to zero makes the crystal metallic, nonmagnetic and superconducting. The left panel of figure 4.2 shows a schematic phase diagram for $YBa_2Cu_3O_{7-\delta}$ as a function of the number of holes in the CuO_2 plane (this is proportional to 1-δ), while the right panel shows the superconducting transition dependence upon doping. The maximum T_c is reached for $\delta \approx 0.1$. The oxygen content is controlled by annealing crystals for several days in flowing oxygen, with the annealing temperature dictating the amount of oxygen entering the crystal. The sample is then quenched to room temperature.

The proximity to antiferromagnetic ordering in $YBa_2Cu_3O_{7-\delta}$ has been taken as evidence for spin fluctuations being responsible for the superconducting pairing. How-

[1] At this oxygen content, the crystal symmetry changes from being tetragonal for δ >0.64 to orthorhombic for smaller δ's.

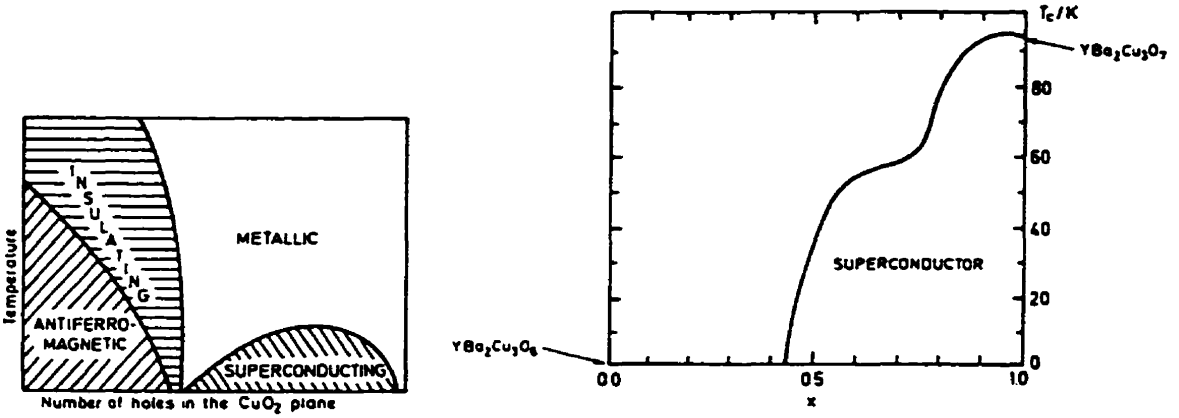

Figure 4.2: Left panel: schematic phase diagram as a function of oxygen doping (or holes in the CuO_2 plane) for $YBa_2Cu_3O_{7-\delta}$. Right panel: variation of the superconducting transition temperature as a function of doping, $x = 1 - \delta$ for $YBa_2Cu_3O_{7-\delta}$ (after [102]).

ever. contrary to UPt_3, there is no coexistence of magnetism and superconductivity. Upon replacing Y by Gd, one can induce an antiferromagnetic transition at 2.2 K but the electrons responsible for this ordering do not participate in the superconductivity (*i.e.* there is still magnetic ordering even when, upon reducing the oxygen content, the sample is insulating) and there is no coupling between the two types of order.

4.1.2 *Electrical resistivity and elastic properties*

We now proceed to discuss the sound velocity, the phonon specific heat and the resistivity. Discussion of previous thermal conductivity results on powders, twinned and untwinned crystals is left for chapter 7.

1. *Sound velocities*

As discussed earlier, the sound velocities are important in estimating the phonon contribution to the thermal conductivity at low temperature in the limit of boundary scattering. In the case of $YBa_2Cu_3O_{7-\delta}$, not many reliable measurements of the complete set of nine elastic constants exist. This is due mostly to the small dimensions of the crystals that can be grown resulting in significant uncertainties on the travelling time of ultrasonic waves. Measurements on ceramics are also not very reliable: these contain voids and intergranular material that influence the results. Nevertheless, in this section, we summarize the elastic properties of $YBa_2Cu_3O_{7-\delta}$ as reviewed by

Dominec [103].

We first start by summarizing results on powders corrected for the void-free state. In polycrystals, only two independent elastic moduli exist and can be represented by longitudinal and transverse velocities. The longitudinal velocities range from 4190 to 5165 m/s while the transverse go from 2350 to 3061 m/s [103]. The resulting Debye temperature is in the range of 329 to 480 K [103]. An average of these figures yield a longitudinal velocity of 4516 m/s and a transverse velocity of 2595 m/s. The average phonon velocity is then (see [5]): $v_{ph} = 2862$ m/s.

A more reliable way to extract the sound velocities is from measurements of the elastic constants as we showed in section 3.1.2. The advantage of this method is that we can average only those modes that participate in the heat transport, namely for transport along the a-axis. We simply average the longitudinal and transverse velocities in this direction. The previous estimate was for an overall phonon velocity average over all modes, c-axis and basal plane included. Calculations of velocities from elastic constants in an orthorhombic crystal are rather elaborate but since most of our results are for the a-axis, the whole procedure becomes very simple. Carrying out the procedure outlined in the books by Truell *et al.* and Dieulesaint and Royer [104, 105] and using the elastic constants (c_{ij}) listed in the review paper of Dominec [103], we find: $v_a^a = \sqrt{\frac{c_{11}}{\rho}}$ =5841 m/s, $v_a^b = \sqrt{\frac{c_{66}}{\rho}}$ =3734 m/s and $v_a^c = \sqrt{\frac{c_{55}}{\rho}}$ =2714 m/s where ρ=6381.62 kg/m^3 is the density, and v_q^ε the velocity of the mode with the propagation direction $\vec{q}$ and polarization ε. Averaging these velocities with the method of Berman [5], and taking only the faster of the two transverse modes, we find an average phonon velocity of v_{ph}=3977m/s. We would like to emphasize that an average of the elastic constants listed by Dominec [103] yield a Debye temperature of 371 K, approximately 10% lower than what can be deduced from the specific heat measurements.

In estimating the maximum phonon contribution to the thermal conductivity using $\kappa_{ph} = \frac{1}{3} c_{ph} v_{ph} \ell_{ph}$, we will be interested in the highest possible velocity. We choose to use the velocity calculated from the elastic constants. This procedure will provide a realistic estimate for the heat conduction of phonons at low temperature.

2. *Resistivity*

The electrical resistivity in $YBa_2Cu_3O_{7-\delta}$ was known early on to be linear, except

for some unexplained slight upward curvature. Gagnon *et al.* [106] performed a systematic study of the resistivity in several crystals in order to reveal any anisotropy that might arise from the presence of chains along the b-axis. They measured the electrical resistivity along the a and b-axes of YBCO on high-quality detwinned single crystals. Below 300 K and above the superconducting fluctuations regime, they find a linear $\rho_a(T)$ with negligible (or even negative) extrapolated residual resistivity. Viewing the b-axis conductivity as the sum of the conductivities in the CuO_2 planes and along the CuO chains, they were able to extract a T^2 dependence for the chains with a large residual resistivity of order 100 $\mu\Omega$cm. As a consequence of this large residual chain resistivity, isotropic electronic transport in the basal plane is predicted at low temperature.

In section 7.2, we will present resistivity measurements for a-axis zinc-doped $YBa_2Cu_3O_{7-\delta}$. We will show that the linear relationship of the resistivity is preserved upon doping but that the extrapolated residual resistivity increases.

4.2 Superconducting properties

There exists a wealth of experiments in the high-T_c, which range from vortex dynamics, tunneling junctions, photoemission and many others, and it is too vast for us to cover here. Instead, we limit ourselves in this first section to discussing thermal properties at high temperature (T>1 K), namely the thermal conductivity[1] and the Righi-Leduc effect along with specific heat data which seems to point at uncondensed electronic carriers at T=0.

4.2.1 Thermal properties

1. *Residual linear term in the specific heat*

There exist numerous specific heat measurements on $YBa_2Cu_3O_{7-\delta}$ performed by various groups. We choose to illustrate the findings of this technique through the review paper by Fisher *et al.* [107].

Many contributions to the specific heat of $YBa_2Cu_3O_{7-\delta}$ (in and out of a magnetic

[1] Low temperature (T<1 K) thermal conductivity will be reviewed in chapter 7.

field) have been observed. These can be separated into five categories: linear, magnetic, hyperfine, lattice and possibly an αT^2 term associated with line nodes. The first, C_{lin} can be written in the form:

$$C_{lin}(H) = [\gamma^*(0) + \Delta\gamma^*(H)]\,T \tag{4.1}$$

$\gamma^*(0)$ includes sample-dependent contributions from non-superconducting regions. It could also be intrinsic and associated with the CuO chains [107]. Recall that a big sample dependent residual term is also seen in UPt_3. A $H^{1/2}$ field dependence to the $\Delta\gamma^*(H)$ has been predicted by Volovik for a gap with line nodes and would be a manifestation of d-wave pairing.

In fitting experimental data, the second term C_{mag} is taken to be a Gaussian-broadened Schottky anomaly. Its origin comes from the moments associated with the Cu^{2+} ions which order under the influence of internal interactions.

The hyperfine contribution $C_{hyp}(H) = D(H)T^{-2}$ is modeled through a quadratic field dependence for the D(H) term. Finally, the lattice specific heat is represented by the harmonic lattice series: $C_{lat} = B_3T^3 + B_5T^5 + ...$ The term B_3 in Fisher *et al.*'s paper will be from now on called β for consistency with our discussion in UPt_3.

Qualitatively speaking, the specific heat over temperature has a large upturn at low temperature in zero field. As the field is increased, this anomaly eventually becomes a Schottky-type anomaly as discussed above. Although probably different in origin, this upturn is reminiscent of what happens in UPt_3 where the extraction of a residual linear term was obscured by a large sudden increase of ill-understood origin in C/T at the lowest temperatures. Due to the large number of fitting parameters, experimentalists proceed to fix certain parameters by global fits performed at different magnetic fields. Fisher *et al.* [107] provide an extensive discussion of the fitting procedure putting special emphasis on reducing systematic errors that could arise from such global fitting. Although not seen in early measurements, many authors now find the predicted $H^{1/2}$ field dependence in the linear term, adding to the evidence that $YBa_2Cu_3O_{7-\delta}$ is a d-wave superconductor (see for example [108, 107]).

From the point of view of thermal conductivity at low temperatures, we will be interested in the maximum phonon contribution to our results. At the lowest temperatures, the anharmonic term can be neglected, and the β term ranges from

0.3–0.4 mJ/molK^4 (see [108, 107] and references therein) which correspond to 2.88–3.84×10^{-3} mJ/K^{4}cm^3. We emphasize an advantage of thermal conductivity over specific heat: thermal conductivity measurements enable us to distinguish the *itinerant* quasiparticles from the large $\gamma^*(0)$ which has many postulated origins.

2. *High temperature thermal conductivity*

Soon after its discovery in 1987, many experimentalists set forth to measure the thermal conductivity in sintered $YBa_2Cu_3O_{7-\delta}$. The thermal conductivity could equally well probe the normal and superconducting state of this compound, something that could not be achieved with electrical conductivity (see for example the review by Uher [109]). Results on detwinned crystals only appeared five years later with the measurements of Yu *et al.* [110] and Cohn *et al.* [111]. The main feature of their results is that the thermal conductivity increases in the superconducting state, giving rise to a large peak centered around 40 K[1].

Cohn *et al.* [111] interpret the appearance of a peak below T_c using a conventional phonon dominated approach. They establish that the thermal conductivity in the normal state is dominated by phononic carriers, accounting for roughly 60–70% of the total conductivity. In going through T_c, the electrons form Cooper pairs which, as seen in chapter 2, are not effective at scattering phonons. This results in an increase in phonon mean-free path and a concomitant increase in thermal conductivity. This is what happens in disordered alloys as shown in figure 2.8. In going to lower temperature, the number of phonons decreases and as a consequence, a peak appears.

Yu *et al.* [110] obtain similar data except for a reverse anisotropy between κ_a and κ_b to that of Cohn *et al.* However, Yu and collaborators interpret their results in terms of a purely electronic scenario. First, they argue that phononic scenarios, such as described above, would predict an enhancement in the c-axis thermal conductivity as well, which is not observed experimentally. Secondly, the quasiparticle scattering rate has been assumed to be unaffected by the superconductivity, much like in the BRT theory. On the other hand, the microwave conductivity measurements of Bonn *et al.* [112] indicate a rapid suppression of the scattering rate below T_c and Yu *et al.*

[1] Note that this peak was also present in powders but much smaller in amplitude due to the disordered nature of the sample.

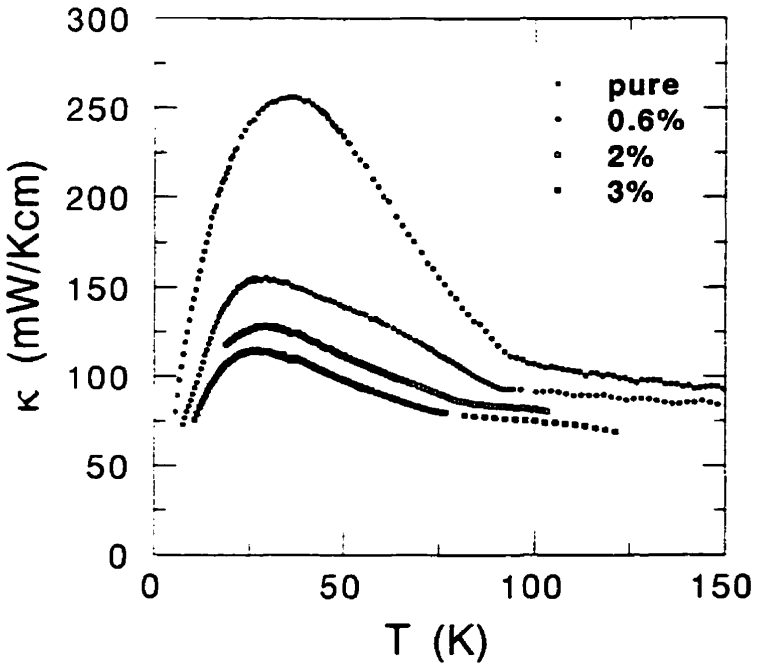

Figure 4.3: High temperature thermal conductivity (a-axis) as a function of temperature for $YBa_2(Cu_{1-x}Zn_x)_3O_{7-\delta}$ crystals with x=0, 0.6, 2 and 3% (after [113]). Notice the rapid drop in the peak height with small zinc doping and the shifting of the peak to lower temperatures (after [113])

base their electronic scenario on this observation. The reduced scattering leads to an increased electronic mean-free path resulting in an increase in thermal conductivity. At the same time, the number of quasiparticles decreases, as the electrons form pairs, and the two competing effects result in a peak. Measurements of the thermal Hall effect (discussed below) also attribute a large fraction of the peak to an electronic scenario.

Figure 4.3 displays the recent thermal conductivity measurements at high temperature of Pu *et al.* [113]. We emphasize that the measurements presented in chapter 7 were performed on the same crystals as that of Pu *et al.*. The motivation for their zinc doping studies was to discriminate an electron-type scenario from a phonon-type scenario. Upon introducing small concentrations of impurities, the phonons should not be affected and the peak below T_c should stay qualitatively the same. On the other hand, impurities will strongly limit the electronic mean-free path and the peak should be strongly suppressed. The results of Pu *et al.* lie in between the two ex-

tremal scenarios. In going from the pure sample to the 0.6%, the peak is reduced by a factor of 1.7, while additional impurity concentration seem to have a smaller impact on the overall magnitude of the conductivity. Hirschfeld and Putikka [50] provide an explanation in terms of a phonon peak centered around 15 K and a peaked electronic contribution strongly suppressed by the zinc impurities.

3. *Thermal Hall effect or the Righi-Leduc effect*

We now proceed to discuss the thermal Hall effect measurements of Krishana *et al.* [114].

When a quasiparticle in a type II superconductor is incident on a pinned vortex, the "handedness" of the superfluid velocity around the vortex core leads to an asymmetric scattering *i.e.* the amplitude for scattering to the right is different from that to the left. However in order to probe this asymmetry, it is desirable to avoid applying an electric field in order to keep vortex motion to a minimum. This complication can be circumvented by the use of a weak thermal gradient and sensing thermally the deflected quasiparticles. This detected transverse thermal current is equivalent to a thermal Hall effect (called the Righi-Leduc effect). Krishana *et al.* [114] used this effect, with a field perpendicular to the planes, to separate the asymmetric quasiparticle scattering from the symmetric phonon scattering on the vortices in order to extract the quasiparticle contribution to the longitudinal thermal conductivity. Furthermore, these authors show that the transverse thermal conductivity κ_{xy} also provides a measurement of the zero-field mean-free path of the in-plane quasiparticles.

Krishana *et al.* find that the Hall thermal conductivity in their twinned crystal is hole-like and anomalously large. In inverting the thermal resistivity tensor, the authors are able to calculate the electronic contribution to thermal conductivity in the plane. They find the familiar peak, observed in longitudinal thermal conductivity, centered around 40 K. This peak roughly amounts to one third of the total measured thermal conductivity. In fitting their κ_{xy} as a function of field for fixed temperatures, they are able to extract a quasiparticle mean-free path ℓ_0 which goes from ~90Å at T_c up to 2500 Å at 15 K. A value up to 6000 Å has now been obtained in high-quality detwinned crystals [115]. By comparing their results for ℓ_0 with the scattering rate deduced by Bonn *et al.* [116], Krishana *et al.* [114] deduce a Fermi velocity

$v_F = 2 \times 10^5$ m/s. The authors conclude that their measurements imply that a large fraction of the thermal conductivity peak below T_c arises from quasiparticle excitation.

5

EXPERIMENTAL ASPECTS

5.1 General introduction

All measurements for this thesis were done using a brand new Oxford Kelvinox 300 dilution refrigerator. It was delivered in October 92, a month after my arrival at McGill University. Such a cryostat can reach a temperature of 8 mK without heat load as demonstrated using a nuclear orientation thermometer. The cryostat is equiped with a 15 T superconducting magnet with a compensated region centered on the bottom plate of the mixing chamber. Furthermore, it came with minimal wiring, most of which was used for diagnostic sensors. A 24-pin connector was already wired down to 4 K while a 26-pin connector was added. Furthermore, in collaboration with B. Ellman, four coaxial cables for ultrasound measurements and two capillaries for stress experiments were also added. Proper heat sinking was provided at all of the cold stages of the refrigerator for all new wiring and tubing while careful choice of materials (for the wiring) and diameter (for the capillaries and wiring) was made in order to keep the heat load on the dilution refrigerator to a minimum. All these improvements were started after the commissioning of the refrigerator by an engineer from Oxford Instruments in January 1993 and completed later in the year. In parallel, a preliminary design of the thermal conductivity setup was built and tested at dilution temperatures leading to a first publication on UPt_3 in 1994 [117]. The final design of the thermal conductivity setup was completed in 1994 while minor improvements continued up until completion of the thesis (strain gauge heater in 1995, new thermometer mount in 1996; see section 5.3).

A major problem that was encountered came from the radio transmitting antennae on top of Mont-Royal in direct line of sight with our laboratory. The antennas

generate high frequency electromagnetic waves (~100 MHz) which couple to cold experimental devices via parasitic capacitance in the wires. Due to the low temperatures and the high resistance of the thermometers (~ 20 kΩ), this parasitic power can become significant and cause the thermometer to self-heat, leading to a bad reading of temperature. This problem is made worse by the nature of the measurement: the thermometers measuring the temperature gradient on the sample are *isolated* from the outside world and have no way to dissipate this extra heat except through the sample itself. In going to lower temperatures, other problems arise: (i) the resistance of the thermometer increases exponentially causing even more Joule heating; (ii) boundary resistances (or Kapitza resistance) can become dominant virtually isolating the thermometers even from the sample itself and preventing it from dissipating this extra heat and; (iii) the cooling power of the dilution refrigerator goes to zero at the base temperature making it harder to extract this extra heat.

Use of low pass capacitive-inductive filters on all electrical lines and the building of a Faraday cage were necessary. The cage consisted of a wooden frame with a double layer of fine copper mesh. This cage rested on an aluminum plate and was used to surround the measuring electronics. The filters were low-pass capacitive-inductive filters from Spectrum Control (part# 19F2456) with an attenuation of 20 dB (70 dB) at 3 MHz (1 GHz). Before these improvements, thermal conductivity measurements were reliable down only to approximately 150 mK. This range has now been extended to below 50 mK for the best conducting samples to which good thermal contacts can be made.

5.2 *Introduction to measurements below 1 K*

In view of the numerous publications on the principles of operation of the ^{3}He- ^{4}He dilution refrigerator (see for example [118, 119]), only a brief description will be given here. When a mixture of ^{4}He and ^{3}He is cooled below 0.87 K, a phase separation takes place. The concentrated phase of almost pure liquid ^{3}He floats on top of the dilute phase consisting of approximately 6% ^{3}He in superfluid ^{4}He. Due to its superfluid properties and zero nuclear spin the ^{4}He is 'inert' and the diluted ^{3}He behaves as an ideal gas. The ^{3}He is pumped out of the lower phase with a powerful roots blower.

Due to the osmotic pressure, the ^{3}He atoms from the concentrated phase migrate across the phase boundary from the concentrated phase to the dilute phase. This phenomenon is analogous to the evaporation of a liquid into a vapour phase and one obtains cooling. In order to operate continuously, the ^{3}He has to be re-injected into the mixing chamber. So as to prevent excessive heat inputs, the gas has to be liquefied by putting it in thermal contact with a bath of pumped ^{4}He and pre-cooled via heat exchangers before re-entering the mixing chamber.

Temperatures were measured by means of a calibrated germanium thermometer from Lakeshore. This GR-200A-30 is calibrated from 50 mK up to 5 K. For lower temperatures, a ruthenium oxide thick film resistor was used[1]. Temperature regulation was done using the TS-530 temperature controller from RV-electronikka used in conjunction with either an AVS-46 resistance bridge from the same company or preferably with a LR-700 resistance bridge from Linear Research. All regulating thermometers were well anchored on the bottom plate of the mixing chamber away from the heater in the field compensated area of the magnet. Electrical current for the magnet was supplied with the PS-120-10 power supply from Oxford Instruments.

5.3 Thermal conductivity: experimental details

The thermal conductivity was measured using a steady state method (see for example [5]). Heat was supplied at one end of a parallepiped shaped sample and removed at the other end. Two thermometers attached at two places along the length of the sample were used to measure the temperature gradient. The thermal conductivity κ is given by :

$$\kappa = \frac{HL}{A\Delta T} \tag{5.1}$$

where H is the rate at which the heat is supplied, L is the distance between the two thermometers, A is the cross-sectional area of the sample and $\Delta T \equiv T_{hot} - T_{cold}$ is the temperature gradient. In all our experiments, we kept $\Delta T/T \sim 5\%$.

This steady-state longitudinal heat-flow method can be used if one assumes that

[1] It was calibrated against the germanium thermometer down to 50 mK. The thermometer displayed a variable range hopping law which is known to hold down to 25 mK [120]. We have used this calibration only down to 40 mK.

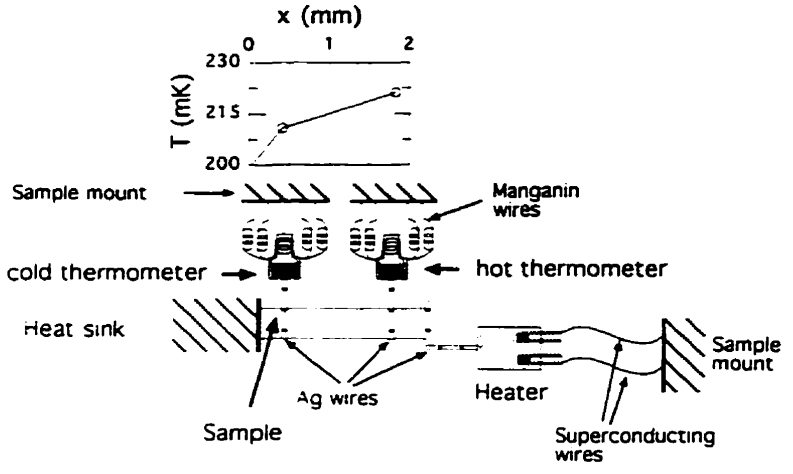

Figure 5.1: Schematic diagram of experimental apparatus for measuring thermal conductivity. Top: Actual temperatures measured on the mount for a regulating temperature of 199 mK and a heater power of 9.2 nW for a pure $YBa_2Cu_3O_{7-\delta}$ sample.

essentially all of the heat supplied at the hot end travels through the sample to the cold end. This assumption can fail due to bad thermal contacts resulting in losses through the measuring electrical leads or supports for the thermometers and heater, or in losses through radiation or conduction by residual gas molecules. Careful design of the experimental setup was achieved such that all heat losses could be safely neglected (see section 5.3.1). A schematic diagram of the thermal conductivity setup is shown in figure 5.1.

In our setup, two kinds of heaters were used. The first kind consisted of a resistive thin film deposited on a quartz transducer. We bought the transducer with one side coated with gold (including a buffer layer of chromium) and on the other side 200 Å of $Co_{80}Zr_{20}$ was deposited by Dr. R. Cochrane at Université de Montréal. This film gave a resistance of about 100 Ω per square and is non-magnetic and non-superconducting at least down to 50 mK [121]. Electrical contacts on the film were made with 25 μm niobium-titanium wire attached to the heater with silver epoxy from Epotech. Thermal contact to the sample was achieved by wire-bonding several (up to six) 50 μm gold wires on the the gold side of the quartz transducer. The wire-bonding was done at École Polytechnique, Département de Génie Physique under the supervision of A. Lecours and P. Ciuranu. The thin film heater was found to

be temperature insensitive with negligible magnetoresistance in the temperature and field ranges studied. On the down side, this kind of heater was time consuming to make and the film was easily damaged by the vapors of the acid flux used to make the soldered contacts on and around the sample. The second kind of heater consisted in a strain gauge from Micro-Measurements. The gauge came encapsulated in a resin with leads already attached. This heater was glued, using GE 7031 varnish to a thin copper plate to which a 100 μm silver wire had previously been soldered with non-superconducting solder from Oxford Instruments. As with the thin film resistor, the gauge was found to be temperature and field insensitive. Because of its low cost and its robustness, the strain gauge is now the preferred heater for thermal conductivity measurements. Finally, the heater current, ranging from 0.1 to 20 μA was provided by a Keithley 224 constant current source.

The thermometers used consisted of 1 kΩ ruthenium oxide thick films (room temperature nominal value) that were given to us by S. Kreizmann of TRIUMF. These thermometers are known to have an excellent sensitivity (see for example [120, 122]) at low temperatures. They were mounted in a similar way as the strain gauge heater. They were glued with GE 7031 varnish to a thin copper plate to which a 100 μm silver wire had previously been soldered with non-superconducting solder. Four 25 μm manganin wires (each 15 cm long coiled like a spring so as to save space) were soldered to each thermometer for four-probe electrical measurement. Later on, a more refined thermometer mount was designed: Copper wires were soldered to the ruthenium oxide and then wound around the small cylindrical part of the thermometer mount to ensure better thermalisation. Manganin wires were then used to connect to the measuring electronics. This thermometer mount is bulkier (approximately 2.8 x 4.5 x 1.8 mm^3 as opposed to 3.1 x 2.7 x 0.5 mm^3 for the plate) and more difficult to assemble but has the advantage that the contacts on the thermometer are permanent. Repeated soldering on the contact pads was found to be quite damaging to the thick film resistors. The measurement of the temperatures T_- and T_+ was made using two SR850 lock-in amplifiers from Stanford Research Systems. Each instrument sends a low frequency (below 20 Hz) ac voltage. This voltage is converted into a current by means of a 2.2 MΩ limiting resistor. The voltage drop across each thermometer is detected at

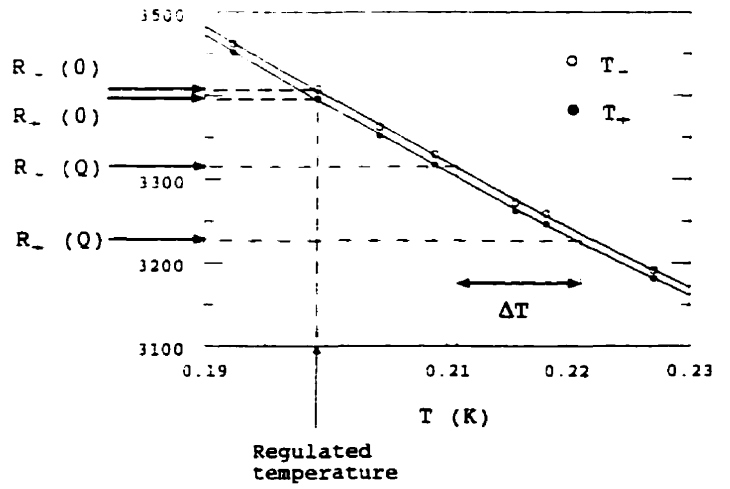

Figure 5.2: Example of analysis performed in order to extract the thermal conductivity. The circles (open for T_- and closed for T_+) represent the data points used to obtain the calibration (solid lines). In this example, the fridge temperature is regulated at 199 mK and a heater power of approximately 9 nW is applied. The new values of the resistances for both thermometers ($R_-(Q)$ and $R_+(Q)$), with the temperature gradient on, are used to read off the temperature. The temperature gradient is then simply the difference between these two temperatures while the sample temperature is the average of the two. Typically, gadients around 5% of the stabilized temperature were used.

the excitation frequency and converted into a resistance. This procedure is repeated at each germanium regulated temperature with and without the heat current on. One therefore obtains an in-situ calibration of the thermometers (from the data at zero heat gradient) and uses these calibrations to obtain the two temperatures T_- and T_+ with the current on. An example of this analysis is presented in figure 5.2 for a pure $YBa_2Cu_3O_{7-\delta}$ sample. We emphasize that the largest source of relative error comes from this calibration. We therefore tried various fits over many temperature ranges until the fit residuals became small yielding errors in the thermal conductivity of the size of the dots.

Both heater and thermometers were mechanically supported by posts made of Vespel from Dupont. The posts were 5.7 mm long with a small cross-sectional area of approximately 0.3 x 0.3 mm^2 so as to prevent significant heat losses from conduction (see section 5.3.1 and section A.2). The posts were cut with a diamond saw and polished to the desired thickness. A platform, made from Ecobond 286 white epoxy, was then shaped at one end so as to provide a flat surface to glue with GE 7031 varnish the copper mount of either a heater or a thermometer. The posts were then

glued to the mount using the same epoxy.

In the case of UPt_3 samples, two types of contacts were made. Each thermometer contact was made by wire-bonding four 50 μm gold wires. Two wires were attached side by side to the sample while the remaining two were thermo-compressed on top. The four wires were then soldered together at the other end with non-supeconducting solder from Oxford Instruments and attached to the silver wire leading to the thermometers. For the heat sink contact, the whole cross-sectional face of the sample was soldered to a copper plate with non-superconducting solder. This plate was then bolted with a brass screw to a mount in good thermal contact with the mixing chamber of the dilution fridge. As to the other end of the sample, a 100 μm silver wire was soldered to it and thermally connected to the heater with non-superconducting solder. This method of mounting enabled us to use the same contacts for measuring thermal and electrical conductivity. In the case of $YBa_2Cu_3O_{7-\delta}$ samples, the contacts were made by R. Gagnon with diffused silver epoxy onto a 100 μm silver wire for the current contacts while, for the voltage contacts, 50 μm silver wire were used. As with the soldered or wire-bonded contacts, this type of contact gave very low thermal contact resistances[1] yielding linear temperature gradients.

5.3.1 Heat losses

As seen in the previous section, the steady-state longitudinal heat- flow method can be used if the heat losses to the outside world are minimal. Due to the low temperatures ($T < 1$ K), heat losses through radiation are small and can safely be neglected (see section A.1).

As to the conduction from residual gas, the only gas that can cause a problem is helium since all other substances are solid at the temperatures in which experiments are carried out. The problem with helium is that it can liquefy and form a superfluid layer between different parts of the dilution refrigerator or even on the sample itself and short out the temperature gradient. The only way to prevent this problem is by pumping all helium exchange gas at 4 K for at least 12 hours. Experiments on gold (see section 5.3.2) not only show that heat losses from experimental leads are

[1] The electrical resistance of these contacts was typically ~100 mΩ (~3.5 mΩ) at room temperature (helium temperature).

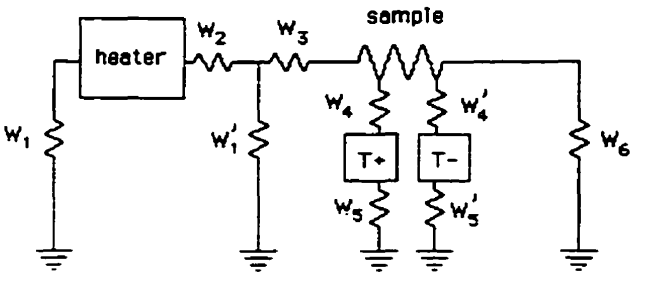

Figure 5.3: Schematic description of the thermal circuit for the thermal conductivity measurement (see section 5.3.1).

negligible, but that the conduction from superfluid helium films can also be avoided.

Finally, we come to the problem of heat losses through the measuring electrical leads or supports. A schematic thermal circuit of the possible paths for the heat current is shown in figure 5.3. Each W_i represents a thermal resistance while the ground symbol represents the heat sink. The setup was designed such that the sum $W_2 + W_3 + W_{sample} + W_6$ was much less than W_1 and W_1', and W_5 (W_5') was much greater than W_4 (W_4'). Figure A.1 (in appendix A.2) gives the detail for each of the W_i. A detailed calculation of the heat losses in the worst case scenario is also done in appendix A.2. Basically, we find that we can safely ignore the heat losses in our experiments on UPt_3 and $YBa_2Cu_3O_{7-\delta}$.

5.3.2 *Results with Au and the Wiedemann-Franz law*

As discussed earlier in section 2.1.3, at low temperatures, the ratio of electronic thermal conductivity over electrical conductivity is proportional to temperature. Verification of the Wiedemann-Franz law on a metallic sample at low temperatures would certainly demonstrate the validity of our thermal conductivity setup especially with regards to Kapitza resistances (see appendix A.2). Given that the setup was designed so that the electrical and thermal conductivity can be measured using the same sample contacts, this eliminates all uncertainty in the Lorenz number with regards to the geometric factor.

In order to achieve this, measurements of both the thermal and electrical conductivity were carried on a gold wire. The geometry of the sample was chosen such that its heat conductance would be comparable to the least conducting sample measured.

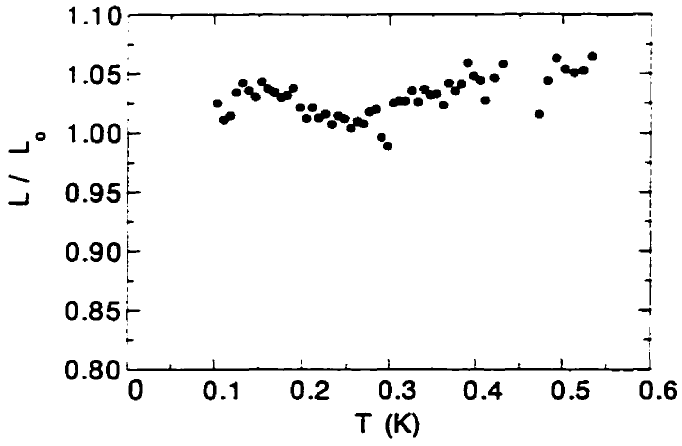

Figure 5.4: Measured Lorenz number divided by Sommerfeld value for the Au sample as a function of temperature.

The wire had a diameter of 25 μm and a length of 1.31 cm (obtained from the room temperature resistivity of 2.35 $\mu\Omega$cm [123]) between the two thermometer (or voltage) contacts. This sample was found to have a residual resistivity ρ_0 of 0.042 $\mu\Omega$cm. Using the Wiedemann-Franz law, this geometry yields a thermal conductance at 100 mK of 2.2 x 10^{-4} mW/K which is comparable to 1.1 x 10^{-4} mW/K found in $YBa_2Cu_3O_{7-\delta}$ but is much less than the 1.8 x 10^{-3} mW/K found for UPt_3 at the lowest temperature achieved. The results for the Lorenz number, obtained in collaboration with M. Chiao, B. Ellman and L. Taillefer and displayed in figure 5.4, are consistent with $L = (1.03 \pm 0.03)L_0$ from 100 mK up to 500 mK so that an agreement within 3% is obtained, demonstrating that heat losses were at a minimum even for such a high thermal resistance sample.

To conclude this experimental techniques chapter, we mention that besides the results presented in this thesis, the thermal conductivity has been measured at dilution refrigerator temperatures on other systems as well, using the same experimental setup. Results on UPd_2Al_3 were obtained by Chiao *et al.* [124] and data on quasicrystals were obtained by Legault *et al.* [125]. A total of three thermal conductivity setups can now be operated simultaneously on our dilution refrigirator and allow measurements in both magnetic field and zero field (in the compensated region of the magnet).

6

THE THERMAL CONDUCTIVITY OF UPt_3

In this chapter, our thermal conductivity results on UPt_3 will be presented. They will be preceeded by a review of thermal conductivity results obtained on poly and single-crystals of UPt_3.

6.1 *Experimental review*

6.1.1 *Previous thermal conductivity results on polycrystalline UPt_3*

Soon after the discovery of superconductivity in UPt_3, many groups set forth to measure the thermal conductivity of polycrystalline samples (see [126, 127, 37, 128]). An example is shown in figure 6.1 where we reproduce the data of Franse *et al.* Power law dependences were observed and it was claimed that the gap had to have zeros at certain points in k-space. However, due to the relatively poor crystal quality at the time the thermal conductivity at low temperatures probably included a significant phonon contribution. To illustrate this, we take a generic sample dimension of 1 mm and make use of $\kappa_{ph} = \frac{1}{3} c_{ph} v_{ph} \ell_{ph}$ with the phonon specific heat $c_{ph} = \beta T^3$ ($\beta = 20$ $JK^{-4}m^{-3}$ [54]) and a phonon mean free path (ℓ_{ph}) of the size of the crystal (see also section 6.3.1). The polycrystalline average phonon velocity is taken to be: $v_{ph} = \frac{1}{3} v^c_{ph} + \frac{2}{3} v^b_{ph}$ with each velocity calculated from equation 6.2 (see section 6.3.1) and from the data of de Visser (see table 3.1 and reference [54]). The calculated polycrystalline velocity is 1730 m/s. At 100 mK, the phonon contribution to κ/T amounts to 2.4 mW/K^2cm namely 84% of Ott *et al.* [126], more than 95% of the data of Jaccard *et al.* [128] and Sulpice *et al.*'s data [37], and it amounts to 80% of the thermal conductivity of Franse *et al.* [127]. On the other hand, as we discuss below, a true T^3 regime is never attained in these samples due to the large number

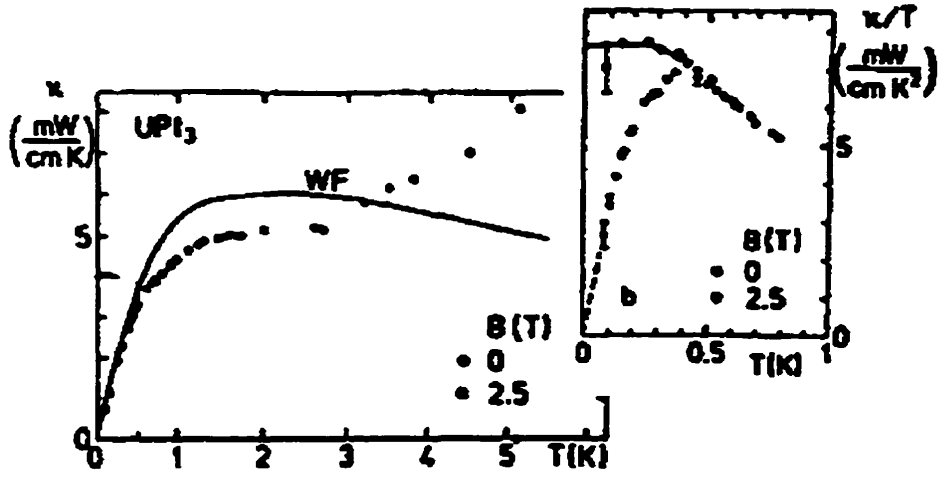

Figure 6.1: Thermal conductivity of polycrystalline UPt_3, left panel: high temperature region; right panel: close-up of low temperature region for both the normal and superconducting state (see [127]). The WF estimate in the left panel is obtained using the temperature dependence of the resistivity on the same sample. Notice that at low temperature the agreement between the WF law estimate and the measured thermal conductivity is very good.

of quasiparticles that scatter the phonons even at 100 mK. Therefore, our estimate is certainly an overestimate of the phonon contribution. We will show later that in single crystals of high quality, even this upper bound for the phonon conduction occupies a much smaller fraction of the total thermal conductivity due to the enhanced electronic mean-free paths.

Furthermore, all these authors, except Ott *et al.*, conclude that their thermal conductivity results obey a law of the form: $\frac{\kappa}{T} = \kappa_0 + \alpha T$. The range of validity of such a law differs from one experiment to the next. κ_0 is taken to be indicative of a residual linear term. Although not mentioned in their paper, Ott *et al.* find a *negative* intercept for the residual thermal conductivity. When discussing single crystals (see 6.1.2), we will see that such negative intercepts are not uncommon. This only means that the fitted expression ceases to be valid at lower temperatures and that the thermal conductivity levels off. The results of the fits are summarized in table 6.1 and the results of Behnia *et al.*, discussed in the next section, are included for comparison.

Table 6.1: Low temperature fits of the form $\frac{\kappa}{T} = \kappa_0 + \alpha T$ to previous thermal conductivity measurements. The temperature range for the validity of the fit is also tabulated along with the references. The results of Behnia *et al.* [129] on single crystals are included for comparison. These results are discussed in section 6.1.2.

κ_0 (mW/K^2cm)	α (mW/K^3cm)	range of validity (mK)	reference
0.55	20	$35 < T < 200$	[128, 37]
0	32	$85 < T < 150$	[127]
-0.34	32	$35 < T < 70$	[126]
1.2	62	$70 < T < 250$	c-axis [129]
-0.7	55	$70 < T < 250$	b-axis [129]

6.1.2 Previous thermal conductivity results on single crystalline UPt_3

Behnia *et al.* [130, 129], were the first to use thermal conductivity in UPt_3 to probe the anisotropy of the superconducting phase. They made use of a whisker (c-axis needle) and a b-axis cut single crystal for their measurement. As suggested by the residual resistivity ratio $\frac{\rho(300K)}{\rho_0} = 290$ (163) and by the ratio of inelastic to elastic terms in the resistivity $\frac{A}{\rho_0} = 1.9$ (0.75) K^{-2} for the b (c)- axis sample, the two crystals did not have the same quality. Their results are displayed in figure 6.2 for the thermal conductivity over temperature as a function of temperature. By using the same procedure as above with the velocities for a single crystal (see section 6.3.1), we estimate the phonon thermal conductivity at 65 mK to be of the order of 3% of the total κ [1]. This small phonon conductivity is a direct consequence of the smallness of the crystals used in their investigation as well as long mean-free paths.

Figure 6.3 displays the anisotropy in thermal conductivity for both directions of the heat current normalized at T_c as a function of reduced temperature. The fact that these authors made use of two crystals with different impurity concentrations precluded any firm conclusion as to what type of gap structure was present in UPt_3. The slight increase in the ratio κ_c/κ_b could even suggest an axial gap (see section 6.3.3) even though most transport measurements pointed to the presence of a line node in

[1] These authors quote their sample dimensions [130]; c-axis: 4 x 0.25 x 0.25 mm^3, b-axis: 4 x 0.35 x 0.6 mm^3. The smallest sample dimension was used for the phonon mean-free path.

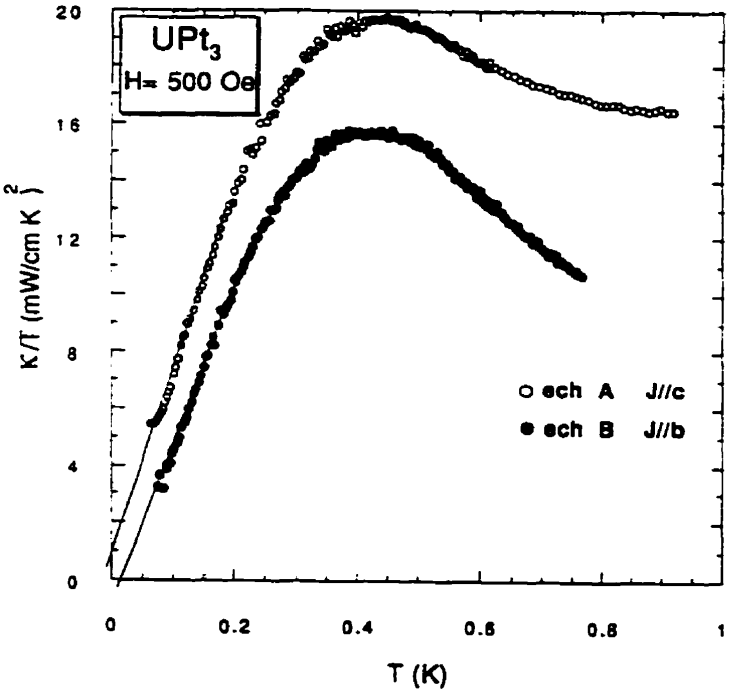

Figure 6.2: Data of Behnia *et al.* for thermal conductivity over temperature as a function of temperature on UPt_3, for sample A with $\vec{J} \parallel \hat{c}$ and for sample B with $\vec{J} \parallel \hat{b}$. The solid lines are linear fits to the low-temperature data (after [130]).

the basal plane (see for example [38]). The ambiguity and inconclusiveness of their study prompted us to perform the same thermal conductivity measurement on *one* single crystal along the b and c-axis.

6.2 Sample characteristics

A single crystal of cylindrical shape (20 mm length, 6 mm diameter) was grown by L. Taillefer using Czochralski pulling in ultrahigh vacuum. Two sections (of length 2 mm) separated by 10 mm were cut out and then annealed at 1200 °C for six days. The specific heat of both sections was measured by Bogenberger and Löhneysen [131] between 0.15 and 1.0 K and found to be identical (within 1%), thus confirming homogeneity (the result for one section is shown in figure 6.4). The two well-separated transitions are complete at $T_c^+ = 0.50$ K and $T_c^- = 0.44$ K, with respective widths of 25 and 20 mK (see inset of figure 6.4). Out of one section, two small and adjacent rectangular pieces were spark cut, each with dimensions 2.0 x 0.7 x 0.7 mm^3. The length of one is parallel to the c-axis and that of the other to the b-axis. The high

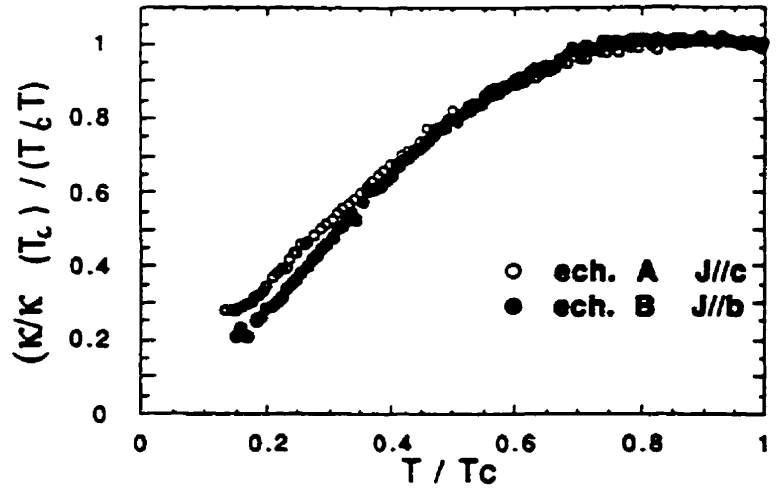

Figure 6.3: Data of Behnia *et al.* for thermal conductivity over temperature normalized at T_{c-} as a function of temperature. Notice the slight anisotropy between the two curves (after [130]).

purity is attested to by the low residual resistivity or conversely the high residual resistivity ratio RRR=$\rho(300K)/\rho_0$=650 and A/ρ_0=2.7 K^{-2} for our c-axis crystal. These values are to be compared with results on the best bulk single crystals of UPt_3 quoted in the literature: A/ρ_0=3.1 K^{-2} and RRR=882 for Huxley *et al.* [132] and A/ρ_0=2.7 K^{-2} and RRR=625 for Shivaram *et al.* [133]. From figure 6.4, a linear extrapolation to T = 0 yields a residual linear term of γ_0 = 18% γ_N with γ_N=440 $mJK^{-2}mol^{-1}$. We will come back to a discussion of residual normal fluid at T = 0 later on in this chapter.

The electrical resistivity, showing the superconducting transition for the b-axis sample, is displayed in figure 6.5. The resistivity obeys the Fermi liquid behavior $\rho(T) = \rho_0 + AT^2$ perfectly below 0.8 K, with ρ_0 = 0.61 (0.23) $\mu\Omega$cm and A = 1.60 (0.59) $\mu\Omega cmK^{-2}$ for $\vec{J} \parallel \hat{b}$ ($\vec{J} \parallel \hat{c}$). The anisotropy in both elastic and inelastic components is virtually the same: 2.65 and 2.71, respectively, and ρ_b/ρ_c = 2.7 to within 1% from 0.5 to 0.8 K giving a temperature independant anisotropy for the electrical resistivity.

6.3 *Thermal conductivity results*

The two components of the thermal conductivity over temperature, κ_b/T and κ_c/T, are displayed in figure 6.6 as a function of temperature.

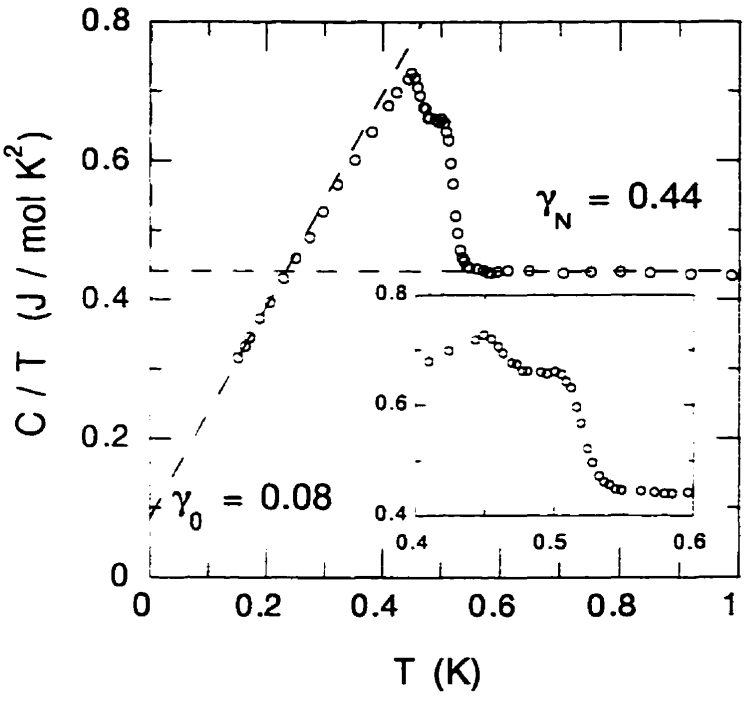

Figure 6.4: Specific heat over temperature as a function of temperature. Above $T_c^+ = 0.5$ K, the specific heat is linear yielding a $\gamma_N = 0.44$ J/molK^2 while a finite intercept of $\gamma_0 = 0.08$ J/molK^2 is observed at T = 0. Inset: Close up of the double superconducting transition region. This specific heat data can clearly resolve both T_c^+ and T_c^-. This data was collected by B. Bogenberger and H. v. Löhneysen [131]

Before going further in the discussion of the thermal conductivity results, let us show that this measurement is a privileged probe in UPt_3 in the sense that the phonons can be neglected over the whole temperature range thereby making the interpretation of the results much more straightforward. Such simplifications will not be possible in the case of $YBa_2Cu_3O_{7-\delta}$.

6.3.1 Phonons

In chapter 2 we discussed the possibility that, upon entering the superconducting state, the phonon contribution, even if it was negligible in the normal state, can become significant at the lowest temperatures. In this section it will be shown that the phonon contribution can be neglected in *both* the normal and superconducting states in UPt_3.

In the superconducting state, as seen in sections 6.1.1 and 6.1.2, an estimate of

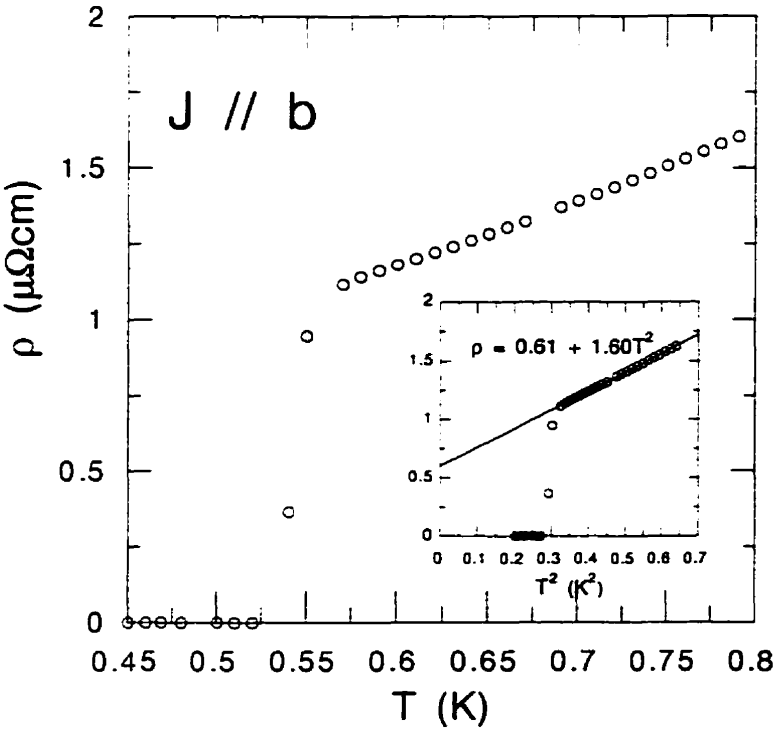

Figure 6.5: Resistivity as a function of temperature for the b-axis sample. Inset: Resistivity as a function of the square of the temperature showing the Fermi liquid behavior: $\rho = 0.61 + 1.60T^2$. A similar plot for the c-axis sample yields: $\rho = 0.23 + 0.59T^2$

the maximum phonon contribution is obtained using the formula:

$$\kappa_{ph} = \frac{1}{3} c_{ph} v_{ph} \ell_{ph} \tag{6.1}$$

where $c_{ph} = \beta T^3$ is the low-temperature phonon specific heat, v_{ph} is the average sound velocity, and ℓ_{ph} is the phonon mean-free path. The maximum contribution will be attained when ℓ_{ph} takes on its maximum value, namely the size of the crystal, equal to 0.7 mm. The sound velocity needs to be averaged over the longitudinal and transverse modes using the following equation [5]:

$$v_{ph} = v_l(2s^2 + 1)/(2s^3 + 1) \tag{6.2}$$

where $s = v_l/v_t$, v_l and v_t are, respectively, the longitudinal and transverse phonon velocities. Using the published sound velocities from de Visser *et al.* [54] (or refer to table 3.1), $v_{ph} = 1880$ (1440) m/s for the b (c) axis and their value of $\beta = 20$ $JK^{-4}m^{-3}$, the phonon heat conduction can be estimated. The maximum phonon contribution to

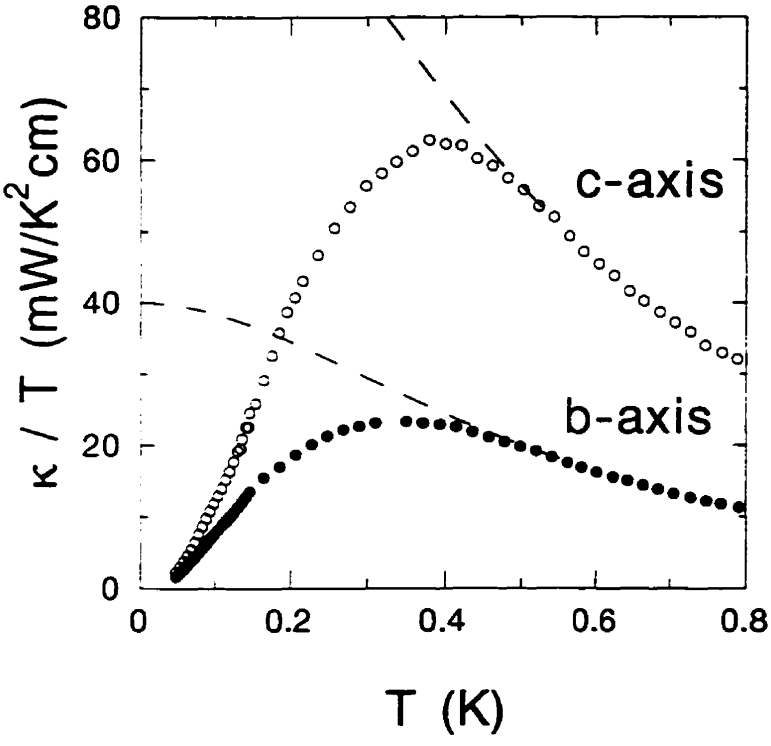

Figure 6.6: Thermal conductivity over temperature of UPt_3 for a heat current along two directions of the hexagonal crystal lattice: $\vec{J} \parallel \hat{c}$ (open circles) and $\vec{J} \parallel \hat{b}$ (solid circles). The dashed lines are a fit to the normal state and agree very well with the thermal conductivity data obtained by applying a field above $H_{c2}(0)$ and correcting for the known magnetoresistance.

the thermal conductivity in the superconducting state will be κ_{ph}=85 (67)T^3 mW/Kcm for the b (c) axis. For T < 150 mK, this represents at most 15% (6%) of our κ_b (κ_c). Recall that in the polycrystals, this fraction could be as large as 80-95%. As emphasized above, our phonon contribution is a smaller fraction of the total thermal conductivity *only* because of the enhanced electronic mean-free paths (*i.e.* lower residual resistivity) due to a lower density of defects. In absolute numbers, the thermal conductivity of our crystal ($\kappa_{avg} = \frac{1}{3}\kappa_c + \frac{2}{3}\kappa_b$) is more than four times larger than that of Franse *et al.* [127] at T_c.

The phonon contribution in the normal state near T_c can be estimated from the high-temperature thermal conductivity data of Franse *et al.* [127] shown in figure 6.1. Using the Wiedemann-Franz law to estimate the electronic heat conduction, one can extract from their results $\kappa_{ph} \approx 0.5\kappa$=4 $mWK^{-1}cm^{-1}$ at 5 K. The T^2 dependence due to electron scattering (the dominant process below 10 K) then yields $\kappa_{ph}(T_c)$ =

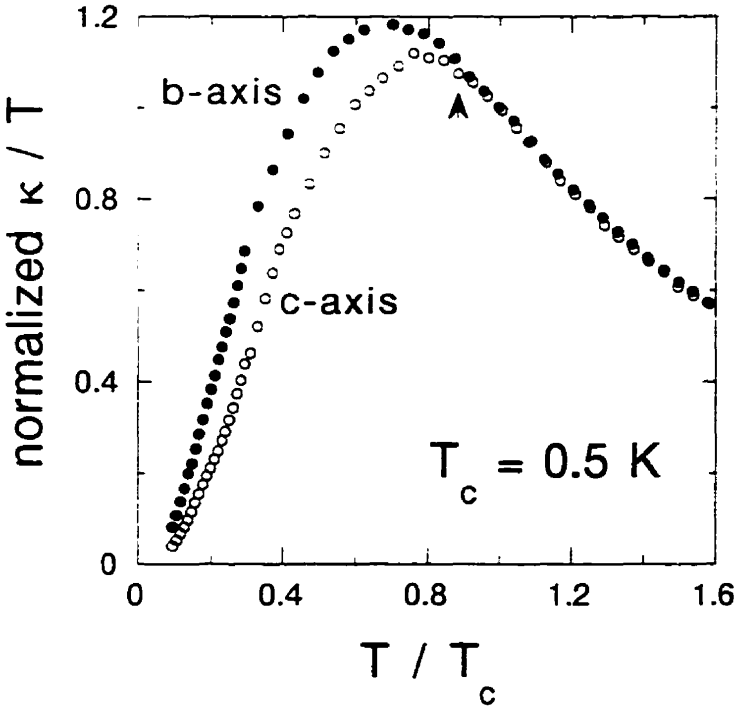

Figure 6.7: Thermal conductivity divided by temperature vs reduced temperature for the two directions of heat current. κ_b/T and κ_c/T are both normalized to unity at T = 0.5 K. Note the additional anisotropy appearing below T_{c-} (arrow).

0.04 mW/Kcm, namely 0.4% of our measured $\kappa_b(T_c)$. We can therefore conclude that heat conduction by phonons can be neglected *both* in the normal and superconducting state of UPt_3.

6.3.2 *Normal state properties*

We have seen in chapter 3 that the normal state of UPt_3 has has all the characteristics of a Fermi liquid: there is a Fermi surface and amongst other properties, the specific heat is linear in temperature with a coefficient γ_N ($C = \gamma_N T$) that is huge. It is interesting to ask whether the heavy electrons, accessed through the linear term in the specific heat, are also the carriers of heat. We make use of $\kappa_e/T = \frac{1}{3}\gamma_N v_F \ell_0$ with γ_N= 440 $mJK^{-2}mol^{-1}$ (see section 6.2) and $v_F \simeq$5000 m/s^1. We also use the scattering rate estimated in section 3.1.2, *i.e.* $\ell_0 = v_F/\Gamma_0$ with $\Gamma_0 = 1 \times 10^{10}$ s^{-1}. We find κ_e/T=64 mW/K^2cm. The measured values are $\kappa_N/T = L_0/\rho_0$ = 40.0

[1]This value is an average over various orbits in the b-c plane [65].

(106) mW/K^{2}cm for the b (c)-axis. The estimated value based on an average Fermi velocity for the b-c plane lies between the measured values for the b and c-axis. This excellent agreement confirms the Fermi liquid picture of heavy and itinerant quasiparticles in UPt_3.

As mentioned earlier, the estimate of Γ_0 will be an important input in the theories to be discussed in this chapter. For the c-axis sample, we have $\Gamma_0 = 1.0 \times 10^{10}$ s^{-1}. In terms of the critical temperature, $\frac{\hbar\Gamma}{k_B T_c} = 0.15$. As a result, Fledderjohann and Hirschfeld use values[1] of the order 0.1 in fitting our thermal conductivity results [51]. This result is substantially larger than that used in previous theoretical treatments [42, 134, 47].

The normal state behavior obeys $\kappa_N(T)/T = (a + bT^2)^{-1}$, with a= 0.025 (0.009) cmK^{2}mW^{-1} and b= 0.100 (0.037) cm mW^{-1} for $\vec{J} \parallel \hat{b}$ ($\vec{J} \parallel \hat{c}$). It is characterized by strong quasiparticle-quasiparticle inelastic scattering as evidenced by the importance of the bT^2 term *i.e.* it is as large as the elastic impurity component at T_c: $a = bT_c^2$. From figure 6.7, we see that the anisotropy is *independent of temperature* above T_c, a feature more clearly seen in figure 6.9 when we plot the ratio κ_c/κ_b and $\kappa_c/\kappa_b \approx 2.8$ up to 0.8 K.

As discussed in section 6.2, we emphasize that the anisotropy in the electrical resistivity is also *independent of temperature* with a similar ratio ρ_b/ρ_c=2.7 within 1% from 0.5 to 0.8 K. This implies that the Lorenz number, although strongly temperature-dependent, is isotropic. By applying a magnetic field of 3 T (*i.e.* larger than $H_{c2}(0)$) and correcting for the known magnetoresistance (see section 3.1.2), the normal state thermal conductivity was measured down to 0.1 K. The Wiedemann-Franz law was obeyed at the lowest temperatures *i.e.* the measured Lorenz number $L = \kappa\rho/T$ yielded L(0.1 K) = $0.99L_0$ where $L_0 = 2.45 \times 10^{-8}$ WΩ/K^2 is the Sommerfeld value. Upon going to higher temperatures, the Lorenz number was found to decrease as a result of electron-electron scattering. At 800 mK, it reached L(0.8 K) = $0.75L_0$.

The picture that emerges for the normal state is then surprisingly simple. The anisotropy is the same for both charge and energy transport, and for impurity and electron scattering: $\frac{\kappa_c}{\kappa_b} = \frac{\sigma_c}{\sigma_b} = 2.7$. This is close to the average Fermi surface

[1] They define $\Gamma = 1/2\tau$.

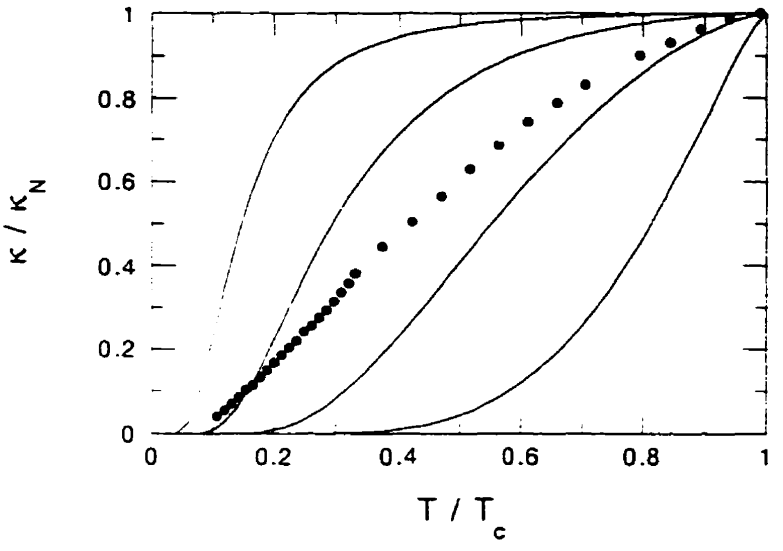

Figure 6.8: Comparison of thermal conductivity of UPt_3 b-axis normalized at T_c^- (solid circles) with various BCS gaps (solid lines): from left to right $\frac{1}{4}$, $\frac{1}{2}$, 1 and 2 times the standard BCS value $\Delta(0) = 1.76 k_B T_c$.

anisotropy $\frac{\langle v_c^2 \rangle}{\langle v_b^2 \rangle} = 2.1$ as calculated from the band structure [66]. This seems to indicate that even though the Fermi surface of UPt_3 is fairly complicated with its five sheets, it is possible to model transport properties with a single ellipsoidal Fermi surface of mass ratio $m_r = \frac{m_b}{m_c} = 2.7$. It is interesting to note that the ratio of the slope of $H_{c2}(0)$ at T_{c+} for both directions is: $\frac{H'_{c2}(\|c)}{H'_{c2}(\|b)} = 1.61 = \sqrt{2.6}$ [135], which agrees closely with the standard relation for an s-wave BCS superconductor:

$$\frac{H'_{c2}(\| \, c)}{H'_{c2}(\| \, b)} = \sqrt{m_r} \tag{6.3}$$

This picture of simple mass anisotropy implies s-wave scattering *i.e.* that both relaxation times $\tau_{elastic}$ and $\tau_{inelastic}$ are isotropic. This in itself is a surprising result: one would expect an isotropic mean-free path for elastic scattering, namely $\ell_0 = v_F \tau_{elastic}$ and an anisotropic inelastic electron-electron scattering due to the complex Fermi surface.

6.3.3 *Unconventional nature of the superconductivity in UPt_3*

Figure 6.8 shows a comparison of our UPt_3 data with the electronic contribution to thermal conductivity as calculated from BRT [16] using a multiple of the conventional gap parameter $\Delta(0) = 1.76 k_B T_c$. For the standard BCS gap, the thermal conductivity

calculated for impurity scattering only, normalized by the normal state conductivity, increases very slowly at low temperature reaching only 4% of its value at T_c by $T = T_c/4$. This is what is observed in pure Al [136], and similarly for other pure superconductors with low T_c/θ_D: 3% in Nb [137], 2%-3% in Sn [138], and 1%-2% in Zn and Cd [23]. On the other hand, in UPt_3, κ/κ_N has already risen to 27% of its normal state value at $T_c/4$ ($\vec{J} \parallel \hat{b}$). More than any power law dependence, this order-of-magnitude difference in the rate of thermal excitation of quasiparticles is compelling evidence for nodes in the gap. Of course, this is reflected in other properties; for the electronic specific heat, $C_{es}/\gamma T_c = \frac{1}{40}$ at $T_c/4$ in conventional superconductors [136], while it equals $\frac{1}{8}$ in UPt_3 (see figure 6.4). Furthermore, as displayed in figure 6.8, a BCS gap of a different amplitude does not qualitatively reproduce the behavior observed in UPt_3 either rising too fast at low temperature and saturating too early or rising too slowly and displaying an exponential behavior over a wide range of temperature.

Our main result is the additional anisotropy which develops in the superconducting state, as seen in figure 6.7. The large, temperature-independent anisotropy of the normal state is considerably reduced at low temperature. This is made evident in figure 6.9, where the ratio $\kappa_c(T)/\kappa_b(T)$ is plotted as a function of temperature. *Such a change can only be due to gap anisotropy.* A conventional *s*-wave gap $\Delta(\vec{k})$, although finite everywhere on the Fermi surface, can be smaller for certain $\vec{k}$ directions and thus lead to an anisotropy in the electronic thermal conductivity κ_e below T_c. This is what happens in gallium [24] (as discussed in section 2.2.3) where $\Delta(\vec{k})$ is smaller for $\vec{k}$ along the hexagonal axis. Despite this anisotropy, the thermal conductivity ratio for the two directions *has* to go to zero (or to infinity depending on which gap is smaller) due to the exponential nature of the thermal conductivity in both directions. An unconventional gap, however, which actually vanishes for certain $\vec{k}$ directions, will not only lead to anisotropy and to a rapid increase in κ_e, but can lead to a finite thermal conductivity ratio for two directions with different nodal structures. This is what we observe in figure 6.9: the ratio κ_c/κ_b extrapolates to a *finite* value at T=0. This definitively excludes an anisotropic *s*-wave gap. We will come back to discuss this in more details below. We conclude that the finite ratio and the sheer magnitude

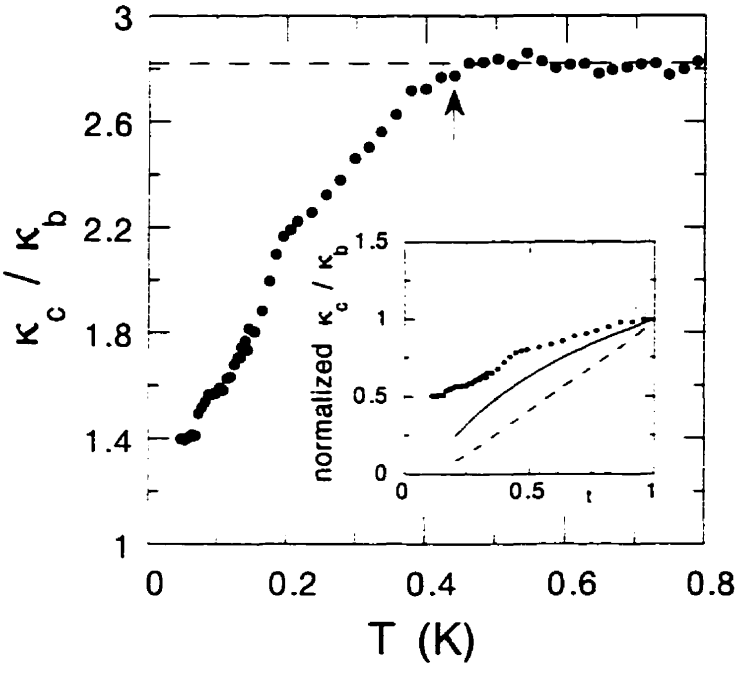

Figure 6.9: Anisotropy ratio vs temperature. The constant anisotropy of the normal state drops below T_{c-} (arrow) excluding the possibility of an axial gap for phase B. Inset: κ_c/κ_b normalised at T_{c-} vs t = T/T_{c-}; data (circles), and theoretical curves for three gap structures: axial (dotted), polar (dashed) and d-wave (solid) (after [45]). Note that the feature at 0.2 K is probably not real and arises from the linear interpolation to our experimental data which enabled us to deduce the ratio.

of κ_c clearly distinguishes UPt_3 from conventional superconductors.

Now that we can exclude a conventional *s*-wave gap, the position of the nodes is the question of interest. A careful distinction must be made between phase A (from T_{c-} to T_{c-}) and phase B (below T_{c-}). Inspection of the data (see figure 6.7) reveals little change in either κ_b or κ_c with the appearance of phase A. This unusual insensitivity is suggestive of a nodal structure isotropic in the b-c plane, such as a line in that plane. Such a line is consistent with both the E_{2u} and E_{1g} models [36] but modeling of the double superconducting transition has proven difficult for theorists and has not yet been carried out. It would necessitate the calculations to be performed for orthorhombic symmetry with two different gaps and appropriate domain averaging [36]. Therefore, the usual approach is to ignore this symmetry breaking and normalize the thermal conductivities at T_{c-} [51, 36, 52] when looking at phase B.

As first introduced by Taillefer *et al.* [139], we define three temperature regimes: (i) the diagnostic regime, (ii) the elastic regime and, (iii) the gapless regime. The truly diagnostic regime is at low temperatures where excited quasiparticles have wavectors near the nodes in the gap, and thermal properties are governed by the topology of the gap about the nodes. As argued by Graf *et al.* [52], only a knowledge of the asymptotic topology of the gap at the nodes is needed, in which case the complicated details of the Fermi surface are unimportant and it can be approximated by an ellipsoid with uniaxial symmetry about the c-axis and anisotropy governed by the anisotropy in the mass tensor[1]. In this context, the gap will be a linear combination of ellipsoidal harmonics Y_{LM} each of which vanishes at certain values of θ (except the *s*-wave gap Y_{00}). The nodes can therefore be points at the poles ($\theta = 0°$), a line around the equator ($\theta = 90°$), or two lines above and below the equator ($\theta = 90° \pm 23°$ for a mass ratio of 2.7). The five lowest harmonics are plotted in figure 6.10 while table 6.2,taken from [36], gives the functional form and the thermal conductivity ratio at T = 0 for some harmonics up to L=5 and M=4. We define the diagnostic regime in the following way: consider a gap with a linear point node at $\theta = 0$ (such as the axial or hybrid I gaps): $\Delta(\theta) = \Delta(T = 0)\sin\theta \simeq \Delta(0)\theta$. The asymptotic topology is obtained for θ such that $\sin\theta \simeq \theta$, namely for $\theta \lesssim 20°$. Thermally excited quasiparticles will have wavevectors predominently in the solid angle defined by $\theta < 20°$ when the temperature is such that $k_B T \simeq \Delta(20°)$. Making use of $\Delta(T = 0) \sim k_B T_c$, we get that the diagnostic regime is for $T/T_c \lesssim 0.3$.

The elastic regime can be defined from our normal state thermal conductivity. We require $a \gg bT^2$; taking bT^2/a <10%, we get the elastic regime when $T/T_c < 0.3$. Finally, in a self-consistent treatment, impurities lead to a broadening of the nodes in the gap of unconventional superconductors, giving rise to a gapless regime defined by $k_B T < 2\hbar\Gamma_0$ [36, 51, 140]. In this regime, the density of excited quasiparticles has a modified energy dependence such that the topology of the gap near the nodes can no longer be accessed by looking at temperature dependence of physical properties. In

[1] We note that calculations with Fermi-surface harmonics has been performed [36]. The authors find that these functions have a large number of nodes which are unlikely to arise out of any microscopic gap equation. Norman and Hirschfeld [36] are unable to fit our experimental data using such harmonics.

section 6.3.4, we will see that theories can account for our data if $\frac{\hbar\Gamma}{k_B T_c} = 0.05$ or less. This means that in our crystal the gapless regime would be below $0.1T_c$, *i.e.* below our lowest data point.

In conclusion, by focussing on data between 0.1 and $0.3T_c$ (namely the diagnostic regime), we avoid all the complications arising from gaplessness (at lower temperatures) and inelastic scattering (at higher temperatures) and a direct comparison with theories will prove very powerful in determining the full symmetry of the order parameter.

Table 6.2: $\kappa_c(0)/\kappa_b(0)$ in the clean limit for several ellipsoidal harmonics Y_{LM} gap functions for an isotropic mass ratio. The Y_{21} and Y_{41} harmonics have E_{1g} symmetry and the Y_{32} and Y_{52} have E_{2u} symmetry (after [36]). The roman numeral following the gap name refers to the k-dependence near the node for $\theta = 0$. Note also that the ratio of 1 for the *s*-wave gap is relevant for a perfectly isotropic gap. In the presence of anisotropy, this ratio goes to zero if $\kappa_b > \kappa_c$, or to ∞ if $\kappa_b < \kappa_c$. For ellipsoidal harmonics, the quantity r^2, which is unity for spherical harmonics, is equal to $r^2 = \cos^2(\theta) + \frac{1}{m_r}\sin^2(\theta)$ where m_r is the mass ratio.

LM	Form	$\kappa_c(0)/\kappa_b(0)$	name
00	r^2	1	*s*-wave
10	$\cos(\theta)$	0	polar
11	$\sin(\theta)$	∞	axial I
20	$3\sin^2(\theta) - r^2$	1	tropical
21	$\sin(\theta)\cos(\theta)$	0	hybrid I
22	$\sin^2(\theta)$	∞	axial II
30	$\cos(\theta)[5\cos^2(\theta) - 3r^2]$	6/7	-
31	$\sin(\theta)[5\cos^2(\theta) - r^2]$	1/2	-
32	$\sin^2(\theta)\cos(\theta)$	1	hybrid II
33	$\sin^3(\theta)$	∞	axial III
41	$\sin(\theta)[7\cos^3(\theta) - 3\cos(\theta)r^2]$	0.647	-
52	$\sin^2(\theta)[3\cos^3(\theta) - \cos(\theta)r^2]$	0.744	-
54	$\sin^4(\theta)\cos(\theta)$	∞	hybrid IV

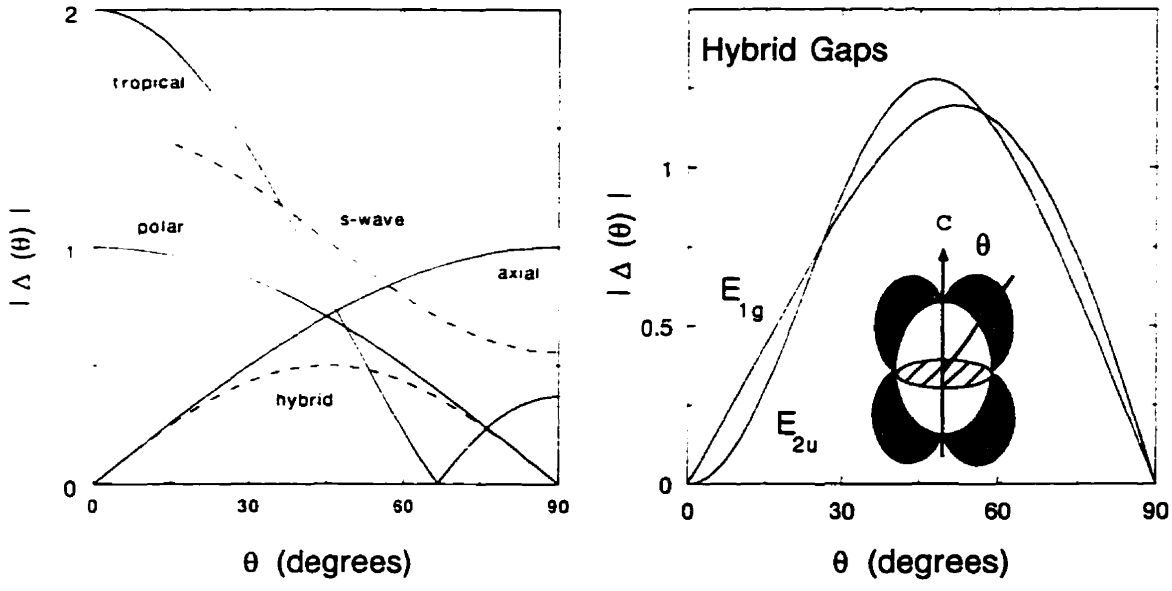

Figure 6.10: Uniaxial gaps vs polar angle θ. Left panel: five lowest ellipsoidal harmonics: anisotropic s-wave, polar, axial, hybrid and tropical. Right panel: two hybrid gaps consistent with E_{1g} and E_{2u} symmetry: $Y_{21} - 0.15Y_{52}$ and $Y_{32} + 0.25Y_{52}$ (after [36]). Note the linear k-dependence of the E_{1g} gap near $\vartheta = 0$ while the E_{2u} has a quadratic k-dependence.

6.3.4 *Comparison with theory*

In contrast with the isotropic phase A, the anisotropy κ_c/κ_b, plotted in the right panel of figure 6.9, starts to drop with the onset of phase B at T_{c-}. This may be an indication of a different nodal structure in the gap of phases A and B. In order to use our results to identify the gap structure in phase B, we adopt a chronological approach and start by comparing our results with the early calculations of thermal conductivity of Hirschfeld *et al.* [134] and Arfi *et al.* [45, 47] and work our way towards more recent calculations. We have already discussed in detail the calculations of Arfi *et al.* [45, 47] and we compare our measurements with their calculations. As we have seen in section 2.3.2, these authors calculated κ_b(T) and κ_c(T) for three simple gap structures assuming resonant impurity scattering: $\Delta(\hat{k}) = \Delta_{max}(T)\cos\theta$ (polar), $\Delta_{max}(T)e^{i\phi}\sin\theta$ (axial), and $2\Delta_{max}(T)e^{i\phi}\sin\theta\cos\theta$ (hybrid I or d-wave). In the inset of figure 6.9, the results of Arfi *et al.* [45] are shown along with our data for the ratio of κ_c/κ_b in the B-phase (*i.e.* κ_c/κ_b normalized at T_{c-}). The fact that the ratio κ_c/κ_b *drops* allows us to discard unambiguously the possibility of an axial gap for phase B

(see table 6.2). This immediately eliminates the axial E_{2g} and E_{1u} (see table 2.3) as candidate representations for the order parameter in the "2D theory" for the phase diagram of UPt_3 [81, 82, 80, 141, 31]. This decrease suggests that there are more thermally excited quasiparticles with velocities along the b-axis than along the c-axis. This could either result from a finite gap being larger along c than along b (anisotropic *s*-wave), from the presence of nodes in the gap along the b-axis in the absence of any along the c-axis (polar gap), or from the presence of nodes along both axes (hybrid gap) provided the nodal structure is such that more quasiparticles have $\vec{v} \parallel \hat{b}$.

As displayed in figure 6.9, another striking finding is that *the ratio does not go to zero as* T—0. Instead, it extrapolates to a large finite value (around half that of the normal state). This definitively excludes a polar gap, which gives $\kappa_c/\kappa_b \rightarrow 0$ as T—0, as a result of the clear difference between excitation of quasiparticles with $\vec{v} \parallel \hat{c}$ (across a finite gap) and with $\vec{v} \parallel \hat{b}$ (in the vicinity of a line node) (see table 6.2). We can also exclude the s-wave gap with $\Delta_c > \Delta_b$ which must go to zero. We therefore conclude that the gap of phase B in UPt_3 *must* have nodes along the c-axis. With the possible exception of recent studies of point-contact spectroscopy [101, 100], no previous experiment could discriminate between a polar gap and a hybrid gap [56]. This leaves the tropical gap, which does not have nodes along the c-axis but still can yield a finite ratio, and the hybrid gaps (refer to table 6.2), as well as various combinations of the three basic nodal elements. Of particular interest are the two lowest hybrid gaps ($\sim \sin^n\theta\cos\theta$, n=1,2), plotted in figure 6.10, because they correspond to two of the states most often postulated for phase B [57, 59]. They belong respectively to the E_{1g} and E_{2u} representation and their overall structures are very similar except near the poles, where the gap opens up linearly in E_{1g} and quadratically in E_{2u}. No experiment to date has been able to discriminate between these two proposed gap structures.

1. *Spherical Fermi surface: the calculations of Fledderjohann and Hirschfeld*

The discovery of a finite thermal conductivity ratio κ_c/κ_b as $T \rightarrow 0$ has prompted theorists to perform detailed calculations for both the E_{1g} and E_{2u} symmetries (see for example [36, 52, 51]). We start by first discussing the results of Fledderjohann

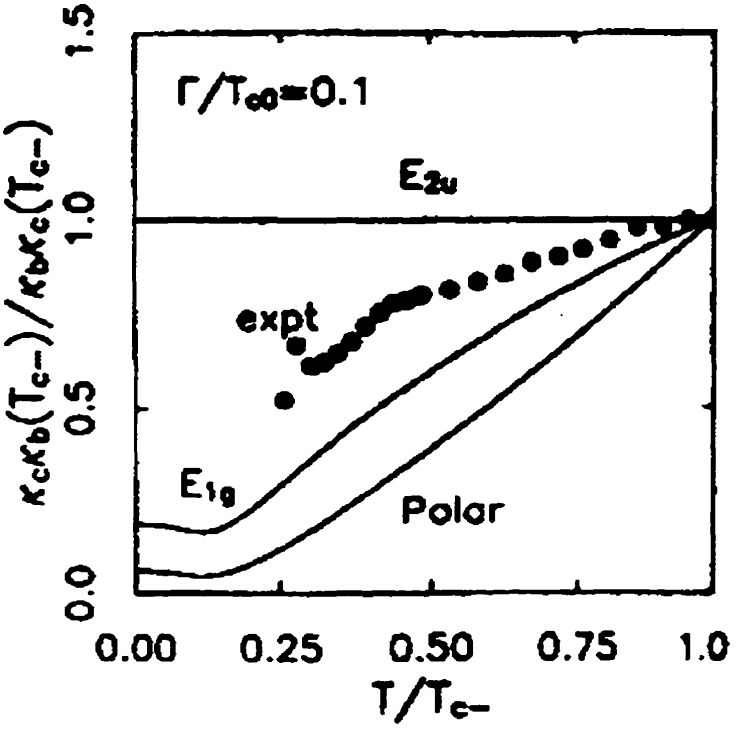

Figure 6.11: Behavior of the anisotropy ratio κ_c/κ_b versus reduced temperature and normalised to 1 at T_{c-}. Our preliminary data (points) are compared with the calculations of Fledderjohann and Hirschfeld [51] for the three indicated gaps with Γ_0=0.1T_c. Note the isotropic result for a hybrid II gap of E_{2u} symmetry.

and Hirschfeld [51]. These authors applied the theory of heat conduction in a weak-coupling BCS superconductor [142] assuming unconventional candidate order parameters of the type polar (*i.e.* Y_{10}), E_{1g} (*i.e.* Y_{21}) and E_{2u} (*i.e.* Y_{32}). Their main focus was on the ratio κ_c/κ_b.

In their self-consistent treatment, they use a spherical Fermi surface and include the inelastic scattering which we know to be important in these samples (above $0.3T_c$). Their result is displayed in figure 6.11 where it is seen that the E_{2u} state yields an isotropic ratio, *i.e.* $\kappa_c(T)/\kappa_b(T) = 1$. One can justify this result from the fact that the number of thermally excited quasiparticles is the same for a quadratic point node as it is for a line (see section 2.3.2). We note that the E_{1g} state appears to reproduce (at least qualitatively) the behavior of the ratio and of the anisotropy. We will now see how inclusion of our later data [143] at lower temperatures and the fact that the Fermi surface is not spherical favors the E_{2u} very strongly over the E_{1g}.

2. *Ellipsoidal harmonics: the calculations of Norman and Hirschfeld*

To consider the possible effect of the Fermi surface, Norman and Hirschfeld [36] extended the treatment of Fledderjohann and Hirschfeld [51] by considering an ellipsoidal Fermi surface and linear combinations of gap functions represented by ellipsoidal harmonics up to L = 5. Some of the harmonics used are given in table 6.2. Norman and Hirschfeld also calculated thermal conductivity with Fermi-surface harmonics and tight-binding basis functions which should in principle be more realistic. However, these should only make a difference above the asymptotic (or diagnostic) regime; these calculations will not be discussed here. The ellipsoidal harmonics approach is exactly equivalent to that of Graf *et al.* [52]. Norman and Hirschfeld find that harmonics with L=M all have axial gaps *i.e.* $Y_{LL} = \sin^L\theta$ and therefore the ratio κ_c/κ_b always diverges. Functions with M=0 are all found to possess only line nodes. These lines are not necessarily in the basal plane (as for the polar gap Y_{10}) but can be at a different "latitude" (as for the tropical gap Y_{20} which has two lines at $\theta = 90° \pm 23°$). Figure 6.12 displays the thermal conductivity ratio κ_c/κ_b as a function of reduced temperature for all the harmonics up to L=5 calculated by Norman and Hirschfeld.

The authors note that none of the *pure* harmonics provides a good fit to the experimental data. They therefore investigated mixed solutions in which mixing of the higher harmonic Y_{41} (Y_{52}) with the lowest harmonic Y_{21} (Y_{32}) is included for the E_{1g} (E_{2u}) symmetry. As we saw in equations 2.50 and 2.49 of chapter 2, the gap is in general a linear combination of harmonics (spherical or ellipsoidal). Furthermore, such a linear combinations can also be multiplied by any function of A_{1g} symmetry (*i.e.* *s*-wave) such that the overall symmetry of the state is preserved. The nodal structure of the best fit for both E_{1g} and E_{2u} symmetries is displayed in the right panel of figure 6.10 while figure 6.13 shows the resulting thermal conductivity and anisotropy ratio. The temperature dependence of κ_b/T is well reproduced by both gap symmetries, even though there is no indication of a residual linear term at T=0 in the data such as predicted by the Γ_0=0.05T_c used in the calculation. This good agreement between the E_{1g} and E_{2u} is not surprising as both symmetries have the same nodal structure in this direction. This is not the case for the c-axis, the direction

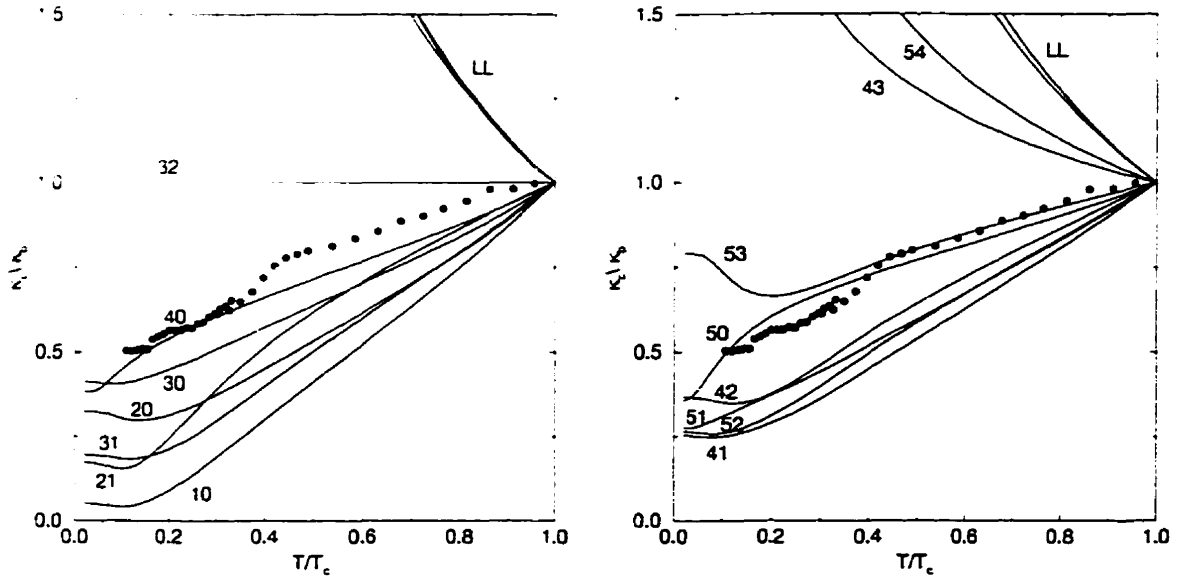

Figure 6.12: Normalized κ_c/κ_b as a function of reduced temperature for various harmonics up to L=5 for ellipsoidal harmonics with a mass tensor anisotropy of 2.8. The curves are labeled by L, M. The scattering rate Γ_0 is $0.1T_c$ in the unitary limit with phenomenological inelastic scattering included (after [36]).

along which the gaps differ. A better agreement is obtained with the E_{2u} curve. The difference in the two gaps is dramatically brought out by looking at the ratio κ_c/κ_b. The data is almost flat and extrapolates to a value of 0.4–0.5 at T=0, as also seen in the recent study by Huxley *et al.* [132], a feature which the E_{2u} gap can easily reproduce, irrespective of Γ_0. On the other hand, the E_{1g} gap above the gapless regime is qualitatively different, being characterized by a smooth extrapolation to zero. If the gapless regime is pushed to even lower temperature by reducing Γ_0 (as seems to be necessary for agreement at the lowest temperatures for κ/T), it does eventually go to zero [36, 51]. We can therefore conclude that the anisotropy of heat conduction favors a hybrid gap of E_{2u} symmetry[1] over one of E_{1g} symmetry for phase B of UPt_3.

Recently, we became aware of very low temperature (down to 15 mK) thermal conductivity data on UPt_3 by Suderow *et al.* [144]. These authors find that $\lim_{T\to 0} \frac{\kappa_b}{\kappa_N} =$ 0.5%. The same limit for the c-axis yields zero intercept. These very low upper

[1] Recall that the A_{2u} gap within weak spin-orbit coupling posseses the same node topology, namely quadratic points at the poles and a line in the basal plane.

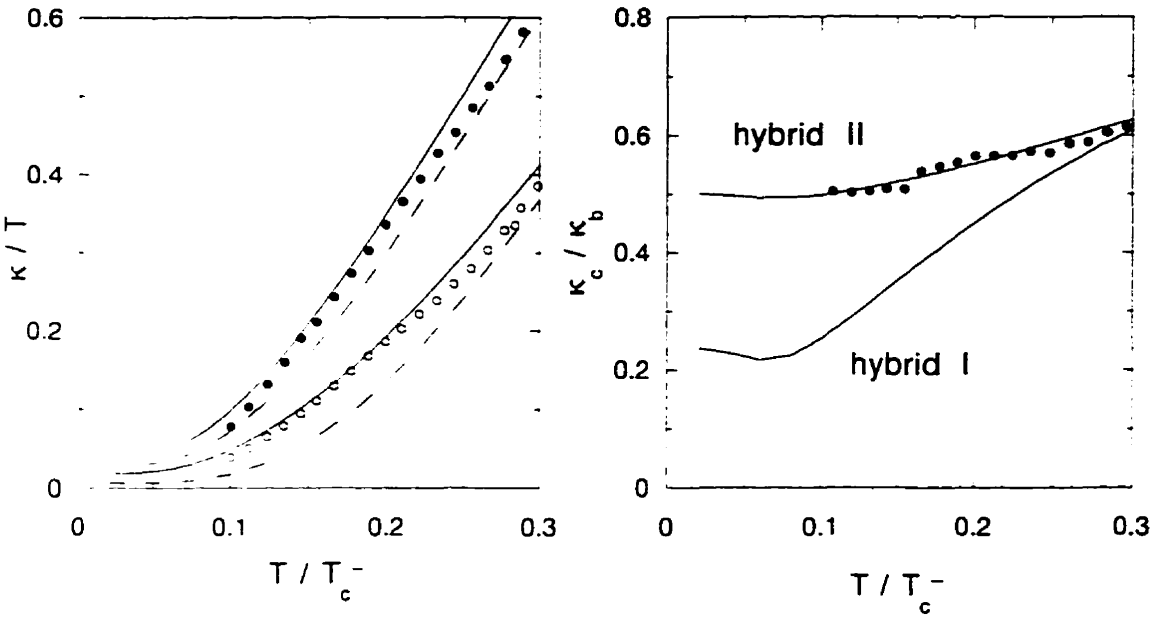

Figure 6.13: κ_i/T (left panel) and κ_c/κ_b (right panel) as a function of reduced temperature for mixed harmonics on an ellipsoid with mass anisotropy of 2.8. In the left panel, the solid (open) circles are for data along the b (c)-axis while the solid (dashed) lines are the theoretical results for the E_{2u} (E_{1g}) gap which correspond to $Y_{32} - 0.2Y_{52}$ ($Y_{21} - 0.15Y_{41}$) (after [36]). In the right panel, hybrid I (hybrid II) refers to E_{1g} (E_{2u}).

bounds on a residual linear term, in perfect agreement with our own data, are difficult to reconcile with values of Γ_0=0.05–0.1T_c in the calculations but are more compatible with a value like $0.01T_c$, namely a factor 20 smaller than what was first estimated by Fledderjohann and Hirschfeld [51] from our normal state thermal conductivity.

3. *The universal regime and normal carriers at $T = 0$*

Graf *et al.* [52, 49] and Norman and Hirschfeld [36] point out that the thermal conductivity ratio at T=0, *i.e.* in the gapless regime, is universal in the case of the E_{2u} gap structure while for E_{1g} this ratio depends on impurity concentration (*i.e.* on Γ_0). In this gapless regime, a new energy scale, γ corresponding to the width of the impurity-induced band, develops and can alter the excitation spectrum near the nodes on the Fermi surface. Instead of removing a node, as would be the case in an extreme case of anisotropic *s*-wave, the impurities can create little regions of normal metal on the Fermi surface leading to a *broadening* of the nodes. In order to distinguish between the E_{2u} and E_{1g} gap *in that regime*, careful thermal conductivity

measurements on crystals with various impurity concentrations would be required at very low temperature. Such studies are not yet available in UPt_3 but the same kind of universal regime can also be investigated in $YBa_2Cu_3O_{7-\delta}$ [49]. Our zinc doping studies on $YBa_2Cu_3O_{7-\delta}$ presented in chapter 7 concentrate specifically on this issue.

4. *An alternative approach: calculations of Moreno and Coleman*

Recently, Moreno and Coleman [145] presented a new approach for calculating the thermal currents in a highly-correlated system. These authors show that the thermal conductivity, like charge conduction, can be regarded as a boundary condition response which is computed as a response to a fictitious gauge field. The authors are not able to reliably reproduce our thermal conductivity results for a polar gap with realistic values of Δ_0/ϵ_F but their approach would seem more promising in the case of the heavy-fermion superconductor UBe_{13} in which the superconductivity develops *before* a Fermi liquid regime has been established (*i.e.* a large Δ/ϵ_F ratio) and where a line node has been suggested to explain NMR measurements [146]. Before ruling out this approach for UPt_3, calculations for the hybrid I and hybrid II gap structures are needed.

6.4 Conclusion

In this chapter, we have presented thermal conductivity results on *one* high-quality single crystal of UPt_3. This is the first conclusive study of anisotropy of thermal conductivity on a heavy fermion superconductor. We conclude that any residual linear term is small (less than 2-3% of the normal state) and that our results are consistent with a scattering rate $\Gamma_0 \sim 0.05T_c$ or less. Such a small scattering rate implies that our results are above the gapless regime and squarely in the diagnostic regime where the data has the power to distinguish between different gap topologies. The main result of our study is the finite ratio κ_c/κ_b as $T \rightarrow 0$. This places severe constraints on the gap structure and allows us to conclude that the gap vanishes at the poles with a quadratic k-dependence as well as along a line of zero in the basal plane, favoring a hybrid II gap structure such as that proposed for the E_{2u} scenario (with strong spin-orbit coupling) of Sauls [31] or the A_{2u} model (with weak spin-orbit

coupling) of Machida *et al.* [83]. We emphasize that ours is the first experimental result that distinguishes between E_{1g} and E_{2u} symmetries, two of the most popular representations for the order parameter.

7

THE THERMAL CONDUCTIVITY OF $YBa_2Cu_3O_{7-\delta}$

The importance of resonant impurity scattering in the cuprates was only realized recently. In this sense, identical theoretical approaches, as those used in UPt_3, may not be as "mature" and detailed comparisons as those made in chapter 6 will not be possible. Furthermore, there are not many detailed experimental verifications of those theories. In this context, our new results on high-quality untwinned single crystals will certainly contribute to the understanding of transport properties in the high-T_c's. We start off this chapter with a review of selected thermal conductivity experiments on sintered, twinned and untwinned $YBa_2Cu_3O_{7-\delta}$ samples at low temperatures. We then present our low temperature thermal conductivity results on untwinned $YBa_2Cu_3O_{7-\delta}$. Using a similar approach as with UPt_3, we will determine the upper bound for the phonon contribution and discuss the possibility of tunneling states as the dominant scattering mechanism. We also discuss the "standard" analysis, namely $\kappa = aT + bT^3$ frequently used in the literature for interpreting thermal conductivity in $YBa_2Cu_3O_{7-\delta}$. From fits to conventional thermal conductivity of phonons with various scattering mechanisms, we will show that an electronic linear term is necessary to account for our data. A discussion of possible specular reflections for phonons is also included as a means of accounting for the large T^3 term that arises from a mixed (phonons + electrons) approach. We then proceed to discuss our measurements in zinc doped a-axis $YBa_2Cu_3O_{7-\delta}$ samples. Discussion with regards to a residual linear term at zero temperature and the possibility of a universal regime will be provided in direct comparison with the paper by Graf *et al.* [49].

7.1 Previous thermal conductivity at low temperature

7.1.1 Results on powdered samples

The earliest papers on sintered samples established the general trend in the thermal conductivity of $YBa_2Cu_3O_{7-\delta}$: a dominant phonon contribution and significant phonon-electron scattering. Subsequent experiments confirmed this behaviour and explored the effects of the role of the microstructure, the effect of oxygen stoichiometry, changes resulting from neutron irradiation, and the very low temperature dependence of the thermal conductivity. In this section, we review only the latter. For a complete review on powdered high-T_c and early results on twinned single crystals, the reader is referred to the extensive review by Uher [109].

In the dilution refrigerator, temperatures can be varied roughly from 5×10^{-4} up to 10^{-2} of T_c. In this temperature range, the thermal conductivity of high-T_c material is expected to be dominated by phonons *i.e.* nearly all electronic carriers should have condensed into the superconducting ground state. In a first measurement, Gottwick *et al.* [147] were able to fit their data remarkably well to $\kappa(T) = aT + bT^3$ with a = 0.16 mW/K^{2}cm and b = 0.47 mW/K^{4}cm. The authors ascribe the linear term to uncondensed quasiparticles and the cubic term to phonon carriers with their mean-free path limited by grain size. Then, they proceed to estimate the fraction of normal carriers resulting from the linear term in the following way: by using the Wiedemann-Franz law, the authors obtain an effective residual resistivity ρ_0^{eff} which they then compare with a linear extrapolation of the normal state resistivity to zero temperature ρ_0^{extr}. The ratio $\rho_0^{extr}/\rho_0^{eff}$ amounts to approximately 15%. Similar trends have been observed by many groups (see the review by Uher [109]). In summary, they all find similar values, namely: $0.092 < a < 0.36$ mW/K^{2}cm and $0.47 < b < 3.60$ mW/K^{4}cm. All these results suggest a normal carrier concentration of approximately 10-15% of the normal state and they seem to establish the presence of uncondensed carriers even at $T_c/1000$. One should note that such an extrapolation fails in good quality single crystals as ρ_0^{extr} can be negative.

7.1.2 Twinned single crystals

Due to their greater structural integrity, single crystals are expected to have a scattering rate smaller than that of their powdered counterparts. This is even more true in the case of phonon heat carriers where previoulsy the mean-free path was limited by grain size, now it will be limited by either the twin boundaries or the sample thickness.

In their early results, Graebner *et al.* [148] find a $T^{1.8}$ dependence to the thermal conductivity down to 30 mK. This approximate power law dependence serves as a basis for their tunneling states model of heat conduction. On the other hand, the results of Sparn *et al.* [149] indicate a thermal conductivity of the form $\kappa(T) = aT + bT^3$ with a = 0.028–0.120 mW/K^{2}cm and b = 1.03–5.50 mW/K^{4}cm for various samples. The T^3 is again attributed to phonons and is enhanced by a factor of approximately 15 over the powdered samples while the T^1 term, again assumed to represent uncondensed quasiparticles is roughly of the same magnitude. The difference in conclusion from both these groups arises from the range over which they both fit their data. Graebner *et al.* [148] fit their $T^{1.8}$ power law from 30 mK up to close to 10 K while the $aT + bT^3$ fit of Sparn *et al.* [149] is valid only up to 300 mK. We will come back to discuss such fits when we present our experimental data in section 7.3.

Later on, Bredl *et al.* [150] measured the heat conduction both parallel and perpendicular to the copper-oxide planes in $YBa_2Cu_3O_{7-\delta}$ ($T_c \doteq 84$ K). In their study, a fit to their data from 0.08 K up to 0.2 K gave a linear term of 0.17 mW/K^{2}cm and a cubic term of 8 mW/K^{4}cm corresponding, according to the authors, to a phonon mean-free path of 0.3 mm (to be compared with a sample thickness of ~0.9 mm). Their results also indicate that a linear term for heat conduction along the c-axis, if present, is at least an order of magnitude smaller than in the basal plane. Furthermore, by applying the internal multilayer (IML) model of Tachiki *et al.* [151], they extract a chain contribution *larger* than the plane contribution and predict a strongly anisotropic thermal conductivity in the plane. Finally, an unpaired carrier concentration of 15%, mostly present in the chains, is obtained within the framework of this model. The anisotropy of the basal plane was investigated at low temperatures by only two groups and these results are the subject of the next paragraph.

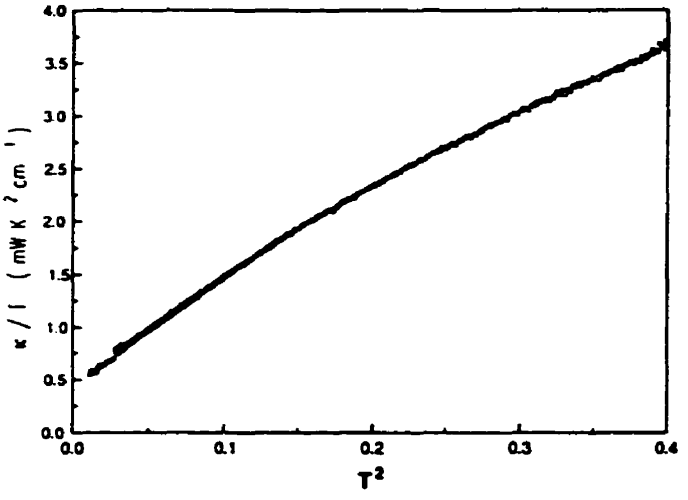

Figure 7.1: The results of Behnia *et al.* [152] for the in-plane anisotropy of the thermal conductivity in $YBa_2Cu_3O_{7-\delta}$. The open circles are for the a-axis while the solid squares are for the b-axis. The results for both directions are exactly on top of each other making it hard to distinguish the individual symbols.

7.1.3 In-plane anisotropy at low temperature

The first low temperature study of the planar anisotropy (or lack of it) came from a collaboration between K. Behnia at Orsay and our group [152]. The crystals were prepared by R. Gagnon in the same way as will be described in section 7.2 and the geometric factors, crucial when studying anisotropy on two different crystals, were obtained from the well-characterized resistivity on the same sample using the same contacts [106]. Behnia *et al.* estimate that an uncertainty of 3% is expected in the anisotropy ratio κ_b/κ_a. They find an isotropic in-plane thermal conductivity with a linear term of 0.47 mW/K^2cm along both directions of the heat current. Their data is shown in figure 7.1. They fit their results with $\kappa = aT + bT^3$ for temperatures lower than 350 mK and a value of b = 10 mW/K^4cm is found and quoted to amount to a mean-free path of 0.3 mm[1]. The isotropy found excludes the attribution of the linear term to the existence of unpaired electron carriers in the chains as postulated by Bredl *et al.* (see previous paragraph). This isotropic regime has not yet been reconciled with the anisotropy in thermal conductivity observed at higher temperature (down to 4 K) [154] and with the results of Zhang *et al.* [155]

[1] A typical crystal thickness of $\sim 100\mu m$ was established later for the crystals grown by R. Gagnon [153].

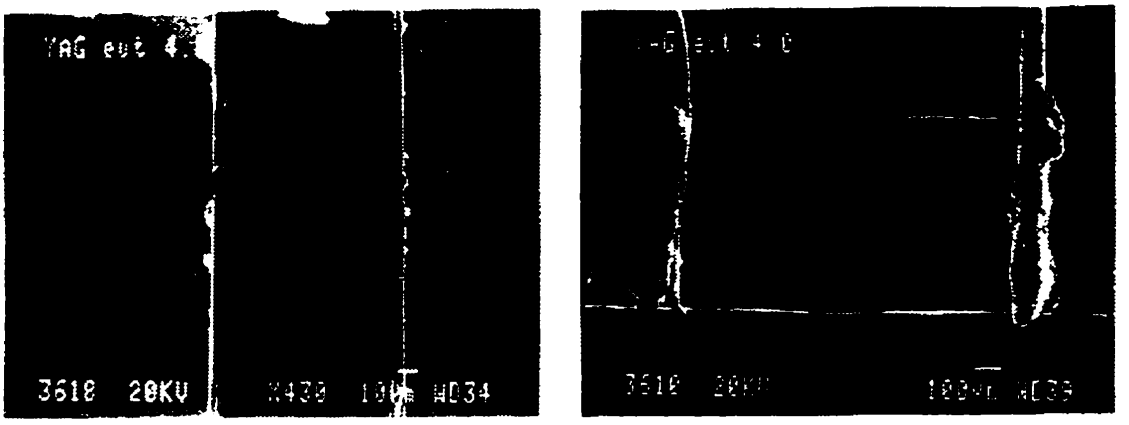

Figure 7.2: Example of a scanning electron microscope picture displaying the geometry of a twinned $YBa_2Cu_3O_{7-\delta}$ sample. The left panel displays the thickness of the sample while the right panel shows a view from the top with both thermometer contacts. Notice the width of the contacts responsible for the uncertainty in the geometric factor.

which show an anisotropic microwave conductivity down to 2 K. This might have to do with a thermal conductivity dominated by an isotropic phonon contribution.

The paper by Wand *et al.* [156] also addresses the question of the anisotropy of the planar conductivity in $YBa_2Cu_3O_{7-\delta}$. Their rather low and broad superconducting transition (T_c = 91 K with $\Delta T_c \leq 1.2$ K) seems to indicate a sample of lower quality than that of Behnia *et al.* (T_c = 93.4 K with ΔT_c = 0.2 K [152]). Furthermore, a large uncertainty of a factor 2 in the geometric factor was a direct consequence of the large contact resistances leading to the inability of measuring the resistivity using the same contacts. Nevertheless, the authors find an isotropic thermal conductivity down to 0.2 K reinforcing the claim of Behnia *et al.* that κ is isotropic in the plane[1].

7.2 Sample characteristics

All $YBa_2Cu_3O_{7-\delta}$ and $YBa_2(Cu_{1-x}Zn_x)_3O_{7-\delta}$ samples were grown by R. Gagnon using a self-flux method (see [106] and references therein), starting with powders of Y_2O_3 (99.9999%), $BaCO_3$ (99.999%), and CuO (99.9999%) mixed in a molar ratio Y:Ba:Cu of 1:18:45. The crystals were grown in yttrium stabilized zirconia (YSZ) crucibles as they are known to contaminate the crystals very weakly (see [106] and

[1] Wand *et al.* seem unaware of the results of Behnia *et al.* and claim that, due to the large uncertainty in their geometric factor, the question of an in-plane anisotropy is still open.

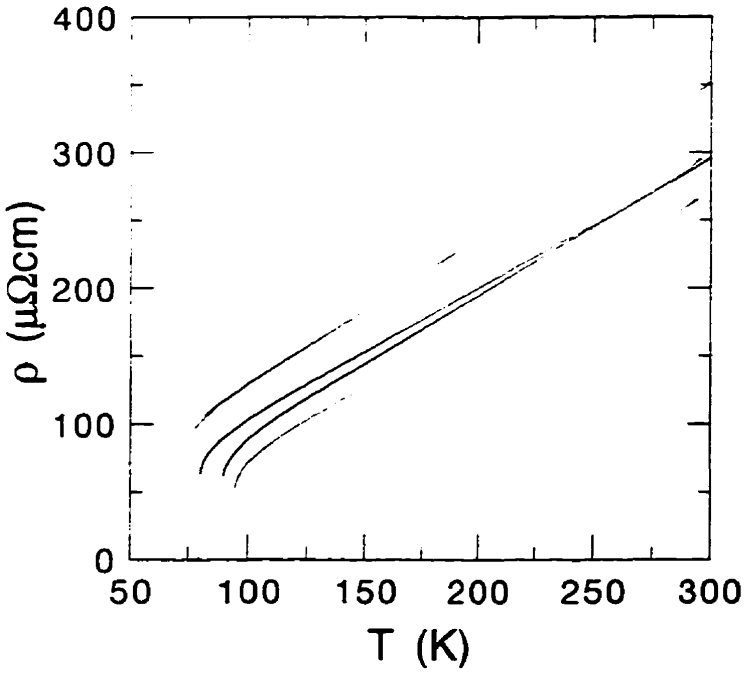

Figure 7.3: Electrical resistivity of detwinned a-axis single crystals (pure and zinc doped). From left to right: 3%, 2%, 0.6% and pure samples. Notice the increase in resistivity and the decrease in the transition temperature with increasing zinc content. All geometric factors were determined using a scanning electron microscope.

references therein). To ensure optimal doping, the crystals were oxygenated for 6 days at 500°C in flowing oxygen gas and quenched at room temperature. Crystals with the most rectangular shapes and without macroscopic defects were chosen for thermal conductivity measurements. The crystals were then detwinned which was achieved by applying a uniaxial pressure of approximately 50 MPa at 550°C in air for less than 30 minutes. Detwinned crystals were then reoxygenated for one day at 500°C. Electrical and thermal contacts on the samples were made, as seen in section 5.3, with silver epoxy, annealed on the crystals at 500°C in oxygen for one hour. Table 7.1 summarizes the characteristics of all $YBa_2(Cu_{1-x}Zn_x)_3O_{7-\delta}$ crystals used in this thesis. Characterization of the samples was done by measuring the resistive superconducting transition with a low frequency resistance bridge (LR-400 or LR-700 from Linear Research). The geometric factors, essential for an absolute comparison between different samples, were obtained using a scanning electron microscope (SEM). An example of a SEM micrograph is shown in figure 7.2 for a twinned $YBa_2Cu_3O_{7-\delta}$

sample, while figure 7.3 shows the resistive superconducting transition of the pure, 0.6%, 2% and 3% zinc doped crystals. Notice the sharpness of T_c which confirms the high quality of the samples and the linearity of the resistivity with temperature. By fitting $\rho = \rho_0 + AT$ above the fluctuation region (*i.e.* above 130 K), we obtain the coefficients ρ_0 and A listed in table 7.1. The dependence of T_c with zinc doping was found to be linear and equal to $\frac{dT_c}{dx}$ =-7 K/% Zn.

Table 7.1: Sample characteristics for the untwinned a-axis zinc doped crystals: x is the nominal zinc content, t is the thickness, w is the width and l is the distance between the voltage contacts, $G = \frac{\ell}{tw}$ is the geometric factor. T_c is the superconducting transition temperature while ρ_0 and A are both extracted from the normal state resistivity (see text).

a-axis zinc doped samples

x (%)	t (μm)	w (mm)	ℓ (mm)	G (m^{-1})	T_c (K)	ρ_0($\mu\Omega$ cm)	A ($\mu\Omega cm K^{-1}$)
0.0	86	0.74	1.3	20585 ± 6%	93.6	-14.5	0.94
0.6	93	0.63	1.2	20415 ± 7%	89.2	-7.5	1.01
2.0	58	0.54	0.7	23154 ± 12%	80.0	10.8	0.94
3.0	69	0.82	1.3	23096 ± 3%	74.6	19.2	1.09

7.3 Thermal conductivity results on pure $YBa_2Cu_3O_{7-\delta}$

Figure 7.4 displays our results for the thermal conductivity over temperature as a function of temperature for the pure (undoped) $YBa_2Cu_3O_{7-\delta}$ a-axis sample.

In this section, we try to ascertain the carriers of heat in the temperature range covered by our experiments, $T \leq 1K$. We show that we cannot account for our results with phonons alone. Then we proceed to analyze our results within the theoretical framework of Graf *et al.* [49] so as to extract the electronic contribution.

7.3.1 Phonons as carriers of heat

1. *Tunneling states*

Early low temperature thermal conductivity in $YBa_2Cu_3O_{7-\delta}$ and $La_{2-x}Sr_xCuO_4$ revealed a T^2 power law dependence (see [109] and references therein). This was

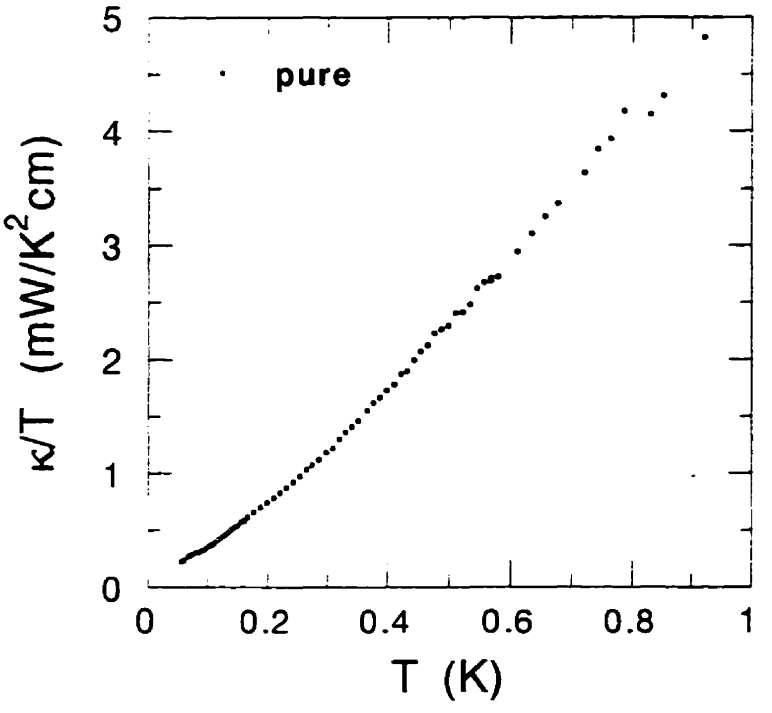

Figure 7.4: Thermal conductivity over temperature versus temperature for the pure sample.

viewed as an indication that the thermal carriers are phonons and that the main scattering mechanism was due to the presence of two-level tunneling systems (TS). It is possible to show that [157]:

$$\kappa(T) = \left(\frac{k_B^3}{6\pi\hbar^2}\right)\left(\frac{\rho v}{\bar{P}\gamma^2}\right)T^2 \tag{7.1}$$

where γ is the TS-phonon coupling constant, v is the phonon mode velocity, ρ is the material density and $\bar{P}$ is the density of TS. Nuñez Regueiro and Castello [157] also give examples[1] of crystalline solids in which TS have been seen to play a major role in the scattering of phonon carriers. These authors postulate that oxygen vacancies, which always exist in these materials, are the most likely candidates for a TS scenario. In fitting their results to equation 7.1, Graebner *et al.* [148] obtain $\bar{P}\gamma^2 = 4.8 \times 10^6$ Jm^{-3}, a value comparable to vitreous silica[2]. Closer inspection of their data reveals systematic deviations from the fit over the whole temperature range.

[1] For example, some materials develop spin-glass characteristics because of magnetic frustration which leads to TS. Examples related to specific materials are given by Nuñez Regueiro and Castello (see [157] and references therein).

[2] This value was obtained using a sound velocity ~7000 m/s. Using the average phonon velocity

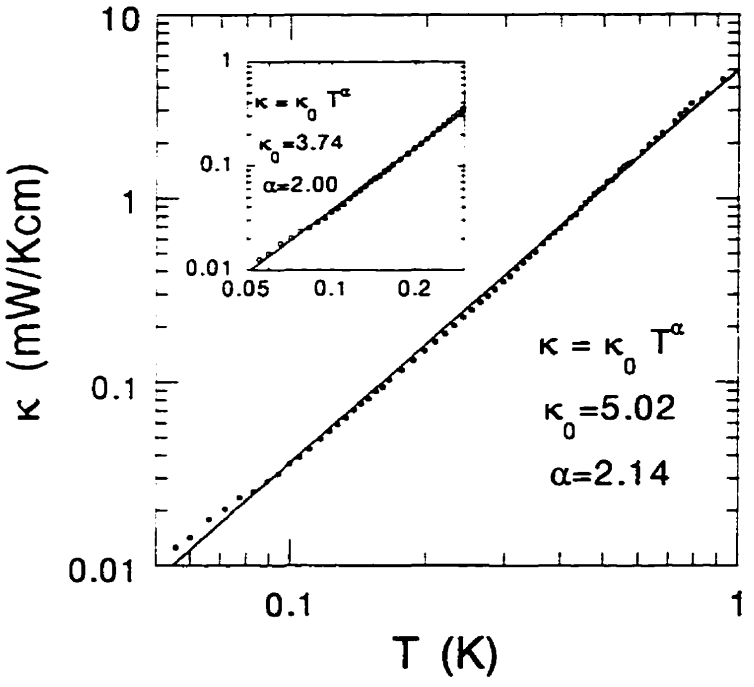

Figure 7.5: Power law fit to the thermal conductivity as a function of temperature. Notice that the exponent found is close to 2. This was taken as evidence for a phonon thermal resistivity dominated by tunneling states (see [157] and references therein). Inset: close-up of low temperature region.

Figure 7.5 shows a log-log plot of our thermal conductivity results with a power law fit. We see that for low temperatures (below T<0.3 K), the power law fits the data fairly well with a quadratic exponent. Using equation 7.1 for our detwinned crystal, we get $\bar{P}\gamma^2 = 8.6 \times 10^5$ Jm^{-3} using v=3977 m/s for the phonon velocity. Our thermal conductivity is about 20 times higher[1] than that of Graebner *et al.* [148] which would mean a TS concentration 20 times lower (assuming the same coupling constant γ for both crystals). This is difficult to reconcile with oxygen vacancies playing the dominant role as the tunneling states since both crystals have approximately the same oxygen content. If one were to believe the TS scenario, a different origin for the tunneling states would have to be invoked. However, the definitive objection to this scenario (only based on power laws) is the sheer magnitude of κ in our crystal

deduced from the elastic constants in Dominec's review paper [103], *i.e.* 3977 m/s, we obtain that $\bar{P}\gamma^2 = 1.7 \times 10^7$ Jm^{-3} for Graebner *et al.*'s crystal.

[1] The fact that our thermal conductivity is significantly larger reflects our higher crystal quality and that our sample is a detwinned single crystal.

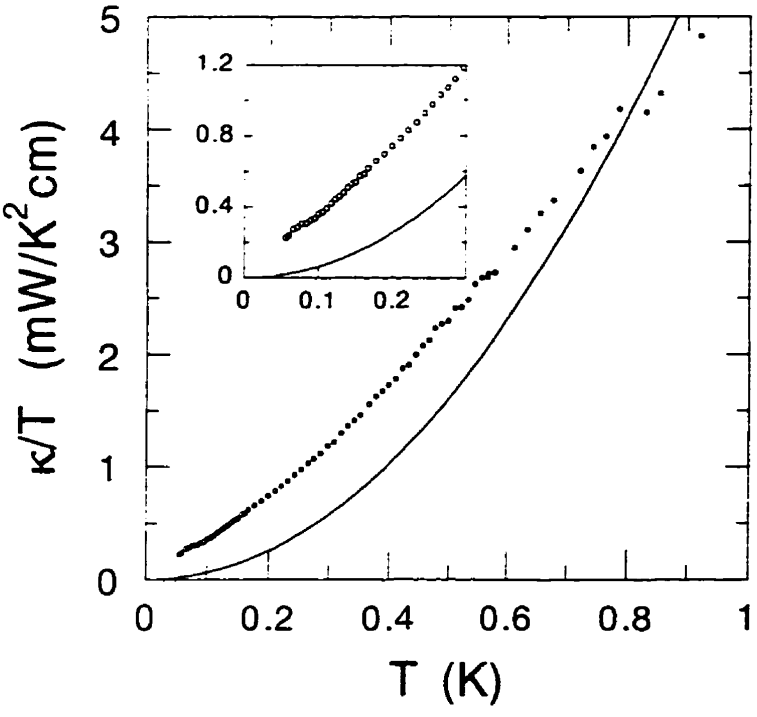

Figure 7.6: Low temperature thermal conductivity over temperature as a function of temperature for the a-axis (open circles) along with the maximum phonon contribution estimated from equation 7.2 with $\kappa_{ph} = 6.43T^3$ mW/Kcm.

which will be shown to be greater than the maximum possible phonon conductivity (in the absence of all scattering except sample boundaries). In light of the systematic deviations over a wide temperature range from the T^2 behavior, we view this approximate power law dependence as arising from a combination of mechanisms other than tunneling states. We therefore abandon this approach and concentrate on the idea whereby both electrons and phonons carry heat with scattering from impurities, electron-phonon, dislocations and sample boundaries.

2. *Expected maximum phonon contribution*

In section 4.1.2, we were concerned with a precise determination of the sound velocities from elastic constants in $YBa_2Cu_3O_{7-\delta}$. In this section, we will use these to put an upper bound on the phonon thermal conductivity.

To estimate this upper bound, we take the measured phonon specific heat coefficient $\beta = 3.84 \times 10^{-3}$ mJ/K^{4}cm^3 (*i.e.* the largest value quoted in the literature,

see section 4.2.1) and the average sound velocity obtained in section 4.1.2, namely v_{ph}=3977 m/s. Then, we take the longest mean-free path possible, namely the sample thickness, 86 μm in the case of the pure a-axis $YBa_2Cu_3O_{7-\delta}$ sample (see table 7.1). We get:

$$\kappa_{ph}/T^3 = \frac{1}{3}\beta v_{ph}\ell = 6.43 \text{ mW/K}^4\text{cm} \tag{7.2}$$

By lumping[1] all numerical constants of equation 2.22 into a single parameter A, and taking $\tau(x) = A$ (equation 2.23 for boundary scattering alone), we get A = 0.25 mW s/K^{4}cm. This number will be used as a reasonable estimate when fitting the thermal conductivity with equation 2.22 when other scattering mechanisms are also present.

Figure 7.6 shows the measured low temperature thermal conductivity for the pure a-axis sample along with the maximum phonon contribution estimated from equation 7.2, which amounts to approximately 35% of the measured κ at 200 mK and 10% at 60 mK. In conclusion, this can either mean two things: (i) we have another conduction mechanism, *i.e.* electrons, with a lower temperature dependence than that of the phonons, or (ii) the phonon mean-free path is larger than the sample thickness as is the case when specular reflections off the crystal boundaries occur. Of course, a combination of the two is possible and we will find that such a possibility explains our thermal conductivity data for zinc-doped samples.

3. *An all phonon conduction?*

In this section, we use a more qualitative argument to reinforce our claim about the presence of quasiparticles at T=0. We proceed by the contrary and show that we need an electronic contribution in our thermal conductivity simply because we cannot fit our results using conventional phonon conduction alone.

With complete disregard for our maximum phonon contribution evaluated above, we calculate a phonon thermal conductivity using equations 2.22 and 2.23 for several values of δ and β and leaving A as an entirely adjustable parameter. Only these two scattering terms were included (in addition to boundary scattering) simply because they have the strongest effect at low temperatures. The value of A was adjusted such

[1] See section 2.1.4 for our choice of units.

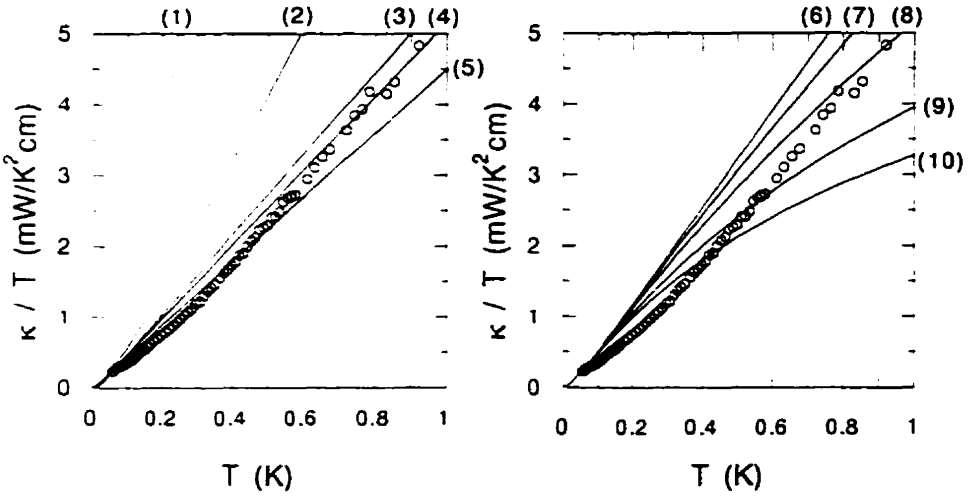

Figure 7.7: A phonon-only fit to the low temperature thermal conductivity of $YBa_2Cu_3O_{7-\delta}$. In the left panel, the scattering term δ is varied for $\beta = 0$. The value of A is chosen such that the curve goes through the experimental point at the lowest temperature. The right panel shows the effect of varying β for $\delta = 10$ with A determined as above. As discussed in section 2.1.4, A is exxpresed in mW s/K^{4}cm, δ in s^{-1}K^{-1} and β in s^{-2}K^{-2}. The parameters are: (1) $A = 3.23$, $\delta = 0$; (2) $A = 6.67$, $\delta = 5$; (3) $A = 15.91$, $\delta = 20$; (4) $A = 21.88$, $\delta = 30$; (5) $A = 63.05$, $\delta = 100$; (6) $A = 9.82$, $\delta = 10$, $\beta = 0.04$; (7) $A = 9.87$, $\delta = 10$, $\beta = 0.4$; (8) $A = 9.95$, $\delta = 10$, $\beta = 1$; (9) $A = 10.16$, $\delta = 10$, $\beta = 2.5$; (10) $A = 10.36$, $\delta = 10$, $\beta = 10$.

that the curve went through the experimental point at the lowest temperature. As we can see from figure 7.7, none of the calculated curves provide a good fit. Basically, we find that, in order to go through the experimental point at the lowest temperature, we need a very large A ($A > 3$ mW s/K^{4}cm, *i.e.* at least 12 times larger than our maximum estimate). This large T^3 term needs to be "brought down" by scattering mechanisms in order to provide an adequate fit at higher temperatures. The large scattering terms then impose a curvature not observed in the experimental data. Another way of saying this is that the $T \to 0$ behavior of κ/T is not T^2 as it must for phonons. We are therefore left with the conclusion that we *need* another conduction mechanism, one which has a weaker temperature dependence than phonons. We conclude that we need an electronic contribution to the heat conduction.

7.3.2 Electronic contribution to thermal conductivity

From our discussion of previous results in section 7.1, the claim that our thermal conductivity results support the fact that there are uncondensed quasiparticles even

at temperatures as low as $T_c/1000$ does not seem very novel. My claim is that the conclusion reached by previous authors was based on an invalid analysis of their data.

Table 7.2: Selected results of a standard analysis $\kappa = aT + bT^3$ for thermal conductivity in powders, twinned and untwinned samples of $YBa_2Cu_3O_{7-\delta}$. In the case of the results of Bernasconi *et al.* [158], the phonon mean-free path ℓ (mfp) is taken as the quoted grain size and the phonon velocity is taken to be 2862 m/s (see section 4.1.2). For Behnia *et al.* [152, 159], no sample dimension was available and therefore a generic thickness of $\sim$ 100 μm was used for the phonon mfp. In the case of Bredl *et al.*, we use the sample dimensions quoted in their paper [150]. The a and b values are taken from fits of the form $\kappa = aT + bT^3$ quoted in the respective papers. The temperature range over which these fits are valid are included when available. For the estimates of the phonon thermal conductivity in crystals, an average velocity of v_{ph}=3977 m/s is used. For both powders and crystal, the phonon specific heat is taken to be β=0.4 mJ/molK^4 = 3.84×10^{-3} mJ/K^{4}cm^3.

Type	a (mW/K^{2}cm)	b (mW/K^{4}cm)	T-range	ℓ (μm)	κ_{ph}/T^3 (mW/K^{4}cm)	reference
powders	0.28	1.4	$T < 0.3K$	20	1.08	[158]
powders	0.17	2.5	$T < 0.3K$	150	8.07	[158]
twinned	0.17	8.00	$0.08 < T < 0.20K$	900	67.3	[150]
twinned	0.32	6.20	$0.18 < T < 0.35K$	100	7.48	[159]
detwinned	0.47	10.0	$0.10 < T < 0.35K$	100	7.48	[152]
detwinned	0.43	8.52	$0.21 < T < 0.35K$	86	6.43	this work
detwinned	0.19	16.6	$0.05 < T < 0.14K$	86	6.43	this work

1. *A standard analysis*

Figure 7.8 presents the usual analysis used until now as applied to our own data (see for example [109]). Line (1) is fitted for temperatures lower than 140 mK, while line (2) is for the range $210 < T < 350$ mK, and the results are displayed in table 7.2 along with previous results on powders, twinned and detwinned samples. We see that our "high" temperature fit agrees well with the results of Behnia *et al.* [152] on detwinned crystals but not our "low" temperature fit (done in a temperature range not measured by Behnia *et al.*). For our "low" temperature fit, our results for parameter a are closer to what is observed in twinned and sintered samples but our term b is significantly larger. Furthermore, for detwinned samples, the b-term obtained from such analysis is always *larger* than the estimated maximum phonon contribution. We conclude that such linear extrapolations over a reduced temperature range do *not* provide an adequate representation of the data. The restricted temperature ranges used are simply a reflection of a changing slope as a function of temperature. Also,

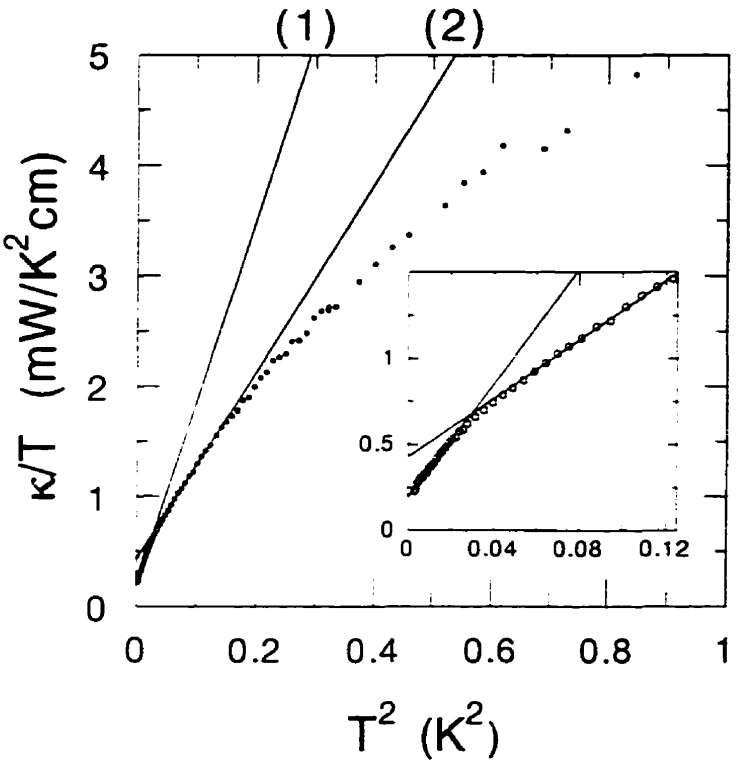

Figure 7.8: Conventional analysis of $YBa_2Cu_3O_{7-\delta}$ thermal conductivity: κ/T vs T^2. Line (1) is fitted fo $T^2 < 0.025$ and line (2) for $0.045 < T^2 < 0.125$. Notice that both fits describe the data over a small temperature range.

we would like to point out that the agreement between our a-term extracted from the "low" temperature fit and the results on powders is likely coincidental. We will therefore adopt a mixed approach in which we consider an electronic linear term and where we treat the phonons using the standard formalism outlined in section 2.1.4.

2. *A mixed approach*

A more reasonable description over a wider temperature range might be obtained if we use equations 2.22 and 2.23 for the phonon conduction combined with an electronic linear term κ_e/T. Having performed this, we show our best fit in figure 7.9 with again only the δ and β as scattering terms. We computed equation 2.22 for several values of δ and β for a fixed A. Then, we varied the linear term from 0 to 0.25 mW/K^2cm adjusting A such that the calculated curve passed through the experimental point at the lowest temperature.

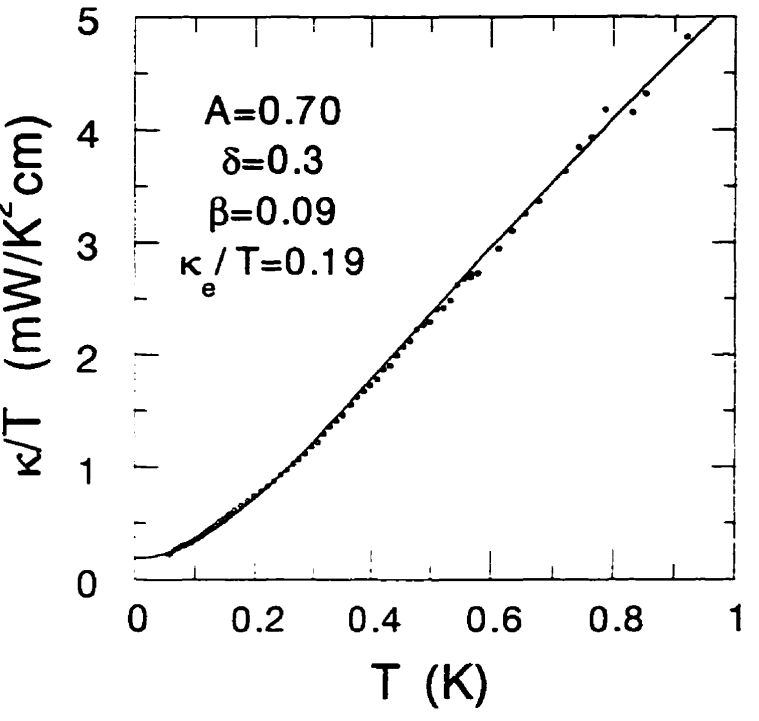

Figure 7.9: Mixed analysis for the pure sample. Notice that the A term is 2.8 times larger than the estimated maximum value.

We immediately see that this fit provides an adequate description of the data over the whole temperature range with only very small systematic deviations from the measured curve. More quantitatively, we have A=0.7 mW s/K^{4}cm, *i.e.* some 2.8 times larger than our maximum estimate for the phonon contribution and κ_e/T = 0.19 mW/K^{2}cm, *i.e.* approximately 2.5 times smaller than the extrapolated result of Behnia *et al.* [152]. On the other hand, the linear electronic term thus obtained comes very close to the value predicted by the theory of Graf *et al.* [49] for $YBa_2Cu_3O_{7-\delta}$, namely 0.11–0.14 mW/K^{2}cm. We will discuss in greater detail the theory of Graf *et al.* in section 7.4. Due to the significant discrepancy in A with what we estimated in section 7.3.1, we searched for mechanisms that could possibly increase the phonon mean-free path such that it could become a few times larger than the sample thickness. Such a mechanism exists and is discussed below.

3. *Specular reflections*

Specular reflections on the crystal faces can lead to a phonon mean-free path *larger*

than the sample dimensions. It is possible to show (see [160, 161]) that if F is the fraction of collisions that are diffuse and therefore 1 - F represents the fraction of specular reflections, the mean-free path is increased by a factor (2-F)/F. Whether a surface appears rough or smooth to phonons depends on the size of the asperities and the phonon wavelength, meaning that F is temperature dependent. Berman *et al.* [160] measured thermal conductivity in diamond at helium temperatures. For temperatures below 6 K, they find a variation proportional to $T^{2.8}$ which means that the mean-free path is temperature dependent[1]. In modeling their results to account for specular reflections, these authors deduce F = 0.5–0.6 which, at 3 K translates into a mean-free path 2.5 times their sample size. In another study, Berman *et al.* [161] find a T^3 thermal conductivity for sand-blasted sapphire crystals with a mean-free path equal to the size of the crystal. Polished crystals did not yield a T^3 relationship but had a phonon mean-free path dependent on temperature which grew as large as 3 times the crystal diameter. From these studies, one concludes that maximum phonon mean-free paths of 2-3 times[2] the sample size can arise from perfectly reflecting sample surfaces.

Although tempting as an explanation of our large T^3 phonon term in our fitted thermal conductivity, we point out that our crystal does not quite fulfill the criteria of well-polished surfaces. When looking at our samples under a microscope with only 50X magnification, we can see growth steps on the (001) surface of pyramidal structure with spiral morphology. Such growth steps were first noticed by Sun *et al.* [162] and extend over the whole sample surface on *one* side only[3] with sizes varying from sub-micron to several tens of microns. Inspection of the other surface at the same magnification reveals no such steps and the surface is mirror-like. Therefore, the phonon mean-free path could be at most twice the sample thickness since reflections would be specular on one face and diffuse on the other.

We conclude that the mixed approach provides a satisfactory fit to the thermal

[1] The T^3 regime is well established in the specific heat at these temperatures and therefore any temperature dependence other than T^3 has to be ascribed to a changing mean-free path.

[2] This number could be larger at lower temperatures as Berman *et al.* only went down to 3 K.

[3] According to R. Gagnon [153], the largest $YBa_2Cu_3O_{7-\delta}$ (and without flux spots) flux grown crystals grow at the liquid-air interface. This results in a smooth surface (for the surface in the flux) and a rough surface (for the surface exposed to air).

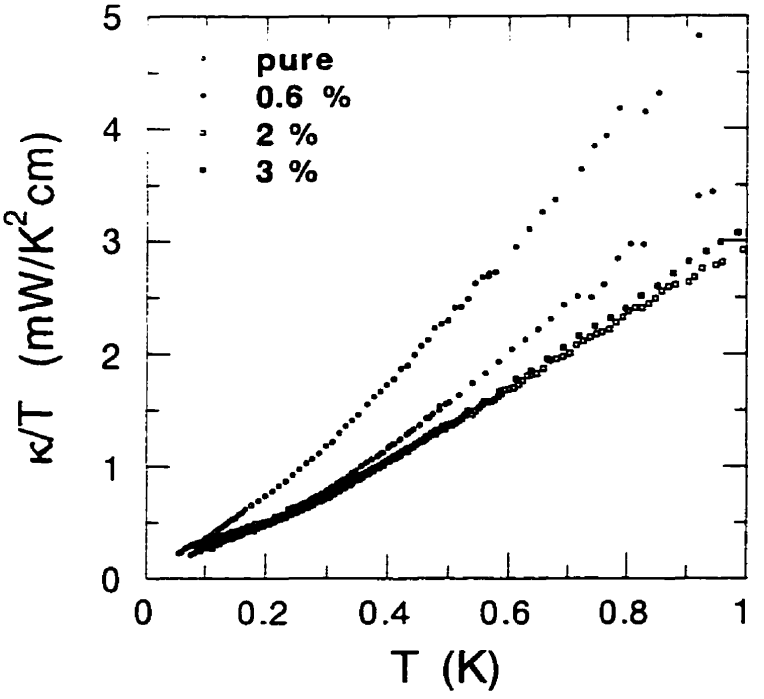

Figure 7.10: Thermal conductivity over temperature for the zinc doped samples. Notice the rapid suppression in going from the pure to the 0.6% sample and then the saturation at higher concentrations.

conductivity of the pure sample. This approach will therefore be extended to zinc doped samples in order to study the universal regime.

7.4 Thermal conductivity results on $YBa_2(Cu_{1-x}Zn_x)_3O_{7-\delta}$

Figure 7.10 shows our results for the four samples measured, namely the pure and the 0.6%, 2% and 3% zinc-doped samples (all nominal concentrations). Notice that at 1 K, the pure sample has a thermal conductivity roughly 40% greater than the 0.6% and some 60% larger than the 2 and 3% samples. The rapid suppression of the thermal conductivity with small zinc concentration and saturation for large zinc content is reminiscent of what happens at high temperature for the peak height (see section 4.2.1). In this case, we remind the reader that the rapid suppression was interpreted in terms of the electronic mean-free path being rapidly reduced by the low concentrations of zinc impurities while for higher concentrations the phonons dominated κ and were much less affected.

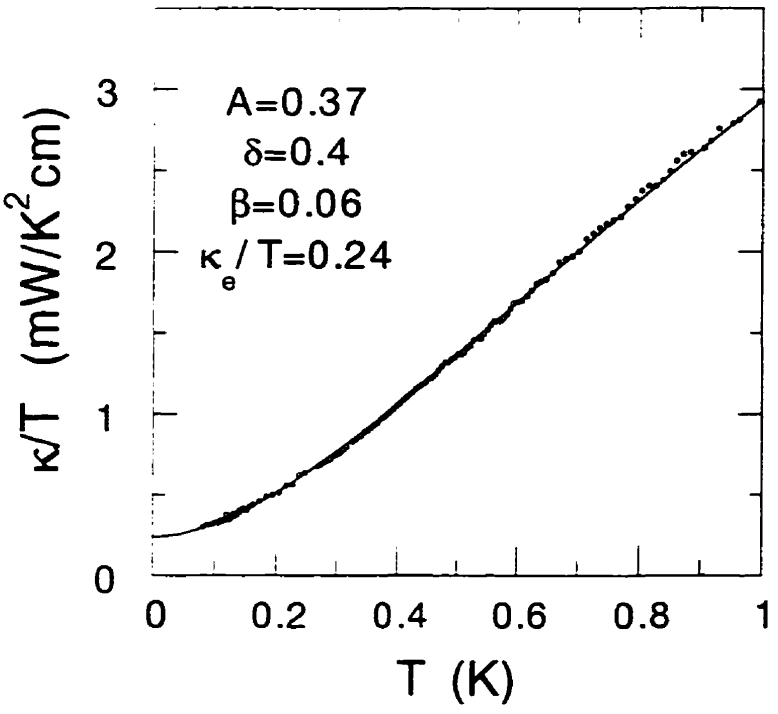

Figure 7.11: Mixed analysis for the 2% sample. Notice that the A term is 2.2 times larger than estimated.

As with the pure sample, an all phonon fit was not possible and we therefore need an electronic term. Such unsuccessful fits will not be discussed here as they yield similar results as those of section 7.3.1. Therefore we adopt the mixed approach explained above and include a linear electronic term along with equation 2.22 for our phononic conduction. The result of such a fit is displayed in figure 7.11 for the 2% sample. The fit accounts very well for the data over the whole temperature range with some negligible systematic deviations. Table 7.3 summarizes the results for all three zinc doped samples.

As with the pure sample where the A term was some ? times larger than expected from our estimate of the average sound velocity, in all three zinc doped samples, this term is again about twice as large as our estimate. This factor 2 comes in naturally if we assume that we have specular reflections on *one* face only as inferred from the presence of growth steps on one side. The linear term obtained from such fits is fairly robust and we estimate that the error on this term is at most ± 0.01.

The parameter δ includes the effects of the strain field of dislocations (δ_{dis}) and

Table 7.3: Fit parameters used in the mixed (electrons+phonons) fitting approach. Refer to section 2.1.4 for the definition of the terms A, δ and β. κ_e/T is the electronic residual linear term. Note that the values of A are about twice as large as A^{vel} calculated from sound velocities and scaled by the sample thickness.

sample	A (mW s/K^{4}cm)	δ ($s^{-1}K^{-1}$)	β ($s^{-2}K^{-2}$)	κ_e/T (mW/K^{2}cm)	A^{vel} (mW s/K^{4}cm)	A/A^{vel}
pure	0.70	0.3	0.09	0.19	0.25	2.8
0.6%	0.5	0.6	0	0.15	0.27	1.9
2%	0.37	0.4	0.06	0.24	0.17	2.2
3%	0.46	0.8	0.02	0.18	0.20	2.3

electron-phonon coupling (δ_{e-ph}). In looking at table 7.3, we cannot find any systematic way to account for the increasing number of electrons with doping and, possibly, the increasing number of dislocations as well. This conclusion applies also to the sheet-like faults term β where no correlation can be drawn with zinc doping. We also would like to emphasize that the apparent decrease in the magnitude of thermal conductivity with increasing zinc content (in going from the 0.6% to the 3%) can be almost entirely attributed to the sample thickness which affects the A term only. We also draw the readers attention to the fact that the 2% sample has an unusually high electronic term. We cannot account for such a discrepancy: using our resistivity measurements, we know that the zinc content of the sample does not seem to be very far off.

7.4.1 *Comparison with theory: the calculations of Graf et al.*

In chapter 6, we briefly discussed the question of a universal regime with respect to the calculations of Graf *et al.* [49]. In the same paper, on top of their analysis for the various gap structures in UPt_3, they provide thermal conductivity calculations for the $d_{x^2-y^2}$ gap structure believed to account for many properties of $YBa_2Cu_3O_{7-\delta}$. Recently, similar theoretical results were also obtained by Hirschfeld and Putikka [50].

We recall that for a clean superconductor with an order parameter that vanishes along a line on the Fermi surface, the density of states is linear in excitation energy.

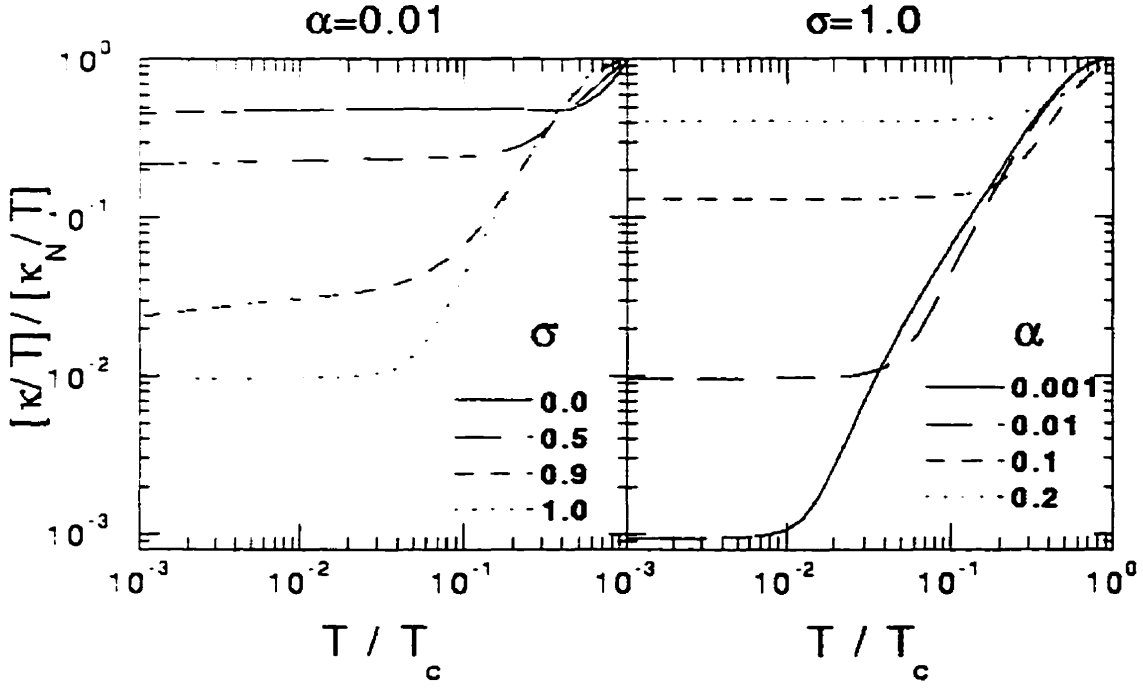

Figure 7.12: Normalized thermal conductivity over temperature as a function of reduced temperature for different phase shifts (left panel) and different scattering rates in the unitary limit (righ panel) (after 49).

In the presence of impurities, a new energy scale γ develops below which the density of quasiparticles is constant and non-zero at zero energy. This can be viewed as a broadening of a node by impurities. Therefore, if the role of the impurities was solely to act as pair breaking, the thermal conductivity should increase. On the other hand, adding impurities also reduces the electronic mean-free path as evidenced by the increased residual resistivity. It turns out that for the $d_{x^2-y^2}$ gap in $YBa_2Cu_3O_{7-\delta}$ and the E_{2u} gap in UPt_3, the increase in quasiparticles arising from the pair breaking action of the impurities is *exactly* compensated by the decrease in the electronic mean-free path (for $\Gamma \ll \Delta_0$). Hence the name universal heat conduction.

In calculating the electrical conductivity (for $\omega \to 0$) and the thermal conductivity, these authors find that the Wiedemann-Franz law is obeyed for $k_BT \ll \gamma$, namely $\lim_{T\to 0} \frac{\kappa}{T} = \sigma_0 L_0$=0.12–0.15 mW/K^{2}cm where we have used the residual conductivity of 0.5–0.6 $(\mu\Omega\text{m})^{-1}$ measured by Bonn *et al.* [112] which agrees perfectly with the theoretical estimate of Graf *et al.* [49] (0.11–0.14 mW/K^{2}cm). We note that this residual conductivity value was obtained from a somewhat high temperature ($T >$

$1K$) on a pure crystal. Recall that from our pure and zinc doped crystals we deduced $\lim_{T\to 0}\frac{\kappa}{T}$=0.15–0.24 mW/K^{2}cm.

Graf *et al.* [49] use a similar formalism already applied for UPt_3 to calculate the thermal conductivity on a cylindrical Fermi surface for a two-dimensional superconducting gap of the form $d_{x^2-y^2}$ for elastic scattering only. Their results are shown in figure 7.12. The parameter $\alpha = 1/(2\pi T_{c0}\tau_0)$ is a measure of the scattering rate (with T_{c0} the superconducting transition and τ_0 the scattering time) while $\tilde{\sigma} = \sin^2\delta_0$ is the normalized cross section and δ_0 is the scattering phase shift. The Born approximation, as we discussed in chapter 2, does not give a good description of the data because of the large intercept at T=0 and we need to appeal to the resonant impurity scattering limit. This is what is shown in the left panel of figure 7.12 where $\alpha = 0.01$ and the phase shift is varied. The right panel of figure 7.12 shows the dependence on α. Using the results of Ong [115] we can deduce a $\tau_0 = 3 \times 10^{-12}$ s which combined with T_c=93.6 K yields $\alpha = 0.004$. This estimate implies that the universal regime is well established at 1 K for *all* samples, including the pure crystal. This results in a constant κ_e/T all the way to 1 K, as we found in our mixed approach. We therefore conclude that the theoretical framework of Graf *et al.* provides an excellent description of our experimental data.

7.5 Conclusion

In this chapter, we presented a systematic study of thermal conductivity for a-axis $YBa_2(Cu_{1-x}Zn_x)_3O_{7-\delta}$ samples at low temperature. We demonstrate the existence of a universal electronic contribution at $T \to 0$ in excellent quantitative agreement with current theories for a *d*-wave gap [49]. We showed that a conventional analysis of the type $\kappa = aT + bT^3$ in $YBa_2Cu_3O_{7-\delta}$ is not adequate and we provided a way to account for the zinc-doped crystals results over the whole temperature range covered by our experiments. For $YBa_2(Cu_{1-x}Zn_x)_3O_{7-\delta}$, a constant electronic linear term up to 1 K is found to be consistent with our results. As to the phonon contribution, a satisfactory quantitative explanation is obtained in terms of scattering by the boundaries and by invoking specular reflections on one side of the crystal.

8

MAGNETISM AND SUPERCONDUCTIVITY IN UPt_3

Besides the thermal conductivity results which occupied most of my time during my Ph. D., other areas of research were also explored: X-ray studies to search for the structural modulation in UPt_3, application of uniaxial stress at dilution refregirator temperature measurements of thermal conductivity in $YBa_2Cu_3O_{7-\delta}$ in high magnetic field, and neutron scattering studies. In this chapter, we choose to include our neutron diffraction results as they have direct implications on current theories of the phase diagram. This chapter is a slightly more detailed version of our published paper [163]. A brief review of relevant theoretical and experimental results will be presented. The implications of our results for the current theories of the phase diagram will also be discussed.

8.1 A brief experimental and theoretical review

Most of the heavy fermion superconductors order antiferromagnetically before the onset of superconductivity, with $T_N \simeq 10\ T_c$. The possible relation between the phenomena is one of the central issues in the field. However, no two compounds have exactly the same magnetic behavior. While both UPt_3 [68] and URu_2Si_2 [164, 165] show an extremely small ordered moment, of order 0.01 μ_B/U atom, it is as large as 0.85 μ_B/U atom in UPd_2Al_3 [166]. The specific heat anomaly at T_N is large in URu_2Si_2 [167], yet absent in UPt_3 [168]. The ordered structure breaks the hexagonal symmetry in UPt_3 and UPd_2Al_3, with the moments aligned in the basal plane, while the tetragonal symmetry of URu_2Si_2 is preserved. The magnetic order and fluctuations are unaffected by the onset of superconductivity in UPd_2Al_3 [169, 170], while a slight decrease in the amplitude of the moment is observed in UPt_3 [92, 93] and a saturation of the moment in URu_2Si_2 [171].

The coexistence of magnetism and superconductivity in these compounds has been viewed as evidence for an unconventional pairing mechanism. Unlike the Chevrel phases, where the electrons responsible for the superconductivity are distinct from those responsible for the magnetism, it appears that in the case of UPt_3, in particular, the same electrons participate in both phenomena. Indeed, in this material a division of labor is implausible in view of the presence of the f-electrons at the Fermi level and the fairly uniform effective mass around the Fermi surface [65, 66].

The unconventional nature of the superconducting state in UPt_3 is most strikingly manifest in the existence of several superconducting phases (see chapter 3). The magnetic field (H)-pressure (P)- temperature (T) phase diagram shows two distinct transitions at T_{c+}=0.5 K and T_{c-}=0.44 K for H=P=0 [70]. Application of a magnetic field in the basal plane ($\vec{H} \perp \hat{c}$) brings the two transitions together at a tetracritical point [172], which shows up clearly on the H_{c2}(T) line as a kink at a field H^* of about 0.4 Tesla [173, 55]. Hydrostatic pressure also causes T_{c+} and T_{c-} to merge, at a critical pressure of about 3.7 kbar [74]. A complete theory for the phase diagram of UPt_3 has been one of the major pursuits in the field over the past five years. As discussed in chapter 3, two types of scenarios are currently debated: in the first type, the proximity of T_{c+} and T_{c-} is considered accidental and the two zero-field phases are attributed to different representations of the order parameter [174, 78, 175]. In the second type, the double transition is viewed as a splitting resulting from the lifting of the degeneracy of a state (within a single representation for the order parameter) by some symmetry-breaking field [81, 80, 82, 31, 90, 87, 176]. An obvious choice for such a field is the antiferromagnetic order, with its moment and propagation vector both lying in the basal plane ($\vec{M}_s \parallel \vec{q} \parallel \hat{a}^*$). The moment configuration has been described so far in terms of a single-$\vec{q}$ structure with a given sample in general possessing three equivalent domains [92, 93, 79]. However, the existing data is also compatible with a triple-$\vec{q}$ structure.

In their neutron study under pressure, Hayden *et al.* [79] found that the antiferromagnetic moment of UPt_3 is fully suppressed by applying 3 to 4 kbar, which is also the critical pressure for the merging of T_{c+} and T_{c-}. The parallel disappearance of magnetism and phase multiplicity under pressure is strong evidence in favor of the

coupling scenarios (the second type), with the antiferromagnetic order acting as the symmetry-breaking field. Within the coupling scenarios, the kink in the H_{c2} curve is basically the result of a sudden reorientation of the (vector) order parameter $\vec{\eta}$ in the basal plane [81, 80, 82]. Both the moment $\vec{M}_s$ and the field $\vec{H}$ will couple to $\vec{\eta}$, each trying to align it in the minimum energy direction. Without loss of generality, let us consider the case of $\vec{M}_s \perp \vec{H}$, with both couplings to $\vec{\eta}$ favoring *parallel* alignment. At low fields, the coupling to the magnetic order dominates and $\vec{M}_s$ determines the orientation of $\vec{\eta}$. Then, when the field is increased to the point where its coupling dominates, a reorientation of $\vec{\eta}$ occurs, causing a kink in $H_{c2}(T)$. Of course, if the field direction is instead made parallel to $\vec{M}_s$, no kink is predicted, since there is no competition between the two couplings. As a result, within a single antiferromagnetic domain (assuming a single-$\vec{q}$ structure for the magnetic order) the upper critical field in the basal plane of UPt_3 is predicted to show a sharp kink only for one direction of the field (say $\vec{H} \parallel \hat{a}$), and no kink for the $\hat{a}^*$ direction 90° away [81, 80, 82]. Experimentally, however, a kink is observed at $H^* \approx 0.4$ Tesla for any high-symmetry direction (0°, 90°, 120° relative to $\hat{a}$) [177]. The theory can be reconciled with a ubiquitous kink by supposing that the moment is not fixed to the lattice but rather follows the field in such a way that $\vec{M}_s \perp \vec{H}$ for all field orientations in the basal plane. This is possible provided the in-plane magnetic anisotropy energy is negligible compared to the Zeeman energy acting on $\vec{M}_s$. Sauls [89] showed that a rotation of $\vec{M}_s$ in the basal plane is accompanied by a modulation of its amplitude M_s with 60° periodicity, which in turn causes $H_{c2}(\theta)$ to exhibit 60° oscillations, such as those observed recently in UPt_3 [135]. The first goal of our experiment was to determine whether a magnetic field lower than one Tesla can indeed cause the magnetic moment to rotate in the basal plane away from its zero-field configuration ($\vec{M}_s \parallel \vec{q} \parallel \hat{a}^*$) and remain perpendicular to $\vec{H}$.

If the magnetic ground state of UPt_3 has only one propagating vector (single-$\vec{q}$), as assumed until now by all authors [68, 92, 93, 79], then there should in general be 3 independent domains with $\vec{M}_s$ oriented at 120° with respect to each other. Agterberg and Walker [178] have recently considered the effect of having 3 possible domains on the H_{c2} curve of UPt_3 in the basal plane. They assume that $\vec{M}_s$ is fixed with

respect to the crystal lattice (i.e. parallel to any one of the 3 a*-axes), but that only the most thermodynamically stable domain will be populated for any given field direction. Within the coupling scenario, the implications are fairly straightforward: the angle between $\vec{M}_s$ and $\vec{H}$ can only range over $\pm 30°$ and the domain selection by the field as it is rotated causes a 60° variation in $H_{c2}(T)$. The limited range of angles could perhaps explain why a straight H_{c2} curve is never observed. The second goal of our experiment was therefore to establish whether a magnetic field of less than one Tesla can select a single domain.

8.2 Neutron diffraction: experimental aspects

Due to its magnetic moment, energy and wavelength, the neutron is a unique probe of magnetism on an atomic scale: neutrons can be scattered by the magnetic moments associated with unpaired electron spins in magnetic samples. In this section, we present the experimental details associated with our neutron diffraction experiments on UPt_3 for which the results will be presented in section 8.3.

The triple-axis spectrometer provides the preferred diffraction geometry for single-crystal neutron diffraction experiments. The three axes are those of the monochromator, the sample and analyser crystal. Each of these needs to be automatically controllable. For this purpose all moving parts rest on air-cushion tables and are computer controlled from a distance.

Our experiments were done with the DUALSPEC triple axis spectrometer at the NRU reactor at Chalk River Laboratories. With this instrument, it is possible to perform many types of experiments *i.e.* elastic and inelastic scattering, and polarized neutron studies all at cryogenic temperatures in the presence of a magnetic field either parallel or perpendicular to the scattering plane. A schematic diagram of a triple-axis spectrometer is shown in figure 8.1. The reader is referred to C. G. Windsor's chapter in the book Methods of Experimental Physics [179], which discusses the numerous applications of triple-axis spectrometers along with the components of neutron beam experiments. We now proceed to discuss some of the relevant parts of the triple-axis spectrometer.

1. *Monochromator and analyzer.* The monochromator crystal is used to select

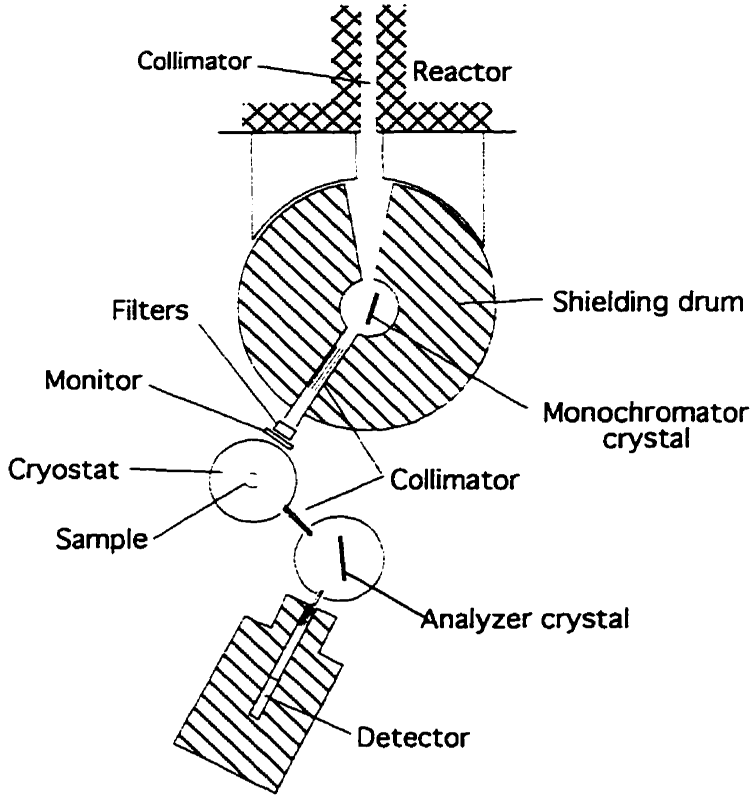

Figure 8.1: Schematic diagram of a triple-axis neutron spectrometer, after [179].

a particular wavelength. The mean wavelength selected, λ, depends on the scattering angle (θ_m) and on the crystal plane spacing (d_m) according to Bragg's law:

$$\lambda = 2d_m \sin\theta_m \tag{8.1}$$

In elastic magnetic scattering experiments (such as those described in section 8.3), the analyzer crystal is tuned to the same wavelength (or energy) as the monochromator. In our case both the analyzer and the monochromator consisted of pyrolytic graphite and the neutron wavelength was chosen at 2.37 Å. A combination of a bent focussing silicon monochromator and graphite analyzer was also tried but gave a slightly lower flux and therefore was abandoned.

2. *Collimation.* The simplest collimators consist of a long rectangular tube lined with absorbing material. Better collimation can also be achieved by use of

Soller collimators which are simply a large number of parallel slits included in the beam guide. In order to have the largest neutron flux, we chose the largest collimation available. It was 0.6 degree between the monochromator and sample and 0.8 degree between sample and analyzer.

3. *Filters.* The filters' main purpose is to remove the thermal neutrons with wavelength greater than the Bragg cut-off. These neutrons can lead to an increase in background and therefore longer counting time would be needed. Use of a cooled beryllium filter with a cut-off at 3.97 Å was made. Furthermore, a pyrolytic graphite filter was also used to remove second-order scattering (or $\lambda/2$ neutron wavelengths) from the crystal monochromator. The filter is oriented to provide maximum scattering of the second-order reflected neutrons. Since antiferromagnetic Bragg peaks occur at half integer Miller indices, contamination from $\lambda/2$ neutrons could show up at these positions and cause increased background.

4. *Monitor.* The purpose of the monitor is to provide a signal proportional to the number of neutrons that pass through it. Due to variation in the neutron flux from the reactor, counts were integrated over fixed monitor counts as opposed to fixed time intervals.

5. *Cryostat.* The cryostat consisted of a continuous flow helium cryostat with a base temperature of approximatly 1.6 K. The cryostat was also equiped with a horizontal field magnet that could provide horizontal fields of up to 3.2 Tesla at any angle in the scattering plane.

6. *Sample.* The sample, used in previous neutron experiments [79], was a high-quality single crystal of UPt_3 that exhibits two sharp successive superconducting transitions, a moment of 0.03 μ_B/U atom and a Néel temperature of approximately 6 K. It was aligned with its hexagonal plane in the scattering plane of the spectrometer. The sample was held in place by means of thin aluminum foil. Thermal contact was insured by the continuous flow of helium gas in the pumped cryostat.

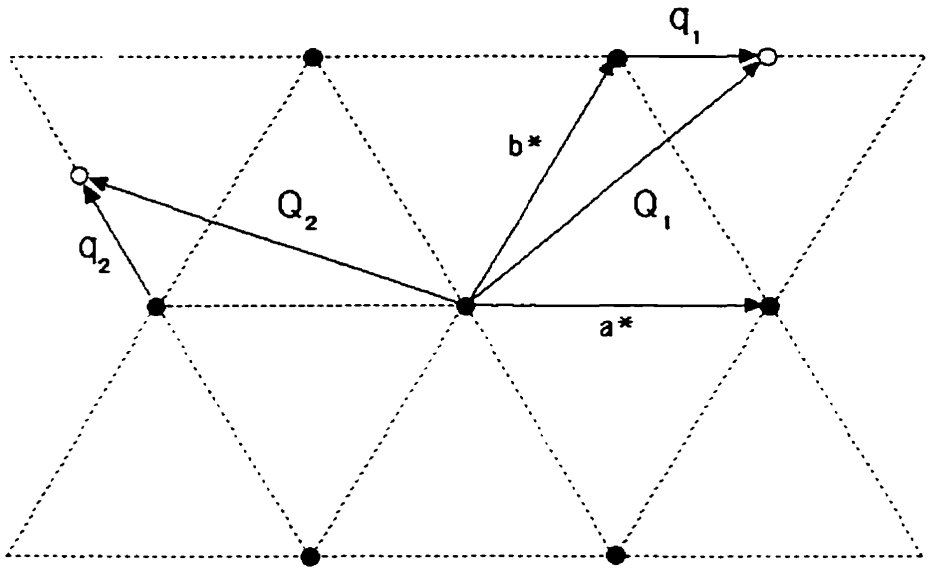

Figure 8.2: Reciprocal space diffraction geometry for both domains. The $\mathbf{q}_i$ indicate the propagation vector while $\mathbf{Q}_i$ show the scattering vector.

7. *Detector.* Detectors usually consist of ^{3}He gas. Capture of a neutron by the gas results in a tritium atom and a proton. These particles ionize the buffer gas which produces a pulse on a wire in the centre of the detector. The number of pulses is then proportional to the number of neutrons that hit the detector.

8.3 Neutron diffraction results

In a first measurement, the magnetic field was applied in the basal plane along the [$\bar{1}$, 2, 0] direction, which is perpendicular to the a* direction and to the wave vector of the $\vec{q_1} = (\frac{1}{2}, 0, 0)$ domain. This should favor the $\vec{q_1}$ domain and remove the $\vec{q_2} = (\frac{\bar{1}}{2}, \frac{1}{2}, 0)$ and $\vec{q_3} = (0, \frac{\bar{1}}{2}, 0)$ domains, each of which is at 30° to the applied field. The intensity of the $\vec{q_1}$ peak, observable at a scattering wave vector $\vec{Q_1} = (\frac{1}{2}, 1, 0)$, which is at an angle to $\vec{M_1} \| \vec{q_1}$ in order to sense the moment (see figure 8.2), should then increase by a factor three on application of a sufficiently strong field. Concomitantly, the intensities due to the $\vec{q_2}$ domain at $\vec{Q_2} = (\frac{\bar{3}}{2}, \frac{1}{2}, 0)$ and the $\vec{q_3}$ domain at $\vec{Q_3} = (\bar{1}, \frac{3}{2}, 0)$ should vanish.

From scans such as those displayed in figure 8.3, in which the crystal angle ψ was rotated through the Bragg position at a fixed temperature of 1.8 K and a fixed

field orientation, namely $\vec{H} \perp \vec{q_1}$, we find that the Bragg peaks corresponding to the three wave vectors persist up to a magnetic field of 3.2 Tesla, as shown in figure 8.4. There is no significant increase in the population of what should be the most thermodynamically stable domain ($\vec{q_1}$). A slight increase of order 30% at 3 Tesla is not inconsistent with the error bars in figure 8.4. This would then be compatible with a roughly equivalent decrease observed in the $\vec{q_2}$ intensity, and suggest that complete domain repopulation could be achieved at higher fields. However, as far as the superconducting phase diagram is concerned, it is important to stress that this anisotropy field is larger than $H_{c2}(0)$, so that the sample is multi-domain in all superconducting phases.

In order to make $\vec{q_2}$ the least favored domain, we rotated the field by 30° to lie along the $\vec{q_2}$ direction. At 1.6 Tesla, we again observed that both the $\vec{q_1}$ and $\vec{q_2}$ modulations remain present. Within the statistical error of 20%, the integrated intensity of the $\vec{q_2}$ modulation observed at a scattering vector $\vec{Q_2}=(\frac{3}{2},\frac{1}{2},0)$ was unchanged between 0 and 1.6 Tesla. For independent (and weakly pinned) domains the intensity would have vanished. A similar independence of field was observed for the $\vec{q_1}$ modulation seen at $\vec{Q_1}=(\frac{1}{2},1,0)$, where the peak should have grown by a factor of $\frac{3}{2}$.

This is in contrast with the behavior of UPd_2Al_3 [180, 181], where a field of less than one Tesla in the hexagonal basal plane perpendicular to $\vec{q}=(1,1,0)$ clearly enhances the population of that particular domain at the expense of the other two. If a similar effect occured in UPt_3, the relative intensities of the $\vec{q_1}$ and $\vec{q_2}$ domains would be expected to follow the solid lines shown in figure 8.4.

In UNi_2Al_3, where the moment is 0.12 μ_B/U atom, intermediate between that of UPt_3 and that of UPd_2Al_3, the propagation vector (0.61,0,0.5) also has a component in the basal plane but it is incommensurate with the crystal lattice [182]. In this case, a field of 3 Tesla is insufficient to produce a monodomain [183].

In zero field cooled (ZFC) experiments, such as those described above, it is possible that domains, having already formed, cannot attain the new thermodynamic equilibrium associated with the applied field. To check for this possibility, we slowly cooled the sample through its 6 K magnetic transition in a field of 3.2 Tesla along the $(\bar{1},2,0)$ direction. All three wave vector modulations were found to have condensed

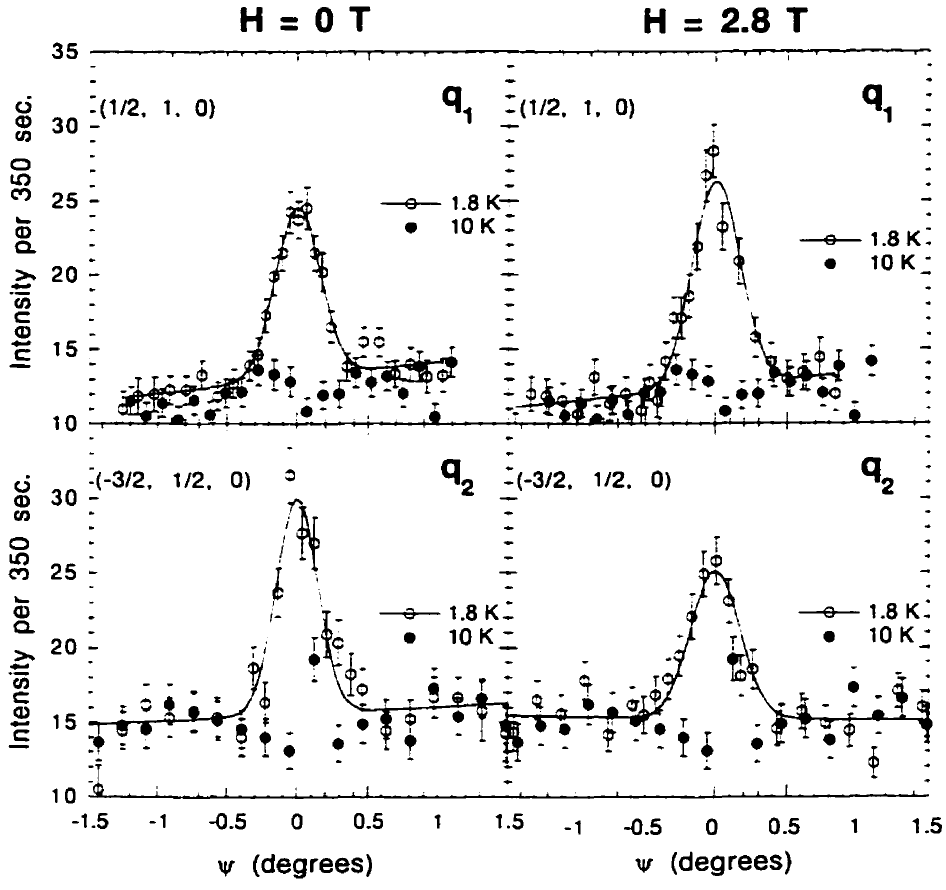

Figure 8.3: Magnetic Bragg peaks at $\vec{q_1}$ and $\vec{q_2}$ for H = 0 and 2.8 Tesla, with $\vec{H} \perp \vec{q_1}$. Selection of a single domain by the 2.8 Tesla field would eliminate the $\vec{q_2}$ Bragg peak and increase the intensity of the $\vec{q_1}$ Bragg peak by a factor up to 3.

with the same intensity as for cooling in zero field. For the $\vec{q_1}$ modulation we can exclude at the 2σ level any increase in peak intensity beyond 30% relative to the ZFC intensities; field selection of one domain would have produced a three-fold intensity increase. These results exclude the possibility that an energy barrier, arising from the reduced orthorhombic symmetry of single-$\vec{q}$ ordered state, might have prevented the attainment of an equilibrium domain configuration at low temperature. We therefore conclude that in UPt_3 the three modulations are present with roughly equal importance for all field strengths at which the superconducting state exists.

Even if all three wave vectors survive the application of a magnetic field, the moments themselves might still rotate away from being longitudinal ($\vec{M}_s \parallel \vec{q}$). To test

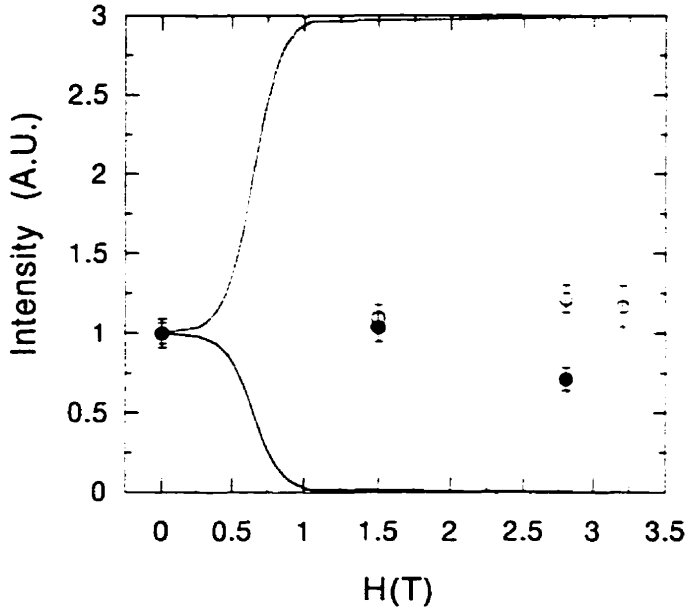

Figure 8.4: Integrated intensity as a function of field for $\vec{q_1}$ (open circles) and $\vec{q_2}$ (solid circles) with $\vec{H} \perp \vec{q_1}$. The solid lines show the expected behavior for both magnetic domains for an anisotropy field of order 0.5 Tesla (as observed in UPd_2Al_3).

this possibility, we monitored the scattering wave vector $\vec{Q} = (\frac{\bar{1}}{2}, \frac{1}{2}, 0)$, where neutron diffraction senses the $\vec{q_2}$ spatial periodicity, but where, in the absence of a field, the scattering amplitude is zero because the moment is parallel to $\vec{Q}$ (see figure 8.5). Moment canting in the field would then give a non-zero amplitude. Applying a field of 2.8 Tesla along $(\bar{1},2,0)$ – perpendicular to $\vec{q_1}$ and at 30° to $\vec{q_2}$ – we observed no measurable growth in intensity above background. The statistics allow us to put an upper-bound of 26° on any rotation at the σ confidence level (a realignment of the $\vec{M_s}$ moment of domain $\vec{q_2}$ by the field would have meant a 60° rotation). This shows that the moment does not follow the field as the latter is rotated in the basal plane, and this for field strengths much greater than H*=0.4 Tesla. This suggests that $\vec{M_s}$ is strongly coupled to the crystal lattice, in agreement with the observation that $\vec{M_s}$ does not rotate upon entering the superconducting state at 0.5 K [93].

Let us look more closely at the single-$\vec{q}$ assumption. Isaacs *et al.* [93] have shown that a collinear structure with three separate domains gives a diffraction pattern consistent with the observed structure factors. The question is: why are all 3 domains

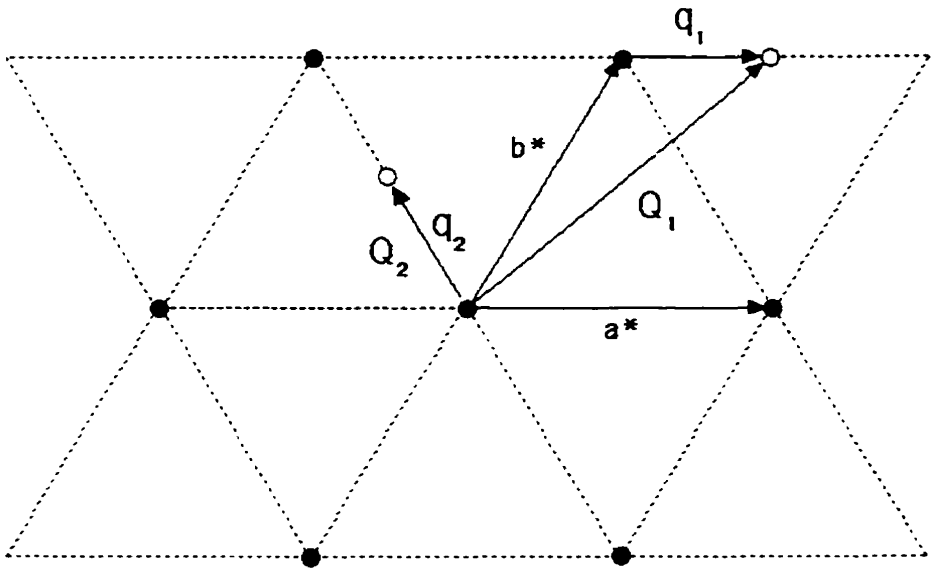

Figure 8.5: Reciprocal space diffraction geometry for both domains. The $\mathbf{q}_i$ indicate the propagation vector while $\mathbf{Q}_i$ show the scattering vector.

equally favored upon cooling in a field of 3.2 Tesla which is only perpendicular to one of the associated moments? For a collinear antiferromagnet, the fact that the transverse susceptibility is larger than the longitudinal susceptibility should lead to the selection of the domain perpendicular to the applied magnetic field, as is seen in UPd_2Al_3. A simple explanation for the ubiquitous presence of all 3 wavevectors is that the magnetic structure might be triple-$\vec{q}$. With a symmetric superposition of three equivalent modulations, the diffraction pattern would be the same as with three single-$\vec{q}$ domains. A magnetic field would have no effect at low fields; it would only produce a single-$\vec{q}$ domain sample when the Zeeman energy developing from distortion of the 3-$\vec{q}$ structure exceeded the binding energy of the 3-$\vec{q}$ state. Triple-$\vec{q}$ structures are known to occur in uranium compounds, such as USb [184] and UPd_3 [185], and are characterized by an insensitivity to applied magnetic fields and uniaxial stress [184]. Now, it is far from obvious that such a magnetic order could break the hexagonal symmetry (in zero field), and even more so that a coupling to the superconducting order can lead to a split transition. Therefore, if such a structure is the correct one for UPt_3, a major reassessment of the coupling theories mentioned above is needed.

8.4 Conclusion

In conclusion, we have shown that basal plane magnetic fields of up to 3.2 Tesla have no effect on the magnetic order in UPt_3, whether it be in rotating the moments or in selecting a domain with a single wave vector. Because the upper critical field of UPt_3 is less than 3.2 Tesla, the absence of rotation makes it difficult to reconcile the fact that a kink in $H_{c2}(T)$ is observed experimentally at 0.4 Tesla [172, 173, 55, 177, 135] for various field directions in the basal plane, with the prediction of current theories [81, 80, 82, 31, 87, 90, 176, 89] that it should only occur for one direction of $\vec{H}$ with respect to $\vec{M}_s$. In this respect, a calculation with *three* fixed domains would prove helpful. Our results also invalidate the respective assumptions (moment rotation and domain selection) underlying two recent explanations [89, 186] for the slight 60° variation of H_{c2} in the basal plane [135]. Finally, there is a distinct possibility that the antiferromagnetic order in UPt_3 has a triple-$\vec{q}$ structure, as opposed to the single-$\vec{q}$ structure assumed until now, which would require a major reassessment of current theories for the superconducting phase diagram.

9

CONCLUSION

In this thesis, we presented a detailed experimental study of thermal conductivity in a heavy fermion and a high-T_c superconductor.

In the case of the heavy fermion compound UPt_3, we presented thermal conductivity results on *one* high-quality single crystal for two directions of the heat current. This is the first study of the anisotropy of thermal conductivity on a heavy fermion superconductor. We concluded that any residual linear term is small and that our results are consistent with a scattering rate $\Gamma_0 \sim 0.05 T_c$ or less. Such a small scattering rate implies that our data (down to 45 mK) do not reach the gapless regime (below $\sim 0.1 T_c$). The main result of our study is the finite ratio κ_c/κ_b as $T \rightarrow 0$. This places severe constraints on the gap structure, and we conclude that the gap vanishes at the poles with a quadratic k-dependence and along a line of zero in the basal plane. This significantly reduces the number of possible candidates for the gap structure of phase B and we are left with a hybrid II gap structure such as that proposed for the E_{2u} scenario (with strong spin-orbit coupling) or the A_{2u} model (with weak spin-orbit coupling). We feel that thermal conductivity in UPt_3 is now a mature subject and that a comprehensive understanding of heat conduction in UPt_3 is near.

We also presented a systematic study of thermal conductivity on a-axis high-quality zinc-doped crystals of $YBa_2Cu_3O_{7-\delta}$ at low temperature. The main result is the existence of universal electronic linear term at $T \rightarrow 0$ in excellent quantitative agreement with current theories for a d-wave gap. We also emphasized that a conventional analysis of the type $\kappa = aT + bT^3$ of low temperature data in $YBa_2Cu_3O_{7-\delta}$ is not adequate and we provided a way to account for the zinc-doped crystals results over the whole temperature range covered by our experiments. A constant electronic linear term up to 1 K is consistent with the results for all zinc concentrations. As to

the phonon contribution, a satisfactory quantitative explanation is obtained in terms of scattering by the boundaries and by invoking specular reflections on one side of the crystal.

Our neutron scattering experiments have shown that applying a magnetic field up to 3.2 Tesla along the basal plane of UPt_3 has no effect on the magnetic order: it neither rotates the moments nor selects a domain with a single wavevector. Because the upper critical field of UPt_3 is less than 3.2 Tesla, the absence of rotation makes it difficult to reconcile the fact that experimentally a kink in $H_{c2}(T)$ is always observed for any direction in the basal plane with the predictions of current theories for the superconducting phase diagram. Moreover, our results also reveal the possibility that the antiferromagnetic order in UPt_3 is a triple-$\vec{q}$ structure, as opposed to the single-$\vec{q}$ structure assumed until now.

APPENDIX

A.1 Losses through radiation

In this section, we present the estimated losses through radiation. We choose the worst possible case: the hottest part of the experimental setup is the heater that provides the temperature gradient and we assume that its temperature is about 1 K for the whole temperature range and that it has an emissivity of 1. The power lost to radiation P_{rad} is then (assuming that the surrounding temperature is 0 K): $P_{rad} = \sigma A T^4$ with σ = 5.67 x 10^{-12} W/cm^{2}K^4 and A = 7 x 10^{-2} cm^2 (see table A.1). The power radiated is then 0.4 nW. This number has to be compared with the total power dissipated in the heater which is of the order of 100 nW and therefore can be neglected.

A.2 Losses through the measuring leads and experimental supports

In this section, we present a detailed calculation of the thermal resistances involved in our thermal conductivity setup showing that heat losses are negligible for all samples measured in the temperature range from 0.1 to 1 K. Experimental data for these calculations are taken from the books by Lounasmaa [118] and Pobell [119] and references therein. Figure 5.3 and figure A.1 show the thermal circuit and the various resistances involved. In table A.1, the geometry and the thermal conductivity of the various parts of the setup used are summarized. These values are then used to compile the thermal resistances shown in table A.2.

In order for heat losses from the heater to be negligible, we want the thermal path from the heater through the sample to the heat sink (i.e. $W_2 + W_3 + W_{sample} + W_6$) to be much less resistive than the direct path from the heater to the heat sink (i.e. W_1 or $W_2 + W_1'$). Also, in order for the heat losses from the thermometer to be

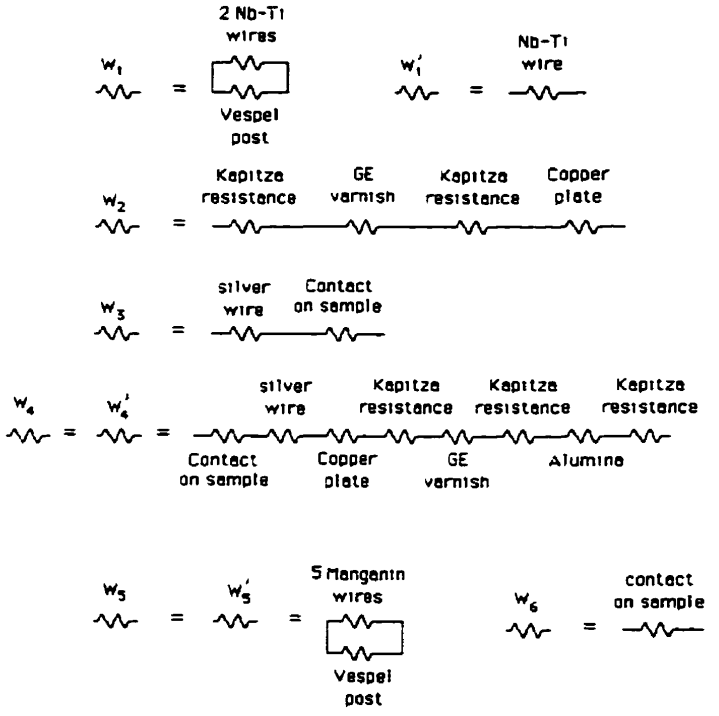

Figure A.1: Detailed description of each thermal resistance involved in the thermal conductivity setup.

negligible, we require $W_4(W_4') \ll W_5(W_5')$. Inspection of table A.2 together with the knowledge that the least conducting sample measured had $W_{sample} < 10^{-3}\ K/mW$, we get: $\frac{W_2+W_3+W_{sample}+W_6}{W_1} = 0.8\%(1.1\%)$, $\frac{W_2+W_3+W_{sample}+W_6}{W_1'+W_2} = 10^{-3}\%(6 \times 10^{-3}\%)$ and $\frac{W_4}{W_5} = \frac{W_4'}{W_5'} = 1\%(0.9\%)$ at 0.1 K (1 K). From these figures, it is clear that heat losses can be safely ignored over the whole temperature range covered by the thermal conductivity experiments presented in this thesis.

Table A.1: Geometry and thermal conductivity of the various components used in the thermal conductivity setup.

Name	Length (cm)	Area (cm^2)	κ(0.1 K) (mW/Kcm)	κ(1 K) (mW/Kcm)
Nb-Ti wire *	2.5×10^{0}	4.9×10^{-6}	1.1×10^{-3}	7.5×10^{-2}
Vespel post	5.7×10^{-1}	9.0×10^{-4}	1.1×10^{-3}	1.8×10^{-2}
GE varnish	1.0×10^{-2} †	7.0×10^{-2}	4.0×10^{-4}	3.0×10^{-2}
Copper plate	1.0×10^{-1}	7.0×10^{-2}	4.0×10^{1}	4.0×10^{2}
Silver wire	1.0×10^{0}	7.9×10^{-5}	1.0×10^{1}	1.1×10^{2}
Alumina	5.0×10^{-2} ‡	4.0×10^{-2}	5.8×10^{-4}	2.9×10^{-2}
Manganin wire	15×10^{0}	4.9×10^{-6}	5.0×10^{-2}	5.0×10^{-1}

*The only data found for this material [119] was a $T^{1.85}$ power law valid for the range $4 < T < 9$ K. Since we know that the electronic contribution to the thermal conductivity has an exponentially activated behavior and that the phonon mean-free path will become limited by the boundaries of the wire giving a T^3 contribution, this power law will certainly be an upperbound to the total heat conduction of the wire at low temperatures.

†This quantity could not be measured and was estimated.

‡Due to the contacts on the thermometer and the ruthenium oxide film, this quantity could not be measured directly, it was therefore estimated.

Table A.2: Thermal resistances (W) of the various components used in the thermal conductivity setup.

Name	W(0.1 K) (K/mW)	W(1 K) (K/mW)	used in
Nb-Ti wire	4.8 x 10^8	6.8 x 10^6	W_1 and W_1'
Vespel post	5.6 x 10^5	3.5 x 10^4	W_1 and W_5
Kapitza resistance *	1.0 x 10^2	1.0 x 10^{-1}	W_2, W_4 and W_4'
GE varnish	3.6 x 10^2	4.8 x 10^0	W_2, W_4 and W_4'
Copper plate	4.0 x 10^{-2}	4.0 x 10^{-3}	W_2, W_4 and W_4'
Silver wire	1.3 x 10^3	1.2 x 10^2	W_3, W_4 and W_4'
Contact on sample †	1.4 x 10^3	1.4 x 10^2	W_3, W_4, W_4' and W_6
Alumina	2.2 x 10^3	4.3 x 10^1	W_4 and W_4'
Manganin wire	6.1 x 10^7	6.1 x 10^6	W_4 and W_4'

*For this thermal resistance, we used a generic value given by Pobell(and references therein) [119] for a boundary between copper and glues: AR_KT^3=0.007 cm^{2}K^4/mW where A = 7.0 x 10^{-2} cm^2 is the area of the contact, R_K is the Kapitza or boundary resistance and T is the temperature.

†The thermal resistance of a contact was estimated from the Wiedemann-Franz law assuming a good metallic contact and an electrical contact resistance of 3.5 mΩ as measured in $YBa_2Cu_3O_{7-\delta}$ at 4.2 K.

BIBLIOGRAPHY

[1] F. Steglich, J. Aarts, C. D. Bredl, W. Lieke, D. Meschede, W. Franz, and H. Schafer. *Phys. Rev. Lett.*, 43:1892–1896, 1979.

[2] J. G. Bednorz and K. A. Müller. Possible high T_c superconductivity in the Ba-La-Cu-O system. *Z. Phys. B*, 64:189–193, 1986.

[3] T. Ishiguro and K. Yamaji. *Organic superconductors.* Springer-Verlag, Berlin, 1989.

[4] A. A. Abrikosov. *Introduction to the theory of normal metals.* Academic Press, New York, 1972.

[5] R. Berman. *Thermal conduction in solids.* Clarendon Press, Oxford, 1976.

[6] P. G. Klemens. Thermal conductivity and lattice vibrational modes. *Sol. St. Phys.*, 7:1–98, 1958.

[7] G. K. White and R. J. Tainsh. Electron scattering in nickel at low temperatures. *Phys. Rev. Lett.*, 19:165–166, 1967.

[8] P. G. Klemens. The thermal conductivity of dielectric solids at low temperatures. *Proc. Phys. Soc. (London)*, A68:108–133, 1955.

[9] W. A. Phillips. Tunneling states in amorphous solids. *J. Low Temp. Phys.*, 7:351–360, 1972.

[10] P. W. Anderson, B. I. Halperin, and C. M. Varma. Anomalous low-temperature thermal properties of glasses and spin glasses. *Philos. Mag.*, 25:1–9, 1972.

[11] N. W. Ashcroft and N. D. Mermin. *Solid state physics.* W. B. Saunders company, Philadelphia, 1976.

[12] J. P. Franck, F. D. Manchester, and D. L. Martin. *Proc. Roy. Soc.*, A263:494–507, 1961.

[13] J. Bardeen, L. N. Cooper, and J. R. Schrieffer. Theory of superconductivity. *Phys. Rev.*, 108:1175–1204, 1957.

[14] M. Tinkham. *Introduction to superconductivity.* McGraw-Hill, New York, 2nd edition, 1996.

[15] P. G. de Gennes. *Superconductivity of metals and alloys.* Addison-Wesley, New York, 2d ed. edition, 1989.

[16] J. Bardeen, G. Rickayzen, and L. Tewordt. Theory of the thermal conductivity of superconductors. *Phys. Rev.*, 113:982–994, 1959.

[17] N. E. Phillips. Heat capacity of aluminum between 0.1 K and 4.0 K. *Phys. Rev.*, 114:676–685, 1959.

[18] R. E. Glover and M. Tinkham. Conductivity of superconducting films for photon energies between 0.3 and 40kT_c. *Phys. Rev.*, 108:243–256, 1957.

[19] J. R. Schrieffer. *Theory of superconductivity.* Addison-Wesley, Redwood city, 1988.

[20] C. B. Satterthwaite. Thermal conductivity of normal and superconducting aluminum. *Phys. Rev.*, 125:873–876, 1962.

[21] P. H. Kes, J. G. A. Rolfes, and D. de Klerk. Thermal conductivity of niobium in the purely superconducting and normal states. *J. of Low Temp. Phys.*, 17:341–365, 1974.

[22] J. L. Olsen. Heat transport in lead-bismuth alloys. *Proc. Phys. Soc.*, A65:518–532, 1952.

[23] N. V. Zavaritskii. Measurement of the anisotropy of thermal conductivity of zinc and cadmium in the superconducting state. *J. Exptl. Theoret. Phys.*, 39:1193–1197, 1960.

[24] N. V. Zavaritskii. Investigation of the thermal properties of superconductors. iii. anisotropy of the thermal conductivity of gallium. *J. Exptl. Theoret. Phys.*, 37:1506–1516, 1959.

[25] C. Kittel. *Introduction to solid state physics.* John Wiley and Sons Inc., New York, 6th edition, 1986.

[26] A. J. Leggett. A theoretical description of the new phases of liquid ^{3}He. *Rev. Mod. Phys.*, 47:331–414, 1975.

[27] M. R. Norman. Magnetic pairing in a lattice of Kondo ions: Application to UPt_3. *Phys. Rev. B*, 39:7305–7308, 1989.

[28] W. Putikka and R. Joynt. Stability of anisotropic superconducting phases in UPt_3. *Phys. Rev. B*, 37:2372–2375, 1988.

[29] M. R. Norman. Anisotropic exchange and superconductivity in UPt_3. *Phys. Rev. B*, 41:170–177, 1990.

[30] G. Burns. *High temperature superconductivity.* Academic Press, New York, 1992.

[31] J. A. Sauls. A theory for the superconducting phases of UPt_3. *J. Low Temp. Phys.*, 95:153–168, 1994.

[32] V. P. Mineev. Superconductivity of heavy fermionic compounds. unpublished, 1992.

[33] Sigrist and Ueda. Phenomenological theory of unconventional superconductivity. *Rev. Mod. Phys.*, 63:239, 1991.

[34] G. E. Volovik and L. P. Gor'kov. Superconducting classes in heavy-fermion systems. *Sov. Phys. JETP*, 61:843–854, 1985.

[35] M. Ozaki, K. Machida, and T. Ohmi. On p-wave pairing superconductivity under hexagonal and tetragonal symmetries. *Prog. Theor. Phys.*, 75:442–444, 1986.

[36] M. R. Norman and P. J. Hirschfeld. Heat transport and the nature of the order parameter in superconducting UPt_3. *Phys. Rev. B*, 53:5706–5715, 1996.

[37] A. Sulpice, P. Gandit, J. Chaussy, J. Flouquet, D. Jaccard, P. Lejay, and J. L. Tholence. Thermodynamic and transport properties of UPt_3. *J. Low Temp. Phys.*, 62:39–54, 1986.

[38] B. S. Shivaram, Y. H. Jeong, T. F. Rosenbaum, and D. G. Hinks. Anisotropy of transverse sound in the heavy-fermion superconductor UPt_3. *Phys. Rev. Lett.*, 56:1078, 1986.

[39] L. Coffey, T. M. Rice, and K. Ueda. Quasiparticle scattering time in p-wave superconductors. *J. Phys. C: Solid St. Phys.*, 18:L813–L816, 1985.

[40] C. J. Pethick and D. Pines. Transport processes in heavy-fermion superconductors. *Phys. Rev. Lett.*, 57:118–121, 1986.

[41] H. Monien, K. Scharnberg, L. Tewordt, and D. Walker. Specific heat, thermal conductivity, and ultrasound attenuation in d-wave superconductors. *Sol. St. Comm.*, 61:581–585, 1987.

[42] P. J. Hirschfeld, D. Vollhardt, and P. Wölfle. Resonant impurity scattering in heavy fermion superconductors. *Solid St. Comm.*, 59:111–115, 1986.

[43] S. Schmitt-Rink, K. Miyake, and C. M. Varma. Transport and thermal properties of heavy-fermion superconductors: A unified picture. *Phys. Rev. Lett.*, 57:2575–2578, 1986.

[44] K. Scharnberg, D. Walker, H. Monien, L. Tewordt, and R. A. Klemm. Attenuation of ultrasound in p-wave superconductors. *Solid St. Comm.*, 60:535–539, 1986.

[45] B. Arfi and C. J. Pethick. Thermal conductivity and ultrasonic attenuation in heavy-fermion superconductors. *Phys. Rev. B*, 38:2312–2325, 1988.

[46] Yu. S. Barash and A. A. Svidzinsky. Low temperature properties and specific anisotropy of pure anisotropically paired superconductors. *Phys. Rev. B*, 53:15254–15264, 1996.

[47] B. Arfi, H. Bahlouli, and C. J. Pethick. Transport properties of anisotropic superconductors: Influence of arbitrary electron-impurity phase shifts. *Phys. Rev. B*, 39:8959–8983, 1989.

[48] B. Arfi. Thermal conductivity in two-dimensional superconductors: Effect of nonmagnetic impurities. *Phys. Rev. B*, 47:523–525, 1993.

[49] M. J. Graf, S.-K. Yip, J. A. Sauls, and D. Rainer. Electronic thermal conductivity and the Wiedemann-Franz law for unconventional superconductors. *Phys. Rev. B*, 53:15147–15162, 1996.

[50] P. J. Hirschfeld and W. O. Putikka. Theory of thermal conductivity in $YBa_2Cu_3O_{7-\delta}$. *Phys. Rev. Lett,*, 77:3909–3912, 1996.

[51] A. Fledderjohann and P. J. Hirschfeld. Thermal conductivity anisotropy in superconducting UPt_3. *Solid State Comm.*, 94:163, 1995.

[52] M. J. Graf, S.-K. Yip, and J. A. Sauls. Thermal conductivity of superconducting UPt_3 at low temperatures. *J. of Low Temp. Phys.*, 102:367–379, 1996.

[53] A. de Visser. *UPt_3, heavy fermions and superconductivity.* PhD thesis, Amsterdam university, 1986.

[54] A. de Visser, A. Menovsky, and J. J. M. Franse. UPt_3, heavy fermions and superconductivity. *Physica B*, 147:81, 1987.

[55] U. Rauchschwalbe. Magnetic properties of heavy fermion superconductors. *Physica B*, 147:1–80, 1987.

[56] N. Grewe and F. Steglich. Heavy fermions. In G. Schneidner, editor, *Handbook on the Physics and Chemistry of Rare Earths*, chapter 14, pages 343–474. Elsevier, Amsterdam, 1991.

[57] L. Taillefer. Current issues in heavy fermion superconductivity. *Hyp. Int.*, 85:379–396, 1994.

[58] H. v. Löhneysen. The superconducting phases of UPt_3. *Physica B*, 197:551–562, 1994.

[59] R. H. Heffner and M. R. Norman. Heavy fermion superconductivity. *Comments in condensed matter physics*, 17:361–408, 1996.

[60] P. A. Midgley, S. M. Hayden, L. Taillefer, B. Bogenberger, and H. v. Löhneysen. Superconductivity and the incommensurate structural modulation in the heavy fermion UPt_3. *Phys. Rev. Lett.*, 70:678–681, 1993.

[61] B. Ellman, A. Zaluska, and L. Taillefer. Structural modulations in UPt_3 single crystal whiskers. *Physica B*, 205:346–348, 1995.

[62] B. Ellman, M. Sutton, B. Lussier, R. Brüning, L.Taillefer, S. Hayden, and G. Shea-McCarthy. Search for structural modulations in UPt_3 using Laue X-ray diffraction. *preprint*, 1996.

[63] G. A. Alers. *Physical acoustics*, volume IIIB, chapter 1. Academic Press, New York, 1965.

[64] L. Taillefer, R. Newbury, G. G. Lonzarich, Z. Fisk, and J. L. Smith. Direct observation of heavy quasiparticles in UPt_3 via the dHvA effect. *J. Magn. Magn. Mat.*, 63-64:372–376, 1987.

[65] L. Taillefer and G. G. Lonzarich. Heavy-fermion quasiparticles in UPt_3. *Phys. Rev. Lett.*, 60:1570–1573, 1988.

[66] M. R. Norman, R. C. Albers, A. M. Boring, and N. E. Christensen. Fermi surface and effective masses for the heavy-electron superconductor UPt_3. *Solid State Comm.*, 68:245–249, 1988.

[67] G. Aeppli, E. Bucher, A. I. Goldman, G. Shirane, C. Broholm, and J. K. Kjems. *J. Magn. Magn. Mat.*, 76-77:385, 1988.

[68] G. Aeppli, E. Bucher, C. Broholm, J. K. Kjems, J. Baumann, and J. Hufnagl. Magnetic order and fluctuations in superconducting UPt_3. *Phys. Rev. Lett.*, 60:615–618, 1988.

[69] G. Aeppli and C. Broholm. Magnetic correlations in heavy fermion systems: neutron scattering from single crystals. In G. Schneidner and G. H. Lander, editors, *Handbook on the Physics and Chemistry of Rare Earths*, chapter 19. Elsevier, Amsterdam, 1994.

[70] R. A. Fisher, S. Kim, B. F. Woodfield, N. E. Phillips, L. Taillefer, K. Hasselbach, J. Flouquet, A. L. Giorgi, and J. L. Smith. *Phys. Rev. Lett.*, 62:1411, 1989.

[71] S. Adenwalla, S. W. Lin, Q. Z. Ran, Z. Zhao, J. B. Ketterson, J. A. Sauls, L. Taillefer, D. G. Hinks, M. Levy, and B. K. Sarma. Phase diagram of UPt_3 from ultrasonic velocity measurements. *Phys. Rev. Lett.*, 65:2298–2301, 1990.

[72] L. Taillefer. Anisotropy and the superconducting phases of UPt_3. *Physica B*, 163:278–284, 1990.

[73] M. P. Greiter. The effect of uniaxial stress on the superconducting transition temperature in the heavy fermion alloy UPt_3. Master's thesis, Cambridge University, 1987.

[74] T. Trappmann, H. v. Löhneysen, and L. Taillefer. Pressure dependence of the superconducting phases in UPt_3. *Phys. Rev. B*, 43:13714–13716, 1991.

[75] S. K. Yip, T. Li, and P. Kumar. Thermodynamic considerations and the phase diagram of superconducting UPt_3. *Phys. Rev. B*, 43:2742–2747, 1991.

[76] D. S. Jin, S. A. Carter, B. Ellman, T. F. Rosenbaum, and D. G. Hinks. Uniaxial-stress anisotropy of the double superconducting transition in UPt_3. *Phys. Rev. Lett.*, 68:1597, 1992.

[77] M. Boukhny, G. L. Bullock, B. S. Shivaram, and D. G. Hinks. Tetracritical points and the superconducting phases of UPt_3: Uniaxial pressure effects. *Phys. Rev. Lett.*, 73:1707–1710, 1994.

[78] D.-C. Chen and A. Garg. Accidental near degeneracy of the order parameter for superconducting UPt_3. *Phys. Rev. Lett.*, 70:1689–1692, 1993.

[79] S. M. Hayden, L. Taillefer, C. Vettier, and J. Flouquet. Antiferromagnetic order in UPt_3 under pressure. *Phys. Rev. B*, 46:8675–8678, 1992.

[80] K. Machida and M. Ozaki. Splitting of superconducting transitions in UPt_3. *J. Phys. Soc. Jpn.*, 58:2244–2247, 1989.

[81] R. Joynt. Phase diagram of d-wave superconductors in a magnetic field. *Super. Sci. Tech.*, 1:210–217, 1988.

[82] D. W. Hess, T. A. Tokuyasu, and J. A. Sauls. Broken symmetry in an unconventional superconductor: a model for the double transition in UPt_3. *J. Phys. Condens. Matter*, 1:8135–8145, 1989.

[83] K. Machida and M. Ozaki. Superconducting double transition in heavy-fermion material UPt_3. *Phys. Rev. Lett.*, 66:3293–3296, 1991.

[84] K. Miyake. *Theory of heavy fermions and valence fluctuations*, page 256. Springer-Verlag, 1986.

[85] Y. Kohori, T. Kohara, H. Shibai, Y. Oda, T. Kaneko, Y. Kitaoka, and K. Asayama. ^{195}Pt Knight shift in the heavy fermion superconductor UPt_3. *J. Phys. Soc. Jpn.*, 56:2263–2266, 1987.

[86] G. M. Luke, A. Keren, L. P. Lee, W. D. Wu, Y. J. Uemura, D. A. Bonn, L. Taillefer, and J. D. Garrett. Muon spin relaxation in UPt_3. *Phys. Rev. Lett.*, 71:1466–1469, 1993.

[87] K. Machida, T. Ohmi, and M. Ozaki. Superconducting properties of a heavy electron material UPt_3. *J. Phys. Soc. Jpn.*, 62:3216–3230, 1993.

[88] J. A. Sauls. The order parameter for the superconducting phases of UPt_3. *Adv. Phys.*, 43:113–141, 1994.

[89] J. A. Sauls. Effects of magnetic order on the upper critical field of UPt_3. *Phys. Rev. B*, 53:8543–8548, 1996.

[90] K. A. Park and R. Joynt. Phase diagram of UPt_3 in the E_{1g} model. *Phys. Rev. Lett.*, 74:4734–4737, 1995.

[91] K. A. Park. *Phase diagram of superconducting UPt_3 in the E_{1g} model.* PhD thesis, University of Wisconsin-Madison, 1995.

[92] G. Aeppli, D. Bishop, C. Broholm, E. Bucher, K. Siemensmeyer, M. Steiner, and N. Stüsser. Magnetic order in the different superconducting states of UPt_3. *Phys. Rev. Lett.*, 63:676–679, 1988.

[93] E. D. Isaacs, P. Zschack, C. L. Broholm, C. Burns, G. Aeppli, A. P. Ramirez, T. T. M. Palstra, R. W. Erwin, N. Stücheli, and E. Bucher. Antiferromagnetism and its relation to the superconducting phases of UPt_3. *Phys. Rev. Lett.*, 75:1178–1181, 1995.

[94] J. P. Brison, N. Keller, P. Lejay, A. Huxley, L. Schmidt, S. Budzin, N. Bernhoeft, V. P. Mineev, A. N. Stepanov, J. Flouquet, D. Jaccard, S. Julian, and G. Lonzarich. Very low temperature properties of heavy fermion materials. *Physica B*, 199-200:70–75, 1994.

[95] E. A. Schuberth, G. Hofmann, F. Gross, K. Andres, and J. Hufnagl. UPt_3 at very low temperatures: specific heat in high magnetic fields. *Europhys. Lett.*, 11:249–254, 1990.

[96] E. A. Schuberth and M. Fischer. Specific heat and magnetization studies in UPt_3 and UBe_{13} at very low temperatures. *Physica B*, 194-196:1983–1984, 1994.

[97] K. Asayama, Y. Kitaoka, and Y. Kohori. NMR study of heavy fermion material. *J. Magn. Magn. Mat.*, 76-77:449–454, 1988.

[98] C. L. Broholm, G. Aeppli, R. N. Kleiman, D. R. Harshman, D. J. Bishop, E. Bucher, D. L. Williams, E. J. Ansaldo, and R. H. Heffner. Anisotropic temperature dependence of the magnetic-field penetration in superconducting UPt_3. *Phys. Rev. Lett.*, 65:2062–2065, 1990.

[99] G. M. Luke, L. P. Le, B. J. Steinlieb, W. D. Wu, Y. J. Uemura, J. H. Brewer, R. Kadono, R. F. Kiefl, S. R. Kreitzman, T. M. Riseman aand Y. Dalichaouch, B. W. Lee, M. B. Maple, C. L. Seaman, P. E. Armstrong, R. W. Ellis, Z. Fisk, and J. L. Smith. *Phys. Lett. A*, 157:173–177, 1991.

[100] G. Goll, H. v. Löhneysen andd I. K. Yanson, and L. Taillefer. Anisotropy of point-contact spectra in the heavy fermion superconductor UPt_3. *Phys. Rev. Lett.*, 70:2008–2011, 1993.

[101] Y. de Wilde, J. Heil, A. G. M. Jansen, P. Wyder, R. Deltour, W. Assmus, A. Menovsky, W. Sun, and L. Taillefer. Andreev reflections on heavy-fermion superconductors. *Phys. Rev. Lett.*, 72:2278–2281, 1994.

[102] M. Cyrot and D. Pavuna. *Introduction to superconductivity and high-T_c materials.* World Scientific, London, 1992.

[103] J. Dominec. Ultrasonic and related experiments in high-T_c superconductors. *Superconductor science and technology*, 6:153–172, 1993.

[104] R. Truell, C. Elbaum, and B. Chick. *Ultrasonic methods in solid state physics.* Academic Press, New York, 1969.

[105] E. Dieulesaint and D. Royer. *Elastic waves in solids.* John Wiley and sons, New York, 1974.

[106] R. Gagnon, C. Lupien, and L. Taillefer. T^2 dependence of the resistivity in the Cu-O chains of $YBa_2Cu_3O_{7-\delta}$. *Phys. Rev. B*, 50:3458–3461, 1994.

[107] R. A. Fisher, J. E. Gordon, S. F. Reklis, D. A. Wright, J. P. Emerson, B. F. Woodfield, E. M. McCarron III, and N. E. Phillips. Magnetic-field dependence of the low-temperature specific heat of some high-T_c copper-oxide superconductors. Evidence for an $H^{1/2}T$ contribution in the mixed state. *Physica C*, 252:237–263, 1995.

[108] K. A. Moler, D. J. Baar, J. S. Urbach, R. Liang, W. N. Hardy, and A. Kapitulnik. Magnetic field dependence of the density of states of $YBa_2Cu_3O_{6.95}$ as determined from the specific heat. *Phys. Rev. Lett.*, 73:2744–2747, 1994.

[109] C. Uher. Thermal conductivity of high-T_c superconductors. *J. of Superconductivity*, 3:337–389, 1990.

[110] R. C. Yu, M. B. Salamon, J. Ping Lu, and W. C. Lee. Thermal conductivity of an untwinned $YBa_2Cu_3O_{7-\delta}$ single crystal and a new interpretation to the superconducting-state thermal transport. *Phys. Rev. Lett.*, 69:1431–1434, 1992.

[111] J. L. Cohn, E. F. Skelton, S. A. Wolf, J. Z. Liu, and R. N. Shelton. Thermal conductivity in the *ab* plane of untwinned $YBa_2Cu_3O_{7-\delta}$. *Phys. Rev. B*, 45:13144–13147, 1992.

[112] D. A. Bonn, P. Dosanjh, R. Liang, and W. N. Hardy. Evidence for rapid suppression of quasiparticle scattering below T_c in $YBa_2Cu_3O_{7-\delta}$. *Phys. Rev. Lett.*, 68:2390–2393, 1992.

[113] S. Pu. Thermal conductivity of the high-T_c superconductor $YBa_2Cu_3O_{7-\delta}$. Master's thesis, McGill university, 1996 (to be published).

[114] K. Krishana, J. M. Harris, and N. P. Ong. Quasi-particle mean-free path in $YBa_2Cu_3O_7$ measured by the thermal hall conductivity. *Phys. Rev. Lett.*, 75:3529–3532, 1995.

[115] N. P. Ong. The thermal hall effect in detwinned $YBa_2Cu_3O_{7-\delta}$. private communication, 1996.

[116] D. A. Bonn, S. Kamal, K. Zhang, R. Liang, D. J. Baar, E. Klein, and W. N. Hardy. Comparison of the influence of Ni and Zn impurities on the electromagnetic properties of $YBa_2Cu_3O_{6.95}$. *Phys. Rev. B*, 50:4051–4063, 1994.

[117] B. Lussier, B. Ellman, and L. Taillefer. Anisotropy of heat conduction in the heavy fermion superconductor UPt_3. *Phys. Rev. Lett.*, 73:3294–3297, 1994.

[118] O. V. Lounasmaa. *Experimental principles and methods below 1 K.* Academic press, London, 1974.

[119] F. Pobell. *Matter and methods at low temperatures.* Springer-Verlag, New York, 1992.

[120] H. Doi, Y. Narahara, Y. Oda, and H. Nagano. New resistance thermometer with small magnetic field dependence for low temperature measurements. In *LT17*, pages 405–406. Elsevier Science Publishers, 1984.

[121] Z. Altounian and J. O. Strom-Olsen. Superconductivity and spin fluctuations in M-Zr metallic glasses (M = Cu, Ni, Co and Fe). *Phys. Rev. B*, 27:4149–4156, 1983.

[122] Q. Li, C. H. Watson, R. G. Goodrich, D. G. Haase, and H. Lukefahr. Thick film chip resistors for use as low temperature thermometers. *Cryogenics*, 26:467–470, 1986.

[123] R. C. Weast, editor. *CRC handbook of chemistry and physics.* CRC Press, Florida, 61st edition, 1980.

[124] M. Chiao, B. Lussier, B. Ellman, and L. Taillefer. Heat conduction in the heavy fermion superconductor UPd_2Al_3. *Physica B, Proceedings SCES96*, 1996 (to be published).

[125] S. Legault, B. Ellman, J. O. Ström-Olsen, L. Taillefer, and S. Kycia. Thermal conductivity of a single-grain quasicrystal of $Al_{70}Pd_{20}Mn_{10}$. In C. Janot and R. Mosseri, editors, *Proceedings of the 5th conference on quasicrystals*, pages 592–595. World Scientific Publishing, 1995.

[126] H. R. Ott, E. Felder, A. Bernasconi, Z. Fisk, J. L. Smith, L. Taillefer, and G. G. Lonzarich. Specific heat and thermal conductivity of superconducting UBe_{13} and UPt_3 at very low temperatures. *Jap. Journal of Applied Phys.*, 26:1217–1218, 1987.

[127] J. J. M. Franse, A. Menovsky, A. de Visser, C. D. Bredl, U. Gottwick, W. Lieke, H. M. Mayer, U. Rauchschwalbe, G. Sparn, and F. Steglich. Specific heat and transport properties of UPt_3. *Z. Phys. B*, 59:15–19, 1985.

[128] D. Jaccard, J. Flouquet, P. Lejay, and J. L. Tholence. Transport and magnetic measurements on UPt_3. *J. Appl. Phys.*, 57:3082–3083, 1985.

[129] K. Behnia, L. Taillefer, J. Flouquet, D. Jaccard, F. Maki, and Z. Fisk. Thermal conductivity of superconducting UPt_3. *J. Low Temp. Phys.*, 84:261–278, 1991.

[130] K. Behnia. *La supraconductivité anisotrope d'UPt_3*. PhD thesis, Université de Paris-sud (Orsay), 1990.

[131] B. Bogenberger and H. v. Löhneysen. Specific heat of UPt_3. private communication, 1992.

[132] A. D. Huxley, H. Suderow, J. P. Brison, and J. Flouquet. Thermal conductivity and symmetry of the superconductivity in UPt_3. *Phys. Lett. A*, 209:365–372, 1995.

[133] B. S. Shivaram, T. F. Rosenbaum, and D. G. Hinks. Unusual angular and temperature dependence of the upper critical field in UPt_3. *Phys. Rev. Lett.*, 57:1259, 1986.

[134] P. J. Hirschfeld, P. Wölfle, and D. Einzel. Consequences of resonant impurity scattering in anisotropic superconductors: Thermal and spin relaxation properties. *Phys. Rev. B*, 37:83–97, 1988.

[135] N. Keller, J. L. Tholence, A. Huxley, and J. Flouquet. Angular dependence of the upper critical field of the heavy fermion superconductor UPt_3. *Phys. Rev. Lett.*, 73:2364–2367, 1994.

[136] R. D. Parks, editor. *Superconductivity*, volume 2, chapter 2 and 4. Dekker, New York, 1969.

[137] J. Lowell and J. B. Sousa. Mixed-state thermal conductivity of type II superconductors. *J. Low Temp. Phys.*, 3:65–87, 1970.

[138] N. V. Zavaritskii. Investigation of the thermal properties of superconductors: 1. tin (down to 0.15K). *J. Exptl. Theoret. Phys.*, 33:1085–1098, 1957.

[139] L. Taillefer, B. Ellman, B. Lussier, and M. Poirier. On the gap structure of UPt_3: phases A and B. *Physica B, Proceedings SCES96*, 1996 (to be published).

[140] M. J. Graf, S.-K. Yip, and J. A. Sauls. Thermal conductivity at very low temperatures in UPt_3. *preprint*, 1996.

[141] R. Joynt. The phase diagram of UPt_3: a status report. *J. Magn. Magn. Mater.*, 108:31–34, 1992.

[142] V. Ambegaokar and A. Griffin. Theory of the thermal conductivity of superconducting alloys with paramagnetic impurities. *Phys. Rev.*, 137:A1151–A1167, 1965.

[143] B. Lussier, B. Ellman, and L. Taillefer. Determination of the gap structure in UPt_3 by thermal conductivity. *Phys. Rev. B*, 53:5145–5148, 1996.

[144] H. Suderow, J. P. Brison, A. D. Huxley, and J. Flouquet. *Physica B, Proceedings SCES96*, 1996 (to be published).

[145] J. Moreno and P. Coleman. Thermal currents in highly correlated systems. *preprint*, 1996.

[146] D. E. MacLaughlin, C. Tien, W. G. Clark, M. D. Lan, Z. Fisk, J. L. Smith, and H. R. Ott. Nuclear magnetic resonance and heavy-fermion superconductivity in $(U,Th)Be_{13}$. *Phys. Rev. Lett.*, 53:1833–1836, 1984.

[147] U. Gottwick, R. Held, G. Sparn, F. Steglich, H. Rietschel, D. Ewert, B. Renker, W. Bauhofer, S. von Molnar, M. Wilhelm, and H. E. Hoenig. Transport properties of $YBa_2Cu_3O_7$: resistivity, thermal conductivity, thermopower and Hall effect. *Europhys. Lett.*, 4:1183–1188, 1987.

[148] J. E. Graebner, L. F. Schneemeyer, R. J. Cava, J. V. Waszczak, and E. A. Rietmaan. *Symp. Proc. Mater. Res. Soc.*, 99:745–748, 1988.

[149] G. Sparn, M. Baenitz, S. Horn, F. Steglich, W. Assmus, T. Wolf, and A. Kapitulnik. Evidence for an intrinsic linear term in the T-dependence of the thermal conductivity of superconducting $YBa_2Cu_3O_7$ and $Bi_2Sr_2CaCu_2O_8$. *Physica C*, 162-164:508–509, 1989.

[150] C. D. Bredl, K. Petersen, S. Arnold, G. Sparn, F. Steglich, S. Takahashi, M. Tachiki, and B. Runtsch. Anisotropic low-temperature heat transport in $YBa_2Cu_3O_{6.9}$ single crystal. *Z. Phys. B - Cond. Matt.*, 86:187–191, 1992.

[151] M. Tachiki, S. Takahashi, F. Steglich, and H. Adrian. Tunneling conductance in layered oxide superconductors. *Z. Phys. B: Cond. Matt.*, 80:161–166, 1990.

[152] K. Behnia, L. Taillefer, R. Gagnon, Z. Gold, and M. Ribault. Low-temperature in-plane thermal conductivity of untwinned $YBaCu_3O_{6.9}$ crystals. *Synthetic Metals*, 71:1611–1612, 1995.

[153] R. Gagnon. private communication, 1996.

[154] R. Gagnon, S. Pu, B. Ellman, and L. Taillefer. Anisotropy of heat conduction in $YBa_2Cu_3O_{6.9}$: Onset of chain superconductivity. 1996 (to be published).

[155] K. Zhang, D. A. Bonn, S. Kamal, R. Liang, D. J. Baar, W. N. Hardy, D. Basov, and T. Timusk. Measurement of the *ab* plane anisotropy of microwave surface impedance of untwinned $YBa_2Cu_3O_{6.95}$ single crystals. *Phys. Rev. Lett.*, 73:2484–2487, 1994.

[156] L. Wand, G. Sparn, F. Steglich, X. Liu, J. Wosnitza, H. v. Löhneysen, A. Erb, M. Kläser, and G. Müller-Vogt. Anisotropy of in-plane thermal conductivity in $YBa_2Cu_3O_{7-\delta}$. *J. Low Temp. Phys.*, 1996 (to be published).

[157] M. N. Nuñez Regueiro and Darío Castello. Thermal conductivity of high temperature superconductors. *Int. J. Mod. Phys. B*, 5:2003–2035, 1991.

[158] Bernasconi et al. *Physica C*, 153-155:1034, 1988.

[159] K. Behnia, H. Aubin, L. Taillefer, and R. Gagnon. Low temperature thermal conductivity of twinned Zn-doped YBCO: evidence for impurity-induced electronic bound states. private communication, 1996.

[160] R. Berman, F. E. Simon, and J. M. Ziman. The thermal conductivity of diamond at low temperatures. *Proc. Roy. Soc. (London)*, A220:171–183, 1953.

[161] R. Berman, E. L. Foster, and J. M. Ziman. Thermal conduction in artificial sapphire crystals at low temperatures. *Proc. Roy. Soc. (London)*, A231:130–144, 1955.

[162] B. N. Sun, K. N. R. Taylor, B. Hunter, D. N. Matthews, S. Ashby, and K. Sealey. Two classes of growth spirals on single crystals of YBCO. *J. of Crystal Growth*, 108:473–481, 1991.

[163] B. Lussier, L. Taillefer, W. J. L. Buyers, T. E. Mason, and T. Petersen. Influence of a magnetic field on the antiferromagnetic order in UPt_3. *Phys. Rev. B*, 54:R6873–R6876, 1996.

[164] C. L. Broholm, J. K. Kjems, W. J. L. Buyers, P. Matthews, T. T. M. Palstra, A. A. Menovsky, and J. A. Mydosh. Magnetic excitations and ordering in the heavy-electron superconductor URu_2Si_2. *Phys. Rev. Lett.*, 58:1467–1471, 1987.

[165] T. E. Mason, B. D. Gaulin, J. D. Garrett, Z. Tun, W. J. L. Buyers, and E. D. Isaacs. Neutron-scattering measurements of long-range antiferromagnetic order in URu_2Si_2. *Phys. Rev. Lett.*, 65:3189–3192, 1990.

[166] A. Krimmel, P. Fischer, B. Roessli, H. Maletta, C. Geibel, C. Schank, A. Grauel, A. Loidl, and F. Steglich. Neutron diffraction study of the heavy fermion superconductors UM_2Al_3 (M=Pd, Ni). *Z. Phys. B*, 86:161–162, 1992.

[167] T. T. M. Palstra, A. A. Menovsky, J. van den Berg, A. J. Dirkmaat, P. H. Kes, G. J. Nieuwenhuys, and J. A. Mydosh. Superconducting and magnetic transitions in the heavy-fermion system URu_2Si_2. *Phys. Rev. Lett.*, 55:2727–2730, 1985.

[168] R. A. Fisher, B. F. Woodfield, S. Kim, N. E. Phillips, L. Taillefer, A. L. Giorgi, and J. L. Smith. Specific heat of UPt_3 in the vicinity of the antiferromagnetic ordering at 5 K. *Solid State Comm.*, 80:263–266, 1991.

[169] B. D. Gaulin, D. Gibbs, E. D. Isaacs, J. G. Lussier, J. N. Reimers, A. Schröder, L. Taillefer, and P. Zschack. Resonant magnetic X-ray scattering study of phase transitions in UPd_2Al_3. *Phys. Rev. Lett.*, 73:890–893, 1994.

[170] T. Petersen, T. E. Mason, G. Aeppli, A. P. Ramirez, E. Bucher, and R. N. Kleiman. Magnetic fluctuations and the superconducting transition in the heavy-fermion material UPd_2Al_3. *Physica B*, 199-200:151–153, 1994.

[171] T. E. Mason, H. Lin, M. F. Collins, W. J. L. Buyers, A. A. Menovsky, and J. A. Mydosh. Antiferromagnetism and superconductivity in URu_2Si_2. *Physica B*, 163:45–48, 1990.

[172] K. Hasselbach, L. Taillefer, and J. Flouquet. Critical point in the superconducting phase diagram of UPt_3. *Phys. Rev. Lett.*, 63:93–96, 1989.

[173] L. Taillefer, F. Piquemal, and J. Flouquet. The anisotropic magnetoresistancce of UPt_3 at low temperaatures. *Physica C*, 153-155:451–452, 1988.

[174] R. Joynt, V. P. Mineev, G. E. Volovik, and M. E. Zhitomirsky. Possible phase diagrams of superconducting UPt_3. *Phys. Rev. B*, 42:2014–2022, 1990.

[175] S. Yip and A. Garg. Superconducting states of reduced symmetry: general order parameters and physical implications. *Phys. Rev. B*, 48:3304–3308, 1993.

[176] R. Heid, Ya B. Bazaliy, V. Martisovitz, and D. L. Cox. Staggered superconductivity in UPt_3: a new phenomenological approach. *Phys. Rev. Lett.*, 74:2571–2573, 1995.

[177] L. Taillefer, K. Behnia, K. Hasselbach, J. Flouquet, S. M. Hayden, and C. Vettier. On the superconductivity phase transitions of UPt_3. *J. Magn. Magn. Mat.*, 90-91:623–627, 1990.

[178] D. F. Agterberg and M. B. Walker. Ginzburg-landau model of hexagonal superconductors: Application to UPt_3. *Phys. Rev. B*, 51:8481–8488, 1995.

[179] C. G. Windsor. *Methods of experimental physics*, volume 23, part A, chapter 3, pages 197–249. Academic press, 1987.

[180] H. Kita, A. Dönni, Y. Endoh, K. Kakurai, N. Sato, and T. Komatsubara. Single crystal neutron diffraction study of the magnetic phase diagram of the heavy fermion superconductor UPd_2Al_3. *J. Phys. Soc. Japan*, 63:726–735, 1994.

[181] T. E. Mason. private communication, 1995.

[182] A. Schröder, J. G. Lussier, B. D. Gaulin, J. D. Garrett, W. J. L. Buyers, L. Rebesky, and S. M. Shapiro. Incommensurate magnetic order in the heavy fermion superconductor UNi_2Al_3. *Phys. Rev. Lett.*, 72:136–139, 1994.

[183] B. D. Gaulin. private communication, 1995.

[184] J. Rossat-Mignod, G.H. Lander, and P. Burlet. In A.J. Freeman and G.H. Lander, editors, *Handbook on the Physics and Chemistry of Actinides*, volume 1, page 415. Elsevier, Amsterdam, 1984.

[185] K. A. McEwen, U. Steigenberger, K. N. Clausen, Y. J. Bi, M. B. Walker, and C. Kappler. Neutron scattering study of the antiferroquadrupolar structure and order parameter of UPd_3. *Physica B*, 213:128–130, 1995.

[186] D. F. Agterberg and M. B. Walker. Theory for the angular dependence of the upper critical field of superconducting UPt_3. *Phys. Rev. Lett.*, 74:3904–3905, 1995.

IMAGE EVALUATION
TEST TARGET (QA-3)

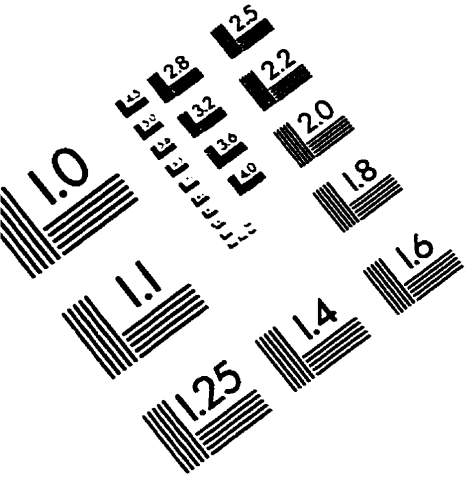

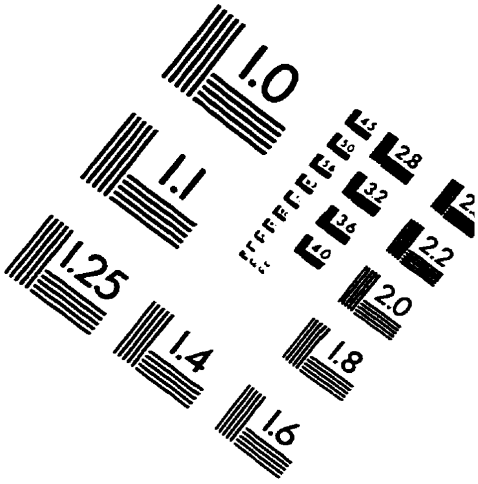

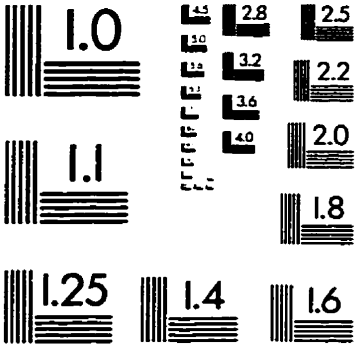

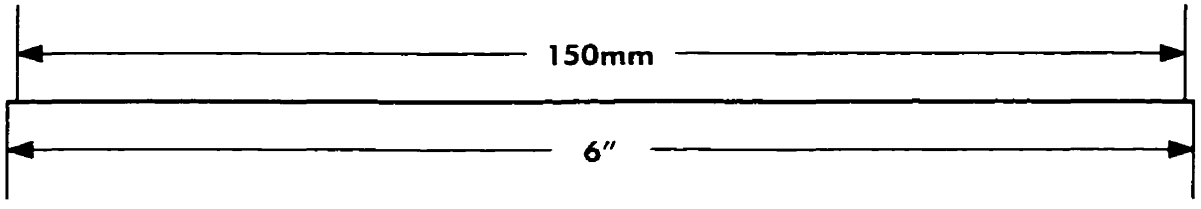

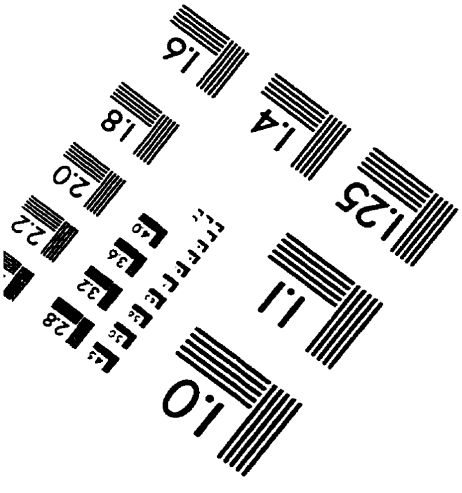

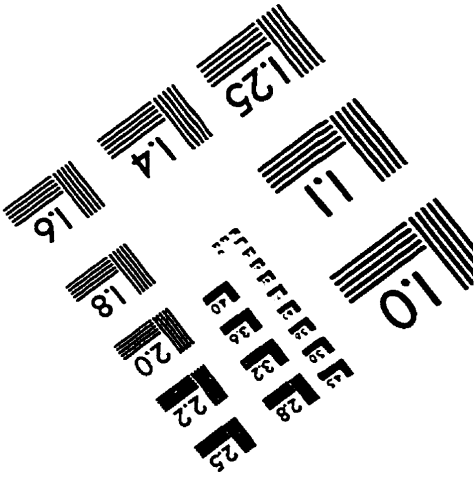

APPLIED IMAGE, Inc
1653 East Main Street
Rochester, NY 14609 USA
Phone: 716/482-0300
Fax: 716/288-5989